High resolution spectroscopy and collision studies with velocity-controlled OH beams

Proefschrift

ter verkrijging van de graad van doctor
aan de Radboud Universiteit Nijmegen
op gezag van de rector magnificus prof. dr. Th.L.M. Engelen
volgens besluit van het college van decanen
in het openbaar te verdedigen op
vrijdag 29 mei 2015
om 14.00 uur precies

door

Hanns Christian Schewe

geboren op 04 januari 1982
te Karlsruhe, Duitsland

Promotor : Prof. dr. G.J.M. Meijer

Copromotoren : Dr. S.Y.T. van de Meerakker

: Dr. N. Vanhaecke
Fritz-Haber-Institut der Max-Planck-Gesellschaft,
Berlin, Duitsland
Laboratoire Aimé Cotton,
Orsay, Frankrijk

Manuscriptcommissie : Prof. dr. D.H. Parker

: Prof. dr. ir. G.C. Groenenboom

: Prof. dr. A. Osterwalder
Ecole Polytechnique Fédérale de Lausanne,
Lausanne, Zwitserland

The work described in this thesis has been performed at the Fritz-Haber-Institut der Max-Planck-Gesellschaft in Berlin, Germany.

High resolution spectroscopy and collision studies with velocity-controlled OH beams

Doctoral thesis

to obtain the degree of doctor
from Radboud University Nijmegen
on the authority of the Rector Magnificus prof. dr. Th.L.M. Engelen
according to the decision of the Council of Deans
to be defended in public on
Friday, 29 May 2015
at precisely 14.00 hours

by

Hanns Christian Schewe

born on 04 January 1982
in Karlsruhe, Germany

Supervisor : Prof. dr. G.J.M. Meijer

Co-supervisors : Dr. S.Y.T. van de Meerakker

: Dr. N. Vanhaecke
Fritz-Haber-Institut der Max-Planck-Gesellschaft,
Berlin, Germany
Laboratoire Aimé Cotton,
Orsay, France

Manuscript Committee : Prof. dr. D.H. Parker

: Prof. dr. ir. G.C. Groenenboom

: Prof. dr. A. Osterwalder
Ecole Polytechnique Fédérale de Lausanne,
Lausanne, Switzerland

The work described in this thesis has been performed at the Fritz-Haber-Institut der Max-Planck-Gesellschaft in Berlin, Germany.

Contents

1 Introduction **1**

1.1 Popular science introduction 1

1.2 What makes cold molecules so special? 2

1.3 Outline of this thesis 5

2 Molecular properties of OH and H_2 **7**

2.1 Energy level structure of OH 8

2.1.1 Electronic ground state 9

2.1.2 First electronically excited state of OH 14

2.2 Stark and Zeeman effect in OH 15

2.2.1 The Stark-effect in OH 15

2.2.2 The Zeeman-effect in OH 18

2.2.3 Combined electric and magnetic fields 21

2.3 A - X transitions and their probabilities 23

2.4 Molecular properties of H_2 27

3 Experimental setup **33**

3.1 Production of molecular beams 35

3.1.1 Production of OH packets 36

3.1.2 Production and characterization of target beams . . 38

3.2 Stark deceleration 46

3.3 Detection methods 51

4 Bunching of molecular beams **55**

4.1 Introduction 55

4.2 Experimental methods and data analysis 59

4.3 Implementation of different bunching schemes 67

4.4 Conclusion 76

5 Spectroscopic investigations on the electric and the magnetic transition dipole moments in the $A-X$ band of OH 79

5.1 Introduction 79
5.2 Experimental setup and procedures 81
5.3 Theoretical descriptions of the E1 and M1 transitions . . . 84
5.4 Determination of the ratio of E1-M1 using Stark-spectroscopy 88
5.5 Observation of the Stark interference 92
5.6 Conclusion and outlook 102

6 Molecular beam and scattering dynamics 105

6.1 Introduction 105
6.2 Kinematics and collision energy 107
  6.2.1 Kinematics of the beams' overlap 112
  6.2.2 Evolution of the scattering signal 116
  6.2.3 Evolution of the collision energy 121
  6.2.4 Evolution of the collision energy distribution 122
6.3 Experimental procedure and data analysis 123
  6.3.1 Tuning of the collision energy 123
  6.3.2 Definition of signals 125
  6.3.3 Calibration of the collision energy 127
  6.3.4 Calibration of flux-mode conditions 140
6.4 Conclusion 145

7 State-to-state inelastic scattering of OH and hydrogen 147

7.1 Introduction 147
7.2 Experimental setup and method 151
7.3 Theory 153
7.4 Results and discussion 154
  7.4.1 State-to-state relative inelastic cross sections of OH scattering with nH_2 or pcH_2 155
  7.4.2 Relative cross sections for OH with para-H_2(J=0) or ortho-H_2(J=1) 159
  7.4.3 Comparison of signal intensity ratios 163
  7.4.4 Comparison of OH colliding with H_2 and other targets 164
7.5 Conclusion 169

8 **Crossed beam scattering with high collision energy resolution** **171**
8.1 Introduction 171
8.2 Scattering experiments and optimization of the collision energy resolution 174
8.2.1 Experimental procedures 182
8.3 Results and Discussion 185
8.3.1 Improving the resolution of the collision energy . . . 186
8.3.2 Investigations on the threshold behaviour 190
8.4 Conclusion 197

9 **Conclusion** **199**

Bibliography **203**

Appendix A **215**

Appendix B **219**

Appendix C **221**

Appendix D **223**

Samenvatting **227**

Summary **231**

Chapter 1

Introduction

1.1 Popular science introduction

One of the most basic characteristics of human beings is the curiosity to understand how things work together. Everyone has experienced the feeling of being attracted to an unknown phenomena in the world for the first time, such as wind in the atmosphere, lightning, or the invisible force of attraction and repulsion between two magnets. Firstly, one tries to get a good view into the unknown, then one goes closer to have a better look. To understand the unknown better, usually the investigations continue by touching it, shedding more light on it to have an even better look or using tools for further interrogations. In natural science, these tools become even more advanced over centuries, e.g., people used to use magnifying glasses, where nowadays microscopes are employed. Nevertheless, the method is still the same in a laboratory: one needs to isolate or control the unknown object of interest in order to have a better or highly resolved look into the structure or the dynamics.

On the other hand, natural scientists not only want to analyse the phenomena, they also want to get an intuitive and quantitative understanding of them. To this end, theoretical models are developed not only to understand, what the underlying processes are, but also to have a quantitative description of such underlying processes. Eventually, many different phenomena can be related or reduced to a few principles or mechanisms, which also define the scientific point of view of the world. Apart from this philosophical aspect, man has used this knowledge and explored these natural properties in countless applications like flaming gas to heat shelters or cook food, and using steam pressure to run an engine, etc.

The goal of molecular physics and chemistry is to understand the phenomena governing the structure and properties of molecules as well as the interactions between them. There exist two basic experimental techniques that can be conducted in an experiment: spectroscopy and collision studies. While spectroscopic studies investigate the interaction of light with molecules, collision studies look into the interaction governing the scattering process of molecules. In this respect, the work of this thesis can be introduced as the next step to use the high amount of control over molecular degrees of freedom to study the interactions with light and other molecules. In fact, the experiments in this thesis are performed using a particular molecule only, the hydroxyl-radical (OH). The tool used to manipulate OH is a Stark-decelerator, which exploits the force that an inhomogeneous static electric field exerts on the molecule's electric dipole. In spectroscopic experiments a so-called interference effect is observed and used when OH interacts with the electromagnetic wave of a laser under the influence of externally applied static electric and static magnetic fields. Collision studies between OH radicals and hydrogen molecules are used to determine the underlying rules that govern the energy transfers resulting in an excitation of the OH radical's rotations.

1.2 What makes cold molecules so special?

A detailed understanding of the properties and dynamics of molecules is of fundamental importance to many areas of physics, chemistry and biology. Since the theory of quantum mechanics became increasingly accepted in the 1920s, numerous experimental and theoretical approaches have been undertaken to understand and to confirm this theory. Now, quantum properties are being explored with many technologies such as lasers and transistors. While many experiments have been performed with ultra-cold atoms so far, ultra-cold molecules are becoming more and more attractive because they offer more degrees of freedom which enrich the interactions, and because the experimental techniques have been developed to be able to cool and control molecules to the temperatures needed to observe quantum mechanical effects. Usually the distinction between the cold and the ultra-cold regimen is made by looking at the scattering wave function of the colliding particles. This scattering wave function can be decomposed into partial waves which describes the contribution of the various angular momenta to the rotational motion. Ultra-cold temperatures ($\leq$ 1 mK) are characterized where in the collisions only a single partial wave is present. The collision process of two bosons or two distinct particles is determined by s-wave scattering while the collisions of identical fermions follow p-wave scattering. In the cold regime, temperatures range between 1 mK $-$ 5 K. In the collision process, several partial waves contribute which causes wave-phenomena like scattering resonances or partial wave interferences [1].

Thus far, the ultra-cold regime has been reached with a small class of atomic species that can be laser-cooled. Many experimental techniques, such as buffer gas cooling [2], Stark- and Zeeman-deceleration [3, 4] have been developed to create molecular ensembles at cold temperatures, while the photo-association of ultra-cold atoms [5, 6] allowed to create molecular ensembles at ultra-cold temperatures [7]. The success of molecular explorations will provide direct cooling techniques for a large variety of molecular species to access the ultra-cold regime. New phenomena and effects in physics and chemistry are expected and predicted for molecular species at these low temperatures. However, the dynamics governing interactions in the cold regime are already dominated by quantum mechanical effects. There, classical mechanics cannot sufficiently describe scattering processes, because the de Broglie wavelengths of the colliding particles are of comparable size or even larger than the effective molecular interaction ranges. Long-range interactions, which are described theoretically by the attractive part within the potential energy surface (PES), have a profound influence on collision processes, leading to new types of novel quantum phases, chemical reactions, strongly correlated quantum systems, and precision measurements [8].

To investigate these phenomena in a meaningful and reproducible way, scientists try to isolate the object of interest from the influence of its surroundings, such as the liquid phase of an ocean or biological system, or the gas phase of the atmosphere. Over centuries, scientists have invented more and more sophisticated experimental techniques to refine results or to observe new effects. To study phenomena in the gas phase, molecular beams are an indispensable tool for the physics and chemistry community [9] [10] [11]. For decades their application in research and technology has aided numerous investigations in spectroscopy or crossed beam collision experiments. During the last decade, the production and the manipulation of molecular beams has been optimized by developing new powerful techniques. New valve designs offer more extreme stagnation conditions such as shorter opening times and the access of larger temperature and pressure ranges [12, 13, 14], which pushed the limits of adiabatic expansion of gases further to regions where the resulting beams are internally colder, and where quantum effects gained considerable influence. This enabled the investigation of a large variety of molecules in novel scattering experiments at low collision energies, for example, in crossed beam experiments with a very small angle collisions at a few Kelvin are investigated [15], while collisions at sub-Kelvin temperatures were observed in merged beam scattering experiments [16, 17]. Collisions and chemical reactions have been observed between ultra-cold molecules, which have been created from ultra-cold atoms [18, 19]. Additionally, when the formation of helium clusters became available, high-resolution spectroscopy was advanced [20, 21].

The manipulation of molecular beams has advanced since 1922, when Otto Stern and Walther Gerlach conducted a groundbreaking experiment where they deflected a beam of silver atoms using the interaction of the atom's magnetic moment with an externally applied inhomogeneous magnetic field. The current progress in technology has allowed better vacuum, the application and the switching of even higher voltages and currents and paved the way for a new generation of experiments. By exploring, for example, the Stark- or the Zeeman-effect of particles with inhomogeneous electric or magnetic fields, respectively, additional manipulation of the motion and quantum-state selection of molecular packets becomes possible [22]. The advent of the Stark- and Zeeman deceleration techniques additionally offer full control over the translational velocity of the particles [3] [4]. The improvement of powerful laser systems and detection techniques allows new ground breaking experiments become possible: the resolution in spectroscopy can be increased due to a longer interaction time between molecule and light, scattering experiments can be performed with unprecedented detail in the collision energy resolution [16] [23], and the deceleration and trapping of molecules in the laboratory frame allows the implementation of further laser cooling [24] or evaporative cooling methods [25].

1.3 Outline of this thesis

The unifying theme of this thesis is to conduct experiments with an improved resolution using Stark-decelerated beams of OH radicals. Different concepts and methods are developed and implemented in the experimental setup. Producing colder OH beams allows the observation of quantum effects in high resolution spectroscopy. In crossed beam scattering experiments, the quantum-state purity as well as the collision energy resolution is increased to obtain inelastic cross sections on a state-to-state level. This thesis is structured as follows:

Chapter 2 introduces the physical and chemical properties of the OH radical and the H_2 molecule, as well as the nomenclature needed to understand the conducted experiments and their analysis. In chapter 3, the reader is acquainted to the experimental setup and its properties; particularly, to the molecular beam sources, the Stark-decelerator and the detection methods.

In chapter 4, an alternative approach is presented for the manipulation of molecular packets using the existing Stark-decelerator. So-called bunching schemes are implemented using different high voltage switching schemes. The aim of this chapter is to demonstrate how the phase-space distribution of the molecular packet can be shaped in one longitudinal and two transverse dimensions. Individual dimensions or combinations of them can only be manipulated using a dedicated high voltage switching scheme. As an application, the distributions are rotated in phase-space such that its width in the velocity-space is minimized. Thus, a cooling of the molecular packet in the corresponding phase-space dimension down to hundreds of micro-Kelvin is achieved.

Chapter 5 describes different methods that are implemented in the experimental setup, which enable the measurement of the ratio of the electric and magnetic transition dipole moments along the $A - X$ band by externally applying a static electric field in a controlled manner. Additionally superimposing a static magnetic field, a Stark-interference is observed which allows not only the determination of the ratio of the electric and the magnetic transition dipole moments but also their relative sign.

Chapters 6, 7 and 8 focus on the OH-H_2 scattering. Chapter 6 introduces the crossed beam setup, which shows an increased sensitivity to inherent properties of molecular beams. The influence of correlations in the molecular beams and the resulting kinematic effects on the scattering process are modeled and simulated in detail with focus on the calibration of the collision energy and the collision energy resolution.

Chapter 7 presents the investigations of Stark-decelerated OH radicals colliding with H_2 molecules. The inelastic scattering process depends crucially on the rotational state of the H_2 molecule. Due to the high quantum-state purity in the experiment the various multipole interactions are studied on a state-to-state level. The experimental observations are compared with theory. Absolute integral cross sections are derived from quantum close-coupling scattering calculations performed on a newly state-of-the-art compiled *ab initio* OH-H_2 PES. The theoretical cross sections reproduce the experimentally observed cross sections qualitatively and quantitatively with very good agreement. The OH - H_2 system is ideal to study the collision process between two diatomic molecules; first because similarities to the OH-rare gas systems are observed, secondly because the increasing complexity of higher order multipole interactions becomes significant.

Chapter 8 illustrates different strategies by which to increase the collision energy resolution. These are implemented in the experimental setup. With this increased resolution, structures in the excitation function are resolved and compared with theory.

Chapter 9 provides a conclusion to this thesis.

Chapter 2

Molecular properties of OH and H_2

The goal of this chapter is to acquaint the reader to the molecular properties of the hydroxyl radical (OH) and the hydrogen molecule alongside with the nomenclature used to describe the experiments throughout the thesis. Different properties of the energy level structure of OH are of interest: the detection of OH requires a detailed knowledge on the electronic, vibrational, and rotational (rovibronic) ground and excited states which determine electromagnetically allowed transitions. Experiments on the manipulation of OH with the Stark-decelerator and the ongoing dynamics in spectroscopic experiments demand detailed knowledge on interactions in external electric and magnetic fields with the effects of nuclear spin included. For the inelastic scattering experiments the ground state energy level structure including the spin-orbit, the rotational, and the Λ-doubling interactions are of interest. This chapter is structured as follows: firstly, the energy level structure of OH in the field-free case is discussed which reviews the coupling of electronic and orbital angular momenta in the ground and the excited state; secondly, the interactions with external static and magnetic fields are discussed. Thirdly, the laser excitation of electric and magnetic dipole transitions between the ground and the electronically excited state are discussed. In a fourth section, molecular properties of H_2 are reviewed.

2.1 Energy level structure of OH

The energy level structure of molecules is defined by the Eigenfunctions $|\Psi_{mol}\rangle$ of its molecular Hamilton operator ($\hat{\mathbf{H}}_{mol}$). Following the Born-Oppenheimer approximation, the nuclear parts of the wavefunction can be separated form the electronic part: $|\Psi_{mol}\rangle = |\Psi_{nuc}\rangle \cdot |\Psi_{el}\rangle$ [26]. Furthermore, the nuclear part is considered to create an effective internuclear potential that defines the different $|\Psi_{el}\rangle$, while the electronic Eigenstates create a potential for the positions of the nuclei. This interdependency of the motion of the nuclei and the electrons leads to the approximation where the electronic, vibrational and rotational motion is treated separately:

$$\hat{\mathbf{H}}_{mol} \approx \hat{\mathbf{H}}_{el} + \hat{\mathbf{H}}_{vib} + \hat{\mathbf{H}}_{rot}. \tag{2.1}$$

This separation can be justified also in terms of electronic, vibrational and rotational energies and periods of the oscillations, because their ratios differ usually by orders of magnitude. In OH, the first electronic excitation along the $A-X$ transition amounts to ~ 32000 cm^{-1}, while the vibrational energy splittings lie around ~ 3000 cm^{-1}. The combination of a heavy oxygen atom and a light hydrogen atom leads to a large rotational constant in OH causing a rotational energy splitting on the order of ~ 100 cm^{-1} in the vibronic ground state. OH is an open-shell molecule with one unpaired electron which gives rise to an electronic orbital ($\mathbf{L}$) and spin ($\mathbf{S}$) angular momentum. Additionally, the hydrogen atom has a nuclear spin angular momentum ($\mathbf{I}$) that causes a hyperfine interaction. In general, the different angular momenta coupling schemes of the electron and the rotation of diatomic molecules are idealized by the five Hund's cases (a) to (e) [27]. For spectroscopic calculations one usually starts in a basis that couples angular momenta such that the Hamiltonian is already almost diagonal by taking molecule specific constants into account. Following the separation of $\hat{\mathbf{H}}_{mol}$ in its different contributions also the wavefunction $|\Psi_{mol}\rangle$ can be found as the tensor product of the eigenfunctions of the different Hamilton operators

$$|\Psi_{mol}\rangle = |\Psi_{el}\rangle|\Psi_{vib}\rangle|\Psi_{rot}\rangle \tag{2.2}$$

where the electronic wavefunction $|\Psi_{el}\rangle$ describes the quantum state of the orbital and the spin part of the electronic structure, the vibrational wavefunction $|\Psi_{vib}\rangle$ defines the vibrational state. The rotational wavefunction

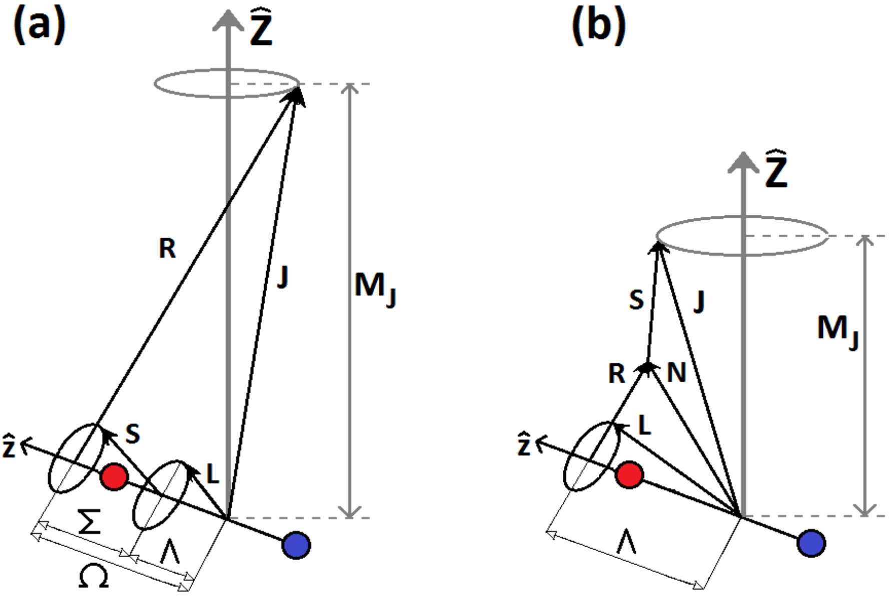

Figure 2.1: The left and the right drawings show Hund's cases (a) and (b), respectively. The $\hat{z}$-axis in the molecule-fixed frame is along the internuclear axis of the molecule. The space-fixed frame is drawn in grey, where $\hat{Z}$-axis depicts the space-fixed quantization axis.

$|\Psi_{rot}\rangle$ is the part which is discussed intensively in the following together with several other couplings like Λ-doubling and hyperfine interactions [28]. In this section the energy level structure of the ground state of OH is described first, which shows an intermediate coupling of the Hund's cases (a) and (b), followed by the excited state which is best described by a Hund's case (b). Figure 2.1 shows schematic drawings of the Hund's case (a) and (b).

2.1.1 Electronic ground state

In the united atom picture the electron configuration in the ground state of OH is: $(1s\sigma)^2$ $(2s\sigma)^2$ $(2p\sigma)^2$ $(2p\pi)^3$, which leads to a ground state of

$^2\Pi$ character. For low rotational states, the Hund's (a) coupling scheme describes the OH molecule best which is depicted schematically in the left graph (a) of Figure 2.1 [27]. Here, **L** and **S** couple electrostatically to the internuclear axis. The projection of **L** and **S** onto the internuclear axis is given by $\Lambda = \pm 1$ and $\Sigma = \pm 1/2$, respectively. They form the total electronic angular momentum $\Omega = \Lambda + \Sigma$. The end-over-end rotation of the two nuclei in OH is described by **R**. Together with **L** and **S** it forms the total molecular angular momentum

$$\mathbf{J} = \mathbf{L} + \mathbf{S} + \mathbf{R}. \tag{2.3}$$

The Hamilton operator describing the rotational motion is given by the end-over-end rotation of the molecule and the spin-orbit coupling

$$\hat{\mathbf{H}}^{v}_{rot} = B_v(\mathbf{J} - \mathbf{L} - \mathbf{S})^2 + A_v\mathbf{L} \cdot \mathbf{S}. \tag{2.4}$$

The rotational constant and the spin-orbit coupling constant are denoted by B_v and A_v, respectively, while both of them are a function of the vibrational quantum number v. In the vibrational ground state, the values are $B_0 = 18.515$ cm^{-1} and $A_0 =$ -139.73 cm^{-1} [29]. The spin-orbit splitting leads to two distinct manifolds, which are denoted by $^2\Pi_{1/2}$ with $\Omega = |\Lambda + \Sigma| = 1/2$ and $^2\Pi_{3/2}$ with $\Omega = 3/2$. Since A_0 is negative, the $^2\Pi_{3/2}$ manifold is lower in energy than the $^2\Pi_{1/2}$. The eigenstates of $\hat{\mathbf{H}}^{v}_{rot}$ can be evaluated with the rigid rotor wavefunctions [27]

$$|J, \Omega, M_J\rangle = \sqrt{\frac{2J+1}{8\pi^2}} D^{(J)*}_{\Omega M_J}(\phi, \theta, \chi), \tag{2.5}$$

The coordinate system in the molecule-fixed (mf) frame is given by ($\hat{x}$, $\hat{y}$, $\hat{z}$), while it is defined by ($\hat{X}$, $\hat{Y}$, $\hat{Z}$) in the space-fixed (sf) frame. Ω and M_J are the projections of **J** onto the molecule-fixed and the space-fixed quantization axis, respectively. In the graphs of Figure 2.1 the $\hat{z}$-axis along the internuclear axis in the molecule-fixed frame and the $\hat{Z}$-axis that could correspond to an external electric or magnetic field vector are chosen as quantization axes. If there is no preferential space-fixed quantization axis the rotational energy levels are degenerate in M_J. The Wigner D-functions[1] relate the orientation of the $\hat{x}$, $\hat{y}$ and $\hat{z}$ to $\hat{X}$, $\hat{Y}$ and $\hat{Z}$ using

---

[1] The complex conjugate of the Wigner D-functions ($D^{(j)*}_{m'm}(\phi, \theta, \chi)$) are eigenfunctions of the Hamiltonian of a spherical and symmetric rigid rotor as they are used in

the Euler angles ϕ, θ and χ.

Since OH has a plane of symmetry ($\hat{x}$, $\hat{y}$), it follows that $\hat{\mathbf{H}}^{v}_{rot}$ is invariant under the inversion of the space-fixed coordinates [26]. Then, parity (p) is a good quantum number. A basis set of symmetrised wavefunctions follows from the linear combinations of the rigid rotor wavefunctions given in equation (2.5). The symmetry of the wavefunction is denoted by $\epsilon = \pm 1$.

$$|J, \mathit{\Omega} \geq 0, M_J, \epsilon = \pm\rangle = \frac{1}{\sqrt{2}}\big[|J, \mathit{\Omega}, M_J\rangle + \epsilon|J, -\mathit{\Omega}, M_J,\rangle\big]. \tag{2.7}$$

This relation also adapts the total parity (p) which is related to the symmetry by [27]:

$$p = \epsilon(-1)^{J-S}. \tag{2.8}$$

However, OH is not a pure Hund's case (a) molecule resulting from the spin orbit interaction (A_0 is finite) in $\hat{\mathbf{H}}^{v}_{rot}$ which mixes the basis wavefunctions of both spin-orbit manifolds such that $\mathit{\Omega}$ becomes a less good quantum number. With increasing J values OH is better described by an intermediate Hund's case (a) and (b) coupling (the Hund's case (b) coupling is discussed in more detail in section 2.1.2). The resulting manifolds are labeled in the literature by F_1 and F_2 to express the difference between the ${}^2\mathit{\Pi}_{3/2}$ and ${}^2\mathit{\Pi}_{1/2}$ manifolds. The eigenfunctions of H^{v}_{rot} are given by [30]:

$$|{}^2\mathit{\Pi}, F_1, J, M_J, \epsilon\rangle = C_1(J)|J, \mathit{\Omega} = \frac{1}{2}, M_J, \epsilon\rangle + C_2(J)|J, \mathit{\Omega} = \frac{3}{2}, M_J, \epsilon\rangle \tag{2.9}$$

$$|{}^2\mathit{\Pi}, F_2, J, M_J, \epsilon\rangle = C_1(J)|J, \mathit{\Omega} = \frac{3}{2}, M_J, \epsilon\rangle - C_2(J)|J, \mathit{\Omega} = \frac{1}{2}, M_J, \epsilon\rangle \tag{2.10}$$

---

equation (2.5). The Wigner D-functions are also used to determine the orientation and projections of an angular momentum operator J from one axis in one frame ($\hat{x}$, $\hat{y}$, $\hat{z}$) onto an axis in a differently oriented frame ($\hat{X}$, $\hat{Y}$, $\hat{Z}$). Geometrically, this can be interpreted as a rotation which is conveniently described by a rotational operator $\boldsymbol{R}(\phi, \theta, \chi)$ where ϕ, θ, χ are Euler angles:

$$D^{(j)}_{m'm}(\phi, \theta, \chi) \equiv \langle j', m'_j|\boldsymbol{R}(\phi, \theta, \chi)|j, m_j\rangle = e^{-im'\phi} d^{(j)}_{mm'}(\theta) e^{-im\chi} \tag{2.6}$$

There exist different conventions to perform this rotation using the Euler angles ϕ, θ and χ. Here, the convention by Zare is used throughout [27].

	$C_1(J)$	$C_2(J)$
$J = 1/2$	0	1
$J = 3/2$	0.173925	0.984759
$J = 5/2$	0.265301	0.964166

Table 2.1: The $C_1(J)$ and $C_2(J)$ coefficients are listed for the relevant rotational states. A complete list can be found for example in [27].

The admixed contribution to the manifold is determined by the coefficients:

$$C_1(J) = \sqrt{\frac{X+Y-2}{2X}} \quad (2.11) \qquad C_2(J) = \sqrt{\frac{X-Y+2}{2X}} \quad (2.12)$$

where X and Y are

$$X = \sqrt{4(J+\frac{1}{2})^2 + Y(Y-4)} \quad (2.13) \qquad Y = \frac{A_v}{B_v} \quad (2.14)$$

This mixed character has a direct influence on the Stark- and Zeeman-interactions which will be discussed in section 2.2. The values $C_1(J)$ and $C_2(J)$ are listed in Table 2.1. However, for low J values the amount of mixing is small such that Ω can be considered a good quantum number. The rotational energy levels in the field-free case are given by:

$$|^2\Pi, F_1, J, M_J, \epsilon\rangle = B_v\big[(J+\frac{1}{2})^2 - 1 - \frac{1}{2}X\big] \quad (2.15)$$

$$|^2\Pi, F_2, J, M_J, \epsilon\rangle = B_v\big[(J+\frac{1}{2})^2 - 1 + \frac{1}{2}X\big] \quad (2.16)$$

The interaction between the electrons' orbital angular momentum **L** and the nuclei's rotation **R** induces a mixing between the $^2\Pi$ ground state and the electronically excited state $^2\Sigma^+$. This is a second order effect which lifts the degeneracy of each rotational level with ϵ = +1 and ϵ = -1 and splits these into a so-called Λ-doublet [31]. The splitting increases with increasing J and is given for the two spin-orbit manifolds by

$$E_{\Lambda}^{^2\Pi,F_1} = (q+\tfrac{1}{2}p)(C_1(J))^2(2J+1) + q(C_1(J)C_2(J))(2J+1)\sqrt{(J-\frac{1}{2})(J+\frac{3}{2})} \tag{2.17}$$

$$E_{\Lambda}^{^2\Pi,F_2} = (q+\tfrac{1}{2}p)(C_2(J))^2(2J+1) - q(C_1(J)C_2(J))(2J+1)\sqrt{(J-\frac{1}{2})(J+\frac{3}{2})} \tag{2.18}$$

with the parameters q = -580.100 MHz and p = 2366.003 MHz [32] [33]. The Λ-doublet splitting in the OH ground state is $E_{\Lambda}^{^2\Pi F_1}$ = 1665.402 MHz (0.055 cm^{-1}). The total parity given by equation (2.8) alternates with J between the energetically lower and upper Λ-doublet states. In literature a spectroscopic parity convention is introduced [34], where the symmetries ϵ = +1 and ϵ = -1 are labeled with e and f exclusive of the J-state, respectively. The left graph of Figure 2.4 shows in its lower part the two spin-orbit manifolds ($X^2\Pi\ F_1$ and $X^2\Pi\ F_2$) of the rotational energy levels of the vibronic ground state. The Λ-doublet splittings are exaggerated to allocate the corresponding quantum numbers and parity labellings.

The nuclear spin ($\mathbf{I}$ = 1/2) of the hydrogen in OH causes a hyperfine interaction. The coupling of $\mathbf{I}$ and $\mathbf{J}$ forms the total hyperfine angular momentum: $\mathbf{F} = \mathbf{I} + \mathbf{J}$ [35]. This leads to an additional splitting: in the ground state each Λ-doublet component splits into two hyperfine levels denoted: $F = 1$ and $F = 2$. The new rotational hyperfine basis set follows from transforming the parity adapted basis defined in equation (2.7) with Clebsch-Gordan coefficients to

$$|^2\Pi, J, \Omega, I, F, M_F, p\rangle = \sum_{M_J, M_I} |^2\Pi, J, M_J, \Omega, p\rangle |I, M_I\rangle \langle J, M_J, I, M_I | F, M_F\rangle, \tag{2.19}$$

or for the basis set given in equation (2.15):

$$|^2\Pi, F_1, J, I, F, M_F, p\rangle =$$
$$= \sum_{M_J, M_I} |^2\Pi, F_1, J, M_J, p\rangle |I, M_I\rangle \langle J, M_J, I, M_I | F, M_F\rangle, \qquad (2.20)$$

where M_F is the projection of the hyperfine quantum number F onto a space-fixed axis. The right graph of Figure 2.4 shows the hyperfine energy level structure of the rovibrational ground state.

2.1.2 First electronically excited state of OH

In the united atom picture the first electronically excited state results from the promotion of an electron from the $(2p\sigma)$ to the $(2p\pi)$ orbital. The resulting electron configuration is $(1\mathrm{s}\sigma)^2$ $(2\mathrm{s}\sigma)^2$ $(2\mathrm{p}\sigma)$ $(2\mathrm{p}\pi)^4$ which leads to an excited state of $^2\Sigma^+$ character. The angular momentum coupling is best described by Hund's case (b), because $\Lambda = 0$ and $\Sigma = 1/2$. Thus, the spin-orbit coupling is non-existing. The total orbital rotational angular momentum ($\mathbf{N}$) is a good quantum number in this coupling scheme [27]. It is defined by: $\mathbf{N} = \mathbf{R} + \mathbf{L}$. In this case the rotational Hamiltonian consists of the end-over-end rotational motion of the molecule and the spin-rotation coupling

$$\hat{\mathbf{H}}^v_{rot} = B_v(\mathbf{N})^2 + \gamma_v \mathbf{N} \cdot \mathbf{S}, \qquad (2.21)$$

where the values of the rotational constants are $B_0 = 16.961$ cm^{-1} and $B_1 = 16.129$ cm^{-1} [29]. The spin-rotation coupling causes a so-called ρ-doubling where each rotational level splits into two. The spin-rotation constants are $\gamma_0 = 0.226$ cm^{-1} and $\gamma_1 = 0.216$ cm^{-1} [36] [37]. The rotational wavefunction is given by $|^2\Sigma^+, N, J, \Omega, M_J\rangle$ [27]. In the literature the levels with $J = N + 1/2$ and $J = N - 1/2$ are labeled with F_1 and F_2, respectively[2]. The total rotational angular momentum follows as $\mathbf{J} = \mathbf{N} + \mathbf{S}$. The total parity ($p$) of each rotational state (N) is given by:

$$p = (-1)^N. \qquad (2.22)$$

---

[2] To prevent confusion of the labeling between the total angular momentum quantum number F and the labeling of the two spin-orbit manifolds F_1' and F_2' of the $^2\Pi$ ground state the labeling is denoted with capital letters and apostrophe: F_1' and F_2'.

The left graph of Figure 2.4 shows the first electronic excited state as $A^2\Sigma^+$ with the corresponding labellings.

The coupling of **I** and **J** forms the total angular momentum including hyperfine interactions in the excited state: $\mathbf{F} = \mathbf{I} + \mathbf{J}$. The corresponding wavefunctions in the excited state are:

$$\begin{aligned} &|^2\Sigma^+, N, J, I, \Omega, F, M_F, p\rangle = \\ &\quad = \sum_{M_J M_I} |^2\Sigma^+, N, J, M_J, \Omega, p\rangle |I, M_I\rangle \langle J, M_J, I, M_I | F, M_F\rangle. \end{aligned} \tag{2.23}$$

The right graph of Figure 2.4 shows in the upper part the first electronic excited state as $A^2\Sigma^+, N = 0$ in detail and its hyperfine splitting.

2.2 Stark and Zeeman effect in OH

2.2.1 The Stark-effect in OH

The Stark effect describes the interaction between an external electric field (**E**) and the permanent electric dipole moment ($\mathbf{d}^{el}$) of a particle. OH has a permanent electric dipole moment of $|\mathbf{d}^{el}| \approx 1.67$ D [35] [38]. It is directed along the internuclear axis in the molecule-fixed (mf) frame, while **E** is defined in the laboratory's space-fixed (sf) frame. Irreducible spherical tensor operators of rank $k = 1$ with $m = -1, 0, 1$ components are used to relate the orientation of $\hat{\mathbf{d}}^{el}(1, m)$ with respect to $\hat{\mathbf{E}}(1, m)$. The interaction energy in the (sf) frame is given by

$$H_{Stark} = -\hat{\mathbf{d}}^{el} \cdot \hat{\mathbf{E}} = -\sum_{m=-1}^{1} (-1)^m \quad {}^{(\mathrm{sf})}\hat{\mathbf{d}}^{el}(1, m) {}^{(\mathrm{sf})}\hat{\mathbf{E}}(1, m) \tag{2.24}$$

In the following, the quantization axis is chosen to be along the electric field vector $|E|\hat{\mathbf{e}}_{\hat{Z}}$ in the $\hat{Z}$-direction in the (sf) frame where $|E|$ is the magnitude of the electric field and $\hat{\mathbf{e}}_{\hat{Z}}$ is the unit vector in $\hat{Z}$-direction. This reduces the components of $\hat{\mathbf{E}}(1, m)$ to $\hat{\mathbf{E}}(1, \pm 1)$=0 and $\hat{\mathbf{E}}(1, 0)$=$|E|\hat{\mathbf{e}}_{\hat{Z}}$=$E_{\hat{Z}}$.

Since $\mathbf{d}^{el}$ is directed along the internuclear axis in the (mf) frame of diatomic molecules, only the tensor component ${}^{(\mathrm{mf})}\hat{\mathbf{d}}^{el}(1, q = 0)$ needs to be considered in the transformation from the (mf) frame to the (sf) frame. Using the Wigner D-function which is defined in equation (2.6), the transformation reduces to:

$$^{(\mathrm{sf})}\hat{\mathbf{d}}^{el}_{\hat{Z}} = ^{(\mathrm{sf})}\hat{\mathbf{d}}^{el}(1, m=0) = \sum_{q=0} D^{(1)}_{m=0,q=0}(\phi,\theta,\chi)^{(\mathrm{mf})}\hat{\mathbf{d}}^{el}(1,0).$$

The interaction energy of the Stark-Hamiltonian then reduces to

$$H_{Stark} = -^{(\mathrm{sf})}\mathbf{d}^{el}|E|\hat{\mathbf{e}}_{\hat{Z}} = -^{(\mathrm{sf})}\hat{\mathbf{d}}^{el}(1,0)\hat{\mathbf{E}}(1,0). \tag{2.25}$$

The Stark-shift of the energy levels is calculated from the matrix elements using the symmetrized wavefunctions of equation (2.7) and equation (2.8):

$$\begin{aligned}
&\langle J,\Omega,M_J,p|H_{Stark}|J',\Omega',M'_J,p'\rangle \\
&= -\frac{1}{2}\big(\langle J,\Omega,M_J| + p\langle J,-\Omega,M_J|\big)H_{Stark}\big(|J',\Omega',M'_J\rangle + p'|J',-\Omega',M'_J\rangle\big) \\
&= -\delta_{M_J,M'_J}\left(\frac{1-pp'}{2}\right)\ ^{(\mathrm{sf})}d^{el}_0 E_0\sqrt{(2J+1)(2J'+1)}(-1)^{M_J-\Omega} \\
&\quad\times\begin{pmatrix} J & 1 & J' \\ M_J & m=0 & -M'_J \end{pmatrix}\begin{pmatrix} J & 1 & J' \\ \Omega & q=0 & -\Omega' \end{pmatrix}.
\end{aligned} \tag{2.26}$$

A non-zero Stark shift is created if the external electric field couples states of opposite parity: $p \neq p'$). This implies directly that $\mathbf{E}$ couples only states of opposite parity. Furthermore, selection rules follow from the Wigner 3-j symbols:

$$J = J'; \quad J = J' \pm 1; \quad M_J = M'_J; \quad \Omega = \Omega' \tag{2.27}$$

Two cases are discussed in the following which are important for the scope of this thesis. The Stark-effect of OH is used in two different regimes in the performed experiments. In the Stark-decelerator very high electric fields exploit the Stark-effect to manipulate the motion of OH radicals, while for spectroscopic experiments a weak electric field is applied where the Stark-shift needs to be calculated hyperfine resolved.

Strong electric fields

At electric field strengths of ≥ 1.5 kV/cm the nuclear spin $\mathbf{I}$ is totally decoupled from $\mathbf{J}$, and J becomes quite a good quantum number. In contrast, F is not a good quantum number anymore, since the hyperfine splitting becomes small compared to the Stark-shift. To calculate the Stark-shift for the rotational energy levels in the vibronic ground state two approximations are made: only the two Λ-doublet components of a single rotational level are considered, because the coupling to the rotational excited $J = 5/2$ state can be neglected since the rotational energy splitting is very large compared to the Stark-shift and compared to the Λ-doublet splitting. In zero-field the wavefunction of the lower Λ-doublet component is given by $|^2\Pi, F_1, J = 3/2, M_J, -\rangle$ and defines the zero energy. The upper Λ-doublet component $|^2\Pi, F_1, J = 3/2, M_J, +\rangle$ lies energetically higher by E_Λ. The Stark interaction is described by off-diagonal elements in the matrix:

$$\begin{pmatrix} 0 & \xi \\ \xi & E_\Lambda \end{pmatrix}. \tag{2.28}$$

The Stark shift of different $M_J\Omega$-components follows after diagonalization. Using equation (2.26), ξ can be calculated as [39]:

$$\xi = -^{(\mathrm{sf})}d_0^{el}|E_0|\frac{M_J\Omega_{eff}}{J(J+1)}, \tag{2.29}$$

where Ω_{eff} is introduced as the 'effective' value of Ω resulting from the mixed spin-orbit states: $\Omega_{eff} = \left[\frac{1}{2}C_1(J)^2 + \frac{3}{2}C_2(J)^2\right]$. The energy levels due to the Stark shift are the eigenenergies:

$$E_{Stark} = \frac{E_\Lambda}{2} \pm \sqrt{\left(\frac{E_\Lambda}{2}\right)^2 + \xi^2}. \tag{2.30}$$

The left graph of Figure 2.2 shows the Stark shift for strong electric fields up to 100 kV/cm. The lower Λ-doublet component $|^2\Pi, F_1, J = 3/2, M_J, -\rangle$ splits in the electric field into two high-field seeking components labeled by $M_J\Omega = 3/4$ and $9/4$, while the upper Λ-doublet state $|^2\Pi, F_1, J = 3/2, M_J, +\rangle$ splits into two low-field seeking components labeled by $M_J\Omega =$ -3/4 and -9/4.

Low electric fields and hyperfine interaction

At low electric fields the Stark-shifts are comparable in energy to the hyperfine splittings $E_{hf} = 0.00264\ \mathrm{cm}^{-1}$ and the Λ-doublet splittings $E_\Lambda = 0.0554\ \mathrm{cm}^{-1}$ [40]. The calculation of matrix elements including the hyperfine basis given in equation (2.20) follows from [41]:

$$\begin{aligned}
&\langle {}^2\Pi, F_1, J, I, \Omega, F, M_F, p | H_{Stark} | {}^2\Pi, F_1, J', I', \Omega', F', M_F', p' \rangle \\
&= -^{(\mathrm{sf})}\, d_0^{el} E_0 \left(\frac{1 + pp'(-1)^{J+J'+2\Omega+1}}{2} \right) \\
&\quad \times (-1)^{J+J+F+F'+I-M_F-\Omega+1} \\
&\quad \times \sqrt{(2F+1)(2F'+1)(2J+1)(2J'+1)} \\
&\quad \times \begin{pmatrix} J & 1 & J' \\ -\Omega & 0 & \Omega' \end{pmatrix} \begin{pmatrix} F' & 1 & F \\ M_F & 0 & -M_F \end{pmatrix} \begin{Bmatrix} F & F' & 1 \\ J' & J & 1 \end{Bmatrix}
\end{aligned} \tag{2.31}$$

The expressions in brackets and parentheses are the Wigner 3-j and 6-j symbols, respectively. The lower left graph in Figure 2.2 shows the Stark shifts of the hyperfine levels as a function of the electric field strength. When comparing the energy level shifts of both graphs in Figure 2.2 the Stark shift is quadratic for low electric fields where the zero-field hyperfine states are hardly mixed. At electric field strengths $\geq$1.5 kV/cm the Stark-shift becomes linear. The coupling induced by the electric field is given by the selections rules of equation (2.27). The electric field only couples states of opposite parity which become completely mixed at higher field strengths, i.e. they no longer have a defined parity.

2.2.2 The Zeeman-effect in OH

The interaction of an external magnetic field **B** with the OH radical happens between the magnetic dipole moments created by the orbital and spin angular momenta **L** and **S**, respectively. The influence of the Zeeman-effect is described by the Hamiltonian:

$$\hat{\mathbf{H}}_{Zeeman} = -\mathbf{d}^{mag} \cdot \mathbf{B} = \mu_0(\mathbf{L} + g_e\mathbf{S}) \cdot \mathbf{B}. \tag{2.32}$$

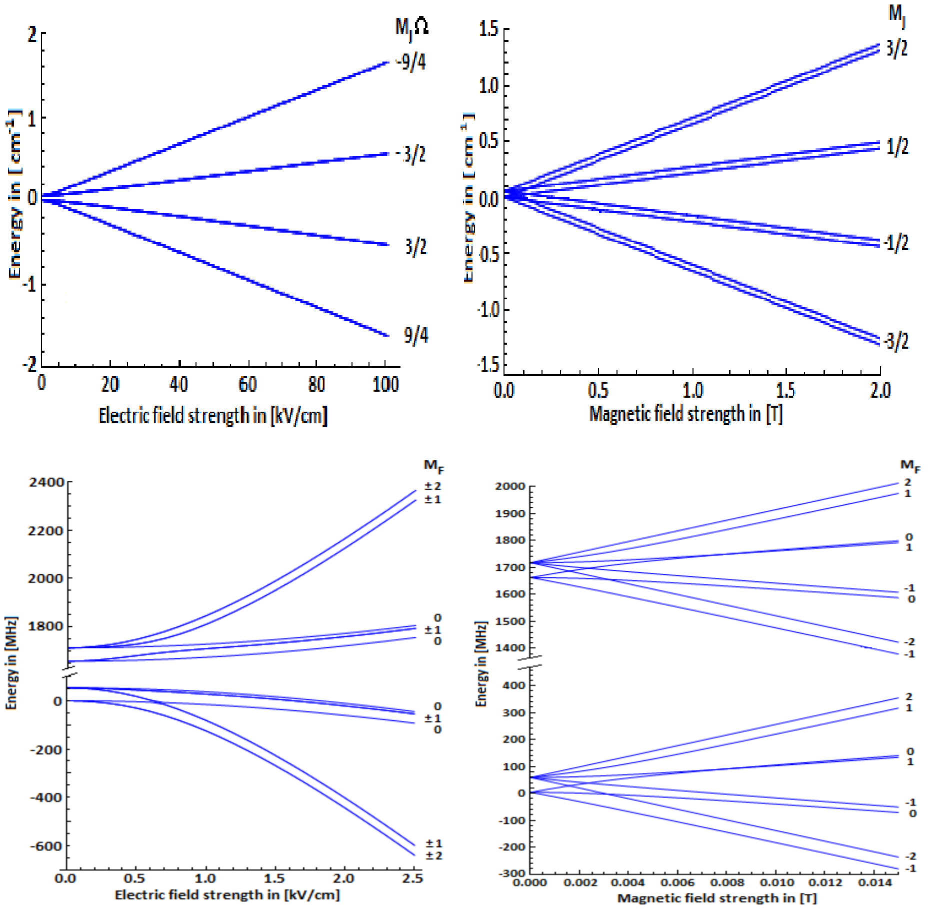

Figure 2.2: The upper left graph shows the Stark shift for strong electric fields up to 100 kV/cm. The low- and high-field seeking states are the $M_J\Omega =$ -3/4 and -9/4 and $M_J\Omega = 3/4$ and 9/4 components, respectively. The lower left graph shows the Stark shifts of the hyperfine resolved energy levels up to electric fields of 1500 V/cm. Here, the different M_F components are labeled. The upper right graph shows the Zeeman-shift of the ground state of OH as a function of the magnetic field. The hyperfine resolved Zeeman-shift is shown in the lower right graph.

where μ_0 is the Bohr magneton and g_e is the electron's g-factor ($g_e \sim 2.00232$) [27]. The minus sign in the right part of equation (2.32) cancels due to the negative polarity of the electron [42]. Again, the quantization axis is chosen to be in the (sf) frame of the laboratory along the magnetic field's direction: $\mathbf{B} = |\mathbf{B}|\hat{e}_{\hat{Z}}$. Using the symmetrized basis set given in equation (2.7), the diagonal matrix elements are given by [26]:

$$\langle J, \Omega, M_J, p|H_{Zeeman}|J', \Omega', M_J', p'\rangle = \frac{(\Lambda + g_e\Sigma)\Omega}{J(J+1)}\delta_{pp'}M_J\mu_0|\mathbf{B}|. \quad (2.33)$$

Practically only the sign in the $(\Lambda \pm g_e|\Sigma|)$ changes in the denominator for the respective spin-orbit manifold $\Omega = 3/2$ and $\Omega = 1/2$, since Σ takes the signed values of +1/2 and -1/2, respectively. The function $\delta_{pp'}$ replaces the term $(1 + pp'(-1)^{J+J'+2\Omega})/2$ which is non-zero, if states of the same parity are coupled. It follows that the Zeeman-interaction only couples states of the same parity. The Λ-doublet components are not mixed, in contrast to the Stark-interaction.

Strong magnetic fields

The ground state of OH has a mixed character of $|\Omega| = 3/2$ and $|\Omega| = 1/2$ due to the spin-orbit interaction which couples directly states of the same parity [43]. To include all contributions the basis wavefunctions which are derived in equation (2.15) are used in a shorter notation ($|^2\Pi, F_1, J' = 3/2, M_J', \pm\rangle = C_2(J)|\Omega' = 3/2\rangle + C_1(J)|\Omega' = 1/2\rangle$) to derive the Zeeman-shift for the vibronic ground state using the expression from equation (2.33):

$$\begin{aligned}
&\langle ^2\Pi, F_1, J = 3/2, M_J, \pm|H_{Zeeman}|^2\Pi, F_1, J' = 3/2, M_J', \pm\rangle \\
=&\big[C_2(J)\langle\Omega = 3/2| + C_1(J)\langle\Omega = 1/2|\big]\big|H_{Zeeman}\big|\big[C_2(J)|\Omega' = 3/2\rangle \\
&+ C_1(J)|\Omega' = 1/2\rangle\big] \\
\approx&\left[C_1(J)^2\frac{2}{15}(1 - \frac{1}{2}g_e) + C_2(J)^2\frac{4}{5}(1 + \frac{1}{2}g_e) + 2C_1(J)C_2(J)\frac{2\sqrt{3}}{15}g_e)\right] \\
&\times M_J\mu_0|\mathbf{B}|.
\end{aligned} \quad (2.34)$$

The first term in the squared brackets is almost zero while the second term is the same as in equation (2.33) multiplied by $C_2(J)^2$. The third term results from the cross term which amounts to almost 20% of the second term once the $C_1(J)$ and $C_2(J)$ coefficients are inserted from Table 2.1. The right graph of Figure 2.2 shows the Zeeman-shift of the ground state of OH as a function of the magnetic field.

Low magnetic field and hyperfine interaction

If the induced Zeeman shift is smaller than or comparable to the hyperfine splitting: $\Delta_{hf} \sim \mu_0|\mathbf{B}|$, the hyperfine structure has to be accounted for. By transforming to the hyperfine basis set using the Clebsch-Gordan coefficients as in equation (2.23) the matrix element follows:

$$\begin{aligned}
&\langle {}^2\Pi, F_1, J, I, \Omega, F, M_F, p | H_{Zeeman} | {}^2\Pi, F_1, J', I', \Omega', F', M'_F, p' \rangle \\
=&\mu_0|\mathbf{B}|(\Lambda + g_e\Sigma)\delta_{pp'} \\
&\times (-1)^{J+J+F+F'+I-M_F-\Omega+1} \\
&\times \sqrt{(2F+1)(2F'+1)(2J+1)(2J'+1)} \\
&\times \begin{pmatrix} J & 1 & J' \\ -\Omega & 0 & \Omega' \end{pmatrix} \begin{pmatrix} F' & 1 & F \\ -M'_F & 0 & M_F \end{pmatrix} \begin{Bmatrix} F & F' & 1 \\ J' & J & 1 \end{Bmatrix} .
\end{aligned} \tag{2.35}$$

The Zeeman- and the Stark-effect are both dipolar interactions which is reflected by the same Wigner 3-j and 6-j symbols appearing. The coupling induced by the magnetic field leads to the same selections rules given in equation (2.27) with the only major difference that the magnetic field does not couple states of opposite parity (which follows from: $\delta_{pp'}$).

2.2.3 Combined electric and magnetic fields

If external $\mathbf{E}$ and $\mathbf{B}$ fields are applied simultaneously, the direction of both fields usually does not coincide. Hence, no common quantization axis is formed. Without losing generality the quantization axis is chosen in the laboratory to be along $B_{\hat{Z}}$. To calculate the influence of the Stark-shift the different tensor components of ${}^{(\mathrm{mf})}\hat{d}^{el}_m$ need to be rotated into the sf-frame using the Wigner rotation matrix to be related to $\mathbf{E}$:

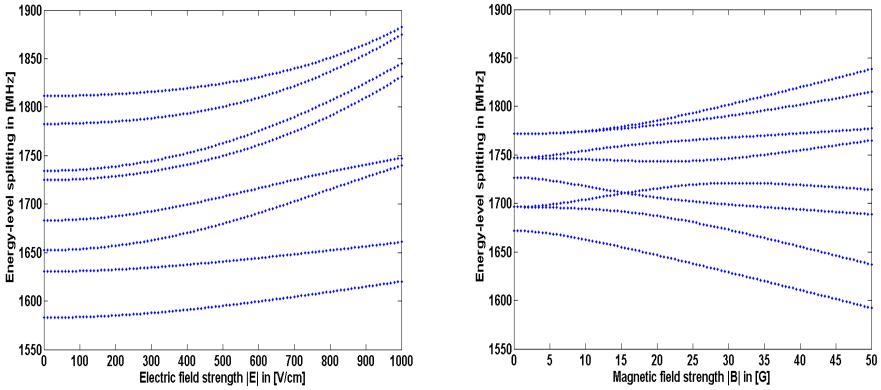

Figure 2.3: The left graph shows the shift of the energy levels as a function of the electric field strength $|\mathbf{E}|$ between 0 V/cm to 1000 V/cm at a constant magnetic field of $|\mathbf{B}| = 46$ G. The right graph depicts the energy level shifts as a function of the magnetic field $|\mathbf{B}|$ between 0 G up to 50 G at a constant electric field strength of $|\mathbf{E}| = 600$ V/cm. The calculations are performed for $\mathbf{E}$ oriented perpendicular to $\mathbf{B}$ such that follows $\mathbf{E} = [E_x = |\mathbf{E}|, E_y = 0, E_z = 0]$ and $\mathbf{B} = [B_x = 0, B_y = 0, B_z = |\mathbf{B}|]$, while the quantization axis is chosen along the Z-axis.

$$\hat{\mathbf{H}}_{Stark/Zeeman} = -^{(\mathrm{sf})}\hat{d}^{mag} \cdot \mathbf{B} -^{(\mathrm{sf})} \hat{d}^{el} \cdot \mathbf{E}$$

$$= -\left(D^{(1)}_{0,0}(\phi, \theta, \chi)^{(\mathrm{mf})}\hat{d}^{mag}_{0} \right) \cdot B_{\hat{Z}} - \sum_{-1}^{1} \left(D^{(1)}_{q,m}(\phi, \theta, \chi)^{(\mathrm{mf})}\hat{d}^{el}_{m} \right) E_q \quad (2.36)$$

The left graph of Figure 2.3 shows the shift of the energy levels as a function of the electric field strength $|\mathbf{E}|$ between 0 V/cm to 1000 V/cm at a constant magnetic field of $|\mathbf{B}| = 46$ G. The right graph depicts the energy level shifts as a function of the magnetic field $|\mathbf{B}|$ between 0 G up to 50 G at a constant electric field strength of $|\mathbf{E}| = 600$ V/cm. The calculations are performed for $\mathbf{E}$ oriented perpendicular to $\mathbf{B}$ such that follows $\mathbf{E} = [E_x = |\mathbf{E}|, E_y = 0, E_z = 0]$ and $\mathbf{B} = [B_x = 0, B_y = 0, B_z = |\mathbf{B}|]$.

2.3 A - X transitions and their probabilities

A detailed knowledge on the laser excitation is essential for the laser induced fluorescence (LIF) detection and to investigate the dynamics induced in spectroscopic experiments (see chapter 5). Within the scope of this thesis only excitations along the $|A^2\Sigma^+, v = 1\rangle \leftarrow |X^2\Pi_{|\Omega|}, v = 0\rangle$ band (hereafter referred to as: A-X transition) are used. For the calculation and interpretation of spectra the laser bandwidth (Δf) determines which transitions and energy levels can be resolved. Experiments are performed using two different laser systems: (1) a pulsed dye laser (PDL) with a bandwidth of $\Delta f^{PDL} \approx 2$ GHz and (2) a continuous wave (cw) ring dye laser system (RDL) with a bandwidth of $\Delta f^{RDL} \approx 2$ MHz. The PDL's bandwidth is broader than the Λ-doublet and the hyperfine splitting of the vibronic ground state, while the RDL allows resolution of all hyperfine transitions. More details on the laser systems and the detection methods are given in section 3.3.

In general, the line strength ($\mathcal{L}$) of an electronic transition is given by the evaluation of the squared absolute value of the transition moment matrix element [27]. In the case of OH an optical excitation from an initial level in the X state to a final level in the A state can be coupled by an electric or a magnetic transition dipole moment $\mu^{el/mag}$. The calculation of the transition dipole matrix elements is analogous to the calculation of the Stark- and Zeeman-effect. Similar to the permanent electric or magnetic dipole moments $\hat{d}^{el/mag}$ in OH, $\mu^{el/mag}$ is defined in the (mf) frame. The laser polarization of the electric and the magnetic field vector is given by $\mathcal{E} = \mathcal{P}^{el}$ and $\mathcal{B} = \mathcal{P}^{mag}$, respectively. They are defined in the (sf) frame. Irreducible tensor operators of rank 1 with the three components $q = -1, 0, 1$ are used to perform the transformation of $\hat{\mu}^{el/mag}$ from the (mf) frame to the (sf) frame

$$\begin{aligned}\hat{\mathbf{H}}_{trans} &= -{}^{(\mathrm{sf})}\hat{\mu}_m^{el/mag} \cdot \mathcal{P}_m^{el/mag} \\ &= -\left[\sum_{q=-1}^{+1} D_{m,q}^{(1)}(\phi, \theta, \chi) \quad {}^{(\mathrm{mf})}\hat{\mu}_q^{el/mag}\right] \cdot \mathcal{P}_m^{el/mag} \qquad (2.37)\end{aligned}$$

where $D_{m,q}^{(1)}$ denotes the Wigner rotation matrix, which is described in section 2.6. As before, it is convenient to define the $\hat{z}$-axis along the OH bond. The component along the internuclear axis is described by ${}^{(\mathrm{mf})}\hat{\mu}_0^{el/mag}$ which causes a parallel transition, while ${}^{(\mathrm{mf})}\hat{\mu}_{\pm 1}^{el/mag}$ are the components perpendicular to the internuclear axis defining perpendicular transitions. The transition dipole moment is defined by: $\langle \hat{\mu}^{el/mag} \rangle = \langle {}^2\Sigma^+, v = 1 | \mu^{el/mag} | {}^2\Pi, v = 0 \rangle$, while the individual components read:

$$
\begin{aligned}
{}^{(\mathrm{mf})}\hat{\mu}_{\pm 1}^{el} &= \frac{\langle \hat{\mu}^{el} \rangle}{\sqrt{2}} && (2.38) \qquad & {}^{(\mathrm{mf})}\hat{\mu}_{\pm 1}^{mag} &= \mp \frac{\langle \hat{\mu}^{mag} \rangle}{\sqrt{2}} && (2.40) \\
{}^{(\mathrm{mf})}\hat{\mu}_{0}^{el} &= 0 && (2.39) \qquad & {}^{(\mathrm{mf})}\hat{\mu}_{0}^{mag} &= 0 && (2.41)
\end{aligned}
$$

OH has only perpendicular components for the A-X transition. The detailed theoretical calculations of the transition dipole moments are given in the supplementary material of [44]: $|\langle {}^{(\mathrm{mf})}\hat{\mu}^{el} \rangle| = 0.05249\ e\ a_0$ and $|\langle {}^{(\mathrm{mf})}\hat{\mu}^{mag} \rangle| = 0.1417\ \mu_B$, where a_0, e and μ_B are the Bohr radius, the elementary charge and the Bohr magneton, respectively.

For individual electronic excitations from an initial level in the X state to a final level in the A state the transition dipole matrix element has to be evaluated. If transitions are induced with the PDL laser system, the initial Π state is described within the basis set given in equation (2.15) which is defined by a linear combination of the symmetrized basis set of equation (2.7). The final Σ state follows from equation (2.22). To calculate the line strength ($\mathcal{L}_{AX}$), the transition dipole moment matrix element reads:

$$
\begin{aligned}
\mathcal{L}_{AX} &\propto |\langle A | {}^{(\mathrm{sf})}\hat{\mu}_m^{el/mag} | X \rangle|^2 \\
&= |\langle {}^2\Sigma^+, N', J', M_J', p' | {}^{(\mathrm{sf})}\hat{\mu}_m^{el/mag} | {}^2\Pi, F_1, J, M_J, p \rangle|^2 \\
&= \Big| \zeta \sqrt{(2J+1)(2J'+1)} \times (-1)^{M_J - \Omega} \begin{pmatrix} J & 1 & J' \\ M_J & m & -M_J' \end{pmatrix} \\
&\quad \times \Big[\sum_q {}^{(\mathrm{mf})}\hat{\mu}_q^{el/mag} \begin{pmatrix} J & 1 & J' \\ \Omega & q & -\Omega' \end{pmatrix} \Big] \Big|^2 .
\end{aligned} \tag{2.42}
$$

Once the RDL is used with its small bandwidth the hyperfine splittings and the Λ-doublet can be resolved. To calculate the line strengths the hyperfine basis in the ground and the excited state are taken into account which are described in equations (2.20) and (2.23), respectively. The transition dipole moment matrix element follows from

$$\begin{aligned}
\mathcal{L}_{AX} &\propto |\langle A|^{(\mathrm{sf})}\hat{\mu}_m^{el/mag}|X\rangle|^2 \\
&= |\langle {}^2\Sigma^+, N', J', \Omega', F', M_F', p'|^{(\mathrm{sf})}\hat{\mu}_m^{el/mag}|{}^2\Pi, F_1, J, F, M_F, p\rangle|^2 \\
&= \Big|\zeta\sqrt{(2J+1)(2J'+1)(2F+1)(2F'+1)} \\
&\quad \times (-1)^{I-J+J'+1-M_F'-\Omega'} \begin{Bmatrix} J & I & F \\ F' & 1 & J' \end{Bmatrix} \\
&\quad \times \begin{pmatrix} J & 1 & J' \\ M_J & m & -M_J' \end{pmatrix} \Big[\sum_q {}^{(\mathrm{mf})}\hat{\mu}_q^{el/mag} \begin{pmatrix} J & 1 & J' \\ \Omega & q & -\Omega' \end{pmatrix}\Big]\Big|^2 .
\end{aligned} \tag{2.43}$$

Electric dipole transitions

In the case of an electric dipole allowed transition (E1) it follows from $\zeta = (\frac{1-pp'}{2})$ that ${}^{(\mathrm{sf})}\hat{\mu}^{el}$ couples only states of opposite total parity:

$$|+\rangle \leftrightarrow |-\rangle \quad \text{or} \quad |-\rangle \leftrightarrow |+\rangle. \tag{2.44}$$

This property enables to probe individual Λ-doublet components using the PDL with its larger bandwidth greater than the Λ-doublet splitting. The selection rules follow from the Wigner 3-j symbols:

$$\Delta J = 0; \pm 1; \quad \Delta M_J = 0; \pm 1; \quad \Delta N = 0; \pm 1; \pm 2 \tag{2.45}$$

which result in the rotational transition branches of $\Delta N = O$, P, Q, R and S. Throughout this thesis the nomenclature of Diecke and Crosswhite [29] which denotes the transitions such that

$$\Delta N_{f_f F_i}(N_i) \tag{2.46}$$

where f_f and F_i describe the component of the ρ-doublet in the upper state and the spin-orbit manifold of the lower state, respectively, while N_i is the rotational quantum number of the lower state. If $f_f = F_i$ only one subscript is used. The most important transitions are indicated in the left graph of Figure 2.4. The various line strengths and transition wavelengths are listed in [45].

If the RDL laser system is used, transitions between hyperfine states can be resolved in the experiment. The observed transitions in the experiment follow from the hyperfine selection rules which are expressed in the 6-j symbol denoted in curly brackets in equation (2.43)

$$\Delta F = 0; \pm 1. \tag{2.47}$$

Magnetic dipole transitions

In the case of the magnetic dipole allowed transition (M1) the change of sign of ${}^{(\mathrm{mf})}\hat{\mu}_q^{el/mag}$ has to be accounted for, when summing over q, which is given in equation (2.40). It follows from the $\zeta = \delta_{pp'}$ that ${}^{(\mathrm{sf})}\hat{\mu}^{mag}$ couples only states of identical parity:

$$|+\rangle \leftrightarrow |+\rangle \quad \text{or} \quad |-\rangle \leftrightarrow |-\rangle. \tag{2.48}$$

The selection rules follow from the Wigner 3-j symbols similarly to the electric dipole transitions:

$$\Delta J = 0; \pm 1; \quad \Delta M_J = 0; \pm 1; \quad \Delta N = 0; \pm 1; \pm 2 \tag{2.49}$$

In the case the hyperfine transitions are resolved with the RDL the selection rules follow from the Wigner 6-j symbol in equation (2.43)

$$\Delta F = 0; \pm 1. \tag{2.50}$$

Usually, M1 transitions are five to six orders of magnitude smaller than E1 transitions [46]. They are, therefore, usually neglected in measurements of quantum-state populations (e.g. via LIF). In OH the E1-to-M1 ratio is $\approx 10^{-3}$ [44]. The quantum-state purity of OH molecules in the Stark-decelerated state (X ${}^2\Pi_{3/2}, v = 0, J = 3/2, f$) is $\approx 99.9\%$. Nevertheless, the population ratio of the two Λ-doublet components e and f is: $n_e/n_f \approx 10^{-3}$. Therefore, in experiments requiring very sensitive state-selective detection, the negligence of higher order transitions could lead to significant misinterpretation of the signals [47]. Throughout this thesis only one particular M1 transition is used ($\langle A^2\Sigma^+, J' = 1/2, N' = 0, p' = +| \leftarrow |X^2\Pi_{3/2}, J = 3/2, N = 1, p = +\rangle$) which is denoted by $P_1'(1)$.

In this section transitions have been discussed in the field free case only. If additionally electric or magnetic fields are present during the spectroscopic investigation, the resulting Zeeman- and Stark-shifts of the energy levels and the mixing of states are included in the wavefunctions of the ground and excited states.

2.4 Molecular properties of H_2

The H_2 molecule possesses two electrons, which leads in the united atom picture to an electronic ground state of $(1s\sigma)^2$, which is of ${}^1\Sigma^+$ character. H_2 is a closed shell molecule that appears as a spin-isomer. The nuclear spins of the hydrogen atoms forming the H_2 molecule can couple either anti-parallel to a total nuclear spin of I = 0 (spin-singlet state) or parallel to I = 1 (spin-triplet state). These two distinct forms are described as the para-H_2 state (pH_2) or the ortho-H_2 state (oH_2), respectively. In the following, the possible nuclear-spin wavefunctions Ψ_{ns} are listed on the left, while on the right the total spin I and the projection quantum number m_I onto the molecular axis are given.

The nuclear-spin coupling has a direct consequence on the population of the rotational energy level structure J and the possible rotational-transitions ΔJ because of quantum mechanical symmetry. These properties have a direct influence on the population distribution after the supersonic expansion. Also the possible and allowed transitions out of the lowest rotational states are important to fully characterize the inelastic collision process in a molecule-molecule scattering experiment. Under permutation of the two nuclei, the total wavefunction of the H_2 molecule must be antisymmetric because the two nuclei are protons (fermionic particles). The total wavefunction is the product of the spatial-wavefunctions (consisting of the electronic-, the vibrational- and the rotational-wavefunction) and

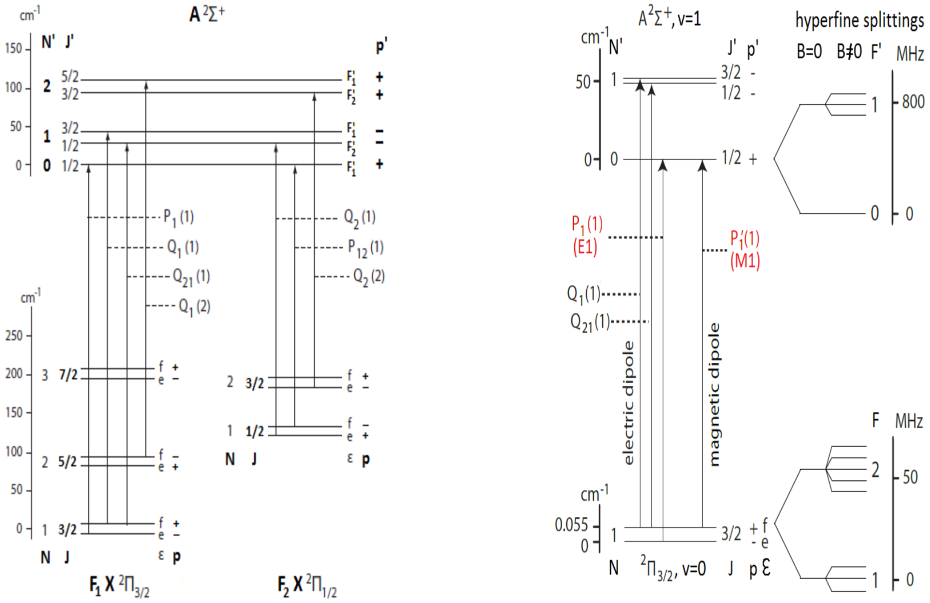

Figure 2.4: The left and the right graph show in their lower parts the rotational energy levels of the vibronic ground state $X^2\Pi$, while the excited state's $(A^2\Sigma^+)$ energy level structure is depicted in the upper part together with the corresponding quantum numbers and parities. The left graph shows the electric dipole allowed P, Q and R transitions which are used to address individual Λ-doublet states of rotational levels of the two spin-orbit manifolds $X^2\Pi F_1$ and $X^2\Pi F_2$ in the ground state. The Λ-doublet splitting is exaggerated to be visible. The right graph shows the electric and the magnetic dipole allowed transition out of the rovibrational ground state.

Spin-singlet state:

$$\Psi_{ns}^{-} = \frac{1}{\sqrt{2}}(|\uparrow\downarrow\rangle - |\downarrow\uparrow\rangle) \qquad (2.51) \qquad (I = 0, m_I = 0)$$

Spin-triplet states:

$$\Psi_{ns}^{+} = |\uparrow\uparrow\rangle \qquad (2.52) \qquad (I = 1, m_I = +1)$$

$$\Psi_{ns}^{+} = \frac{1}{\sqrt{2}}(|\uparrow\downarrow\rangle + |\downarrow\uparrow\rangle) \qquad (2.53) \qquad (I = 1, m_I = 0)$$

$$\Psi_{ns}^{+} = |\downarrow\downarrow\rangle \qquad (2.54) \qquad (I = 1, m_I = -1)$$

the spin-wavefunction:

$$\Psi_{total} = \Psi_{el} \cdot \Psi_{vib} \cdot \Psi_{rot} \cdot \Psi_{ns} \tag{2.55}$$

- The electronic wavefunction Ψ_{el} is symmetric under the permutation because of the symmetry of the Σ-state.
- The vibrational ground state $v = 0$ is also symmetric under the permutation. It is usually described by a symmetric harmonic oscillator function.
- The symmetry of the rotational wavefunction Ψ_{rot} depends on the rotational quantum number J. Permutation of the two nuclei in a diatomic molecule is equivalent to a rotation of the molecule around 180°, which is also an inversion of position coordinates (which is equivalent to an inversion of the spatial-wavefunction). Odd rotational states (J = 1,3,5,...) show a change of sign of the rotational-wavefunction, which is an antisymmetric behaviour. Even rotational states (J = 0,2,4,...), however, show no change of sign of the rotational-wavefunction, which is a symmetric behaviour under permutation.
- The spin-wavefunction Ψ_{ns} also shows different symmetry behaviour depending on the nuclear-spin coupling. The singlet state (2.51) shows an antisymmetric behaviour under permutation of nuclei [3],

---

[3] Permutation of spin 1 and 2: $\frac{1}{\sqrt{2}}(|\uparrow_1\downarrow_2\rangle - |\downarrow_1\uparrow_2\rangle) = (-1) \cdot \frac{1}{\sqrt{2}}(|\downarrow_2\uparrow_1\rangle - |\uparrow_2\downarrow_1\rangle)$

which is also indicated by the superscripted Ψ_{ns}^{-}. All of the spin-triplet states Ψ_{ns}^{+} show a symmetric behaviour under interchange of nuclei.

In order to conserve the antisymmetry of the total wavefunction under interchange of fermions, the product of the $\Psi_{ns} \cdot \Psi_{rot}$ must be antisymmetric in the vibronic ground state. Therefore, odd rotational states (antisymmetric) can only be populated, if the spin-triplet state (symmetric) is present, and even rotational states (symmetric) can only be populated, if the spin-singlet state (antisymmetric) is achieved. Additionally, these symmetry properties allow only changes of the rotational quantum number by ΔJ = 2, such that for pH_2 only rotational states of even quantum number (J = 0,2,4,...) are allowed, while for oH_2 only odd ones (J = 1,3,5,...) are allowed, which is shown in the rotational level-scheme in Figure 3.4.

A transition from an ortho to a para state (or reversely) requires a simultaneous change of the total nuclear-spin state and of rotational state by $\Delta J = 1$. This so-called nuclear spin conversion can be induced by the perturbation from a magnetic field gradient. Such magnetic fields can be created, for example, in a collision with other molecules possessing a magnetic moment [48] or on a surface with magnetic centres [49]. If $N[oH_2]$ and $N[pH_2]$ are the Boltzmann factors defining the population distribution of the ortho- or the para-state at a given temperature T, the concentration of oH_2 molecules in a sample of H_2 is defined as

$$X[oH_2] = \frac{N[oH_2]}{N[oH_2] + N[pH_2]}. \tag{2.56}$$

Since the first vibrational state of H_2 has a excitation energy of $\approx$ 6300 K, only the rotational energy levels E_J need to be considered for the temperature range relevant in this experiment. Figure 2.5 shows the concentration $X[oH_2]$ as a function of T between 0 K and 400 K, where

$$N[oH_2] = 3 \sum_{J=1,3,5,...} (2J+1)e^{\frac{-E_J}{kT}} \quad \text{and} \quad N[pH_2] = \sum_{J=0,2,4,...} (2J+1)e^{\frac{-E_J}{kT}} \tag{2.57}$$

are used. In the equation defining $N[oH_2]$, the factor 3 accounts for the nuclear spin degeneracy. In the presence of a paramagnetic catalyst thermal equilibrium can be achieved at each temperature. From the temperature dependency of the thermodynamic equilibrium, it follows that $X[oH_2] = 0.75$ in the high-temperature limit, while in the low-temperature limit the equilibrium state is only composed of pH_2. At an ambient temperature of 300 K, $X[oH_2] = 0.7492$ according to equation (2.56). This mixture, containing both ortho and para states, is called normal-H_2 (nH_2).

In the experiments performed here, the conversion is undertaken in a separate setup that was originally dedicated to grow a crystal of pure pH_2 for an optical Raman-shifting experiment. The conversion setup consists of a helium-cryostat, where nH_2 is condensed at a stabilized temperature of 17 Kelvin. There, the liquid nH_2 is guided through a cell filled with iron-oxide powder as conversion catalyst, which carries out the conversion process within hours. The stagnation pressure and the flow rate are adjusted by a flow-meter, such that the para-conversion process ($nH_2 \rightarrow$ para-converted H_2 (pcH_2)) is optimized.

The pcH_2 sample is stored in aluminium bottles to preserve its purity. Special care is taken in the experimental setup to use the least possible amount of materials which contain paramagnetic centres, especially the least amount of stainless steel components. Without the presence of a catalyst, the nuclear-spin conversion of H_2 in the gas-phase from ortho-to-para states and reverse is very slow and takes months [49]. The actual purity of the produced pcH_2 sample is determined in spectroscopic experiments described in section 3.1.2.

It is important to distinguish between a single H_2 molecule's quantum state and a sample of an H_2 gas-mixture. A single H_2 molecule is either in the para-state or the ortho-state, which are labeled pH_2 or oH_2, respectively. The H_2 gas-mixtures used in the experiment are normal-H_2 (nH_2) and para-converted-H_2 (pcH_2), which always contain pH_2 and oH_2 at different ratios.

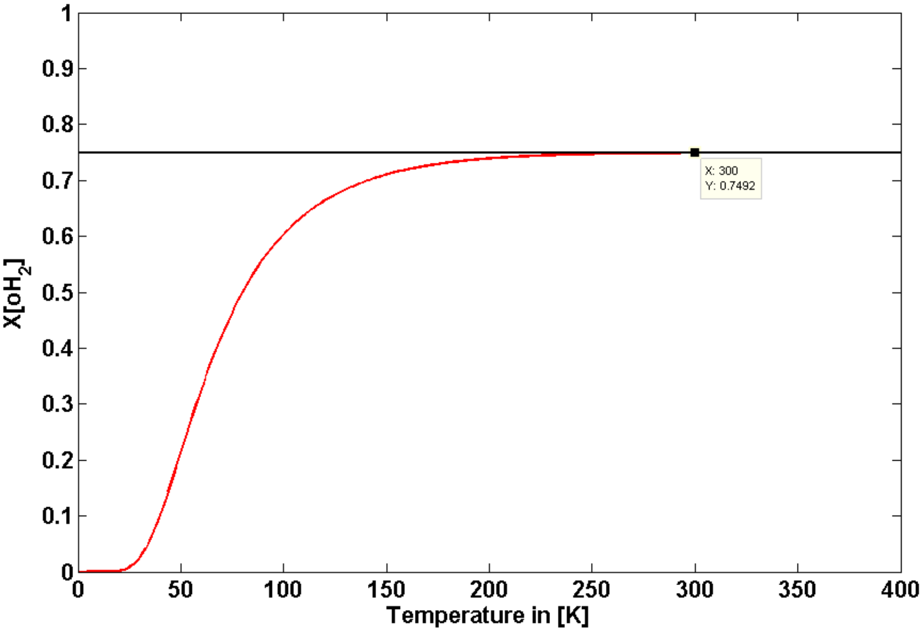

Figure 2.5: The concentration of oH_2 ($X[oH_2]$) in a sample of H_2 is plotted as a function of the temperature in Kelvin. At each temperature thermal equilibrium is assumed.

Chapter 3

Experimental setup

In this chapter those properties and parameters of the setup are introduced which are important to conduct the performed experiments. Figure 3.1 shows a sectional view of the molecular beam setup incorporating the Stark-decelerator. It consists of three basic units: (1) the source chamber on the far upper right, where molecular packets of OH radicals are produced to be coupled into the Stark-decelerator; (2) the Stark-decelerator unit with a 2.6 meter long Stark-decelerator is the heart of the experimental setup; and (3) the detection chamber, where the laser induced fluorescence (LIF) detection of OH takes place.

The chapter is structured as follows: the process of supersonic expansion is described in paragraph 3.1 followed by the description of the two molecular beam sources: one produces OH radicals for Stark-deceleration the second one produces the target beams for scattering experiments. Paragraph 3.2 comprises the technique of Stark-deceleration: not only the mechanical properties of the stainless steel electrode arrays and the high voltage switching is described but also the theoretical simulations of the motion of molecular packets in the applied electric fields is explained. The last paragraph 3.3 covers the properties of the LIF detection scheme using two different laser systems.

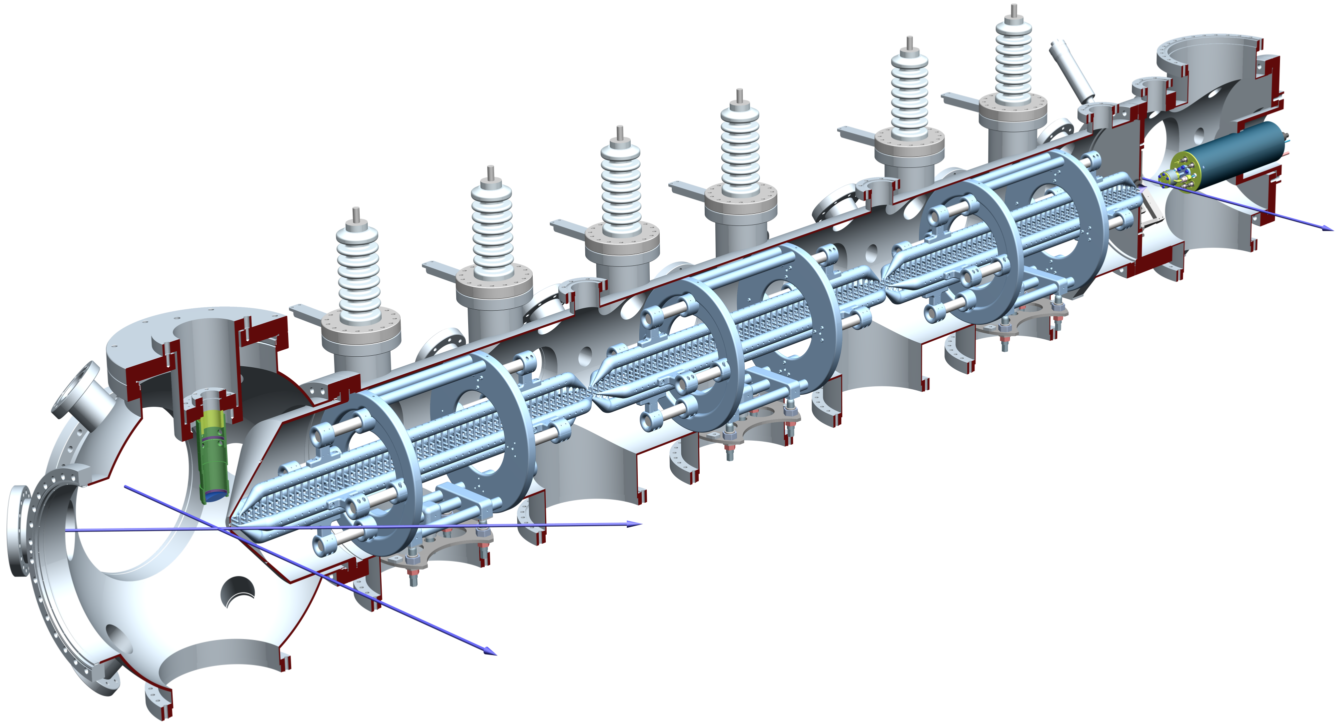

Figure 3.1: The Figure shows a sectional view of the molecular beam setup incorporating the Stark-decelerator. It consists of three units: (1) the source chamber on the far upper right, where the OH radicals are produced 3.1; (2) the Stark-decelerator unit, where the stainless steel electrode arrays are mounted and the high voltages are applied 3.2; and (3) the detection chamber, where the laser induced fluorescence (LIF) detection takes place.

3.1 Production of molecular beams

The atomic or molecular beams in this experimental setup are produced by supersonic expansion from pulsed valves [9] [11]. A beam is created by the escape of a gas from a high pressure region of a gas cell through a small orifice into vacuum. Inside the high pressure volume the particles obey the Maxwellian velocity distribution which is well defined by the parameters of the temperature (T_0), the stagnation pressure (p_0) and the volume (V) of the gas cell. If the mean free-path of the particles is smaller than the diameter of the orifice, the particles collide very frequently while expanding into the vacuum. If the ratio of the stagnation pressure and the vacuum pressure (p_{vac}) is large the velocity of the expanding beam is faster than the speed of sound and collisions are still taking place in the expansion region. An important parametre in this process is $\gamma = C_p/C_V$, where C_p and C_V denote the specific heat capacity at constant pressure and at constant volume [9], respectively. For example, for an ideal mono-atomic gas $\gamma = 5/3$, since only translational degrees of freedom are available. The value of γ changes if particles possess rotational or vibrational degrees of freedom.

The collisions between particles in the expansion region result in a propagation of all particles with almost the same velocity. The number of particles with a uniform velocity distribution increases with the distance from the nozzle, while the probability of collisions decreases resulting in a terminal temperature (T_f) corresponding to a final enthalpy (H_f). The result of this adiabatic cooling of all degrees of freedom is ultimately a very narrow velocity distribution compared to the Maxwellian velocity distribution and an internally cold beam. The difference of the enthalpy available per particle in the cell (H_0) and after the expansion (H_f) defines the kinetic energy available: $H_0 - H_f = 1/2\overline{m}v^2$ where v is the final beam velocity and $\overline{m}$ is a weighted mean mass that accounts for the mixture of differently heavy carrier gases and particles of interest. Assuming that C_p is constant within the expansion process it follows

$$v^2 = \frac{2}{\overline{m}}(H_0 - H_f) = \frac{2}{\overline{m}}\int_{T_f}^{T_0} C_p dT = \frac{2k_B}{\overline{m}}\Big(\frac{\gamma}{\gamma - 1}\Big)(T_0 - T_f) \tag{3.1}$$

where k_B is the Boltzmann constant [11]. The so-called 'sudden-freeze radius' defines a distance behind the orifice where the particles collide on average for the last time. In most setups the skimmer is placed at this distance to extract part of the expanded beam, because the expansion is finished. Here, T_f usually reaches values ≤ 1 K and the final beam velocity is defined by

$$v = \sqrt{\frac{2k_B}{m}\Big(\frac{\gamma}{\gamma - 1}\Big)T_0}. \tag{3.2}$$

Taking into account that for the expansion of an ideal gas $\gamma = 5/2$ [11], this equation can be simplified to:

$$v = \sqrt{\frac{5k_B T_0}{m}}. \tag{3.3}$$

In a typical beam the narrow velocity distribution ranges between Δv 1 - 15 % of v, corresponding to a translational temperature of 1 K. The rotational energy level spacings are small compared to the vibrational ones and cooling of the rotational degree of freedom is therefore efficient, resulting in rotational temperatures $T_{rot} \approx 1$ - 10 K. The vibrations cool least well, and the vibrational temperature is often considerably higher ($T_{vib} \approx 100$ K). Nevertheless, the vibational spacing is so large that the vast majority of molecules ($\geq$95 %) reside in the vibrational ground state.

3.1.1 Production of OH packets

In the source chamber depicted in Figure 3.1 a commercial General Valve (Series 99) is mounted to release pulses that are coupled into the Stark-decelerator. Nitric acid (HNO_3) is seeded in a carrier gas and expanded from this pulsed valve, where a short quartz capillary is mounted around the orifice. OH radicals are produced by photo dissociation with an ArF-excimer laser (193 nm) directly behind the beam orifice, early in the expansion. After the expansion process is finished, most of the OH radicals occupy the lowest rotational and vibrational level of the electronic ground state (X $^2\Pi_{3/2}$, v = 0, J = 3/2). All four ground state energy levels, which are split into the Λ-doublet ($\epsilon = e$ and f) and hyperfine components (F=1 and F=2), are populated equally.

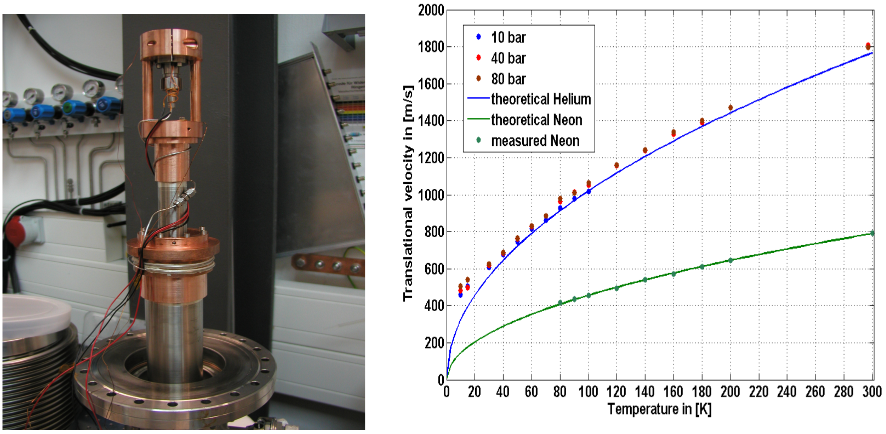

Figure 3.2: The left picture shows the Even-Lavie valve mounted on top of the helium-cryostat. The right graph shows the characterization measurements of the target beam setup. The final velocity of helium and neon packets are determined by fast ion gauge (FIG) measurements and plotted as dots against the set temperature that is actively stabilized. As a comparison, the theoretical final velocities following equation (3.3) for an ideal gas expansion are plotted as solid lines.

3.1.2 Production and characterization of target beams

Design, construction and characterization of a secondary beam source has been an essential part within the work of this thesis. The left picture of Figure 3.2 shows an Even-Lavie (EL)-valve [12] mounted in an oxygen-free copper housing on top of a helium cryostat (Oerlikon Leybold Vacuum: Cryohead 7/25). The temperature of the valve is measured using silicon diodes (Lake Shore: DT-670-SD) and it is actively stabilized between 10 and 300 Kelvin using a heating cartridge and a Temperature Controller (Lake Shore, Model 331). Figure: 7.1 shows a schematic drawing where this setup is used as secondary beam source for crossed-beam scattering experiments. The target beam source is depicted in the upper left part, where an additional copper tube is mounted around the valve-housing for radiation shielding. This setup has been characterized using helium and neon beams, while the scattering experiments are performed with molecular beams of H_2.

The characterization of this beam source is performed using pure helium and neon to simulate an ideal gas expansion best. For the characterization measurements the valve setup is actively stabilized at different temperatures (corresponding to T_0), where the stagnation pressure and the trigger pulse duration of the opening time are optimized to produce the fastest beam, which should be the internally coldest beam. The final velocity of helium or neon packets are determined by measuring time of flight (TOF) spectra using a fast ion gauge (FIG) at two different positions downstream. The right graph of Figure 3.2 depicts the final velocities plotted as dots against the stabilized temperature. As a comparison with an ideal gas expansion, the theoretical final velocities following from equation (3.3) are plotted as solid lines. The square root dependence of the final velocity as a function of the valve temperature is quantitatively well reproduced by the measurements.

For the scattering experiment several properties of the collision target of the OH radicals are of main interest. For a conclusive analysis of the undergoing inelastic processes knowledge over the population distribution of the quantum states prior to collision is indispensable. From a kinematic point of view, the translational velocity $\underline{v}_{H_2}$ and the velocity distribution, which is here defined as the standard deviation $\sigma_{v_{H_2}}$, define the collision energy and the collision energy distribution. Experimentally, they are determined from TOF measurements with a FIG after the supersonic expansion. Since H_2 appears in two nuclear-spin configurations (see section 2.4), the so-called ortho or para H_2, the ratio of both in the molecular beam is investigated spectroscopically after the supersonic expansion at the collision zone, where the OH and H_2 packets collide (see Figure: 7.1).

TOF measurements with the FIG: The left and the central graph of Figure 3.3 show TOF measurements, where the beams are detected right at the collision zone, which is located 50 cm from the orifice and 9 cm further downstream, respectively. The intensity of the FIG signals of nH_2 and pcH_2 are plotted plotted against the delay time as blue and red traces. The trigger pulse, which is applied to open the valve, defines $t = 0$ μs. The drift time between the two mean arrival times τ_1 and τ_2 and the distance D between the two measurement positions is used to determine the mean translational velocity of the pulse: $v = D/(\tau_2 - \tau_1)$.

The determination of the mean arrival time is not as straight forward as it might seem, however, especially for very fast beams of helium and H_2. In the right graph of Figure 3.3 the measured TOF traces are fitted with a Gaussian function to compare the measured pulse shape with the model one. Two main properties can be observed immediately: firstly, there is a periodic, high-frequency oscillation modulating the signal, which is most probably an artefact from the amplifier of the FIG, and, secondly, the measured pulse profile is slightly asymmetric and is skewed towards later arrival times. A Fast Fourier Transformation routine was used to filter the signal from these higher frequencies. The mean arrival times τ_i were finally determined by fitting the derivative of the filtered trace with a linear function to account for the skewness. This procedure is exemplified in the right graph of Figure 3.3. When the trigger schemes for the experimental data acquisition in the collision experiments (see chapters 6, 7, and 8) are set up, not the mean arrival time of the pulse is chosen to have maximum overlap with the mean arrival time of the OH pulse, but the part with the highest intensity. If the mean value of the fit from the Gaussian function is used to determine the mean arrival times, these drift times are longer than those determined from the fit of the derivatives. Since the pulse duration is increasing with increasing drift times, the time difference between the part with the highest intensity and the mean of the pulse will be increasing with increasing drift times. In column two of Table 3.1 the mean translational velocities are listed for the different valve temperatures ($\mathrm{T}_{\mathrm{valve}}$) that have been used.

To be able to quantify the velocity distribution, the shape of the TOFs are analyzed in detail. The width of the TOFs has two origins, the finite opening time of the valve (*tpd* - trigger pulse duration) and the remaining velocity spread (defined via the standard deviation: $\sigma_{v_{H_2}}$), which is still present after the supersonic expansion. The width of the TOFs increases with increasing drift time, because faster molecules fly ahead while the slower ones lag behind; leading to a spatial divergence of the pulse. Apart from the broadening of the whole pulse shape, a correlation between velocities and position in the pulse is imprinted with increasing drift time. In terms of the spatial position within the pulse, this correlation causes the faster molecules to be in the front part of the pulse, while slower molecules tend to be at the end. When a TOF is measured at a certain position downstream, the correlation is established already to a certain extent. Therefore, the measured duration is a convolution of both broadening effects. The different effects can be deconvoluted when measurements at two different positions are taken, because only the velocity distribution is responsible for an additional broadening of the pulse during the free flight, while the broadening due to the finite opening time stays constant. The finite opening times of $\approx$20 μs, which are listed in Table 3.1, could be responsible for $20-30\%$ of the whole pulse duration, as can be observed in the TOF spectra of Figure 3.3. To extract $\sigma_{v_{H_2}}$ from the measured TOFs, a convolution of two Gaussian functions is used to model the pulse shape ($\mathrm{PS}_{\tau_{Gi}}(x)$) and its propagation in space, where x are spatial coordinates and τ_{Gi} are the mean arrival times from Gaussian fits of the TOFs:

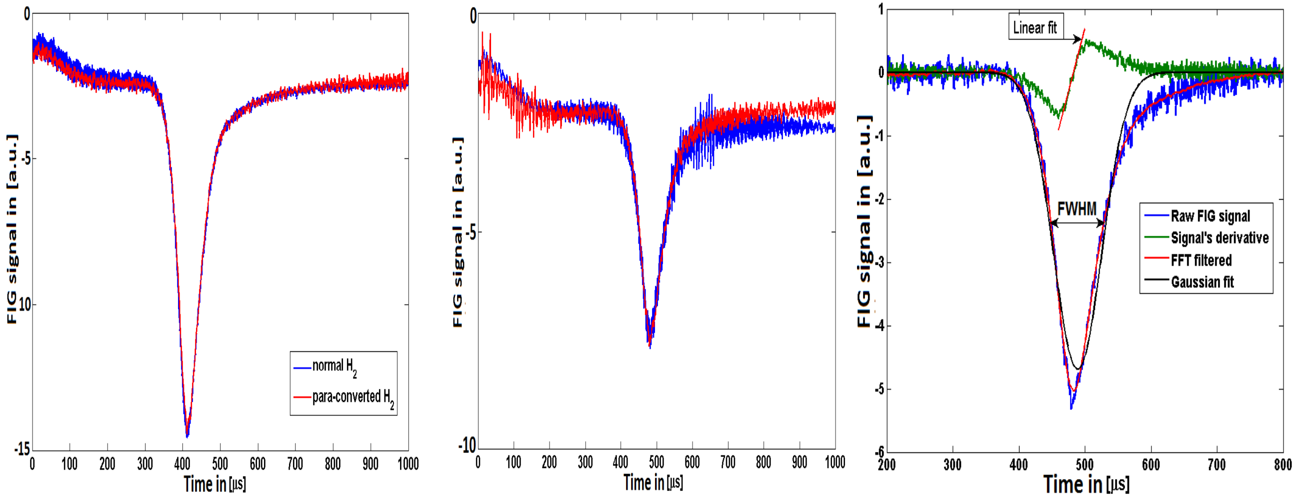

Figure 3.3: The left and the central graph show the TOF of nH_2 (blue trace) and pcH_2 (red trace) taken at the collision zone and 90 mm further downstream, respectively. The right graph illustrates the detailed analysis of the TOF profile.

$$PS_{\tau_{Gi}}(x) = A_i e^{\left[\frac{-(x-v\tau_{Gi})^2}{2((d_{tpd})^2+(\sigma_{v_{H_2}}\tau_{Gi})^2)}\right]} \tag{3.4}$$

The numerator $x - v\tau_{Gi}$ in the exponent accounts for the translational propagation, while the two terms in the denominator d_{tpd} and $\sigma_{v_{H_2}}\tau_{Gi}$ describe the individual broadening effects. The term $\sigma_{v_{H_2}}\tau_{Gi}$ describes the broadening due to the velocity distribution. The term d_{tpd} describes the finite spatial length of the pulse resulting from the finite opening time of the valve. The term A_i in front of the exponential is a normalization factor. In a TOF measurement the arrival time at a certain position is measured, rather than the position at a certain time. The transformation to the time domain is done by using $t = x/v$:

$$PS_{\tau_{Gi}}(t) = B_i e^{\left[\frac{-v^2(t-\tau_{Gi})^2}{2((d_{tpd})^2+(\sigma_{v_{H_2}}\tau_{Gi})^2)}\right]}, \tag{3.5}$$

where B_i in front of the exponential is a normalization factor and different to A_i in equation (3.4).
Although the fitting of the pulse shape with a Gaussian function is not appropriate to determine the mean velocity as shown in the right graph of Figure 3.3, the comparison of the full width at half maximum ($FWHM$) of the Gaussian fit agrees very well with the width of the TOF trace at that level, where the signal intensity is approximately at half of the maximum's intensity. From the Gaussian fit of the TOF the $FWHM$ relates to the pulse duration $w_i = 1/(2\sqrt{2ln2})FWHM$. To quantify the values of σ_v and d_{tpd}, they are related to the fitted w_i and τ_{Gi} by:

$$\sigma_{v_{H_2}} = \sqrt{\frac{w_2^2 - w_1^2}{\tau_{G2}^2 - \tau_{G1}^2}} \tag{3.6}$$

$$d_{tpd} = \sqrt{\frac{w_2^2\tau_{G1}^2 - w_1^2\tau_{G2}^2}{\tau_{G1}^2 - \tau_{G2}^2}}. \tag{3.7}$$

The H_2 pulse properties at each temperature are optimized by adjusting the opening time with the trigger pulse duration tpd_{ex} and the stagnation pressure p_{ex} to achieve the fastest beam possible. To compare tpd_{ex} with the fitted d_{tpd}, a trigger pulse duration tpd_{fit} can be calculated from the fit by using the translational velocity v that approximates the temporal broadening of the packet at $\tau = 0$: $d_{tpd} = v \cdot tpd_{fit}$. The physical meaning of d_{tpd} is the spatial extension of the packet, which is related to the trigger pulse duration and the velocity of the outflowing gas. In column five and six of Table 3.1 the fitted values of $\sigma_{v_{H_2}}$ and tpd_{fit} are listed for the different settings of the valve during the experiments. Comparing tpd_{ex} and tpd_{fit} show the same order of magnitude but different temperature tendencies: while the best settings for tpd_{ex} increase slightly with increasing temperature, the temporal duration of tpd_{fit} decreases with increasing $\mathrm{T}_{\mathrm{valve}}$. However, it is questionable to what extent the parameters tpd_{ex} and tpd_{fit} can be linked at all: tpd_{fit} is part of the free-flight model that only includes the propagation without any interaction between the particles. In contrast tpd_{ex} is the duration of the current pulse that is applied at the EL-valve, which does not directly correspond to the actual opening time of it. The particles collide frequently during the adiabatic expansion in between the valve orifice, where the pulse duration is defined as the actual opening time of the valve, and the 'sudden freeze radius', where the particles propagate in free-flight.

$\mathrm{T}_{\mathrm{valve}}$ [K]	p_{ex} [bar]	tpd_{ex} [μs]	v_{H_2} [m/s]	σ_v [m/s]	tpd_{fit} [μs]
40	5	21.0	938	14.3	36.1
56	10	21.0	1072	13.8	21.7
65	16	20.7	1151	16.1	17.6
82	16	21.8	1320	20.6	11.9
107	17	22.5	1530	22.4	8.9

Table 3.1: The valve settings of the temperature, the stagnation pressure and the applied trigger pulse duration are listed in the first, second and third column. The evaluated beam velocities, the widths of the velocity distributions and the fitted trigger pulse durations are listed in the fourth, fifth and sixth column, respectively.

Population of rotational states in the beam: REMPI The population distribution of rotational states in the H_2 beam in the collision zone is determined spectroscopically. The LIF zone with its PMT is removed and replaced by an ion optics setup with a time-of-fight mass-spectrometer (TOF-MS) at the centre of the collision zone. Ions are detected with a micro channel plate (MCP) detector. In the same way as in the scattering experiment, the two H_2 mixtures are expanded from the Even-Lavie valve. The resulting molecular beam is skimmed and collimated. The only difference is at the collision zone, where a focused pulsed dye laser is used to detect H_2 via resonance enhanced multi photon ionization (REMPI). The population of different J-levels of the vibronic ground state is probed when recording spectra via a (3+1) REMPI scheme using R-transitions along the band: C $^1\Pi_u$, v=2 $\leftarrow$ X $^1\Sigma^+$, v=0 [50]. Spectra are taken in a range between 289.4 - 289.9 nm.

The right graph of Figure 3.4 shows the spectra of the valve settings

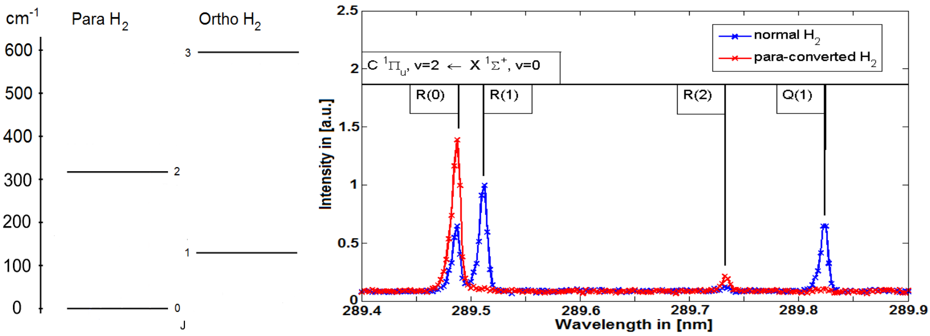

Figure 3.4: Left graph: the rotational level structure shows the corresponding ortho and para levels. Right graph: in the spectra of nH_2 (blue trace) and pcH_2 (red trace) different transitions out of various J-levels are identified very clearly. The difference of the ortho-to-para ratio of the two H_2-mixtures is evident.

at 82 K. A clear difference for the two gas mixtures is observed: in the spectrum of nH_2 (blue spectrum) four different transitions can be identified clearly: R(0) and R(1) around 289.5 nm, R(2) around 289.73 nm, and Q(1) around 289.82 nm. Three rotational states are found to be populated after the supersonic expansion: J = 0, 1 and 2. The spectrum of pcH_2 (red spectrum) shows very different features, since only the R(0) and R(2) transitions are identified. Here, only the J = 0 and J = 2 states are populated. Both spectra support the assumption that after the supersonic expansion basically all H_2 molecules end up in the lowest J-level of the corresponding nuclear-spin configuration. The purity of the pcH_2 mixture is very high, since no population of odd J-states can be observed by eye. Therefore, statistical methods are used to determine the population of J-states in pcH_2.

For a direct, quantitative determination of the different J-state populations, the knowledge of the ionization probabilities during the (3+1)-REMPI process is lacking. However, the ortho-to-para ratio can be determined differently by comparing the two spectra. The spectrum of the nH_2 is used to fit the peaks of the R(0) and the R(1) transitions. A correction factor is determined such that the ratio of the peak intensities (and the different areas under the transitions) corresponds to the ratio that should be found from spin statistics of nH_2: $\frac{n_{J=1}}{n_{J=0}} = \frac{3}{1}$. By fitting the R(0) and the R(1) transition in the spectrum of pcH_2 and by using the correction factor from the nH_2 a purity of the pcH_2 sample is determined of: $\leq 2\%$ oH_2 + $\geq 98\%$ pH_2. In this analysis, the intensity in the R(2) transition is neglected, and we therefore conclude that the sample contains more than 98% of pH_2.

Para-to-ortho back-conversion is found to occur under our experimental conditions, although on a timescale much longer than required for a single experiment. After three days, a significant change in the spectra for pcH_2 is observed. Fresh para-converted H_2 samples are introduced every day to ensure the same sample purity during the scattering experiments. Also in the spectra of nH_2 at lower temperatures of the valve no indication was found that the ortho-to-para ratio of 3/1 changed due to the shift of the thermodynamic equilibrium.

The only remaining question is, how many molecules populate the rotational J=2 state in the beam. In Table 3.2 the Boltzmann distribution in the valve is calculated before the expansion. A thermodynamic equilibrium of the H_2 mixtures at the stabilized temperature can be assumed. These distributions set an upper limit for the population or the rotational levels in the beam, because during the supersonic expansion process only further depopulation due rotational cooling can happen. An other argu-

T_{valve}	J=0	J=2	J=4	J = 1	J = 3
40 K	100.0 %	0.0 %	0.0 %	100.0 %	0.0 %
56 K	99.9 %	0.1 %	0.0 %	100.0 %	0.0 %
65 K	99.8 %	0.2 %	0.0 %	100.0 %	0.0 %
82 K	99.0 %	1.0 %	0.0 %	100.0 %	0.0 %
107 K	95.9 %	4.1 %	0.0 %	100.0 %	0.0 %

Table 3.2: Calculated Boltzmann distribution before the expansion at various stabilized temperatures of the valve.

ment is found later on in section 7.4.1, where the measured cross sections of OH-pcH_2 are presented and compared to theory.

3.2 Stark deceleration

Stark-deceleration has become an established method for the controlled manipulation of molecular beams [51] since its first experimental demonstration in 1999 [52]. This experimental technique exploits the force exerted on polar molecules by external inhomogeneous electric fields. Sophisticated design and application of external electric fields allows the manipulation of motional degrees of freedom and the quantum-state the selection of a part of a molecular packet of neutral molecules. This paragraph reviews briefly the principles of Stark-deceleration and introduces the physical quantities essential for the understanding of the following experiments.

Mechanical design and potential shapes

The mechanical design of the Stark-decelerator is depicted in the central part of Figure 3.1. The actual apparatus consists of three modules which are mechanically decoupled. Pairs of cylindrical electrodes are mounted parallel and equidistantly from the beam axis while their orientation alternates periodically between the horizontal and the vertical direction. Each

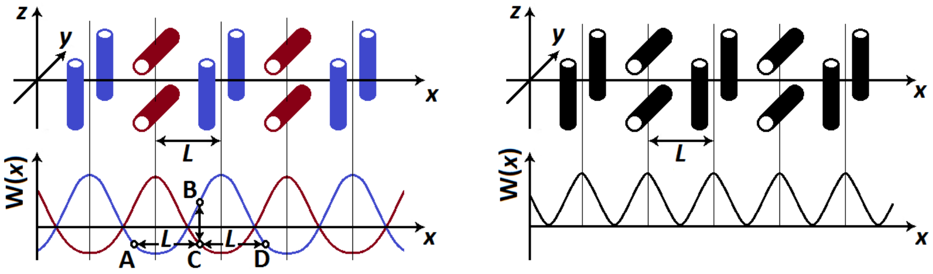

Figure 3.5: The left graph shows the electric field configuration, where $\pm HV$ is applied only to the horizontal (red) and vertical (blue) electrode pairs, while the vertical and horizontal electrode pairs are grounded, respectively. The right graph depicts the electric field configuration of *static burst*, where $\pm HV$ is applied to all electrode pairs simultaneously.

electrode has a diameter of 4.5 mm. Each electrode pair has a centre-to-centre distance of 7.5 mm, constraining a square opening of $3{\times}3$ mm^2 for the propagation of the molecular beam. The apparatus contains in total 317 electrode pairs while the centre-to-centre distance between adjacent pairs is L = 8.25 mm. The mechanical design and construction and the high voltage switching electronics are described in detail in [53] alongside with challenges faced with high-voltage discharges and switching [54].

The molecular packets enter the differentially pumped decelerator chamber by passing through a skimmer (diameter 2 mm). A small 40 mm long hexapole, which is not visible in Figure 3.1, is used to collimate OH radicals into the opening of the Stark-decelerator. Voltages are applied onto opposite electrodes of each pair that are of the same magnitude but of opposite polarity ($\pm HV$). The voltages are switched between $\pm HV$ and ground potential, while the applied polarities on the horizontal or vertical electrode pairs are switched separately. This allows to create three different inhomogeneous, electric field configurations:

- a *vertical* electric field configuration, where $\pm HV$ is applied to the vertical electrodes only, while the adjacent horizontal electrodes are grounded. The left graph of Figure 3.5 schematically illustrates the spatial arrangement of the blue coloured vertical electrodes in the upper part and the created electric field strength in the longitudinal x-direction in the lower part.

- a *horizontal* electric field configuration, where $\pm HV$ is applied to the horizontal electrodes only while the adjacent vertical electrodes are grounded. The left graph of Figure 3.5 shows the horizontal electrodes and potential curve red coloured together with the vertical configuration.
- a *static burst* electric field configuration, where $\pm HV$ is applied simultaneously to the horizontal and vertical electrodes. The right graph of Figure 3.5 depicts the charged electrodes black coloured in the upper part, while the created electric field strength in the longitudinal x-direction shown in the lower part is twice as frequent as the horizontal and vertical configuration.

Assume the horizontal electric field configuration is switched on when molecules are at position A. Molecules in a low-field-seeking quantum state gain potential (Stark-) energy during their flight from position A to B, because they fly into a high field region, and they therefore loose kinetic energy and decelerate. Vice versa molecules in a high-field-seeking quantum state gain kinetic energy and accelerate. If the field configuration is not changed, the molecules continue to fly to position C, in which case the molecules in the low-field-seeking and high-field-seeking quantum states regain and loose the same amount of kinetic energy, respectively. If the electric field configuration is switched to the vertical one, when the molecules reach position B, the low-field-seeking molecules loose potential energy once more and are decelerated effectively, while the high-field-seeking ones are accelerated. Molecules undergo the same effective loss of kinetic energy again, if the electric field is switched off or back to the horizontal configuration when the molecules are at position C. Repeating this procedure successively removes kinetic energy. The amount of kinetic energy gained or removed per stage is determined by the position of the synchronous molecule when the fields are switched. The phase-angle ϕ quantifies this relative position of the synchronous molecule within a stage [55]. The left graph of Figure 3.5 shows that the horizontal and the vertical potential energy have a periodicity of $2L$. In general, the x-position of a molecule can be described by its reduced position $x2\pi/2L$ introducing the periodicity of 2π. $\phi = 0$ is chosen to be the position between two adjacent electrode pairs, while $\phi = \pi/2$ and $\phi = -\pi/2$ follow as the x position at the grounded and charged electrode electrode pair, respectively. In general, deceleration and acceleration is defined by positive and negative phase-angles, respectively, while $\phi = \pm 90°$ corresponds to the situation in which the maximum amount of kinetic energy is removed or gained per stage, respectively. Molecules can be decelerated to a standstill if the number of stages of the Stark-decelerator is sufficient.

In general the spatial symmetry of and the application of the voltages onto the horizontal and vertical electrode pairs allows to relate the created potentials: in the longitudinal x-direction the $W^{hor}(x, y, z) = W^{ver}(x + L, z, y)$. The left graph of Figure 3.6 shows the electric field strength $E^{hor}(x, y, z = 0)$ $(E^{ver}(x, y = 0, z))$, while in the x- and the $y(z)$-direction the extension of three stages and of 3 mm (spatial transverse acceptance) is plotted, respectively. At the charged electrode pairs $(E^{hor}(x = \pi, y, z = 0))$ the electric field strength increases along the $|y|(|z|)$-direction going further away from the x-axis and closer towards the charged electrodes. In the $y(z)$-direction the electric field strength is well approximated by a parabola corresponding to a harmonic potential and has a minimum in between of both charged electrodes along the molecular beam axis. This focuses low-field-seeking molecules towards the molecular beam axis, while high-field-seeking ones are deflected. As a function of the x-position the harmonic potential becomes less confining and even slightly defocussing at the position of the grounded electrodes. Along the $z(y)$-axis basically no gradient of the electric field strength is present leading to an effective free-flight in the vertical (horizontal) direction. The transverse motion of the molecules is commonly described by introducing an effective transverse potential, which is very accurately modeled with a harmonic potential [55] [56] [57].

The right graph of Figure 3.5 shows the *static burst* electric field configuration, where $\pm HV$ is applied to the black coloured horizontal and the vertical electrode pairs simultaneously. The lower part of the graph illustrates that the created potential along the x-axis has a periodicity L. This electric field configuration is ideal to guide molecules through the Stark-decelerator, because if the voltages are not switched the low field seeking molecules are decelerated and accelerated in the same amount while traveling through the periodic potential in the x-direction. Thus, free-flight conditions are generated effectively. Additionally, in both transverse directions the molecules are confined and focused towards the x-axis.

Out of the molecular beam entering the Stark-decelerator, a certain fraction of molecules can be transported throughout the Stark-decelerator, and kept together as a packet without any losses. For this, the molecules have to be within a certain position interval, and their velocity has to be in a certain velocity interval, at the beginning of the Stark-decelerator. This area in 'phase-space' from which molecules are 'accepted' by the decelerator depends on the time sequence of the applied voltage pulses.

This motion of molecules in the Stark-decelerator are simulated using Monte Carlo methods. The initial 6D phase-space distribution of the molecular packet is approximated by discrete random Gaussian distributed samples. Since the static electric field configurations and the induced Stark-shift on the molecules are known, the equations of motions are solved using Runge-Kutta methods. Performing the calculation in short time steps the propagation of the molecules is simulated looking at their trajectories. The particular volume in 6D phase-space from which stable trajectories through the decelerator originate defines the acceptance of the decelerator. The number density of the molecular packet leaving the Stark-decelerator depends on the number density of the initial molecular packet and the acceptance. Numerical and analytical investigations show that the acceptance is a function of ϕ [58] [59]. The right graph of Figure 3.6 shows the longitudinal phase-space, where regions of acceptance as a function of ϕ are plotted. The x-axis is given in reduced position coordinates of radians, while the calibration of the v_x-axis depends on the Stark-shift and the mass of the molecule and the created electric field configuration. These investigations have led to optimizations of the $\pm HV$ switching schemes. Operation of a Stark-decelerator is commonly per-

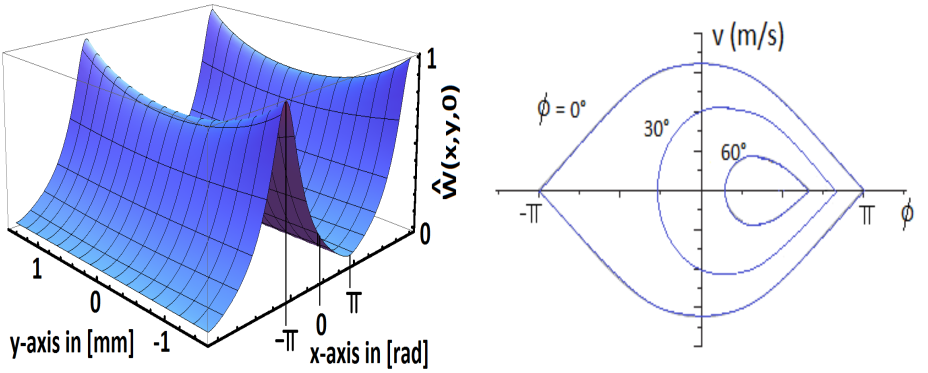

Figure 3.6: The left graph shows the normalized electric field configuration in the x-y-plane in one stage, corresponding to the case where the horizontal electrode pairs are charged and the vertical ones grounded. The right graph shows different areas of 'acceptance' in phase-space for different phase-angles ϕ.

formed by using a constant ϕ in the so-called $s = 1$ or $s = 3$ mode, where the *horizontal* and *vertical* electric field configurations are switched after the synchronous molecule has traveled the distance of one and three stages, respectively. This leads to the same longitudinal deceleration (or acceleration) per switching cycle. In both modes of operation there is focusing in each transverse direction. However, in the $s = 3$ mode the intermediate stage causes supplementary transverse focusing yielding an effective decoupling of the longitudinal and transverse motion compared to the $s = 1$ mode [58]. This guarantees an optimal operation of the Stark-decelerator [57].

3.3 Detection methods

The detection method of the OH molecules is laser induced fluorescence (LIF). This spectroscopic technique involves basically two steps: first the molecular target is excited by illumination with laser radiation. The probing of selected quantum states is performed by scanning the wavelength of the excitation laser. Transitions are induced along the A $^2\Sigma^+$, v' = 1 ← X $^2\Pi_{3/2}$, v = 0 band around 282 nm. In the left part of Figure 3.1 two blue arrows illustrate the two pathways where the laser intersects the spherical chamber horizontally in the $x - y$ plane. The lifetime of the excited state is 748 ns [45]. The following emission decays with a high probability along the A $^2\Sigma^+$, v' = 1 → X $^2\Pi_{3/2}$, v = 1 band around 314 nm. Fluorescent photons are collected vertically from the top along the z-axis by a lense and imaged onto a photomultiplier tube (PMT).

These experimental arrangements allow an extremely high sensitivity, because the detection is almost background free. Stray light photons are created at the entrance and exit (Brewster) windows and by Rayleigh scattering with the residual gas. This is minimized using light baffles and optical filters in front of the PMT. Several different filters are used leaving a transmission window around 314 nm improving the signal-to-noise ratio. Laser radiation for the LIF detection is created by different laser systems:

Ring dye laser (RDL)

A continuous wave ring dye laser (Coherent 899-21, Dye: Rhodamine 6G) is pumped by an injection seeded YAG (Millenia). The frequency is stabilized relative to a Helium Neon laser (SIOS SL 03). The dye-laser radiation is frequency doubled in an external cavity (Spectra Physics, LAS WaveTrain), where typically a power of 4 mW is achieved. The inherent bandwidth of the dye laser at the fundamental frequency is less than 1 MHz, but taking drifts and the frequency stabilization into account, the laser is kept stable within ±1 MHz in the fundamental (and ±2 MHz after the frequency doubling) over several hours. The laser polarization vector $\underline{\mathcal{E}}$ is determined by the SHG setup to be horizontal. A $\lambda/2$-plate is used to rotate $\underline{\mathcal{E}}$ manually in any desired angle within an accuracy of 0.5°. A more detailed description of this laser system is given in [60].

The detection with the RDL takes place under unsaturated conditions since the laser power is quite low. In this case only a small fraction of the probed state's population (n_0) is excited, while stimulated emission can be neglected. The number of excited molecules (n) is related to the transition frequency (ω) dependent parameter of the absorption coefficient $\alpha(\omega)$ and the laser intensity (I): $n = \alpha(\omega) I n_0$. Since I fluctuates in time, it is measured constantly with a semiconductor diode (Thorlabs). Therefore, the measured signal (Sig) is directly proportional to

$$Sig \propto n/I = \alpha(\omega) n_0. \tag{3.8}$$

Pulsed dye laser (PDL)

A pulsed dye laser (Sirah: Precision Scan, Dye: Rhodamine 6G) is pumped by a pulsed Nd:YAG laser (Spectra-Physics: Quanta Ray) at a repetition rate of 10 Hz. The output of the PDL is frequency doubled using a BBO crystal creating a laser pulse with a duration of ~8 ns, a pulse energy of 4 mJ/pulse and a bandwidth of ~2 GHz. With these high laser pulse intensities the optical transitions are saturated. Absorption and stimulated emission take place repeatedly distributing the initial ground state population (n_0) equally over the substates of the ground (n) and the excited state (n') which can be coupled by the laser $\frac{n}{g} = \frac{n'}{g'}$ where $g = 2J + 1$ and $g' = 2J' + 1$ define the number of substates of an individual rotational J-state in the ground and excited state, respectively. Under saturation conditions the ground state population is related to the number of excited substates by the so-called excitation rate

$$\Gamma_f = \frac{n'}{n_0} = \frac{g'}{g + g'} \tag{3.9}$$

which is independent of the laser intensity and the absorption coefficient. Since only the excited substates can possibly fluoresce, the ground state populations relate to the measured signals by: $Sig \propto n' = \Gamma_f n_0$.

Chapter 4

Bunching of molecular beams

4.1 Introduction

Cold molecules have become a indispensable tool for many investigations and applications in physics and chemistry [8] today. Among various experimental techniques [61], the Stark-decelerator offers the advantages to produce internally cold and quantum-state selected molecular packets, whose velocity can be tuned over a wide range [51]. Many experiments, however, could be greatly improved with a larger number of molecules in the packet: in metrology experiments, where high resolution spectroscopy is used, the statistics would become better [62] [63] [64] [65]; the detection of inelastic or reactive processes in molecular collisions could be improved [66] [47]. Loading more molecules into storage rings [67] [68] [69] or traps [70] [71] [72] does not only increase the timescale for experimental investigations [73] [74] [75], it also allows the application of further cooling techniques like evaporative cooling [25] paving the way to enter the regime of dipolar quantum gases [76] [1].

Apart from the optimum operation of the experimental components like the molecular beam sources or the detection laser systems, one alternative to optimize an experiment can be to manipulate the phase-space distribution of the atomic or molecular packets. So-called bunching methods are standard strategies in different areas of physics. The method of bunching is illustrated schematically in two steps in Figure 4.1. There, the horizontal axis defines a spatial coordinate, while the vertical axis shows the corresponding velocity coordinate. On the left, the circle depicts an initial phase-space distribution, e.g. a molecular packet after a Stark-decelerator. In the first step of the bunching method the molecular packet travels a certain distance in free flight. On the way, the faster molecules overtake the slower one, which corresponds to a shearing out of the distribution in phase-space. The longer the free flight lasts the more elongated and tilted the distribution becomes. In the second step, a harmonic potential is applied around the packet. This slows down the faster molecules in the front of the packet and accelerates the slower ones in the rear of the packet. In phase-space, this corresponds to a rotation of the distribution. Depending on the duration the harmonic potential is applied, the distribution can be rotated such that its width becomes minimal in either the velocity (blue distribution) or the spatial (red distribution) coordinate.

In general, bunching schemes can be used to cool motional degrees of freedom. However, bunching is not referred to as cooling method, since the phase-space density is conserved [77]. The bunching procedure allows to generate colder but spatially larger or more dense but hotter packets, respectively. The bunching method does not increase the number density, however the number of molecules available in the packet are just used more efficiently.

Bunching methods are implemented, for example, in charged particle acceleration physics, where the terms 'rebunching' and 'bunch rotation' refer to the narrowing of the particle distribution in position and velocity space [78] [79] [80]. Similar procedures using magnetic field gradients have been applied to produce cold atomic samples [81] [82], where it is described as 'δ-kick cooling'. Also the use of time-varying magnetic fields for bunching of atoms [83] [84] or neutrons [85], both in position space and in velocity space has been proposed.

The first experimental demonstration of the bunching of neutral polar molecules with time-varying electric fields has been performed by Crompvoets and co-workers [86]. A so-called 'buncher' consisting of additional electrostatic components has been mounted behind a Stark-decelerator. A molecular packet leaving the Stark-decelerator underwent free flight conditions before entering a first hexapole which collimates the motion in both

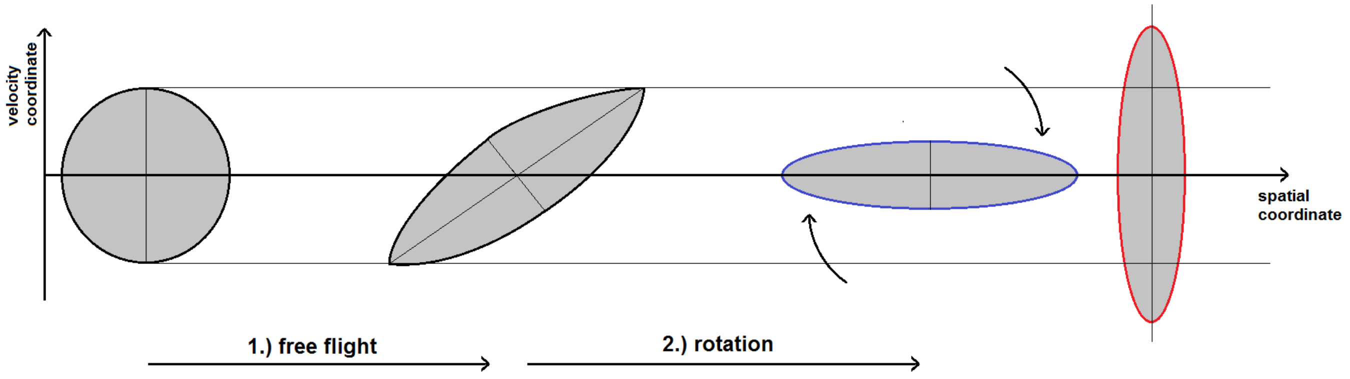

Figure 4.1: The method of bunching is illustrated schematically in two steps. The horizontal axis defines a spatial coordinate, while the vertical axis shows the corresponding velocity coordinate. On the left, the circle depicts an initial phase-space distribution, e.g. a molecular packet after a Stark-decelerator. In the first step of the bunching method the molecular packet travels a certain distance in free flight. On the way, the faster molecules overtake the slower one, which corresponds to a shearing out of the distribution in phase-space. The longer the free flight lasts the more elongated and tilted the distribution becomes. In the second step, a harmonic potential is applied around the packet. This slows down the faster molecules in the front of the packet and accelerates the slower ones in the rear of the packet. In phase-space, this corresponds to a rotation of the distribution. Depending on the duration the harmonic potential is applied, the distribution can be rotated such that its width becomes minimal in either the velocity (blue distribution) or the spatial (red distribution) coordinate. Thus, velocity or spatial focusing is achieved, respectively, while the latter is also referred to as (δ-kick) cooling.

transverse directions. Farther downstream the molecular packet entered a second Stark-decelerator consisting of five electrode pairs, which dimensions (electrode sizes and relative distances) were twice as large, compared to the first one, in order to increase the spatial volume of the harmonic potential relative to the size of the molecular packet. By applying the harmonic potential for differently long durations longitudinally focused or longitudinally cold molecular packets were created. Combined with a second hexapole, this ’buncher’ is routinely used to couple molecular packets into a storage ring [87] or a molecular synchrotron [68] [69]. Longitudinal focusing has been implemented directly in a Stark-decelerator without using additional electrostatic components to reach a higher density for spectroscopic investigations [62]. First a deceleration sequence has been applied for about three quarters of the Stark-decelerator. Then, the high voltage ($\pm HV$) has been switched off to provide free-flight conditions. Once the molecular packet has traveled to the last stage, $\pm HV$ has been applied with $\phi = 0°$ to focus the molecular packet in position space. Further bunching schemes have been used to realize a molecular synchrotron, where the molecular packet needs to be confined spatially to avoid the spreading of the molecular packet. Here, the rods of adjacent hexapoles are switched to different values of $\pm HV$ to create a harmonic potential [68] [69].

In this chapter, bunching in the longitudinal and the two transverse dimensions is demonstrated. Individual dimensions or combinations of them can be manipulated simultaneously depending on the high voltage switching scheme of the Stark-decelerator setup only. No additional electro-static components or more advanced electronics are required. Such, shaping of the 6D phase-space distribution can be performed in any desired dimension to prepare the molecular packet for an optimum use for subsequent experiments. This allows, for example, to cool the bunched dimensions of the molecular packet down to temperatures of hundreds of micro-Kelvin.

In previous experiments [55] [56] [57] time-of-flight (TOF) spectra have been simulated using trajectory simulations, which have been compared with measured TOF spectra. These TOF measurements correspond to a projection of the number of molecules of the phase-space distribution as a function of the arrival time. In the present experiment the narrow bandwidth RDL allows to map the number of molecules as a function of both the arrival time and the velocity distribution. These measured spectra are compared with simulated Doppler-broadened spectra on a quantitative level to determine a final temperature within the molecular packet.

4.2 Experimental methods and data analysis

Experimental procedures

The production method of OH radicals, the manipulation of the motion with electric fields and the detection of OH radicals have already been described in greater detail in sections 3.1, 3.2 and 3.3. Here, only the relevant parts and details for the experiment are summarized. OH radicals are produced within the supersonic expansion of nitric acid (HNO_3) seeded in an argon carrier gas by photo dissociation with an ArF-excimer laser (193 nm). After the expansion from the pulsed valve the OH radicals pass through a skimmer with an initial mean longitudinal velocity of $v_{ini}^{OH} =$ 625 m/s. A small hexapole collimates the OH radicals in both transverse directions before they enter the Stark-decelerator.

Throughout all experiments performed here, voltages of ± 15 kV are applied to opposing electrodes of each pair. Depending on which electrode pairs are switched on at a time, the different electric field configurations (EFC) of *horizontal*, *vertical* or *static-burst* are created which are illustrated in Figure 3.5. The timings for the HV-switching of the three EFCs are determined by calculating the motion of the synchronous molecule and by using the appropriate phase-angles ϕ to realize the bunching scheme: first a normal HV-switching scheme for deceleration is applied with $\phi \geq 40^\circ$. This already segregates a 6D phase-space distribution out of the initial OH packet, which can be transported stably through the Stark-decelerator. The free-flight conditions are established by keeping one or none EFC switched on for the amount of time while the molecular packet travels through several stages. Depending on the bunching scheme the last

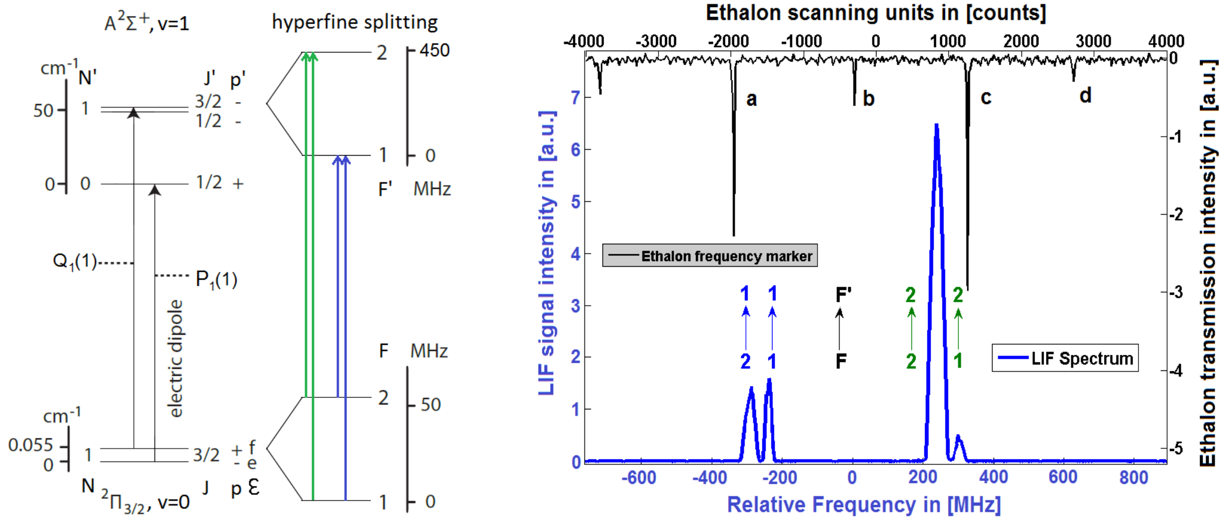

Figure 4.2: The left graph shows in its left part an energy level scheme of the ground state and the excited state of OH, where the $Q_1(1)$ transitions along the $|A^2\Sigma^+, v'=1, N'=1, -\rangle \leftarrow |X^2\Pi_{3/2}, v=0, J=3/2, +\rangle$ band is depicted. In the right part the hyperfine splitting of the ground and the excited state are labeled by F and F', respectively. The hyperfine transitions excited to the final states $F'=1$ and $F'=2$ are coloured blue and green, respectively. They are also labeled in the spectrum in the right graph. For all the bunching measurements the most intense line $F'=2 \leftarrow F=2$ is used. The black trace shows the calibration measurements of the etalon's transmission fringes as a function of the scanning units in [counts], which are plotted as the top horizontal axis. The fringes, indicated by a, b, c and d are used to determine a counts-to-MHz ratio which is used to calibrate the relative frequency given as the horizontal axis at the bottom in [MHz].

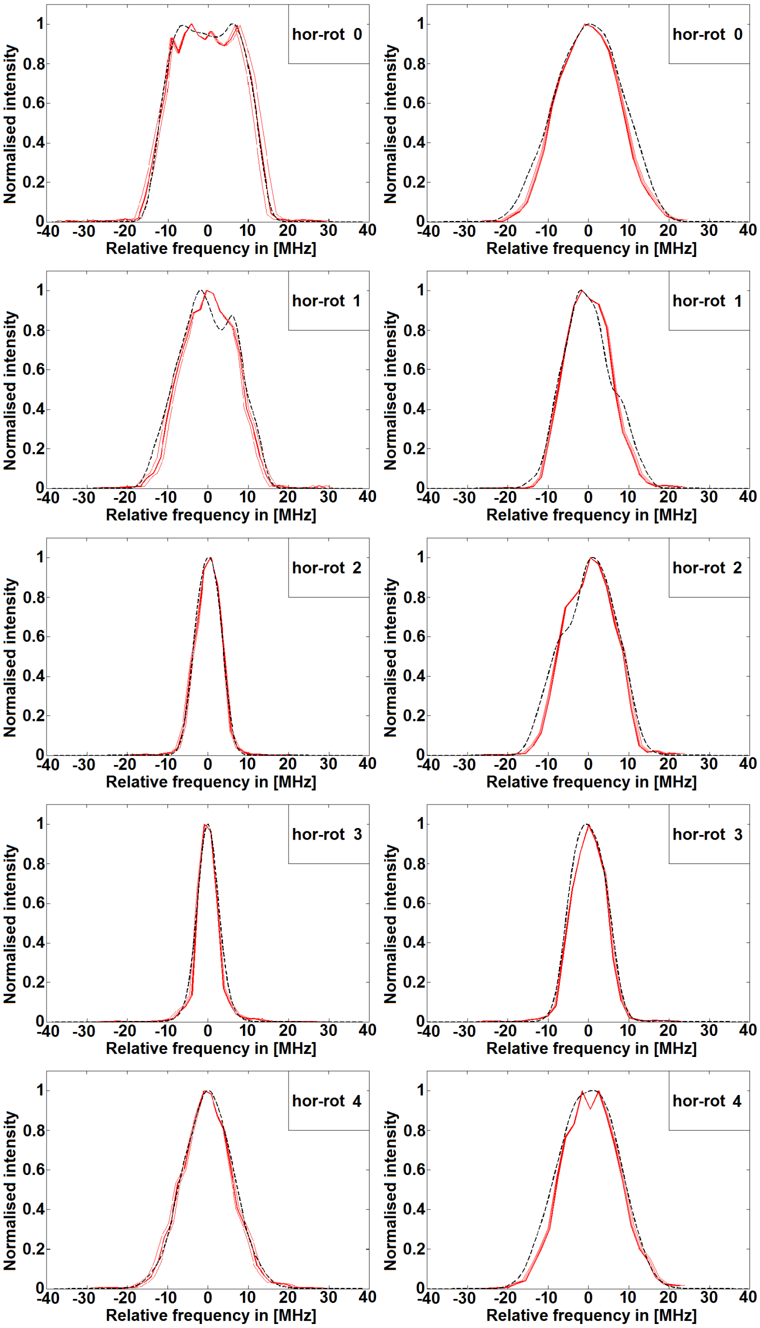

Figure 4.3: Transverse bunching only is depicted for the 90°- and 45°-detection schemes. In all graphs the measured and the simulated intensities are shown in red and black lines, respectively. The profiles are normalised to one to enable a quantitative comparison of the Doppler-broadening.

few stages are used to perform the rotation of the distribution in phase-space.

The upper left graph of Figure 2.2 shows the two low-field seeking branches ($M_J\Omega$ = -3/4 and $M_J\Omega$ = -9/4) of the rovibrational ground state. Once phase-angles of $\phi \geq 40°$ are used, trajectory simulations show that the acceptance in phase-space for molecules in the $M_J\Omega$ = -3/4 branch is so small that their number in the packet leaving the Stark-decelerator can be neglected compared to the amount of molecules in the $M_J\Omega$ = -9/4 branch. When the electric field strength goes to zero, the $M_J\Omega$ = -9/4 component correlates to the $|X^2\Pi_{3/2}, v = 0, J = 3/2, f, p = +, F = 2\rangle$ hyperfine state in field-free conditions, which is depicted in the lower left graph of the same Figure 2.2. Therefore, simulations of molecules of the $M_J\Omega$ = -9/4 branch are sufficient to be considered in the comparison with the measured spectra using a transition out of the $F = 2$ hyperfine state.

The bunched molecular packet is finally detected via laser induced fluorescence (LIF). OH radicals are excited with the RDL along the $Q_1(1)$-line around 35461.50 cm^{-1} [45] [29]. The left graph of Figure 4.2 shows in its left part an energy level scheme of the ground state and the excited state, where the $Q1(1)$ transition ($|A^2\Sigma^+, v = 1, N = 1, p = -\rangle \leftarrow |X^2\Pi_{3/2}, v = 0, J = 3/2, f, p = +\rangle$) is depicted. In the right part the hyperfine splitting of the ground and the excited state are labeled by F and F', respectively. Those hyperfine transitions excited to the final state of $F' = 1$ and $F' = 2$ are coloured blue and green, respectively, originating from the $F = 1$ and $F = 2$. In the right graph of Figure 4.2 all four hyperfine transitions are identified and labeled in the spectrum shown in the right graph. For this, OH packets are guided with $\phi = 0°$ through the Stark-decelerator. The black trace shows the transmission fringes of the RDL frequency as a function of the etalon in scanning units of [counts] on the horizontal top axis. The positions of the fringes are used to calibrate the count-to-MHz ratio. The relative frequency in [MHz] is drawn as the horizontal axis at the bottom of the graph. The zero point of the relative frequency axis is determined on an absolute scale using a commercial wavemeter defining the origin of the rotational transition of the $Q_1(1)$ line. For all the bunching measurements the most intense transition $F' = 2 \leftarrow F = 2$ is used for the detection. The experimental error in the determination of the line width is given by the error of the frequency calibration. The four transmission fringes indicated by a, b, c and d are used to determine three counts-to-MHz ratios defining a systematic error of the calibration. In all graphs, where simulated and measured spectra are compared, three spectra are plotted illustrating the error in calibrating the relative frequency.

Detection schemes and data analysis

This section summarizes how a comparison of the Doppler-broadened line-shapes of experimentally measured spectra with simulated ones using the 6D phase-space distribution from the trajectory simulations is achieved. In general, in the experiment an OH packet is bunched using a certain HV-switching scheme. Figure 3.1 depicts two pathways how the RDL can be aligned through the detection chamber. If the laser is shot along the y-axis and along the $-x$-y-axis, the detection happens in 90° or 45° with respect to longitudinal (translational) direction of the OH packet, respectively. The narrow bandwidth RDL allows to determine the Doppler-broadened line-shapes measuring a spectrum along these two pathways. To extract the signal of the bunched packet only, the PMT signals are gated electronically to count only photons during the arrival time of the bunched packet. The relative frequency axis and its calibration error are determined using the transmission fringes of the small etalon. Such spectra of different switching schemes are plotted as red lines in the graphs of the Figures 4.3, 4.4, and 4.9.

The same HV-switching sequence is used in the simulations to generate the 6D phase-space distribution leaving the Stark-decelerator. These velocity distributions are used to calculate the Doppler profiles as follows:

- **90°-detection:** If the laser beam is shot along the y-axis the measured line profile Δf_y is directly mapping the v_y-phase-space distribution. The simulation of the Doppler broadening follows from the

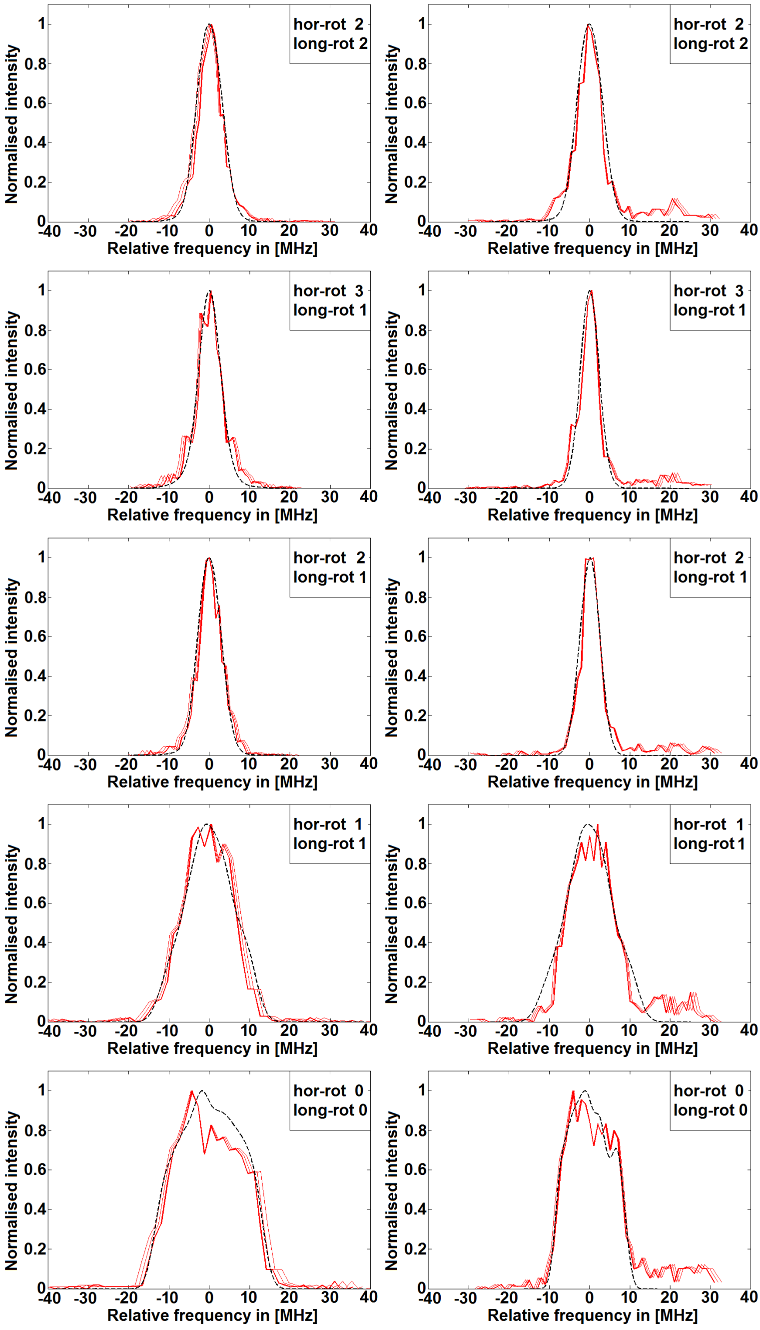

Figure 4.4: The 2D-bunching sequences are depicted for the 90°- and 45°-detection schemes. In all graphs the measured and the simulated intensities are shown in red and black lines, respectively. The profiles are normalised to one to enable a quantitative comparison of the Doppler-broadening.

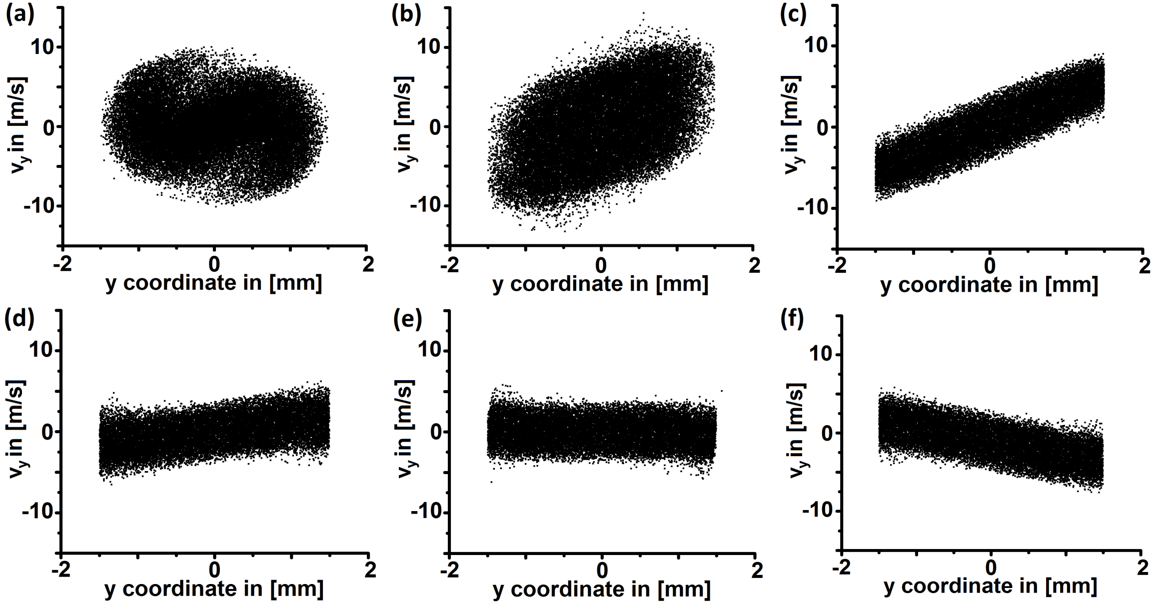

Figure 4.5: Six (transverse) phase-space distributions, that result from numerical trajectory simulations, are depicted as an example to illustrate the bunching process in the transverse direction, which can be compared to the schematic illustration of Figure: 4.1. At the upper left graph (a) shows the phase-space distribution after deceleration with a certain phase-angle. Graphs (b) and (c) display the elongation of the particles in the packet during free-flight. The lower three graphs (d), (e) and (f) show the progression of the rotation in phase-space, where the harmonic potential is applied for even longer times, respectively. The central graph (e) illustrates an optimal focusing of the distribution in the v_y-velocity space.

relation

$$\mathit{\Delta} f_y = f_0(1 + \frac{\mathit{\Delta} v_y}{c}), \tag{4.1}$$

where f_0 is the transition frequency of the $Q_1(1)$ line and c is the speed of light. To ensure that the alignment of the laser is actually perpendicular to the longitudinal axis of the OH packet in the 90°-detection scheme the laser is shot through the same alignment of pinholes in the y and $-y$-direction such that the corresponding spectra (and the corresponding central transition frequencies) show no relative (Doppler) shift.

- **45°-detection:** In this detection scheme two effects must be taken in to account: the longitudinal and transverse velocity distribution of the v_x-v_y-phase-space causes a Doppler broadening ($\mathit{\Delta} f_{xy}$); and the longitudinal velocity component in the x-direction of the molecular packet results in a Doppler shift (δf_{xy}) of the central transition frequency. The simulated spectra follow from

  $$\mathit{\Delta} f_{xy} = f_0(1 + \frac{\mathit{\Delta} v_{xy}}{c}) \quad \text{and} \quad \delta f_{xy} = f_0(1 + \frac{\bar{v}_{xy}}{c}). \tag{4.2}$$

  The mean velocity ($\bar{v}_{xy}$) of the molecular packet is determined as an input parameter defining the HV switching scheme. An identical value of $\bar{v}_{xy}$ follows from the sample mean of the simulated particles of the packet leaving the Stark-decelerator. The measured Doppler shift resulting from the 90°- and 45°-detection scheme and the simulated value of δf_{xy} are used to adjust the angle of the 45°-detection scheme to actually be 45°.

Further experimental conditions are taken into account in all spectra simulations: (1) The diameter of the laser-spot is ≈1.5 mm. Therefore, only this illuminated central part of the total 16x3x3 mm^3 volume of the OH packet is taken into account in the simulations. (2) At each laser frequency f_{RDL} each simulated molecule's contribution to the signal $Sig(f_{\text{RDL}})$ is summed up by weighting its Doppler-shifted transition frequency f_i^{Dop}, that is given in the 90° and 45°-detection scheme by equation (4.1) and equation (4.2), respectively, with the bandwidth of the laser which is given by ±2 MHz in section 3.3:

$$Sig(f_{\mathrm{RDL}}) = \frac{1}{\sigma_{\mathrm{RDL}}\sqrt{2\pi}} \sum_{i=1}^{N} exp\left[\frac{-(f_i^{Dop} - f_{\mathrm{RDL}})^2}{2\sigma_{\mathrm{RDL}}^2}\right], \tag{4.3}$$

The simulated spectra are plotted as black, dashed lines in the graphs of Figures 4.3, 4.4, and 4.9. Qualitatively, they reproduce the line shapes correctly, quantitatively, the agreement for almost all spectra is within the systematic error of the frequency calibration. This allows to relate a temperature (T_i, where the index $i = x, y, z$ defines the longitudinal or transverse dimensions) to the molecular packet using the velocity distribution (σ_{v_i})

$$\frac{1}{2}k_B T_i = \frac{1}{2}m_{OH}\sigma_{v_i}^2 \tag{4.4}$$

with the constants m_{OH} and k_B are the mass of OH and the Boltzmann constant, respectively. This relation follows from the Maxwell-Boltzmann statistics, where the particle's velocities are assumed to be normal distributed [88]. In the graphs of Figures 4.3, 4.4, and 4.9 the Doppler-profiles show different shapes, while some of them differ strongly from normal distributions. Thus, no Gaussian functions are used to fit the Doppler profiles. Instead, the standard deviation of the simulated packet leaving the Stark-decelerator is used to quantify $\sigma_{v_i} = \sqrt{\frac{1}{N}\sum_{j=1}^{N}(v_{i_j} - \bar{v}_{i_j})^2}$ the velocity distributions of the molecular packets leaving the Stark-decelerator independent of any, possibly underlying, distribution function.

4.3 Implementation of different bunching schemes

In the following different bunching schemes are discussed. First the general implementation of a bunching scheme is introduced. Then, the demonstration in this experimental setup is shown together with a quantitative analysis.

Transverse bunching

The following scheme is used in general to implement bunching in one transverse direction in a Stark-decelerator: the first few stages are used to accelerate or decelerate a molecular packet. Then, free-flight conditions in the longitudinal and the horizontal (vertical) directions are realized by keeping the *horizontal* (*vertical*) EFC switched on, while the packet propagates multiple stages. During this time the molecular packet is confined in the vertical (horizontal) direction. For the few last stages the *vertical* (*horizontal*) EFC is switched on to apply a harmonic potential in the horizontal (vertical) direction which corresponds to a rotation of the phase-space distribution. The amount of rotation depends linearly on the duration the harmonic potential is applied.

To demonstrate the transverse bunching in this experimental setup, first a molecular packet is decelerated with $\phi = 60°$, s = 3 until stage 265 from 625 m/s to 498 m/s. Then, the *horizontal* EFC is switched on to have free-flight conditions for 43 stages. The rotations in the transverse-horizontal phase-space are performed during the last 8 stages, where the *vertical* EFC of 4 stages can be used. Figure 4.3 depicts graphs of Doppler profiles measured in the 90°- and 45°-detection scheme in the left and right column, respectively. The graphs in the first row show the measurements where no *vertical* EFC is applied during the last 8 stages, which is labeled by: hor-rot 0. The corresponding phase-space distribution after the free-flight is plotted in graph (c) of Figure 4.5. These measured Doppler profiles reflect the velocity distribution after the free-flight. The graphs between the second and the fifth row illustrate measurements, where consecutively one more vertical stage is switched to $\pm HV$. The rotation of the horizontal phase-space distribution is directly observed in the graphs showing the 90°-detection, while the corresponding phase-space distributions are depicted in the graphs (d), (e) and (f) of Figure 4.5. Thereby, a focusing in the horizontal velocity space is best achieved using three vertical stages (labeled: hor-rot 3), where the Doppler profile shows a minimal width.

The left graph of Figure 4.6 shows the non-normalised intensity of the

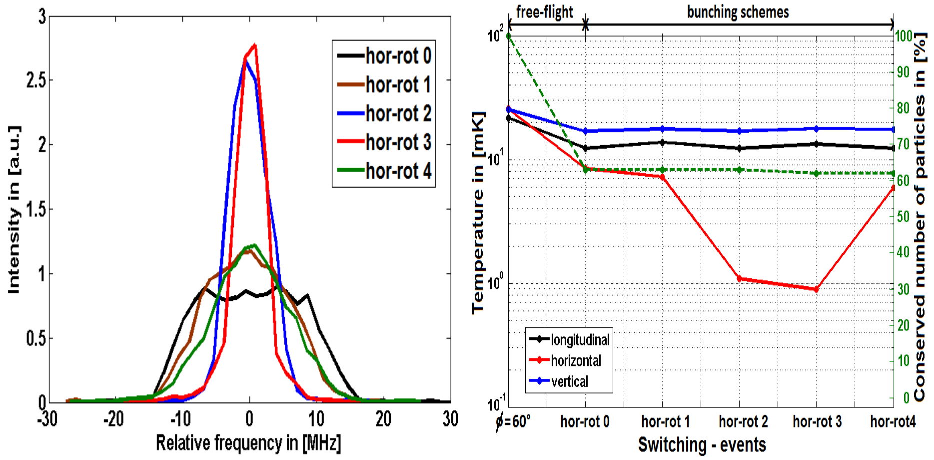

Figure 4.6: The left graph shows the increase of the peak intensity due to the focusing in velocity space. The right graph displays on the left vertical axis the molecular packet's temperatures of the longitudinal, the horizontal and the vertical direction (T_x, T_y and T_z) on a logarithmic scale. The right vertical, green axis depicts the relative number of conserved particles of the packet. Both, the temperatures and the particle numbers are plotted as a function of the corresponding $\pm HV$ switching schemes for bunching.

measured Doppler profiles as a function of the relative frequency in the 90°-detection scheme. Here, the transverse bunching is observed as a focusing in velocity space which results not only in a narrower Doppler profile but also in a superelevation of the peak intensity because more molecules are resonantly excited with the laser at the same f_{RDL}.

The right graph of Figure 4.6 illustrates the same progression of different bunching schemes. The temperatures according to equation (4.4) are plotted as a function of the applied $\pm HV$ switchings for the longitudinal (x-direction), the horizontal (y-direction) and vertical (z-direction) in black, red and blue coloured lines, respectively. As a reference, the first switching illustrates the temperatures of the OH-packet at stage 265 after it has been decelerated, which is labeled with $\phi = 60°$. After the free-flight (labeled by: hor-rot 0) all temperatures have dropped a little. During the following bunching scheme it is obvious, that only bunching in the horizontal direction is performed due to a changing T_y, while T_x and T_z stay unaffected. In the horizontal direction a minimum temperature of $T_y = 889\ \mu\mathrm{K}$ could be achieved. The vertical axis on the right shows the number of molecules which can be conserved relative to the number present in the separatrix at stage 265. During the free-flight $\approx$38% of the particles are lost in this particular bunching scheme. However, taken into account that the bunching superelevates the intensity by a factor 2.5 relative to the free-flight, it is evident that the number of molecules being resonant to the laser at the same f_{RDL} is increased with an optimal focused packet in velocity space.

In general, the packet can also be rotated further to be focused in the transverse position space producing a thin packet in the corresponding transverse direction. Even lower temperatures can be achieved by including longer distances of free-flight, which decreases the final number-density of the packet simultaneously. Thus, the more the distribution is spatially elongated, the shorter the harmonic potential needs to be applied to rotate the phase-space distribution. The shorter the duration for the rotation becomes the larger will be the influence of the anharmonicities of the transverse potential leading to differently large rotations which result in a non-uniform focusing. This pure transverse bunching can be used to optimize spectroscopic experiments (see chapter 5) or possible trap loading schemes [89] [90].

2D-bunching: combining longitudinal and transverse bunching

In general, a combination of bunching in the longitudinal and one transverse direction is implemented in a Stark-decelerator by firstly decelerating or accelerating a molecular packet for a certain amount of stages; secondly, by using the *static-burst* EFC, which causes a free-flight in the longitudinal direction, while the molecular packet is confined in both transverse directions. It is followed by switching to the *horizontal* (*vertical*) EFC, where the molecular packet propagates under free-flight conditions in the longitudinal and the horizontal (vertical) direction, while it is confined in the vertical (horizontal) one. The combination of the *static-burst* and the *horizontal* (*vertical*) EFC allows to individually adjust the duration of free-flight of each direction; thirdly, the last few stages of the Stark-decelerator are used to rotate the molecular packet in the longitudinal direction by applying ϕ=0° for a certain amount of stages, while the rotation in the horizontal (vertical) direction is performed as before by using the *vertical* (*horizontal*) EFC for a certain amount of stages.

Such a two dimensional bunching is demonstrated in this setup. A molecular packet is decelerated with $\phi = 80°$, s = 3 until stage 220 from 625 m/s to 496 m/s. Then, the free flight conditions are established at first only in the longitudinal direction until stage 265 by switching to the *static-burst* EFC, followed by a free-flight in the longitudinal and the horizontal direction for 47 stages using to the *horizontal* EFC. During the last 4 stages the phase-space rotations are induced in each dimension.

The graphs in the left and right column in Figure 4.4 depict the measured and the simulated Doppler profiles of the 90°- and the 45°-detection scheme in red solid lines and black dashed lines, respectively. The simulated profiles reproduce the measured ones within the experimental error, throughout. The graphs in the first row show the measurements where no EFC is applied during the last 4 stages. These measured Doppler

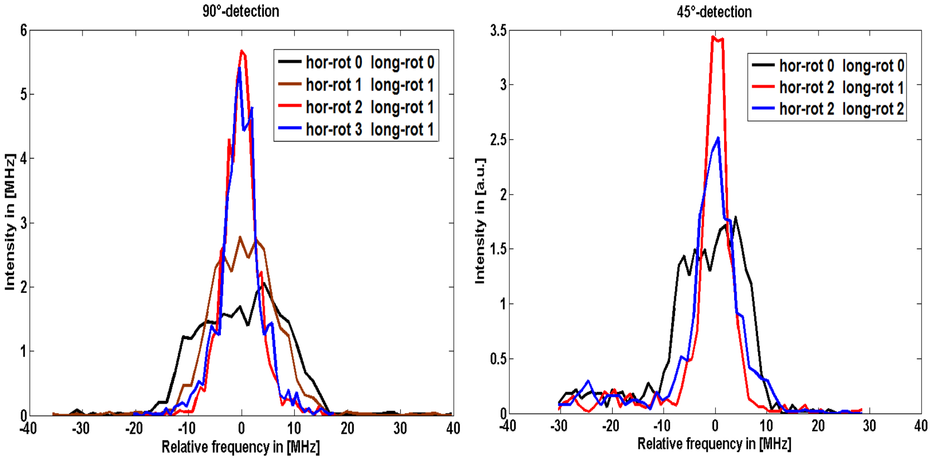

Figure 4.7: The left and the right graph depict the superelevation of the signal measured in the 90°- and 45°-detection scheme due to the focusing in v_y- and $-v_x$-v_y velocity space, respectively.

profiles of the 90°- and the 45°-detection scheme reflect the velocity distribution after the free-flight in the y- and in the $-x$-y-direction which are labeled by: hor-rot 0 long-rot 0, respectively. The graphs of the second, the third and the forth row illustrate measurements, where the *vertical* EFC is switched on for one, two and three stages continuously (the corresponding labels are: which are labeled by: hor-rot 1 long-rot 1, hor-rot 2 long-rot 1, and hor-rot 3 long-rot 1). This induces a bunching in the horizontal direction whose progression is observed by narrower line-widths in the 90°-detection. The induced bunching in the longitudinal direction cannot be observed independently because in the 45°-detection the $-v_x$-v_y velocity distribution contribute to the Doppler-broadening, where, nevertheless, smaller line-widths are observed. The graphs in the last row show the results where $\phi = 0°$ is switched with the *horizontal* EFC followed by horizontal bunching using the *vertical* EFC for 3 stages.

The left and the right graph of Figure 4.7 depict the increase of the signal intensity measured in the 90°- and 45°-detection scheme due to the focusing in y- and $-x$-y velocity space, respectively. The left graph

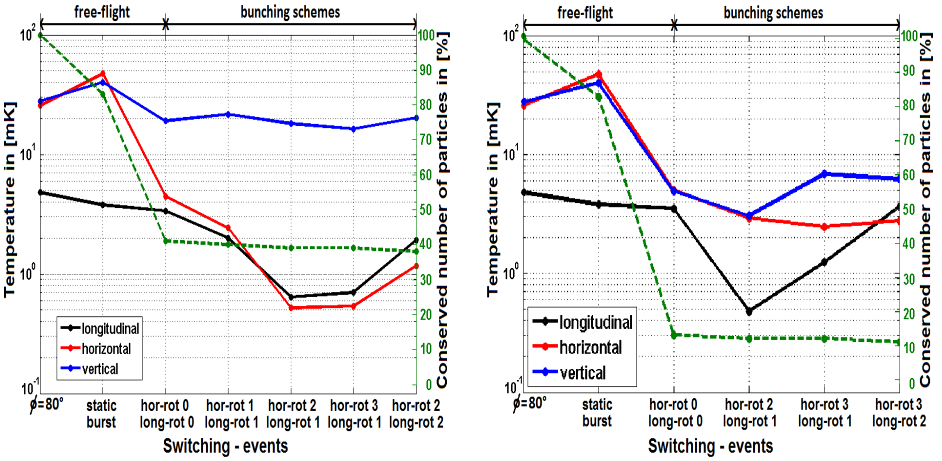

Figure 4.8: The left graph shows the numerical results of the longitudinal and horizontal bunching scheme, while the right graph depicts the results of the bunching in all three dimensons. The left vertical axis illustrates the temperatures on a logarithmic scale of the longitudinal, horizontal and vertical direction in black, red and blue solid linesrespectively, as a function of the corresponding switching scheme in both graphs. The right vertical axis shows the percentage of the conserved number of particles.

of Figure 4.8 depicts the numerical results of the temperatures and the particle numbers as a function of the corresponding bunching schemes in the longitudinal and both transverse directions. By timing the switching of the *vertical* EFC for 3 stages such, that it corresponds to a switching of $\phi = 0°$ in the longitudinal direction, an optimal amount of rotation to achieve a focusing in both the longitudinal and the horizontal velocity space is performed. Thus, minimal temperatures of $T_x = 640\ \mu$K and $T_y = 520\ \mu$K are achieved, while the temperature in the vertical dimension stays unaffected with $T_z = 18.05$ mK. The right vertical axis shows the relative number of conserved particles in the packet on the green scale. Roughly ≈18% and ≈40% of the particles are lost during the free-flight using the *static-burst* and *horizontal* EFC, respectively, before the rotations in phase-space are induced.

This 2D-bunching is ideally suited for crossed beams scattering experiments. There, the velocity distributions in the scattering plane define the relative velocity vectors and hence the collision energy. In chapter 8 the influences of the initial velocity distributions of the molecular packets on the collision energy and the collision energy distribution are discussed in more detail.

Bunching in the longitudinal direction only is in principle performed by not applying the transverse free-flight and the transverse phase-space rotations in the $\pm HV$ switching-sequences. Such a bunching scheme consists of a longitudinal free-flight using the *static-burst* EFC followed by switchings of $\phi = 0°$ using the *horizontal* or *vertical* EFC. The free-flight can also be realized by switching off the $\pm HV$ complete [62]. However, switching to the *static-burst* EFC has no only the advantage to keep the molecular packet confined in both transverse directions, which greatly minimizes the particle loss, it also guarantees that the molecules are exposed to an electric field. For certain molecular species this can be important to prevent non-adiabatic transitions [91, 92], which results also in a loss of molecules.

3D-bunching: bunching along all three directions

In general, bunching in the longitudinal and both transverse directions is implemented in a Stark-decelerator, by firstly decelerating or accelerating a molecular packet for a certain amount of stages; secondly, by switching no $\pm HV$ on, free-flight conditions are achieved in all three dimensions equally long. If different durations of free-flight are needed in the different directions, combinations of the *static-burst*, *horizontal* or *vertical* EFC can be used. The phase-space rotations in the longitudinal direction are again induced by applying $\phi = 0°$. To apply the harmonic potential in both transverse directions either the *static-burst* EFC or a combination of the *horizontal* and the *vertical* EFC can be used.

To demonstrate such a 3D-bunching in this setup, firstly a molecular packet is decelerated with $\phi = 80°$, s = 3 until stage 220 from 625 m/s to 496 m/s. Secondly, the free flight conditions are established first by applying the *static-burst* EFC until stage 265, followed by a free-flight in all three dimensions, where no EFC is switched on for 47 stages. During the last 4 stages the phase-space rotations are induced in each dimension. The right graph of Figure 4.8 illustrates the progression of the temperatures T_x, T_y and T_z as a function of the applied $\pm HV$ switchings. The temperatures of the first second and third switchings are determined from the phase-space distributions at stage 220 after the deceleration with $\phi = 80°$, s = 3 (labeled: $\phi = 80°$), at stage 265 after the *static-burst* EFC has been applied (labeled: static-burst) and at detection zone, if no further $\pm HV$ switching has been applied (labeled by: hor-rot 0 long-rot 0), respectively.

The switching scheme labeled by hor-rot 2 long-rot 1 corresponds to a switching of the *static-burst* EFC for two stages leading to a rotation of the transverse distributions in the horizontal and the vertical phase-space, while in the longitudinal direction $\phi = 0°$ is switched once. Thus, an ideal rotation in the longitudinal direction is performed, where a minimum T_x = 480 μK is achieved. Compared to T_x = 4.8 mK after the deceleration and T_x = 3.5 mK after the free-flight a factor 10 and 7 colder beam is created, respectively. Both transverse distributions are not focused perfectly in their velocity-spaces using one stage each. Here, a final T_y = 2.9 mK (T_z = 3.1 mK) shows a decrease of the temperature by a factor of 10 and 1.7 with respect to the temperatures after the deceleration and free-flight. To improve the transverse focusing more stages were needed, which leads to a less perfect longitudinal focusing. This is illustrated by the switching schemes labeled by: hor-rot 3 long-rot 1 focus and hor-rot 3 long-rot 2. In all the switching schemes shown here the *static-burst* EFC is used entirely, because a combination of the *horizontal* and the *vertical* EFC would be an application of two times $\phi = 0°$ in the longitudinal direction. This leads to an over-focusing of the velocity component in the longitudinal phase-space causing a larger T_x. The particle loss during the whole free-flight amounts to ≈87% since there is no confining potential in any direction. The left and the right graph of Figure 4.9 show the measurements of the 3D-bunching in the 90°- and the 45°-detection scheme, respectively, using the switching scheme labeled by: hor-rot 2 long-rot 1.

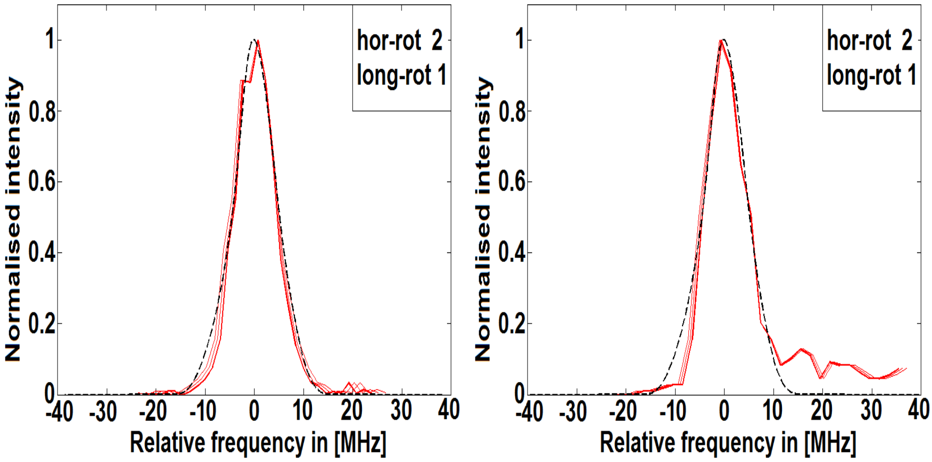

Figure 4.9: The left and the right graph show the measurements of the 3D bunching in the 90°- and the 45°-detection scheme, respectively, using the switching scheme labeled by 2 rotations 1 focus.

4.4 Conclusion

In this chapter the general implementation of bunching schemes of a molecular packet in the longitudinal and the transverse directions as well as combinations of both using a Stark-decelerator is demonstrated. Simply by adjusting the non-standard high-voltage switching of the Stark-decelerator, individual dimensions of the phase-space distribution of the molecular packet can be shaped to optimize the subsequent experimental procedure. This makes the Stark-decelerator an even more versatile tool, additionally to the quantum-state filtering and the velocity control. The methods shown also have the technical advantage that no further mechanical components, such as a hexapole, are required for the electro- or magneto-static manipulation of the particles' motion. Neither, additional electronic components are needed.

Using a narrow bandwidth laser for the detection in the experiment enables the measurement of the Doppler-broadened line-shapes, which is a direct measurement of the velocity distribution along the axis of the laser propagation. By shooting the laser in two different angles relative the direction of propagation of the molecular packet, the longitudinal and the transverse-horizontal velocity-space are probed. The corresponding line-profiles of the Doppler-broadening are simulated using trajectory simulations. The bunching in various dimensions is demonstrated in particular by reproducing the measured Doppler profiles with simulated ones.

Bunching schemes are implemented to focus the phase-space distributions in their velocity-spaces such that molecular packets are generated with beam-temperatures corresponding to several hundreds of micro-Kelvin. Depending on the bunched dimensions, the corresponding temperature is decreased by an order of magnitude compared to a normally Stark-decelerated packet. In general, the various dimensions can be cooled even more by increasing the distance of free-flight. However, certain limitations come along with longer free-flight: (1) in the transverse bunching process more molecules are lost during a longer free-flight which decreases the final number-density of the packet. Thus, the larger the distribution is spatially elongated, the shorter the harmonic potential needs to be applied to rotate the phase-space distribution. The anharmonicities of the transverse potential however cause differently large rotations leading to a non-uniform focusing. (2) for longitudinal bunching schemes the mechanical dimensions of the electrode pairs restricts the length of the elongated packet, which can still be rotated within a harmonic potential. The anharmonicities can be minimized by implementing an even more advanced switching scheme. Using a genetic algorithm certain parameters, such as the average confining potential, can be optimized by switching the $\pm HV$ more often [93].

Additionally, the bunching of any desired dimension allows to shape the phase-space distribution of the molecular packet to suit best to the subsequent experimental requirements. In particular, the transverse bunching is a prerequisite for the high resolution spectroscopy described in the following chapter. The reduction of the Doppler-broadening allows to resolve individual lines in spectra. The 2D-bunching can be used to minimize the velocity distributions in the scattering plane of a crossed beam experiment leading to an increase of the collision energy resolution. The optimization of loading a molecular packet into a trap are possible applications of the 3D-bunching. Depending on the experimental setup and requirements an optimum set of parameters can be found from simulations.

Chapter 5

Spectroscopic investigations on the electric and the magnetic transition dipole moments in the $A - X$ band of OH

5.1 Introduction

The hydroxyl radical (OH) plays a central role in many fields of physics and chemistry. Since it is one of the most abundant radicals in the atmosphere and in interstellar space, it is one of the most extensively studied molecular radical to date. Magnetic dipole allowed transitions (M1) are orders of magnitude weaker than the corresponding electric dipole allowed transitions (E1). They are therefore usually neglected in quantitative measurements of quantum state populations (e.g. via laser induced fluorescence). Nevertheless, in experiments requiring very sensitive state-selective detection, this approximation could lead to significant misinterpretation of the data. This is the case for instance in the measurement of effects caused by the possibly existing permanent electric dipole moment (EDM) of the electron [94] [95] [96] or in fully state-resolved collision experiments [47].

In general, strengths of higher order transition, such as the magnetic dipole or the electric or magnetic quadrupole transitions, are difficult to determine quantitatively even if they are detectable. Precise measurements are subject to large systematic errors since the signals are either very low or the comparison with stronger transitions like the E1 differs by orders of magnitude, where the accuracy suffers especially by the comparison of (statistical) errors or calibration issues. We investigate magnetic dipole allowed transitions in the $A - X$ system of OH with two different methods:

1.) **Stark-spectroscopy:** we apply a low homogeneous static electric field ($\underline{SEF}$), which slightly mixes parities of the Λ-doublet in the rovibrational ground-state. This admixes a small amount of the E1 transitions to the signal of the allowed M1 transitions. The contributions of the E1 transitions to the signal are on the same order of magnitude as the M1 transitions, which enables the detection of both types of transitions in a single experimental measurement. By applying the linear polarized laser $\underline{\mathcal{E}}$ either parallel or perpendicular to the direction of $\underline{SEF}$, the magnitude of the magnetic transition dipole moment $\hat{\mu}^{mag}$, relative to the electric transition dipole moment $\hat{\mu}^{el}$ is accurately determined; and compared to theoretical calculations within [44].

2.) **Stark-interference technique:** by superimposing an additional static magnetic field ($\underline{SMF}$) upon the $\underline{SEF}$ the energy levels are split into its Zeeman sub-levels. This allows the observation of the individual interference of the cross terms of the E1 and M1 transition dipole moments, which is known in atomic spectroscopy as the Stark interference technique [97]. In atomic spectroscopy this method is used as a precision method to investigate the influence of small effects like the parity non-conservation and the anapole moment [98] [99] [100]. This technique is also proposed to enable the measurement of effects caused by the possibly existing permanent electric dipole moment (EDM) of the electron [94] [95] [96]. Here, we report on the first observation of the Stark-interference in molecular species. With this method, not only the magnitude of $\hat{\mu}^{mag}$ relative to $\hat{\mu}^{el}$ is accurately determined, but also their relative sign.

In the following, a first section on the experimental settings and procedures introduces the properties and parameters of the experiment. In the second section follows the theoretical description of the spectroscopic dynamics induced in the OH radical. The following two sections describe the observations and results gained by fitting the theoretical model to the experimental data using the two different techniques of Stark-spectroscopy and Stark-interference. The conclusion summarizes the results and gives an outlook on possible implications.

5.2 Experimental setup and procedures

This section summarizes only the experimental parts relevant for the spectroscopic investigations. The left graph of Figure 5.1 shows a schematic overview of the experimental setup. The production method of OH radicals and the operation of a Stark-decelerator have already been explained in great detail in chapter 3. Throughout these spectroscopic experiments, samples of OH molecules are prepared by switching the Stark-decelerator with phase-angle $\phi = 0°$ at a longitudinal velocity of 625 m/s in the s = 3 mode.

This produces quantum-state selected packets containing both low-field seeking Stark components ($M_J\Omega$ = -3/4 and $M_J\Omega$ = -9/4) of the ground state $|X^2\Pi_{3/2}, v = 0, J = 3/2, f, p = +\rangle$, which is depicted in the upper left graph of Figure 2.2. Towards lower electric field strengths the $M_J\Omega$ = -9/4 component correlates to the $|X^2\Pi_{3/2}, v = 0, J = 3/2, f, p = +, F = 2\rangle$ hyperfine state in field-free conditions, while molecules that populate the $M_J\Omega$ = -3/4 state in an external electric field distribute among the $F = 1$ and $F = 2$ hyperfine state in field-free conditions. The lower left graph of Figure 2.2 shows this behaviour resolved for the different M_F hyperfine components. A transverse bunching scheme is applied to narrow the horizontal temperature T_y and hence the Doppler-broadening of each transition which turns out to be essential to resolve the individual Zeeman-splittings when low static magnetic fields are applied. The bunching switching-sequence is carried out in the same way as described in section 4.3. However, the switching-sequence is optimized such that the molecules populating different $M_J\Omega$-states become of similar temperature. This reduces the Doppler-broadening along the transverse horizontal direction from 8.4 MHz ($M_J\Omega$ = -1/2) and 24.9 MHz ($M_J\Omega$ = -3/2) to 4.3 MHz and 4.9 MHz, respectively. Appendix A contains details on the high-voltage switching scheme and the packet properties as well as the corresponding the temperatures and Doppler-profiles. The packet's spatial dimensions are 16x3x3 mm^3.

After leaving the Stark-decelerator, the molecules enter the detection chamber by flying through an aperture in a metallic shield, which serves as a differential pumping stage. It also shields the detection zone from any kind of residual electric field from the Stark-decelerator. After a flight distance of 6.25 cm the molecules arrive in the centre of the detection chamber, where the detection zone is. Here, a coordinate system is defined such that the longitudinal axis of the decelerator defines the x-axis, perpendicular to it in the horizontal plane lies the y-axis (where the cw laser is aligned), and the z-axis is vertically to it (along the LIF zone). Two plane capacitor plates are mounted symmetrically along the x-axis separated by 25 mm from each other; both are displaced by 12.5 mm from the centre. Each plate has a diametre of 44 mm and a hole-diametre of 4 mm, where the OH beam enters the detection zone. Voltages are applied individually to the plates to create a homogeneous static electric field $\underline{SEF}$. Two coils of copper wire with a diameter of 60 mm are mounted symmetrically along the z-axis. Each one is displaced by 16 mm from the centre of the interaction zone. The coils create a homogeneous static magnetic field $\underline{SMF}$ along the z-axis. The field strengths of the $\underline{SEF}$ and $\underline{SMF}$ are tuned by the voltages and the currents applied, respectively. The fields are reversed by reversing the polarity of the applied voltages and by reversing the direction of the applied current, respectively. The current running through the coils to generate the desired $\underline{SMF}$ is produced by an arbitrary current waveform generator which has been designed for a Zeeman-decelerator. The arbitrary waveform generator can output bipolar currents of 1000 A peak-to-peak amplitude with frequencies ranging from DC to 40kHz. In this experiment, the current generator is set to produces a square pulse of 400 μs, while the pulse is switched on 200 μs before the arrival of the molecular cloud to provide a stable homogeneous $\underline{SMF}$ during the detection. The field distributions of the $\underline{SEF}$ and the $\underline{SMF}$ are calibrated and simulated to determine the actual field strengths and field configurations

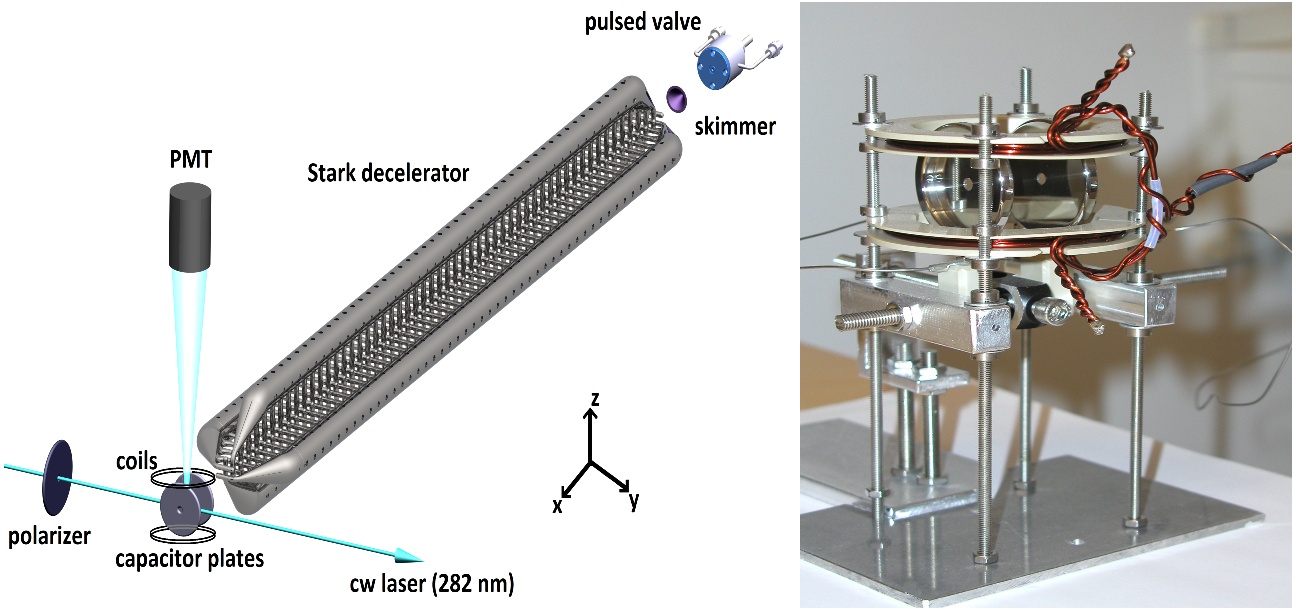

Figure 5.1: The left graph shows a schematic drawing of the experimental setup. The production and manipulation of the OH packet with the Stark-decelerator are described in section 3.1 and 3.2, respectively. Transverse bunched OH packets (details are given in section 4.3 and Appendix A) enter the centre of the detection chamber where two capacitor plates and two coils are mounted to create a $\underline{SEF}$ along the x-direction and a $\underline{SMF}$ along the z-direction. Their self-made design and mounting are shown in the picture on the right. The RDL laser system is used to perform the excitation for the LIF detection, while the $\lambda/2$-plate is used to rotate the linear polarized $\underline{\mathcal{E}}$ relative to $\underline{SEF}$.

and to evaluate systematic errors (see Appendix B).

The OH radicals are finally detected via laser induced fluorescence (LIF) with the continuous wave ring dye laser described in chapter 3.3. A power of 4 mW is achieved within a laser-spot diameter of approximately 1.5 mm. It illuminates only the central part of the OH packet slicing a 16x1.5x3 mm^3 volume. An active frequency stabilization keeps the laser frequency stable and limits the bandwidth to ±2 MHz in the SHG. The SHG unit determines the laser polarization vector $\underline{\mathcal{E}}$ to be linear polarized and parallel to the $\underline{SEF}$. A λ-half plate is used to rotate the $\underline{\mathcal{E}}$ manually in any desired angle relative to $\underline{SEF}$. The laser beam's $\underline{k}$-vector intersects along the y-axis perpendicular to both the $\underline{SEF}$ and the $\underline{SMF}$. In general, transitions are induced along the $|A^2\Sigma^+, v' = 1\rangle \leftarrow |X^2\Pi_{3/2}, v = 0\rangle$ band around 282 nm. Fluorescing photons from the $|A^2\Sigma^+, v' = 1\rangle \rightarrow |X^2\Pi_{3/2}, v = 1\rangle$ transition around 314 nm are collected vertically along the z-axis by a lens and collimated on a photomultiplier tube (PMT). The main source of stray light is the laser radiation, which is sufficiently suppressed by light baffles and by optical filtering in front of the PMT. Single photons are detected as voltage peaks which are counted individually.

5.3 Theoretical descriptions of the E1 and M1 transitions

The spectroscopic investigations are performed on distinct transitions which are depicted in the left graph of Figure 5.2. We assume the rovibronic ground state to be populated only with Stark-decelerated OH radicals in the low-field seeking state: $|X^2\Pi_{3/2}$, v=0, N=1, J=3/2, f, p=+ $\rangle$. Previous microwave transition experiments showed that in the excitation region, all Zeeman sublevels are equally populated within each hyperfine component [44]. The excited state is $|A^2\Sigma^+$, v'=1, N'=0, J'=1/2, p'=+ $\rangle$. The spectroscopic investigations are in particular performed along the P_1'(1) line, which is the magnetic dipole allowed transition indicated by M1:

$$\begin{aligned} &|A^2\Sigma^+, v' = 1, J' = 1/2, N' = 0, p' = +\rangle \\ \leftarrow\ &|X^2\Pi_{3/2}, v = 0, J = 3/2, N = 1, f, p = +\rangle \end{aligned} \tag{5.1}$$

The $\mathrm{P}_1(1)$ line is the electric dipole allowed transition of the lower Λ-doublet component which is depicted by E1:

$$|A^2\Sigma^+, v' = 1, J' = 1/2, N' = 0, p' = +\rangle$$

$$\leftarrow |X^2\Pi_{3/2}, v = 0, J = 3/2, N = 1, e, p = -\rangle \tag{5.2}$$

The right part in the left graph of Figure 5.2 illustrates the hyperfine splitting where the ground state splits in the F=1 and F=2 components and the excited state into the F'=0 and F'=1 components. Spectra are measured along the P_1'(1) line. By applying a small $\underline{SEF}$ the parities are slightly mixed in the ground state. This also allows the electric transition dipole moment to contribute to the transition, which is in $|\underline{SEF}| = 0$ V/cm only coupled by the magnetic transition dipole moment. The right graph of Figure 5.2 shows two spectra where $|\underline{SEF}| = 1000$ V/cm is applied. The red and blue coloured spectra show the parallel and perpendicular alignment of the laser polarization vector $\underline{\mathcal{E}}$ relative to $\underline{SEF}$, respectively. Four transitions are identified in the spectrum. Those excited to the final state of F'=0 and F'=1 are coloured blue and green, respectively. The transition (F'=0 ← F=2) becomes dipole-allowed although ΔF=2, because the hyperfine states of the F=1 and F=2 are slightly mixed in the presence of the $\underline{SEF}$, too.

Using the two transitions (F'=0 ← F=2) and (F'=0 ← F=1) has some major advantages: the fluorescence signal is recorded independent of the type of the excitation transition (either E1 or M1) and it is independent of the polarization of the fluorescing photons. The radiative lifetime of the excited state is $\tau = 748$ ns [45], which corresponds to a natural linewidth of $\Delta\nu \approx 0.213$ MHz. A transverse bunching scheme reduces the Doppler broadening of the different hyperfine transitions to 5.2 MHz and 5.5 MHz for the F=1 and the F=2 component. Furthermore, the Zeeman splitting of the hyperfine components is illustrated in the left graph of Figure 5.2. For the used transitions the ground state hyperfine components split into its Zeeman sublevels, while the excited state shows no Zeeman splitting when a $\underline{SMF}$ is applied. To resolve individual Zeeman sublevels under the experimental conditions a $|\underline{SMF}| \geq 20$ G is needed.

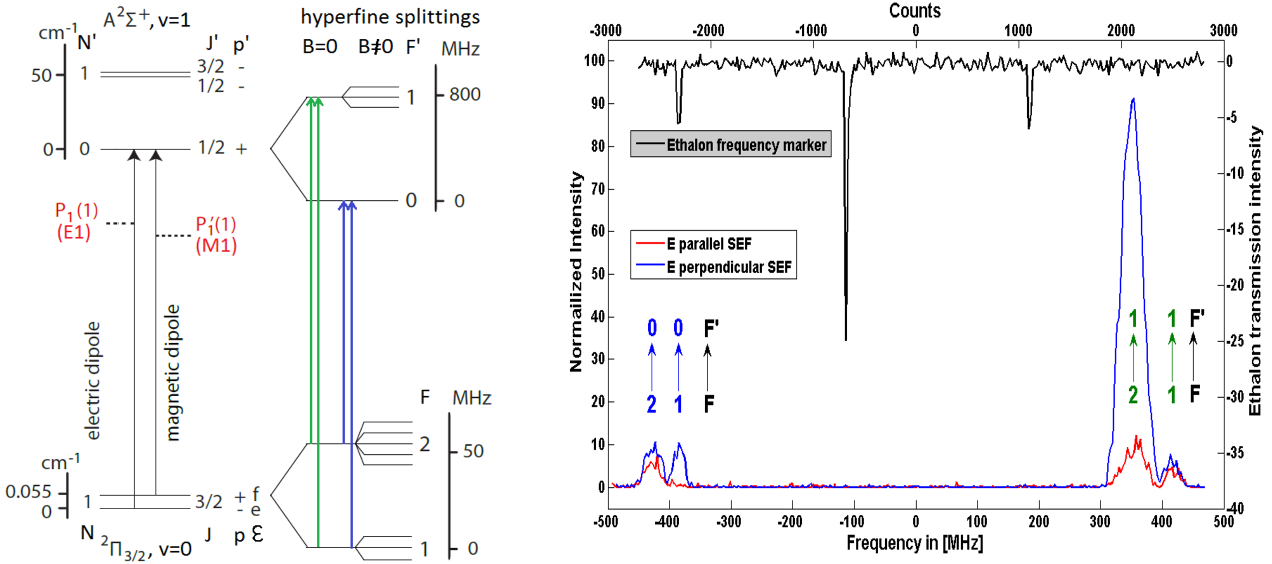

Figure 5.2: The left graph depicts in its left part the energy level scheme of the ground state and the excited state. The $P_1(1)$ and the $P'_1(1)$ line indicate the E1 and the M1 transitions, respectively, which are used in the experiment exclusively. The right part illustrates the hyperfine splitting with and without the Zeeman-splitting in the presence of a magnetic field B. The right graph shows two spectra with $|\underline{SEF}| = 1000$ V/cm. The frequency axis is calibrated relative to the origins of the rotational transition of the $P'_1(1)$ line around 35429.10 cm^{-1}. The red and blue coloured spectra show the parallel and perpendicular alignment of the laser polarization vector $\underline{\mathcal{E}}$ relative to $\underline{SEF}$, respectively. Four transitions are labeled in the spectrum and indicted in the level scheme of the right graph.

Theoretical calculations of the E1 and M1 transitions

Spectra are calculated where the energy level structure of the ground state and the excited state of OH is determined from

$$H = H_{mol} + H_{Stark} + H_{Zeeman} \tag{5.3}$$

where H_{mol} comprises the rotational Hamiltonian, spin-orbit coupling, Λ-doubling and the hyperfine interactions, which is described in sections 2 and 2.1.2. The Stark and the Zeeman shift (see section 2.2) are included by H_{Stark} and H_{Zeeman}, respectively depending on the experimentally applied $\underline{SEF}$ and $\underline{SMF}$.

In the space-fixed frame the quantization axis is chosen parallel to the $\underline{SMF}$ along the z-axis. The ground and the excited state are defined in parity adapted basis sets: $|^2\Pi, F_1, N, J, F, M_F, p = \pm\rangle$ and $|^2\Sigma^+, J', N', F', M'_F, p' = +\rangle$. The molecule-fixed transition dipole moment operators ($\hat{\mu}^{el/mag}$) only have components perpendicular to the OH bond axis for the $\Sigma \leftarrow \Pi$ transition which is described in section 2.3. *Ab initio* calculations [101] [44] predict the ratio of the transition dipole moments to be

$$\left| \frac{c\langle\hat{\mu}^{el}\rangle}{\langle\hat{\mu}^{mag}\rangle} \right| = 50.8, \tag{5.4}$$

where c is the speed of light. The E1 transition has been determined to be ≈2500 times stronger than the M1 transition. Standard angular momentum algebra is used to calculate the spherical components of electric and magnetic transition dipole moments in the space-fixed frame. Spectra are calculated including the laser polarization vectors

$$\left| \langle {}^2\Sigma^+, N', F', M'_F, p'| -^{(\mathrm{sf})} \hat{\mu}^{el} \cdot \underline{\mathcal{E}} \quad -^{(\mathrm{sf})} \hat{\mu}^{mag} \cdot \underline{\mathcal{B}} |^2\Pi, J, F, M_F, p\rangle \right|^2 . \tag{5.5}$$

5.4 Determination of the ratio of E1-M1 using Stark-spectroscopy

In this experiment only a small $\underline{SEF}$ is applied in the interaction volume which mixes the parities in the ground state. This also allows to control the amount of E1 contributing to the M1 transition. The amount of admixing corresponds to $\approx 2\%$ of the E1 amplitude such that the contributions of each transition are of similar strength:

$$
\begin{aligned}
\mathcal{L}_{\Sigma\leftarrow\Pi} \quad \propto \\
\propto \Big| \langle {}^2\Sigma^+, + | -^{(\mathrm{sf})}\, \hat{\mu}^{el} \cdot \underline{\mathcal{E}} -^{(\mathrm{sf})}\, \hat{\mu}^{mag} \cdot \underline{\mathcal{B}} | \big[0.98 | {}^2\Pi, + \rangle + 0.02 | {}^2\Pi, - \rangle \big] \Big|^2 \\
\approx \Big| \langle {}^2\Sigma^+, + | -^{(\mathrm{sf})}\, \hat{\mu}^{mag} \cdot \underline{\mathcal{B}} | {}^2\Pi, + \rangle \Big|^2 + 0.0004 \Big| \langle {}^2\Sigma^+, + | -^{(\mathrm{sf})}\, \hat{\mu}^{el} \cdot \underline{\mathcal{E}} | {}^2\Pi, - \rangle \Big|^2 .
\end{aligned}
\tag{5.6}
$$

These conditions allow precise and quantitative measurement of M1 relative to E1 transitions at the same time in one experimental protocol. The left and the right graphs of Figure 5.3 show spectra of the experimental settings where the laser polarization is aligned perpendicular ($\underline{SEF} \perp \underline{\mathcal{E}}$) and parallel ($\underline{SEF} \parallel \underline{\mathcal{E}}$) to the static electric field, respectively. In both three dimensional graphs the averaged normalized LIF signals are plotted in red lines as a function of the relative laser frequency in MHz and at five different $\underline{SEF}$: ± 200 V/cm, ± 100 V/cm, and 0 V/cm. In a single scan each data point is averaged 200 times at a fixed $\underline{SEF}$. Scans at the different $\underline{SEF}$ are performed in random order until 4000 averages are accumulated for each data point. The calibration of the LIF signal and the relative laser frequency is done as explained in section 3.3.

The (F'=0 ← F=1) and (F'=0 ← F=2) transitions are clearly identified in the spectra and labeled in both graphs. By comparing the intensities of the transition (F'=0 ← F=1) a major difference is observed depending on the different orientation of $\underline{\mathcal{E}}$ relative to $\underline{SEF}$. The permanent dipole moment ${}^{(\mathrm{mf})}\hat{d}^{el}$ of OH, which points along the internuclear axis, is aligned along the $\underline{SEF}$. Since ${}^{(\mathrm{mf})}\hat{\mu}^{el}$ has only components perpendicular to the internuclear axis, the scalar product ${}^{(\mathrm{sf})}\hat{\mu}^{el} \cdot \underline{\mathcal{E}}$ has its maximal value when $\underline{SEF} \perp \underline{\mathcal{E}}$. The intensity increases quadratically as a function of $|\underline{SEF}|$ because the amount of admixed E1 amplitude has a quadratic influence on the intensity. In the setting of $\underline{SEF} \parallel \underline{\mathcal{E}}$ the scalar product ${}^{(\mathrm{sf})}\hat{\mu}^{el} \cdot \underline{\mathcal{E}}$ becomes zero and the measured intensity consists of pure M1 contributions as a function of $|\underline{SEF}|$.

A three dimensional fitting procedure is performed to determine the ratio of the transition dipole moments for a comparison with the theoretical value given in equation (5.4). The normalized intensities are fitted as a function of the relative laser frequency given in counts, the five applied $\underline{SEF}$ and the two orientations of $\underline{\mathcal{E}}$ relative to the $\underline{SEF}$. There are free parameters in the fitting procedure:

1. Three fit-parameters are needed to centre the experimentally scanned parameters: a general offset (`globaloffset`) for the minimum of the $\underline{SEF}$, a frequency offset (`foffset`) to determine the origin of the relative frequency and the angular offset (ϕ `offset`) to determine the angular deviation in the experiment from the ideal cases of $\underline{SEF} \parallel / \perp \underline{\mathcal{E}}$.
2. To model the intensity and the line profile of the two transitions the population distributions and the Doppler profiles of both ground state hyperfine levels (F=1 and F=2) are determined from trajectory simulations of OH molecules leaving the Stark-decelerator. A custom fit-function is designed where the relative population (`relpop2to1`) and the line profile of the transitions, which is given by the temperature (`T`), are fixed parameters. In this designed fit-function a high degree polynomial times a Gaussian function has been used to represent the simulated Doppler profile best. In Appendix A, the lowest graph on the right in Figure 9.1 depicts the Doppler-profiles that are determined from trajectory simulations. The same analysis has been used that is presented for the bunching experiments in chapter 4. The free parameters, that are determined in the fitting, are the linear frequency conversion factor (`CountsperMHz`), a parameter proportional to $|\underline{\mathcal{E}}|$ (and $\underline{\mathcal{B}}$ `globalamplitude`) and the ratio of the magnetic and electric transition dipole moments (μ`scsd`).

The blue surfaces in the graphs of Figure 5.3 represent the result of

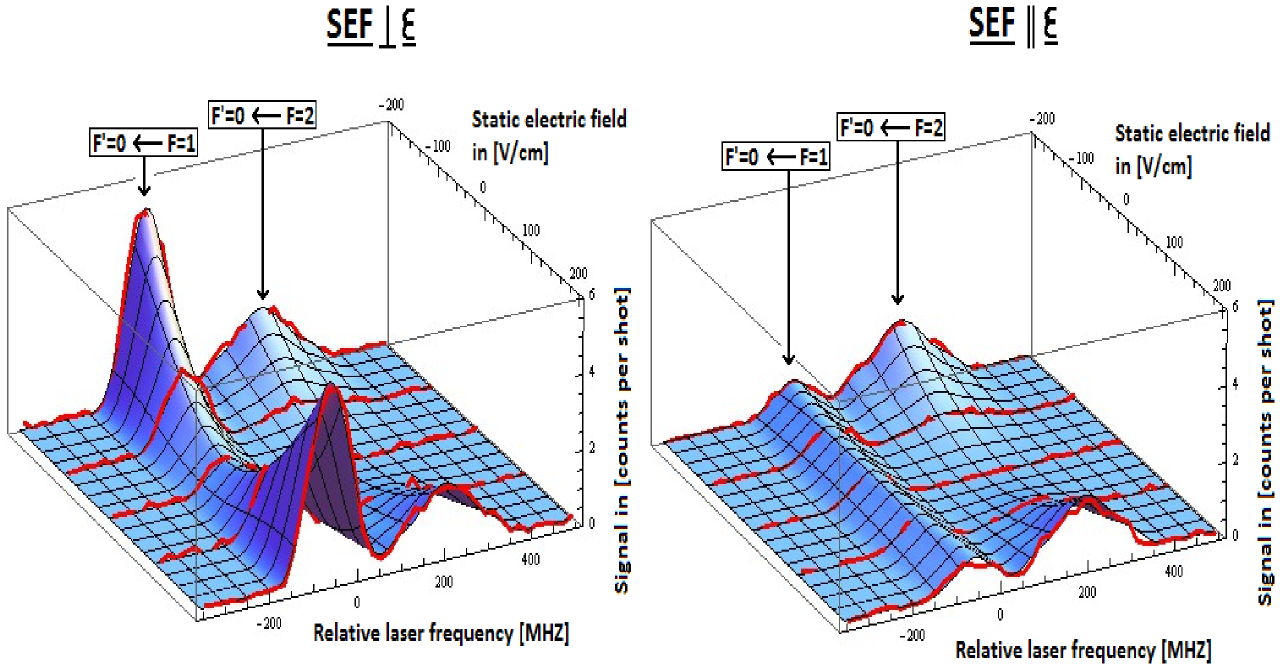

Figure 5.3: The left and the right graph illustrate the two series of measurements, where the orientation of $\underline{SEF} \perp \underline{\mathcal{E}}$ and $\underline{SEF} \parallel \underline{\mathcal{E}}$ is applied, respectively. In both graphs, the experimental spectra are shown as red lines in a three dimensional graph where the normalized intensity is plotted against the scanned relative laser frequency and the different strengths of $\underline{SEF}$. The blue surface represents the best fit.

the fitting procedure to the experimental data, which are depicted in red. The determined value of `globaloffset` shows that the minimum of the parabola is at $\underline{\mathcal{E}} = 0$, where no E1 is admixed. The value for ϕ`offset` ≈ 0. Its error of 0.3° strongly suggests that the left and the right graph represent the experimental conditions of $\underline{SEF} \perp \underline{\mathcal{E}}$ and $\underline{SEF} \parallel \underline{\mathcal{E}}$ are realized in the setup, respectively. The factor found for `CountsperMHz` lies within the experimentally calibrated value and its error of `CountsperMHz` $= 4.80 \pm 0.15$. Finally, the fitting result of μ`scsd` gives an experimental ratio for the transition dipole moments of:

$$\left| \frac{c\langle \mu_{el} \rangle}{\langle \mu_{mag} \rangle} \right| = 51.4 \pm 0.7 \tag{5.7}$$

which agrees well with the theoretical ratio of 50.8 given in equation (5.4) within the error-bar.

The experimental setup incorporates several, possible sources of systematic errors. The accuracy of $|\underline{SEF}|$ could differ due to actually different applied voltages or a different distance of the plates. By measuring the voltage output and the plate distances the error can be reduced to $\leq 1\%$. The homogeneity of $\underline{SEF}$ is simulated using the SimIon software. The plate configuration leads to an inhomogeneity of about 1%. The influence of a magnetic field originating from earth or any electronics next to the chamber cannot be detected when residual magnetic fields are calibrated, see Appendix B. Magnetic field strengths on the order of the earth's field only cause a splitting in the ground state, since the upper state does not have a Zeeman splitting. This would lead to an additional line broadening of ≈ 1.5 MHz. Systematic errors in the fitting procedure are reduced using the optimized custom-fitfunction including all possible information on the population distributions and Doppler profiles of the OH packet leaving the Stark-decelerator. If the normalized spectra were fitted to different fit-functions instead of the custom fit-function more fit-parameters would be needed, which would not fit better without losing information on the experimental properties. Also the procedure to perform a three-dimensional fit circumvented the problem of error propagation completely.

Conclusion

The fit-result of the experimental data determines $|c\langle\mu_{el}\rangle/\langle\mu_{mag}\rangle| = 51.4 \pm 0.7$, which agrees with the theoretical value of 50.8 [44] within the errorbar. This general method of admixing a small but controlled amount of the E1 transition to the signal of the allowed M1 transition enables to measure transitions with signals that are two orders of magnitude higher than the M1 intensity. Since the detection of both types of transitions happens in a single experimental measurement, the error is kept an order of magnitude smaller compared to previous measurements [44].

5.5 Observation of the Stark interference

By superimposing additionally to the $\underline{SEF}$ an $\underline{SMF}$, the energy levels are split into their Zeeman sub-levels. Since the $\underline{SEF}$ still mixes the parities in the ground state slightly, the interference of the cross terms of $\hat{\mu}^{el}$ and $\hat{\mu}^{mag}$ can be observed in each individual Zeeman sub-level:

$$\begin{aligned}
\mathcal{L}_{\Sigma\leftarrow\Pi} \quad &\propto \\
&\propto \left|\langle {}^2\Sigma^+,+| -^{(\mathrm{sf})}\, \hat{\mu}^{el}\cdot\underline{\mathcal{E}} -^{(\mathrm{sf})}\, \hat{\mu}^{mag}\cdot\underline{\mathcal{B}}\,|\big[0.98|{}^2\Pi,+\rangle + 0.02|{}^2\Pi,-\rangle\big]\right|^2 \\
&\approx \left|\langle {}^2\Sigma^+,+| -^{(\mathrm{sf})}\, \hat{\mu}^{mag}\cdot\underline{\mathcal{B}}|{}^2\Pi,+\rangle\right|^2 + 0.0004\left|\langle {}^2\Sigma^+,+| -^{(\mathrm{sf})}\, \hat{\mu}^{el}\cdot\underline{\mathcal{E}}|{}^2\Pi,-\rangle\right|^2 \\
&\quad + 0.04\cdot\mathbf{Re}\big[\langle {}^2\Sigma^+,+| -^{(\mathrm{sf})}\, \hat{\mu}^{mag}\cdot\underline{\mathcal{B}}|{}^2\Pi,+\rangle\langle {}^2\Sigma^+,+| -^{(\mathrm{sf})}\, \hat{\mu}^{el}\cdot\underline{\mathcal{E}}|{}^2\Pi,-\rangle\big].
\end{aligned} \tag{5.8}$$

In this experiment a small $\underline{SMF}$ is applied in the interaction volume along the z-axis perpendicular to both the $\underline{SEF}$ and the wave-vector $\underline{k}$ of the detection laser. The laser polarization is aligned such that $\underline{\mathcal{E}}$ and $\underline{\mathcal{B}}$ have an angle of 45° relative to $\underline{SEF}$ and $\underline{SMF}$, which maximizes the interference effect. The cross term $(0.04\cdot\mathbf{Re}\big[\langle {}^2\Sigma^+,+| -^{(\mathrm{sf})}\, \hat{\mu}^{mag}\cdot\underline{\mathcal{B}}|{}^2\Pi,+\rangle\langle {}^2\Sigma^+,+| -^{(\mathrm{sf})}\, \hat{\mu}^{el}\cdot\underline{\mathcal{E}}|{}^2\Pi,-\rangle\big])$ in equation (5.8) has the property to reverse its sign if either $\underline{SEF}$ or $\underline{SMF}$ or $\underline{k}$ is reversed or if the polarization vector of either $\underline{\mathcal{E}}$ or $\underline{\mathcal{B}}$ is rotated by 180°. This leads to different intensities of the same transition. A different interpretation is to say that the intensity as a function of $\underline{SEF}$ or $\underline{SMF}$ is not minimal at the zero field value and it is non-symmetric around the zero field value. The intensity of a transition can actually become smaller than the pure M1 contribution due to destructive interference in contrast to the experiment described in section 5.4, where the allowed M1 amplitude defines the minimal contribution to the intensity and where some E1 amplitude is admixed as a function of $\underline{SEF}$ additionally.

To investigate the interference effect qualitatively and quantitatively, the same spectroscopic transitions in OH are used, which are given in equation (5.1) and equation (5.2). Only in the ground state the applied $\underline{SMF}$ induces a relevant Zeeman splitting since the Zeeman splitting in the excited state is negligible, as illustrated in the left graph of Figure 5.2. The central two graphs of Figure 5.4 show spectra of $\underline{k}$ (1000 averages taken in 20 scans) while the two graphs on the right show the spectra of $-\underline{k}$ (250 averages taken in 5 scans). Experimentally, $\underline{k}$ is reversed by shooting the laser from the opposite side through the chamber. The upper and lower graphs illustrate spectra where the direction of $\underline{SEF}$ is +600 V/cm and −600 V/cm, respectively. The laser polarisation is aligned in 45° relative to $\underline{SEF}$ and $\underline{SMF}$, while a $\underline{SMF}$ = 46 G is applied. The normalized intensities in [arbitrary units] are plotted against the relative frequency in [MHz] as solid red lines in all four graphs. One can easily see that the intensities of the spectra are not symmetric if only $\underline{SEF}$ or if only $\underline{k}$ is reversed. If both $\underline{SEF}$ and $\underline{k}$ are reversed at the same time, the spectra show the same intensity distribution.

Spectra are calculated using equation (5.8) where the Stark- and the Zeeman-shifts are included in the ground and the excited state [93] [102]. The line shapes are modeled with a Gaussian function. The upper and lower left graphs of Figure 5.4 show calculated spectra for the cases of $\underline{SEF}$=+600 V/cm and $\underline{k}$ ($\underline{SEF}$=−600 V/cm and $-\underline{k}$) and $\underline{SEF}$=−600 V/cm and $\underline{k}$ ($\underline{SEF}$=+600 V/cm and $-\underline{k}$), respectively. The influence of the interference on the intensity of the spectral lines is clearly visible. Furthermore, the intensity distribution of the spectra interchanges into each other by reversing the laser's wave-vector and/or one of the external applied static fields. Additionally, a comparison of the measured spectra with the two calculated ones in the upper row of the Figure illustrates the interference effect qualitatively.

Quantitatively, the spectra are analysed again by fitting the calculated spectra to the measured data. However the fitting procedure is different compared to the one in section 5.4. Here, the normalized intensities are fitted as a function of the relative laser frequency [counts] and different applied $\underline{SEF}$ at a given $\underline{SMF}$. The free parameters in the fitting procedure are:

1. Two fit-parameters are needed to centre the experimentally scanned parameters: a general offset (`globaloffset`) for the minimum of the $\underline{SEF}$ and a frequency offset (`foffset`) to determine the origin of the relative frequency. The linear frequency conversion factor (`CountsperMHz`) is determined as a free parameter in the fitting.
2. To fit the intensities of each of the eight transitions the population distribution and the (interfering) E1 and M1 amplitudes have to be modeled. In order to determine the ratio of the transition dipole moments for a comparison with the theoretical value given in equation (5.4), the intensity is fitted by the absolute square of the sum of the product of a fit-parameter times the M1 amplitude and the E1 amplitude (—E1 + μ`scsd`M1—^{2}). The initial quantum state distributions are unknown, because the last switchings of the decelerator take place in a magnetic field of several Gauss. The magnetic field has to be turned on 200 μs before the molecules arrive in the interaction zone for the sake of its temporal stability during the laser detection. The amount of re-scrambling of the M_F states is unknown. Therefore, all eight initial populations are used as independent fit-parameters (`pop1 - pop8`). The line profile is modeled by a Gaussian function where the Doppler broadening of the line width is fitted by the parameter T. Furthermore, the electric field is influenced by the metallic coils. A small potential is needed for the current creating the $\underline{SMF}$. This results in an angular offset off of the beam axis of $\chi = 3°$ which is implemented as well.

This fitting procedure is used to determine the orientation of $\langle\mu_{el}\rangle$ relative

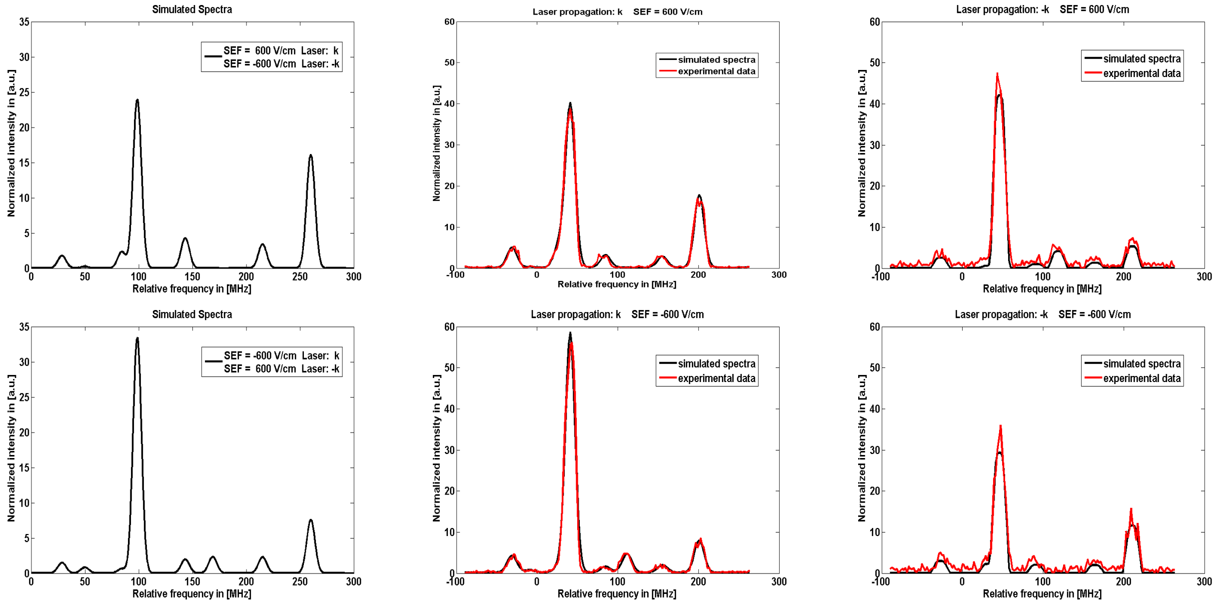

Figure 5.4: The left graphs show theoretically calculated spectra using equation (5.8). The two central graphs show spectra where the laser propagates in direction of $\underline{k}$ while the two graphs on th eright show two spectra where the laser propagation is reversed $-\underline{k}$. The upper (lower) central graph and the lower (upper) right one illustrate spectra where the direction of $\underline{SEF}$ is + 600 V/cm (− 600 V/cm), respectively. The laser polarisation is aligned in the plane of and in 45° relative to $\underline{SEF}$ and $\underline{SMF}$, while a $\underline{SMF} = 46$ G is applied. The experimentally determined spectra and the fitted ones are plotted as red and black solid lines, respectively.

to $\langle\mu_{mag}\rangle$. Their relative sign is determined by the cross term in equation (5.8). Additionally, the ratio of both transition dipole moments can be extracted from the fit. Both three-dimensional graphs in Figure 5.5 depict the normalized intensities in red solid lines as a function of the relative laser frequency and for five different applied $\underline{SEF}$. The upper and the lower graph represent cases where a $\underline{SMF}$ = 46 G and −30 G is applied throughout measurements, respectively. The black solid lines show the best fit of the calculated spectra to all experimental data. The values of the fit-parameters are listed in Table 5.1. All line intensities fit beautifully as a function of the relative frequency and the asymmetries of each transition as a function of applied $\underline{SEF}$ agree very well for all eight lines. The best fit of the calculated spectra is plotted in solid black lines in all four graphs of Figure 5.4 as well. The fit-results for the ratio of the transition dipole moments agree with the theoretical value ($|c\langle\mu_{el}\rangle/\langle\mu_{mag}\rangle| = 50.8$) within the standard error of the mean for the cases of $\underline{SMF} = -30$ G/$\underline{k}$ and $\underline{SMF} = 46$ G/$-\underline{k}$, while the standard error is 2.6 % and 5.1 %. For the measurements of $\underline{SMF} = 46$ G/$\underline{k}$ the theoretical value agrees within two times the standard error (2× 2.1 %). The relative sign of the two transition dipole moments is negative!

Intensity comparison of a single transition by reversing $\underline{SEF}$

Measuring an intensity difference of a single line very accurately by reversing the $\underline{SEF}$ is a different approach to explore the asymmetric intensity distribution due to the interference. A comparison with the theoretical intensity ratio of an individual transition can be calculated or the simulated intensity distribution of the transition can be fitted to the experimental data. The advantage is that this method is universally applicable to determine the ratio of the transition dipole moments and its relative orientation even if ${}^{(\mathrm{sf})}\hat{\mu}^{mag}$ is so small, that the M1 transition cannot be measured within the signal-to-noise ratio. This method is demonstrated using the most intense transition within these experimental conditions which corresponds to the ($M_F = 1$, F = 1) component in an applied magnetic field at zero electric field. The left graph of Figure 5.6 depicts the measured normalized intensities while $\underline{SEF}$ is toggled between ± 1000 V/cm at a constantly applied $\underline{SMF}$ = 46 G.

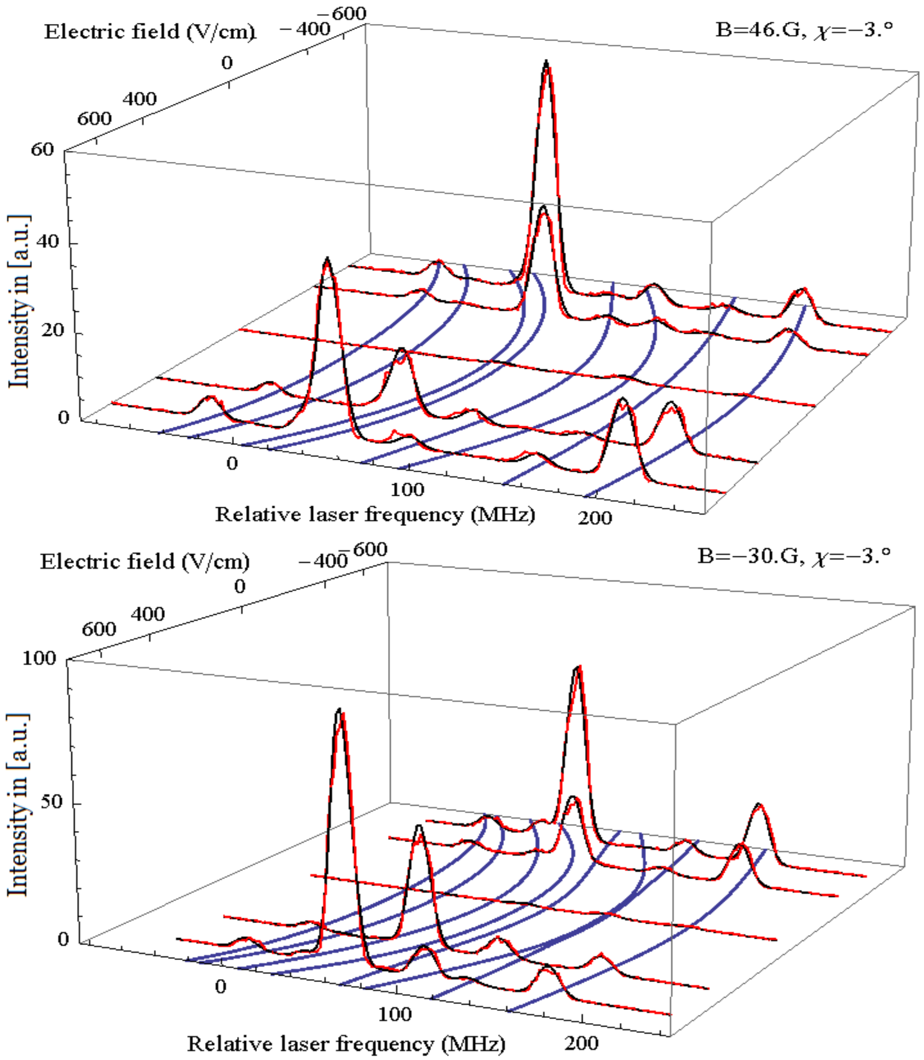

Figure 5.5: Both 3D graphs show the normalized intensities as a function of the relative laser frequency [MHz] and different applied $\underline{SEF}$ in red solid lines. The upper and the lower 3D graph represent cases where the $\underline{SMF} = 46$ G and -30 G is applied throughout the measurements. The black solid lines show the best fit of he calculated spectra to the experimental data. The values of the fit-parameters are listed in Table 5.1.

	$\underline{SMF} = 46$ G	and $\underline{k}$	$\underline{SMF} = 46$ G	and $-\underline{k}$	$\underline{SMF} = -30$ G	and $\underline{k}$
	Estimate	Stan Err	Estimate	Stan Err	Estimate	Stan Err
μ`scsd`	-1.041	0.021	-0.951121	0.051	-1.0095	0.026
`globaloffset`	0.209	0.028	1.08196	0.075	0.206	0.052
`foffset`	24.202	0.123	28.96	1.288	57.29	0.17
`countsperMHz`	4.8229	0.0045	4.934	0.021	5.0298	0.0078
`T`	0.01208	0.00016	0.007	0.00013	0.01191	0.00015
`pop1`	1.092	0.017	0.113	0.005	1.604	0.030
`pop2`	0.800	0.077	0.091	0.017	1.519	0.134
`pop3`	1.558	0.100	0.294	0.037	2.822	0.132
`pop4`	0.793	0.063	0.072	0.015	0.567	0.586
`pop5`	1.981	0.012	0.198	0.007	2.739	0.016
`pop6`	1.267	0.085	0.145	0.033	1.631	0.130
`pop7`	0.462	0.191	0.017	0.079	4.507	3.325
`pop8`	2.534	0.117	0.266	0.030	3.124	0.222
$\left\lvert \frac{c\langle\mu_{el}\rangle}{\langle\mu_{mag}\rangle} \right\rvert$	52.9	1.1	48.3	2.6	51.3	1.3

Table 5.1: The fitted parameters are listed for the best fit shown in the two graphs of Figure 5.3 and the lowest two graphs of Figure 5.4.

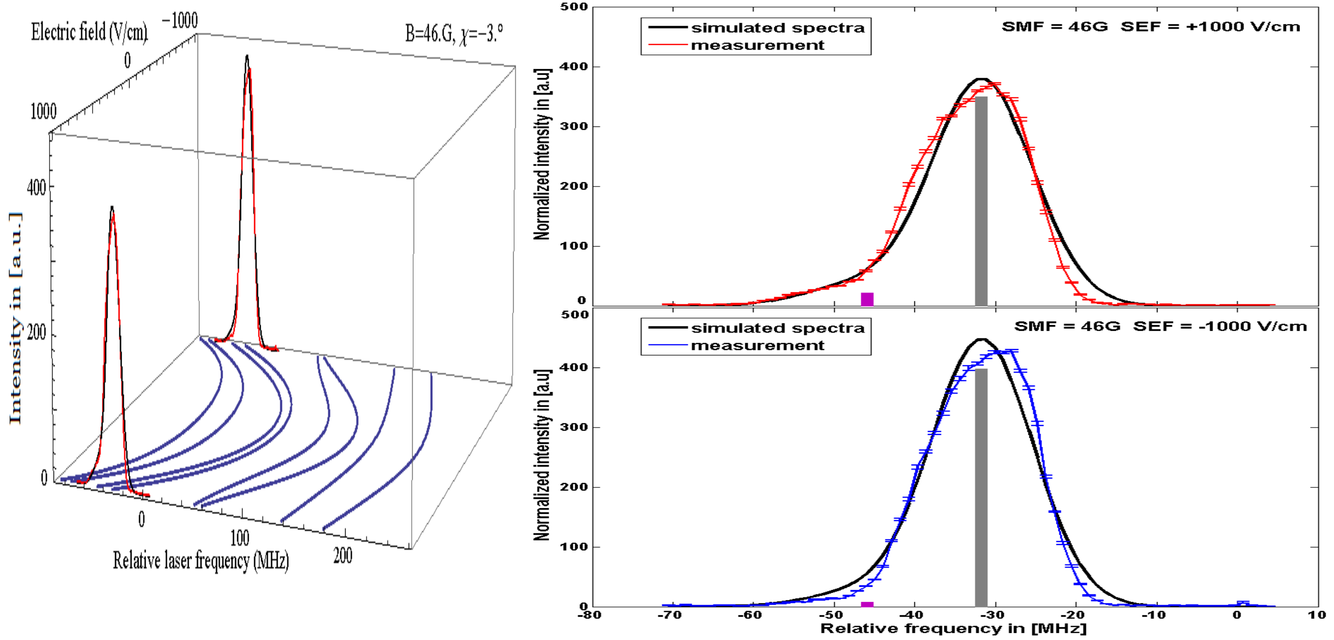

Figure 5.6: The left graphs shows the signal measurement of a single transition, where $\underline{SEF}$ is reversed. The right graphs shows the comparison with the theoretical model.

The central and the right graph show the normalized intensity and the fitted transition for the $\underline{SEF}$ of + 1000 V/cm and − 1000 V/cm, respectively. Already by eye one observes that both measured transitions show an asymmetric line profile which is tilted towards higher (relative) frequencies. Additionally, both profiles show a line width of ≈ 17 MHz (FWHM). According to the simulations in Appendix A the Doppler broadening (≈ 5.3 MHz) and the bandwidth of the laser (≈ 2 MHz) should lead to a line width of ≈ 13 MHz (FWHM). The asymmetry has three origins: firstly, a second, more than ten times weaker transition corresponding to the (M_F = 0, F = 2) transition has its centre around ν_0 = -46 MHz in the left slope of the main peak. Its contribution is best visible in the upper right graph of Figure 5.6. Secondly, inhomogeneities of the $\underline{SEF}$ and $\underline{SMF}$ cause asymmetric line profiles. The second order Zeeman shift in the excited state state is quadratic and causes a broadening of ≈ 0.5 MHz at a simulated inhomogeneity of ≈ 1% of $|\underline{SMF}|$ [102]. The inhomogeneity of the $\underline{SEF}$ is ≤ 1.5 % causing a broadening of ≈ 3.0 MHz. This accounts well for the additional broadening of the line profile. Although the fit model uses two Gaussian functions to account for the two transitions, it is insufficient to reproduce this line profile or to disentangle the two effects using a more sophisticated analysis. The fit-result of the ratio of the transition dipole moments is

$$\left|\frac{c\langle\mu_{el}\rangle}{\langle\mu_{mag}\rangle}\right| = 69.1 \pm 9.7. \tag{5.9}$$

The accuracy of the standard error is with 14% much larger compared to the previous method. The absolute value agrees with the theoretical value from equation (5.4) within two times the standard error. The fitting method produces less accurate results, because only two, rather than eight, transitions are fitted at two, rather than five, different values of $\underline{SEF}$. An increase in the accuracy could result from a more detailed fit-function taking the asymmetric line shape into account.

However, the spectra can be evaluated in a different manner, which makes a more sophisticated fitting procedure gratuitous. The absorption cross section ($\sigma_{\Sigma\leftarrow\Pi}$) determines the capability of a molecule to absorb a photon at a particular wavelength and polarization. It is the product of the line strength given in equation (5.8) times a shape function ($\zeta(\nu_0-\nu)$)

which describes the intensity distribution of the line profile including all broadening effects. The shape function does not change by reversing the <u>*SEF*</u>, if its magnitude does not change. The shape function has the property $\int_{-\infty}^{-\infty} \zeta(\nu_0 - \nu) d\nu = 1$. The absorption cross section follows for a particular transition between an initial (i) and a final (f) state

$$\sigma_{f \leftarrow i} = \int_{-\infty}^{-\infty} \mathcal{L}_{f \leftarrow i} \cdot \zeta(\nu_0 - \nu) d\nu. \tag{5.10}$$

Since the measured intensities originate from two transitions which cannot be disentangled in the experimental spectra, the calculated absorption cross section includes both transitions. The absorption cross sections $\sigma^{\pm}$ refer to the evaluated areas under the peaks shown in the upper and lower right graphs of Firgure 5.6, respectively. Their ratio is

$$\frac{\sigma^{+}}{\sigma^{-}} = 0.902 \pm 0.025. \tag{5.11}$$

The theoretical ratio of both absorption cross sections is directly given by the ratio of the line strengths, which are indicated as stick intensities in the central and left graph of Figure 5.6. Comparing the intensity difference of individual line strength, the (F = 1, M_F = 1) transition is more intense at − 1000 v/cm, while the (F = 2, M_F = 0) transition is less intense. However the absolute line strengths differ and lead to a calculated ratio of 0.926 which reproduces the experimentally determined ratio of equation (5.11) within the experimental standard error of < 3 %. Additionally, the relative sign of the two transition dipole moments is determined to be positive or negative, if the value of the ratio of the absorption cross sections (σ^{+}/σ^{-}) is larger or smaller than one, respectively. Here, the relative sign is negative, which coincides with the results of the previous experiments.

Conclusion

An interference-effect of the electric and magnetic transition dipole moments is observed in OH. This interference is similar to the effect which is known as Stark-interference in atomic species [98]. Two experimental methods explore the interference effect to accurately measure the ratio of

$|c\langle\mu_{el}\rangle/\langle\mu_{mag}\rangle|$. The theoretical value of 50.8 is reproduced by both methods within the experimental standard error of the mean with an accuracy of < 3 %. Moreover, the relative sign of the two moments is determined with this method to be negative.

Two experimental approaches are used to investigate the interference effect qualitatively and quantitatively: firstly, eight transitions of theoretically calculated spectra are fitted to the experimental data which are taken under different orientations and magnitudes of the $\underline{SEF}$, $\underline{SMF}$ and $\underline{k}$. The fitting procedure allows the accurate determination of the ratio of the two transition dipole moments and their relative sign. Secondly, measuring the ratio of the absorption cross sections of a single transition by reversing the orientations of the $|\underline{SEF}|$ allows a comparison with the ratio of theoretical line strengths and hence with the ratio of the transition dipole moments. This method proves to be more powerful than the first one for a number of reasons: only the most intense line needs to be measured instead of eight transitions. The data analysis is easier because the absorption cross section can be evaluated independent of the line profile. It is elaborate to model an asymmetric line shape to guarantee a good fit even though eight transitions at various $\underline{SEF}$ or $\underline{SMF}$ contribute to the fitting procedure.

5.6 Conclusion and outlook

The production of cold and controlled molecules with a Stark-decelerator enables high-resolution spectroscopic experiments, which allow the observation of quantum effects in molecules such as the Stark-interference. Three different methods are implemented in the experimental setup, which enable measurements to directly compare magnetic and electric transition dipole moments, although they differ by orders of magnitude in strength. By applying static electric and magnetic fields in a controlled manner, the amplitude from magnetic and electric dipole transitions are mixed into one signal at a comparable intensity. Therefore, a single laser power is required which does not have to be calibrated. Additionally, a single detection method is used which does not require any calibration either.

One can measure the lines with signals that are two orders of magnitude higher than the M1 intensity, and nevertheless deduce the magnetic transition dipole moment within a couple of percent, and even as a signed quantity. The resulting comparison is very accurate and excludes many systematic errors present in previous studies [44]. The theoretically calculated ratio of the two transition dipole moments could be reproduced within an error of less than 2% with the two methods presented here. The method can easily be applied to many other transitions in OH, and also to many other molecular systems. In general, accurate experimental data are crucial for improving theoretical descriptions. In the OH A-X case, the most recent theoretical calculations of the dipole moments might suffer from systematic errors induced by the Born-Oppenheimer approximation, through the relevant Franck-Condon factors [101] [44]. However, these systematic errors must be less or equal to 2% given the accuracy and reproducability of the present experiments.

Currently, great effort is undertaken to realize laser cooling of molecules [103] and to implement a magneto-optical trap for molecules [104, 105]. In general, to achieve laser cooling of an atom or a molecule, many photons must be scattered using a so-called 'closed cycling transition'. Every photon absorption has to be followed by a spontaneous decay back to the initial state, in order to repeat the cycle again. However, in a real system there are no absolutely closed-cycles, and spontaneous decays to other states happen. Many of these laser-cooling schemes rely on the electric dipole selection rules to close the cycles rotationally and vibrationally [106]. If magnetic dipole transitions are only $\approx 10^{-3} - 10^{-4}$ less probable than electric dipole transitions, they must be considered as possible loss channels.

Chapter 6

Molecular beam and scattering dynamics

6.1 Introduction

Molecular beams are an indispensable tool in the physics and chemistry community. For decades their application in research and technology is numerous for investigations in spectroscopy or crossed beam collision experiments [9, 10, 11]. During the last decade, new powerful techniques have been developed to optimize the production and the manipulation of molecular beams. More sophisticated valve design allowed more extreme stagnation conditions such as shorter opening times and the access of larger temperature and pressure ranges [12, 13, 14]. This pushed the limits of adiabatic expansion of gases further to regions where the resulting beams are internally colder and quantum effects gain considerable influence. This enabled the investigation of a large variety of molecules at milliKelvin temperatures which allowed novel scattering experiments at low collision energies [15]. The formation of smaller and larger helium clusters became available, which advanced high-resolution spectroscopy [20, 21].

This progress in technology offers powerful sources of cold molecular beams, which paved the way for a new generation of experiments. By exploring for example the Stark- or the Zeeman-effect of particles with inhomogeneous electric or magnetic fields, respectively, additional manipulation of the motion and quantum-state selection of the molecular packet becomes possible, which enables full control over internal and external degrees of freedom of the particles [3, 4]. Combined with powerful laser systems and detection techniques new ground breaking experiments become possible: scattering experiments are performed with unprecedented detail in the collision energy resolution [16] [23] and the deceleration and trapping of molecules in the laboratory frame allows the implementation of further laser cooling [24] or evaporative cooling methods [25]. Thus far, the ultracold regime could be reached with a small class of atomic species that can be laser-cooled. The success of these explorations will provide a direct cooling technique for a large variety of molecular species to access the ultracold regime. New phenomena and effects in physics and chemistry are expected and predicted for molecular species at these low temperatures [8, 1].

The kinematics and dynamics of molecular beams is completely described by its 6D phase-space distribution (PSD). It has become a standard procedure for the description of certain experiments and for theoretical investigations to either analytically calculate or to simulate the phase-space propagation in time and under the influences of external fields. The dynamics and the amount of control over the particles in a Stark- or Zeeman-decelerator as well as in traps depend crucially on the PSDs and the applied potentials. The technological improvements leading to colder and better controlled molecular beams go alongside with a increased sensitivity to certain parts of the PSDs. Careful modeling of the PSDs is needed to accurately analyze the measured signals. During the crossed beam scattering experiments, which are presented in chapters 7 and 8, the evaluation of the data revealed inconsistencies: the thresholds of rotationally inelastic channels are observed at lower collision energies than the actual threshold if the collision energy is calibrated like in previous experiments [107] [108]. Additionally, in the high resolution experiment described in chapter 8 sharp structures in the excitation functions are resolved reproducibly, which can only be observed if the collision energy resolution is higher than the analytically calculated one [109].

In this chapter, a general analytic model is presented to determine the evolution of the collision energy and the collision energy distribution as a function of the molecular beams' overlap in time, where the molecular beams are modeled each by a 6D PSD. Already existing methods from number density-to-flux transformations [110] [111], and more detailed models, which include the velocity distributions, are taken into account [112] [113]. The creation of scattering products, the collision energy and the collision energy distribution are derived as a function of the overlap of the molecular packets in time. Together with the 6D PSDs of the H_2 packets and the OH packets leaving the Stark-decelerator, the actual contributions to the measured quantities are accurately identified. Constraints of the experimental setup are implemented in a numerical simulation. The results describe the evolution of the scattering signals that are essential for the calibration of the collision energy as well as the collision energy distribution both qualitatively and quantitatively.

6.2 Kinematics and collision energy

The kinematics of the scattering process of two particles can be described by the two-body problem in classical mechanics. Since detection or measurements of physical quantities are performed in the laboratory, a natural choice for a frame of inertia is, where the laboratory is at rest, i.e. the so-called laboratory frame (lab frame). The motion of the particles is described at any time by their masses m_i, their positions in space $\underline{\mathrm{r}}_i$ and their velocities $\underline{\mathrm{v}}_i$, which is illustrated in Figure 6.1.

Another frame of inertia can be defined, in which the centre of mass $\underline{\mathrm{r}}_{CM}$ of both particles is at rest at all times. This so called centre-of-mass (CM) frame is very convenient because the two-body problem can be reduced to two one-body problems. In the lab frame the centre-of-mass is moving with the velocity $\underline{\mathrm{v}}_{CM}$. The motion is described by the relative position $\underline{\mathrm{r}}_{rel}$ and the relative velocity $\underline{\mathrm{v}}_{rel}$. Two different quantities are introduced: the total mass $M = m_1 + m_2$ and the reduced mass $\mu = (m_1 \cdot m_2)/M$, which appears like the 'effective' inertial mass in the collision. The transformation of positions and velocities between the lab frame and the CM frame is given by the relations:

lab frame → CM frame:

$$\underline{r}_{rel} = \underline{r}_1 - \underline{r}_2 \tag{6.1}$$

$$\underline{r}_{CM} = (m_1\underline{r}_1 + m_2\underline{r}_2)/M \tag{6.2}$$

$$\underline{v}_{rel} = \underline{v}_1 - \underline{v}_2 = \underline{u}_1 - \underline{u}_2 \tag{6.3}$$

$$\underline{v}_{CM} = (m_1\underline{v}_1 + m_2\underline{v}_2)/M \tag{6.4}$$

CM frame → lab frame:

$$\underline{r}_1 = \underline{r}_{CM} + (\mu/m_1)\underline{r}_{rel} \tag{6.5}$$

$$\underline{r}_2 = \underline{r}_{CM} - (\mu/m_2)\underline{r}_{rel} \tag{6.6}$$

$$\underline{v}_1 = \underline{v}_{CM} + (\mu/m_1)\underline{v}_{rel} \tag{6.7}$$

$$\underline{v}_2 = \underline{v}_{CM} - (\mu/m_2)\underline{v}_{rel} \tag{6.8}$$

In the CM frame the positions and velocities of the particles are given by:

$$\underline{r}_{1CM} = \underline{r}_1 - \underline{r}_{CM} \tag{6.9}$$

$$\begin{aligned} \underline{u}_1 &= \underline{v}_1 - \underline{v}_{CM} \\ &= (\mu/m_1)\underline{v}_{rel} \end{aligned} \tag{6.10}$$

$$\underline{r}_{2CM} = \underline{r}_2 - \underline{r}_{CM} \tag{6.11}$$

$$\begin{aligned} \underline{u}_2 &= \underline{v}_2 - \underline{v}_{CM} \\ &= -(\mu/m_2)\underline{v}_{rel}. \end{aligned} \tag{6.12}$$

The total momentum of the system vanishes in the CM frame, since both momenta $m_1\underline{u}_1$ and $m_2\underline{u}_2$ have equal magnitude but point to opposite directions. The CM frame is therefore often also referred to as the centre-of-momentum frame.

Collision energy: The kinetic energy T of both particles in the lab frame is given by $T = \frac{1}{2}m_1|\underline{v}_1|^2 + \frac{1}{2}m_2|\underline{v}_2|^2$. Using the transformation relations (6.7) and (6.8) gives

$$T = \frac{M}{2}|\underline{v}_{CM}|^2 + \frac{\mu}{2}|\underline{v}_{rel}|^2, \tag{6.13}$$

where the first part denotes the amount of kinetic energy associated with the CM motion, while the second part is the relative kinetic energy that is contributing in the collision. This collision energy E_c is the crucial parameter, because it determines the possible inelastic processes:

$$E_c = \frac{\mu}{2}|\underline{v}_{rel}|^2 = \frac{\mu}{2}|\underline{v}_1 - \underline{v}_2|^2 = \frac{\mu}{2}(\underline{v}_1^2 + \underline{v}_2^2 - 2|\underline{v}_1||\underline{v}_2|\cos\alpha). \tag{6.14}$$

The magnitude of the relative velocity $\underline{v}'_{rel}$ after the collision is determined by the conservation of energy. Depending on the amount of energy ΔE_{int} that is exchanged with internal degrees of freedom, the kinetic energy $\frac{1}{2}\mu|\underline{v}'_{rel}|^2$ is changed after the collision by: $\mu|\underline{v}_{rel}|^2 + 2\Delta E_{int} = \mu|\underline{v}'_{rel}|^2$. Three different cases are distinguished:

- **Elastic collisions:** $\Delta E_{int} = 0$, the total amount of kinetic energy before and after the collision stays the same. However, the kinetic energy of each particle changes usually.
- **Inelastic collisions:** $\Delta E_{int} < 0$, the kinetic energy after the collision is smaller, because part of the initial kinetic energy excites an internal degree of freedom of one or both particles. The maximum energy that can be transfered is E_c.
- **Superelastic collisions:** $\Delta E_{int} > 0$, the kinetic energy after the collision is larger, because an internal degrees of freedom of one or both particles has been de-excited.

The magnitude of the relative velocity after the collision is given by

$$\underline{v}'_{rel} = \underline{v}_{rel}\sqrt{\frac{E_c + \Delta E_{int}}{E_c}}, \tag{6.15}$$

but the direction particles are scattered into cannot be determined from kinetics alone. A more detailed knowledge of the interaction potential and the dynamics on the PES need to be taken into account. The angle between $\underline{v}'_{rel}$ and $\underline{v}_{rel}$ is called the scattering angle θ. One speaks of *forward*, *sideward* or *backward* scattering, if θ lies preferentially around 0°, 90°, 180° for the majority of particles.

A very useful, graphical tool to illustrate the relations between all parameters of the lab frame and the CM before and after the collision is the so called *Newton-diagram*, which is schematically drawn in the right graph of Figure 6.1. The magnitude of $|\underline{v}'_{rel}| = |\underline{v}_{rel}|$ stays the same in an elastic collision. The direction of each particle after the collision lies on a circle (solid lines) which radius is given by $|\underline{u}_1|$ and $|\underline{u}_2|$. The possible deflection angles in the lab frame can be deduced from the diagram. The kinematics of inelastic collisions can also be illustrated in this diagram in the CM frame. Since part of the collision energy is transfered into an internal degree of freedom, it holds that $|\underline{v}'_{rel}| < |\underline{v}_{rel}|$. Due to the conservation of momentum ,$\underline{u}_1$ and $\underline{u}_2$ still have opposite directions, however their magnitudes are smaller, which corresponds to smaller radii illustrated by dashed line circles for the velocity of each particle. The *Newton-diagram* allows to calculate the most extreme deflection angles in the lab frame even without the knowledge of the differential cross section. The knowledge on possible product distributions in the lab frame after the collision is inevitable for the analysis of scattering signals and to judge whether or not the detection happens in flux-mode or in density mode (see section 6.3.4).

Collision energy distribution: The distribution of the collision energy depends on the finite uncertainties of the experimental parameters. Each beam has a velocity spread $\varDelta v$ around its mean velocity $\bar{v}$ in longitudinal (*long*) and transverse (*trans*) directions, which is usually quantified by the variance $(\varDelta_{var}\underline{v})$ or the standard deviation $(\varDelta_{std}\underline{v})$ [1]. The distribution of the collision energy can be quantified by determining the absolute error of the collision energy given in equation (6.14)

$$(\varDelta_{std}E_c)^2 = \mu^2\Big[[\underline{v}_1 - \underline{v}_2\cos\alpha]^2\varDelta^2_{std}v_1 + [\underline{v}_2 - \underline{v}_1\cos\alpha]^2\varDelta^2_{std}v_2 + [\underline{v}_1\underline{v}_2\sin\alpha]^2\varDelta^2_{std}\alpha\Big]. \tag{6.16}$$

---

[1] The standard deviation of a sample of q elements is usually defined as the square root of the variance: $[\varDelta_{std}(q)]^2 = \varDelta_{var}(q) = \sum_{i=1}^{n}(q_i - \bar{q})^2 = \sum_{i=1}^{n} q_i^2 - \frac{1}{n}(\sum_{i=1}^{n} q_i)^2$, where the sample mean value is defined as: $\bar{q} = \langle q \rangle = \frac{1}{n}\sum_{i=1}^{n} q_i$. Throughout this chapter and the following two chapters 7 and 8 on OH-H_2 scattering the statistical spread of parameters is described by $\varDelta(q)$ to avoid confusions with the scattering cross section σ. In the special case, where the sample shows properties of a certain statistical distribution, the spread can also be expressed in terms of the full width at half maximum (FWHM) of the distribution's function. Those special cases are explicitly stated and the corresponding definition of the spread is indicated (e.g. in the case of a Gaussian distribution the spread can be defined by: $\varDelta_{FWHM} = 2.35\varDelta_{std}(q)$).

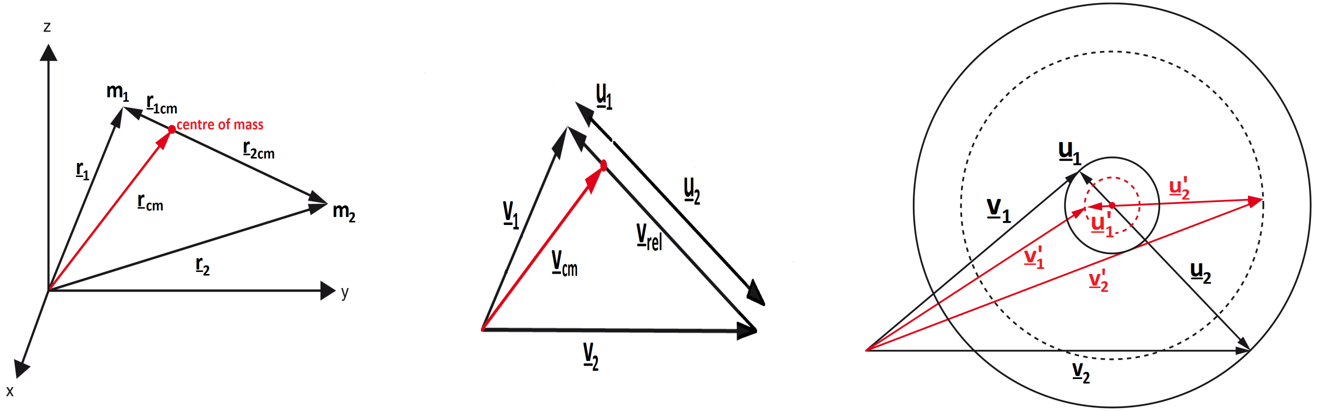

Figure 6.1: The left graph illustrates schematically the spatial coordinate system, where the particles are given by their point masses m_1 and m_2, and the relation between the lab frame and the CM frame. The central graph shows the relation of the velocities of the two frames. The right graph depicts a *Newton-diagram*, which shows the particles' propagation before and after the collision to within the lab frame and the CM frame.

6.2.1 Kinematics of the beams' overlap

To describe the kinematics of the scattering process in greater detail, the time-dependent approaching and overlap of the two molecular packets has to be considered up to the moment of detection with the laser. In the following t will denote time as a parameter, while τ defines the moment of detection, when the probe laser fires. In Figure 6.2 three different graphs show schematically the propagation of two molecular packets for three consecutive timings $t = \tau_{-2}, \tau_{-1}$ and τ_0. Each packet propagates along its dashed centre line, which cross under 45°. The transverse divergence of each packet is indicated by a corresponding cone. In the left graph for $t = \tau_{-2}$ the packets are approaching each other and have not overlapped yet. In the central graph ($t = \tau_{-1}$) the packets start to overlap. In the right graph ($t = \tau_0$) the central parts of the packets overlap, which is also the moment when the detection with the laser is performed. The three lower graphs in Figure 6.2 illustrate that only those parts of the velocity distribution of each packet can scatter which are present in the intersection volume at the corresponding timings.

Two kinematic effects can be observed during the process of overlap. In the central graph ($t = \tau_{-1}$), the two packets start to overlap under a larger angle than 45°. Up to the moment of detection more products will have been created under an angle which is on average larger than 45°. This leads to a slightly higher collision energy than the one calculated, if only the mean value of 45° was used in equation (6.14). Additionally the dynamics during free flight of the molecular packets must be accounted for. Here, the faster molecules are more likely to be in the front part of the packet, while the slower ones end up in the rear part [114]. This has happened especially on the H_2 side, where the drift distance prior to collision is long ($\approx$ 45 cm). During the overlapping process up to the moment of detection, there will have been on average more collisions of molecules which propagate faster than the mean velocity of the packets. At each timing different parts of the velocity distribution of each packet are scattering which results in different mean collision energies. If the detection is performed before the two packets will have overlapped completely (which is the usual case in a pulsed crossed beam experiment) the detected products will have scattered on average with higher collision energies than the one calculated in equation (6.14), where the mean velocities and the mean crossing angle of both packets are used. In fact the mean collision energy shows a dependence on which parts and for how long the packets have been overlapping before the detection. But not only is the mean collision energy a function of the overlap, it affects the distribution of the collision energy, too. Qualitatively, it can be deduced that only parts of both velocity distributions have overlapped prior to the moment of detection, which influences the collision energy distribution.

The time-dependent description of the scattering process is routinely carried out in so called number density-to-flux transformations [110]. This formalism simulates the experimental conditions to relate the measured signals to physical meaningful parameters like cross sections or rate constants. The details of the temporal and spatial creation of scattering products are simulated as a function of the packets' intersection volume and the detection conditions are taken into account. In the following, the theory of the number density-to-flux transformation is recapitulated, because it is indispensable for the data analysis in section 6.3. The formalism of the number density-to-flux theory can be used to a certain extent. It will be extended to simulate not only the creation of scattering products $\langle N \rangle_\tau$ as function of time, but also to extract the mean collision energy ($\langle E_c \rangle_\tau$) and the collision energy distribution ($\langle \Delta E_c \rangle_\tau$) at any moment of detection τ. A physically intuitive model is presented here, while in Appendix C a formal description is given.

The propagation of a packet of particles can be described by a continuous probability number-density distribution in 6D phase-space (PSD). The expression $n_i(\underline{\mathrm{r}}_i, \underline{\mathrm{v}}_i, t)$ (the index i describes particle species like e.g. OH) defines the probability to find a number of particles at a position $\underline{\mathrm{r}}_i$ with a velocity $\underline{\mathrm{v}}_i$ at time t. If the complete PSD is known at a definite time t_0, it can be separated into the spatial and the velocity part: $n_i = P_i^r(\underline{\mathrm{r}}_i, t_0) \cdot P_i^v(\underline{\mathrm{v}}_i, t_0)$. In the absence of external forces, the spatial propagation in time is determined by the velocity distribution $P_i^r(\underline{\mathrm{r}}_i, t) = P_i^r(\underline{\mathrm{r}}_i^0 - \underline{\mathrm{v}}_i t, t)$, where $\underline{\mathrm{r}}_i^0$ defines the spatial distributions of a packet at a definite time,

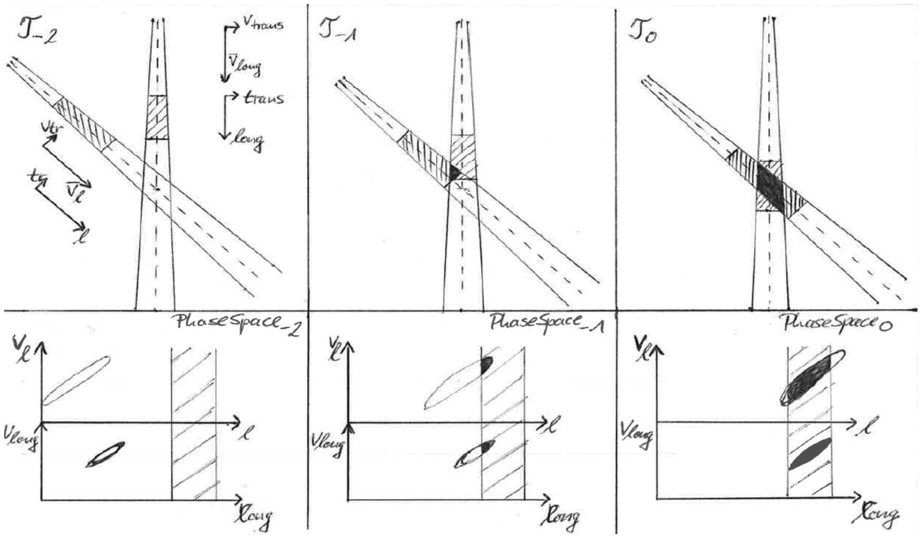

Figure 6.2: The left, middle and right graph in the upper row illustrate the overlap of two molecular beams at three consecutive timings. The dashed areas show schematically the spatial extensions of the packets. In the left graph coordinate systems indicate the longitudinal and the transverse direction of the position and velocity space of each beam. In the lower row the corresponding phase-space diagrams show the longitudinal propagation of each packet in time. The shaded area in each diagram depicts schematically the intersection volume, which is defined by two cones. The black areas of each PSD show the parts that can possibly scatter at a particular moment. The detection volume is assumed to be a lot larger than the intersection volume. Therefore, it is not indicated.

when the properties are well known or when they can be estimated well. For example, the 6D PSD of the OH-packet is well defined from trajectory simulations. If there are no further external forces applied, the PSD is given after the last switching-off of the electric fields. The normalized PSD of a packet can be expressed by:

$$n_i(\underline{\mathrm{r}}_i, \underline{\mathrm{v}}_i, t) = P_i^r(\underline{\mathrm{r}}^0 - \underline{\mathrm{v}}_i t, t) \cdot P_i^v(\underline{\mathrm{v}}_i, t), \tag{6.17}$$

Recalling the dynamics of the overlap, which is shown schematically in Figure 6.2, the spatial overlap (SO) of the two packets defines those parts of the PSD that can be involved in a scattering event at time t. The pure SO of the two packets can be calculated by performing the 3D integral over the spatial dimensions, while a delta function is used $\delta_{\underline{\mathrm{r}}_{OH}\underline{\mathrm{r}}_{H_2}}$ to account for only those parts present in the intersection volume:

$$\Pi_{SO}(t) = \int_{3D}\int_{3D} \delta_{\underline{\mathrm{r}}_{OH}\underline{\mathrm{r}}_{H_2}} P_{OH}^r(\underline{\mathrm{r}}_{OH}, t) P_{H_2}^r(\underline{\mathrm{r}}, t) d^3\underline{\mathrm{r}}_{OH} d^3\underline{\mathrm{r}}_{H_2} \tag{6.18}$$

If additionally the integration over both velocity spaces is performed, a quantity is defined that can be interpreted as the phase-space probability distribution. At this point, the significance of delta function $\delta_{\underline{\mathrm{r}}_{OH}\underline{\mathrm{r}}_{H_2}}$ becomes obvious, because it accounts for only those parts of the two velocity spaces, which are present in the intersection volume. This quantity is proportional to the number of particle-pairs that could collide in the intersection volume at time t:

$$\begin{aligned}\Pi_{PSP}(t) = \int_{3D}\int_{3D}\int_{3D}\int_{3D} \Big[&\delta_{\underline{\mathrm{r}}_{OH}\underline{\mathrm{r}}_{H_2}} n_{OH}(\underline{\mathrm{r}}_{OH}, \underline{\mathrm{v}}_{OH}, t) \times \\ &n_{H_2}(\underline{\mathrm{r}}_{H_2}, \underline{\mathrm{v}}_{H_2}, t)\Big] d^3\underline{\mathrm{r}}_{OH} d^3\underline{\mathrm{r}}_{H_2} d^3\underline{\mathrm{v}}_{OH} d^3\underline{\mathrm{v}}_{H_2}\end{aligned} \tag{6.19}$$

The relative velocity between two particles in the CM is defined in equation (6.4) as $\underline{\mathrm{v}}_{rel} = \underline{\mathrm{v}}_{OH} - \underline{\mathrm{v}}_{H_2}$. In this case, the distribution of relative velocities $P^v(\underline{\mathrm{v}}_{rel}, t)$ can be derived by a convolution of the two velocity distributions of $P_{OH}^v(\underline{\mathrm{v}}_{OH}, t)$ and $P_{H_2}^v(\underline{\mathrm{v}}_{H_2}, t)$:

$$P^v(\underline{\mathrm{v}}_{rel}) = \int_{3D} P_{H_2}^v(\underline{\mathrm{v}}_{OH} - \underline{\mathrm{v}}_{rel}) \cdot P_{OH}^v(\underline{\mathrm{v}}_{OH}) \quad d\underline{\mathrm{v}}_{OH} \tag{6.20}$$

or equivalently:

$$P^v(\underline{\mathrm{v}}_{rel}) = \int_{3D} P_{OH}^v(\underline{\mathrm{v}}_{H_2} + \underline{\mathrm{v}}_{rel}) \cdot P_{H_2}^v(\underline{\mathrm{v}}_{H_2}) \quad d\underline{\mathrm{v}}_{H_2}. \tag{6.21}$$

In the following three paragraphs, first the number density-to-flux transformation is presented as it is commonly established by [110] [111]. To link the product creation and the actual measured signals in more detail the velocity distributions of the colliding packets have to be included into the simulation [112] [113]. In the second and third paragraph it is shown how this theory can be extended together with the definitions that have just been made to determine the collision energy and the collision energy distribution, respectively.

6.2.2 Evolution of the scattering signal

The rate of an inelastic collision process to scatter from an initial state i to a final state f at one well defined relative velocity $\overline{v_{rel}}$ and into a particular solid angle is defined as:

$$\begin{aligned}\frac{dN_{i\rightarrow f}}{dt} =& \overline{v_{rel}} \cdot \frac{d\sigma_{i\rightarrow f}(\overline{v_{rel}})}{d\omega} \int_{3D}\int_{3D} \Big[\delta_{\underline{\mathrm{r}}_{OH}\underline{\mathrm{r}}_{H_2}} P^r_{OH}(\underline{\mathrm{r}}_{OH}, t) \times \\ & P^r_{H_2}(\underline{\mathrm{r}}_{H_2}, t)\Big] d^3\underline{\mathrm{r}}_{H_2} d^3\underline{\mathrm{r}}_{OH},\end{aligned} \tag{6.22}$$

where $N_{i\rightarrow f}$ denotes the created product number density, $\frac{d\sigma_{i\rightarrow f}(\overline{v_{rel}})}{d\omega}$ is the differential cross section, which gives the probability distribution to scatter into a particular solid angle, and $P^r_{OH}(\underline{\mathrm{r}}_{OH}, t)$ and $P^r_{H_2}(\underline{\mathrm{r}}_{H_2}, t)$ describe the number density distributions of the two colliding reagent packets as a function of their coordinates in 3D space and time. The integral performed here accounts for the spatial overlap as it has already been defined in equation (6.18). The fixed relative velocity is related to the definitions in equation (6.4) by the use of the Euclidean norm (or 2-norm: $\overline{v_{rel}} = ||\overline{\underline{\mathrm{v}}_{rel}}||_2$). The state-to-state transition labeling ($i \rightarrow f$) will be changed to a superscripted f from now on, because in the experiment the initial F1(J = 3/2,f) state is very well defined and the final state can be individually addressed by the laser detection. If this was not the case, an additional average over all initial reagent densities and an average over all final product densities would be needed in the equation.

In the saturated LIF detection (see section 2.3) different rotational states are selectively probed by using selected transitions of the P- and Q-branches of the (A $^2\Sigma^+$, v' = 1 ← X $^2\Pi_{3/2}$, v = 0) band of OH. In order to relate the measured fluorescence intensities to the collisional induced populations, the fraction of excited M_J-levels relative to all M_J-levels of the initial and the final states need to be taken into account. These laser excitation rates are included in the factor Γ^f, which are listed in Table 6.3.

Usually, knowledge of the angular distribution of the scattering products, and hence of the differential cross section $\frac{d\sigma^f(\overline{v_{rel}})}{d\omega}$, is essential for the analysis of the signals to account for the detection conditions. In this setup the detection volume is defined by the laser beam spot. A very large laser-diameter (9mm) is used to ensure that all products are uniformly illuminated independent of their direction of propagation after the collision. In section 6.3.4 measurements and simulations explicitly prove that these conditions, the so-called flux-mode, are achieved. Therefore, the LIF detection method in this setup is not sensitive to changes of the differential cross section, as in fact an integration over all solid angles $d\Omega$ is performed by illuminating the whole cloud of scattering products. Therefore, the measured signal per unit time is proportional to the absolute integral cross section $\sigma^f(\overline{v_{rel}}) = \int \frac{d\sigma^f(\overline{v_{rel}})}{d\omega} d\Omega$:

$$\begin{aligned} \frac{dN^f}{dt} =& \Gamma_f \cdot \overline{v_{rel}} \cdot \sigma^f(\overline{v_{rel}}) \int_{3D}\int_{3D} \Big[\delta_{\underline{r}_{OH}\underline{r}_{H_2}} P^r_{OH}(\underline{r}_{OH}, t) \times \\ & P^r_{H_2}(\underline{r}_{H_2}, t)\Big] d^3\underline{r}_{OH} d^3\underline{r}_{H_2}. \end{aligned} \tag{6.23}$$

The number of products $\langle N^f \rangle_\tau$ at the moment of detection $t = \tau$ is not simply determined by those that have just been created as it is done in equation (6.23). All the contributions that accumulated from earlier scattering times need to be added up as well. Therefore, an integration over all earlier times ($-\infty$) up to the moment of detection $t = \tau$ needs to be performed:

$$\begin{aligned} \langle N^f \rangle_\tau =& \Gamma_f \cdot \overline{v_{rel}} \cdot \sigma_f(\overline{v_{rel}}) \int_{-\infty}^{\tau}\int_{3D}\int_{3D} \Big[\delta_{\underline{r}_{OH}\underline{r}_{H_2}} P^r_{OH}(\underline{r}_{OH}, t) \times \\ & P^r_{H_2}(\underline{r}_{H_2}, t)\Big] d^3\underline{r}_{OH} d^3\underline{r}_{H_2} dt. \end{aligned} \tag{6.24}$$

In the following the equation (6.23) of the number of products per unit time will be advanced such that not only one well fixed $\overline{v_{rel}}$ can be calculated. The probability distribution of relative velocities ($P^v(\underline{\mathrm{v}}_{rel})$) has to be included, which was derived in the relations (6.20) and (6.21). The cross section $\sigma^f(\underline{\mathrm{v}}_{rel})$ is also a function of the relative velocity, which can vary a lot due to $P^v(\underline{\mathrm{v}}_{rel})$. The term of the fixed relative velocity and the cross section must be replaced by: $\overline{v_{rel}} \cdot \sigma_f(\overline{v_{rel}}) \rightarrow \int_{3D} \underline{\mathrm{v}}_{rel} \cdot \sigma_f(\underline{\mathrm{v}}_{rel}) \cdot P^v(\underline{\mathrm{v}}_{rel}) d^3\underline{\mathrm{v}}_{rel}$. The integration over the product of the relative velocity and the cross sections with the whole velocity distribution from $-\infty$ to ∞ accounts for the contribution of the cross section at each relative velocity. An alternative explanation is that the integral $\bar{\underline{\mathrm{v}}}_{rel} = \int_{3D} \underline{\mathrm{v}}_{rel} \cdot P^v(\underline{\mathrm{v}}_{rel}) d^3\underline{\mathrm{v}}_{rel}$ determines the expected value or the mean value of the relative velocity. The cross section gives an additional weighting that accounts for the different probabilities to drive the transition at each relative velocity.

However, this also implies that the rate $\frac{dN^f}{dt}$ is not only a function of $\underline{\mathrm{v}}_{rel}$ and $\sigma_f(\underline{\mathrm{v}}_{rel})$, but also of $P^v(\underline{\mathrm{v}}_{rel})$. Since the parts of $P^v(\underline{\mathrm{v}}_{rel})$ which are present in the intersection volume change as a function of the overlap in time, also the rate of signal production changes and cannot be integrated easily over time. In the following a different way of calculating the production of the scattering signal is given, where in a first step the instantaneous signal production $\bar{N}_f^t$ is defined at a particular time t, when the pulses are overlapping:

$$\begin{aligned}\bar{N}_f^t =& \Gamma^f \left[\frac{\int_{3D}\int_{3D}\int_{3D} \underline{\mathrm{v}}_{rel}\sigma^f(\underline{\mathrm{v}}_{rel})\delta_{\underline{\mathrm{r}}_{OH}\underline{\mathrm{r}}_{H_2}} P_{OH}^r(\underline{\mathrm{r}}_{OH},t) P_{H_2}^r(\underline{\mathrm{r}}_{H_2},t)}{\int_{3D}\int_{3D}\int_{3D} \delta_{\underline{\mathrm{r}}_{OH}\underline{\mathrm{r}}_{H_2}} P_{OH}^r(\underline{\mathrm{r}}_{OH},t) P_{H_2}^r(\underline{\mathrm{r}}_{H_2},t)} \times \right. \\ & \left. \frac{P^v(\underline{\mathrm{v}}_{rel}) d^3\underline{\mathrm{r}}_{OH} d^3\underline{\mathrm{r}}_{H_2} d^3\underline{\mathrm{v}}_{rel}}{P^v(\underline{\mathrm{v}}_{rel}) d^3\underline{\mathrm{r}}_{OH} d^3\underline{\mathrm{r}}_{H_2} d^3\underline{\mathrm{v}}_{rel}} \right]. \end{aligned} \tag{6.25}$$

In the denominator, the spatial integrals account for the part of the velocity distribution, that is present in the intersection volume, while the integration over the relative velocity space defines the amount of produced signal. The integrals over the whole phase-space in the denominator normalize the contributing parts of the probability number-density distribution. Since the contributing parts might change as a function of the overlap in time, the normalization must be performed at each instantaneous moment, although the probability number-density distribution themselves are normalized already.

For the temporal evolution of the scattering products, the argument still holds that all contributions from earlier times must be summed up. However, it must also be taken into account that the number-density changes at different overlaps and therefore a different amount of scattering products is produced. A weighted average has to be performed to account for the corresponding probabilities to induce scattering products. The weighting function is given by $\mathit{\Pi}_{PSP}(t)$ of equation (6.19). The scattering signal $\langle \bar{N}^f \rangle_\tau$ at the moment of detection τ is finally given by the integration over time, starting from $(-\infty)$:

$$\begin{aligned}\langle \bar{N}^f \rangle_\tau =& \mathit{\Gamma}_f \left[\frac{\int_{-\infty}^{\tau} \bar{N}_f^t \cdot \mathit{\Pi}_{PSP}(t)dt}{\int_{-\infty}^{\tau} \mathit{\Pi}_{PSP}(t)dt} \right] = \\ =& \mathit{\Gamma}_f \left[\frac{\int_{-\infty}^{\tau} \int_{3D} \int_{3D} \int_{3D} \underline{\mathrm{v}}_{rel} \cdot \sigma^f(\underline{\mathrm{v}}_{rel}) \cdot \delta_{\underline{\mathrm{r}}_{OH}\underline{\mathrm{r}}_{H_2}} P_{OH}^r(\underline{\mathrm{r}}_{OH}, t)}{\int_{-\infty}^{\tau} \int_{3D} \int_{3D} \int_{3D} \delta_{\underline{\mathrm{r}}_{OH}\underline{\mathrm{r}}_{H_2}} P_{OH}^r(\underline{\mathrm{r}}_{OH}, t)} \times \right. \\ & \left. \frac{P_{H_2}^r(\underline{\mathrm{r}}_{H_2}, t) P^v(\underline{\mathrm{v}}_{rel}) d^3\underline{\mathrm{r}}_{OH} d^3\underline{\mathrm{r}}_{H_2} d^3\underline{\mathrm{v}}_{rel} dt}{P_{H_2}^r(\underline{\mathrm{r}}_{H_2}, t) P^v(\underline{\mathrm{v}}_{rel}) d^3\underline{\mathrm{r}}_{OH} d^3\underline{\mathrm{r}}_{H_2} d^3\underline{\mathrm{v}}_{rel} dt} \right].\end{aligned} \tag{6.26}$$

At last the equation is written such that only terms and coordinates of the lab frame are used. Terms with CM properties like the relative velocity have to be transformed with the given definitions. Equations (6.20) and (6.21) relate the distribution of relative velocities to the velocity distributions of the incoming OH and H_2 beams. By using the definition of the relative velocity from equation (6.4) together with the Jacobian determinant[2] follows after the integral transformation for the instantaneous

---

[2] In this case, where a quantity is a function of $f(\underline{\mathrm{v}}_{rel})$, the relation is given by the integral and the use of equation (6.20) (or equation (6.21)):

$$\int_{3D} f(\underline{\mathrm{v}}_{rel}) P^v(\underline{\mathrm{v}}_{rel}) d^3\underline{\mathrm{v}}_{rel} = \int_{3D} \int_{3D} f(\underline{\mathrm{v}}_{rel}) P_{H_2}^v(\underline{\mathrm{v}}_{OH} - \underline{\mathrm{v}}_{rel}) P_{OH}^v(\underline{\mathrm{v}}_{OH}) d^3\underline{\mathrm{v}}_{OH} d^3\underline{\mathrm{v}}_{rel}.$$

signal production

$$\begin{aligned} \bar{N}_f^t =& \Gamma^f \left[\frac{\int_{3D}\int_{3D}\int_{3D}\int_{3D} (\underline{v}_{OH} - \underline{v}_{H_2}) \sigma^f (\underline{v}_{OH} - \underline{v}_{H_2}) \delta_{\underline{r}_{OH}\underline{r}_{H_2}}}{\int_{3D}\int_{3D}\int_{3D}\int_{3D} \delta_{\underline{r}_{OH}\underline{r}_{H_2}}} \times \right. \\ & \left. \frac{n_{OH}(\underline{r}_{OH}, \underline{v}_{OH}, t) n_{H_2}(\underline{r}_{H_2}, \underline{v}_{H_2}, t) d^3\underline{r}_{OH} d^3\underline{r}_{H_2} d^3\underline{v}_{OH} d^3\underline{v}_{H_2}}{n_{OH}(\underline{r}_{OH}, \underline{v}_{OH}, t) n_{H_2}(\underline{r}_{H_2}, \underline{v}_{H_2}, t) d^3\underline{r}_{OH} d^3\underline{r}_{H_2} d^3\underline{v}_{OH} d^3\underline{v}_{H_2}} \right] \end{aligned} \tag{6.27}$$

and the temporal evolution:

$$\begin{aligned} \langle \bar{N}^f \rangle_\tau =& \Gamma_f \left[\frac{\int_{-\infty}^{\tau} \bar{N}_f^t \cdot \Pi_{PSP}(t) dt}{\int_{-\infty}^{\tau} \Pi_{PSP}(t) dt} \right] \\ =& \Gamma_f \left[\frac{\int_{-\infty}^{\tau} \int_{3D}\int_{3D}\int_{3D}\int_{3D} (\underline{v}_{OH} - \underline{v}_{H_2}) \sigma^f (\underline{v}_{OH} - \underline{v}_{H_2}) \delta_{\underline{r}_{OH}\underline{r}_{H_2}}}{\int_{-\infty}^{\tau} \int_{3D}\int_{3D}\int_{3D}\int_{3D} \delta_{\underline{r}_{OH}\underline{r}_{H_2}}} \times \right. \\ & \left. \frac{n_{OH}(\underline{r}_{OH}, \underline{v}_{OH}, t) n_{H_2}(\underline{r}_{H_2}, \underline{v}_{H_2}, t) d^3\underline{r}_{OH} d^3\underline{r}_{H_2} d^3\underline{v}_{OH} d^3\underline{v}_{H_2} dt}{n_{OH}(\underline{r}_{OH}, \underline{v}_{OH}, t) n_{H_2}(\underline{r}_{H_2}, \underline{v}_{H_2}, t) d^3\underline{r}_{OH} d^3\underline{r}_{H_2} d^3\underline{v}_{OH} d^3\underline{v}_{H_2} dt} \right]. \end{aligned} \tag{6.28}$$

If then the transformation of coordinates is done the Jacobian determinant $|J|$ has to be included and the limits of the integral can be kept:

$$\int_{3D} f(\underline{v}_{rel}) P^v(\underline{v}_{rel}) d^3\underline{v}_{rel} = \int_{3D}\int_{3D} f(\underline{v}_{OH} - \underline{v}_{H_2}) P^v_{H_2}(\underline{v}_{H_2}) \times$$

$$P^v_{OH}(\underline{v}_{OH}) |J| d^3\underline{v}_{OH} d^3\underline{v}_{H_2}.$$

If, for instance, a Cartesian coordinate system is used for the definition of the vectors, the Jacobian determinant differs just by +1 if equation (6.20) is used or -1 if equation (6.21) is used. The definition of the orientation of the relative velocity vector in space defines the difference.

6.2.3 Evolution of the collision energy

During the discussion of the overlap dynamics as shown in Figure 6.2 it has already been pointed out that the collision energy changes as a function of the packets' overlap in time. The definition of the collision energy is given in equation (6.14) by $E_c = \mu/2|\underline{v}_{rel}|^2$. Only the term $\underline{v}_{rel}$ needs to be defined within the formalism that has been used in this section to determine the quantity $\langle \bar{N}^f \rangle_\tau$. In the following, first an instantaneous mean collision energy (E_c^t) is defined, which can be defined for any moment a product can be created. The collision energy at the moment of detection $\langle \bar{E}_c \rangle_\tau$ follows from this quantity. In analogy to equation (6.27) the average instantaneous collision energies that are produced during an inelastic collision process per unit time and unit volume, is denoted as:

$$\begin{aligned}E_c^t =& \frac{\mu}{2}\left[\frac{\int_{3D}\int_{3D}\int_{3D} |\underline{v}_{rel}|^2 \delta_{\underline{r}_{OH}\underline{r}_{H_2}} P^v(\underline{v}_{rel}) P^r_{OH}(\underline{r}_{OH},t)}{\int_{3D}\int_{3D}\int_{3D} \delta_{\underline{r}_{OH}\underline{r}_{H_2}} P^v(\underline{v}_{rel}) P^r_{OH}(\underline{r}_{OH},t)} \times\right. \\ & \left.\frac{P^r_{H_2}(\underline{r}_{H_2},t) d^3\underline{r}_{OH} d^3\underline{r}_{H_2} d^3\underline{v}_{rel}}{P^r_{H_2}(\underline{r}_{H_2},t) d^3\underline{r}_{OH} d^3\underline{r}_{H_2} d^3\underline{v}_{rel}}\right].\end{aligned} \tag{6.29}$$

The denominator describes the calculation of the expected value of the squared relative velocity, while $\delta_{\underline{r}_{OH}\underline{r}_{H_2}}$ accounts for only those parts of the relative velocity distribution, which are present in the intersection volume. The denominator normalizes the contributing parts of the probability number-density distribution. In the next step, all quantities are written such that only the coordinates of the lab frame are used in the equations. Again the coordinate transformation of the integral over the relative velocity needs to be performed like in equation (6.27)

$$\begin{aligned}E_c^t =& \frac{\mu}{2}\left[\frac{\int_{3D}\int_{3D}\int_{3D}\int_{3D} |\underline{v}_{OH} - \underline{v}_{H_2}|^2 \delta_{\underline{r}_{OH}\underline{r}_{H_2}} n_{OH}(\underline{r}_{OH},\underline{v}_{OH},t)}{\int_{3D}\int_{3D}\int_{3D}\int_{3D} \delta_{\underline{r}_{OH}\underline{r}_{H_2}} n_{OH}(\underline{r}_{OH},\underline{v}_{OH},t)} \times\right. \\ & \left.\frac{n_{H_2}(\underline{r}_{H_2},\underline{v}_{H_2},t) d^3\underline{r}_{OH} d^3\underline{r}_{H_2} d^3\underline{v}_{OH} d^3\underline{v}_{H_2}}{n_{H_2}(\underline{r}_{H_2},\underline{v}_{H_2},t) d^3\underline{r}_{OH} d^3\underline{r}_{H_2} d^3\underline{v}_{OH} d^3\underline{v}_{H_2}}\right].\end{aligned} \tag{6.30}$$

To derive the quantity that describes the mean collision energy at a certain moment of detection τ, the same argument is still valid as before:

the contributions from all earlier times of all E_c^t have to be summed up, where a weighted average has to be done to account for the corresponding probabilities to produce collision energies. The weighting function is again given by $\mathit{\Pi}_{PSP}(t)$ of equation (6.19). This is finally given by the integration over time starting from the earliest time $(-\infty)$ up to the moment of detection (τ):

$$\langle E_c \rangle_\tau \quad = \quad \left[\frac{\int_{-\infty}^{\tau} E_c^t \cdot \mathit{\Pi}_{PSP}(t) dt}{\int_{-\infty}^{\tau} \mathit{\Pi}_{PSP}(t) dt} \right] \tag{6.31}$$

At this point a comparison with probability theory can be made: to a certain extent the expected value of the collision energy was determined as a function of time. The actual expected value of the collision energy would be given, if the temporal integral was performed until $+\infty$, where the complete PSD of both packets would have contributed. One would say, therefore, that equation (6.31) gives the mean value of the collision energy, but only up to the moment of detection.

6.2.4 Evolution of the collision energy distribution

To complete the formalism of the overlap dynamics, an expression for the collision energy distribution is defined as a function of the packets' overlap in time. The quantity describing the collision energy distribution is the second central moment or the variance $\mathit{\Delta}_{var}^2 E_c^t$. It is defined as the spread of v_{rel}^2 around the expected value of $\langle v_{rel}^2 \rangle$. The determination of $\langle v_{rel}^2 \rangle$ was described in the previous section, when E_c^t was derived. At a particular moment of overlap the instantaneous variance is given by:

$$\begin{aligned} \mathit{\Delta}_{var}^2 E_c^t = & \frac{\mu^2}{4} \left[\frac{\int_{3D} \int_{3D} \int_{3D} [v_{rel}^2 - \langle v_{rel}^2 \rangle]^2 \delta_{\underline{r}_{OH} \underline{r}_{H_2}} P^v(\underline{v}_{rel})}{\int_{3D} \int_{3D} \int_{3D} \delta_{\underline{r}_{OH} \underline{r}_{H_2}} P^v(\underline{v}_{rel})} \times \right. \\ & \left. \frac{P_{OH}^r(\underline{r}_{OH}, t) P_{H_2}^r(\underline{r}_{H_2}, t) d^3\underline{r}_{OH} d^3\underline{r}_{H_2} d^3\underline{v}_{rel}}{P_{OH}^r(\underline{r}_{OH}, t) P_{H_2}^r(\underline{r}_{H_2}, t) d^3\underline{r}_{OH} d^3\underline{r}_{H_2} d^3\underline{v}_{rel}} \right] . \end{aligned} \tag{6.32}$$

After transforming certain quantities such that only coordinates of the lab frame are used, the same equation reads as:

$$\begin{aligned}\mathit{\Delta}^2_{var}E^t_c = & \frac{\mu^2}{4}\left[\frac{\int_{3D}\int_{3D}\int_{3D}\int_{3D}[|\underline{v}_{OH}-\underline{v}_{H_2}|^2-\langle|\underline{v}_{OH}-\underline{v}_{H_2}|^2\rangle]^2\delta_{\underline{r}_{OH}\underline{r}_{H_2}}}{\int_{3D}\int_{3D}\int_{3D}\int_{3D}\delta_{\underline{r}_{OH}\underline{r}_{H_2}}}\times\right. \\ & \left.\frac{n_{OH}(\underline{r}_{OH},\underline{v}_{OH},t)n_{H_2}(\underline{r}_{H_2},\underline{v}_{H_2},t)d^3\underline{r}_{OH}d^3\underline{r}_{H_2}d^3\underline{v}_{OH}d^3\underline{v}_{H_2}}{n_{OH}(\underline{r}_{OH},\underline{v}_{OH},t)n_{H_2}(\underline{r}_{H_2},\underline{v}_{H_2},t)d^3\underline{r}_{OH}d^3\underline{r}_{H_2}d^3\underline{v}_{OH}d^3\underline{v}_{H_2}}\right].\end{aligned} \tag{6.33}$$

The quantity describing the collision energy distribution at a certain moment of detection τ must account for the time evolution. Again, when all the contributions from all earlier times of all $\mathit{\Delta}^2_{var}E^t_c$ are summed up, a weighted average is performed to account for the corresponding contributions to whole collision energy distribution, which is given by $\langle\mathit{\Delta}^2_{var}E_c\rangle_\tau$. The weighted average is again performed by calculating the temporal integral from $-\infty$ to the moment of detection τ, while weighting with $\mathit{\Pi}_{PSP}(t)$:

$$\langle\mathit{\Delta}^2_{var}E_c\rangle_\tau = \left[\frac{\int_{-\infty}^{\tau}(\mathit{\Delta}^2_{var}E^t_c)\cdot\mathit{\Pi}_{PSP}(t)dt}{\int_{-\infty}^{\tau}\mathit{\Pi}_{PSP}(t)dt}\right] \tag{6.34}$$

6.3 Experimental procedure and data analysis

This section summarizes details on the implementation and the methods of the scattering experiment. Firstly, it is explained, how an energy-resolved scattering experiment is performed and how signals can be measured and identified. In a second part, the calibration of the collision energy and of the scattering dynamics is shown.

6.3.1 Tuning of the collision energy

Tuning of the velocities of the incoming molecular packets (6.14) enables collision-energy resolved investigations of the rotational inelastic scattering process. Stabilizing the Even-Lavie valve at a certain temperature sets $\underline{v}_{H_2}$, while the programmed deceleration and/or acceleration switching scheme of the Stark-decelerator determines $\underline{v}_{OH}$. Changing the temperature on the H_2 side varies the collision energy in a large range, while the Stark-decelerator conducts more detailed variations of the collision energies. Throughout the experiments here, nitric acid is expanded in the seed gas krypton and coupled into the Stark-decelerator with a mean velocity of 495 m/s, where $\underline{v}_{OH}$ is tuned between 170 - 690 m/s. The EL-valve settings produce $\underline{v}_{H_2}$ = 1320 m/s and $\underline{v}_{H_2}$ = 1530 m/s (with T = 82 K and T = 107 K, respectively, the relevant valve settings are given in Table 3.1) to be able to scan two intervals of collision energies between 70 - 105 cm^{-1} and between 100 - 150 cm^{-1}, respectively.

In previous experiments, $\underline{v}_{OH}$ was varied by using a constant phase-angle to either accelerate or decelerate the molecular packet [66] [107]. Using different phase-angles changed the final velocities. Here, we programmed the Stark-decelerator such that the HV-switching scheme consists of two phase-angles: $-\phi$ for acceleration and then $+\phi$ for deceleration. These schemes of switching the HV-bursts has been referred to as: acc/dec-method. Analogously, the dec/acc-method realizes first a deceleration with $+\phi$ then an acceleration with $-\phi$. Switching unequal periods of acceleration and deceleration within the same burst produces different final velocities. Although the same final velocity of the OH-packet is produced, the acc/dec-method has some advantages compared to the use of just one phase-angle:

- The produced molecular packets have the same spatial dimensions independent of their final velocity, which makes the analysis of the spatial overlap less prone to systematic errors.
- Trajectory simulations show that the phase-space acceptance in the Stark-decelerator varies for the different M_J-components due to a different Stark-shift in the same electric field. The population distribution of different M_J-components in the electric field is not equal, which leads to an unequal population distribution of the hyperfine states of the F = 1 and the F = 2 in a field-free surrounding [3]. If the phase-angle is varied also the stable 6D phase-space volume of different M_J-components changes. If the acc/dec method is used to

vary the final velocity, the ratio of different M_J-components stays always the same.

6.3.2 Definition of signals

The population in the excited rotational states in the OH radical after the collision with H_2 are probed state-selectively via saturated LIF. Individual fluorescence photons can be measured as single voltage peaks and are counted as events. To disentangle the photons resulting from the scattering process from those of a different origin, the experiment is triggered such that the H_2 beam is only shot at every second repetition of the experiment. The scattering signal at a certain collision energy (E_c) is defined as the number of counted photons with an H_2 packet present $^{(on)}\mathcal{N}^{(E_c)}$ (induced collisions + background) minus the number of photons without an H_2 packet present $^{(off)}\mathcal{N}^{(E_c)}$ (background measurement). Various effects sum up to the background signal: (1) inelastically scattered photons from the stray light at the filters contribute, (2) higher order transitions can come into play: if for example the population of the F1(3/2,e) is probed via the $P_1(1)$ line, the M1 transition out of the F1(3/2,f) along the $P_1^{\prime}(1)$ might have an influence or (3) initial population in particular low field-seeking states like the F1(5/2,f) and F2(1/2,f) that are also Stark-decelerated, can add to the signal.

To reduce the influence of long term drifts in the experiment, the collision energy was varied in a quasi-continuous cycle. The Stark decelerator was programmed to produce a different velocity of the OH radicals every third shot of the experiment (first and second shot are used for H_2 valve (on) and (off)). The trigger pulses that synchronize the components of the experiment, are adjusted to match the arrival time of both molecular packets in the collision zone. In this experiment, a single cycle consisted of 76 measurements using 19 different velocities of the OH packet. In the first 38 measurements, the velocity of the OH packet was varied from low to high values; in the next 38 measurements, the OH velocity was varied from high to low velocities. To accumulate more data these cycles are repeated for a certain amount of average (ave). To determine the final scattering signal at a certain E$_c$, first the mean values of

$$ {}^{(on/off)}\overline{\mathcal{N}}^{(E_c)} = \frac{1}{ave}\sum_{k=1}^{ave} {}^{(on/off)}\mathcal{N}_k^{(E_c)}, \tag{6.35} $$

the standard deviations (std)

$$ {}^{(on/off)}\Delta_{std}^{(E_c)} = \sqrt{\frac{1}{ave}\sum_{k=1}^{ave}[{}^{(on/off)}\overline{\mathcal{N}}^{(E_c)} - {}^{(on/off)}\overline{\mathcal{N}}^{(E_c)}]^2}, \tag{6.36} $$

and the standard error of the mean (se)

$$ {}^{(on/off)}\Delta_{se}^{(E_c)} = \frac{{}^{(on/off)}\Delta_{std}^{(E_c)}}{\sqrt{ave}} \tag{6.37} $$

were calculated.

The final scattering signal Sig_{sc} is defined as

$$ Sig_{sc}^{(E_c)} = {}^{(on)}\overline{\mathcal{N}}^{(E_c)} - {}^{(off)}\overline{\mathcal{N}}^{(E_c)}, \tag{6.38} $$

and a confidence interval (ci) determined by

$$ \Delta_{ci}^{(E_c)} = \sqrt{[{}^{(on)}\Delta_{se}^{(E_c)}]^2 + [{}^{(off)}\Delta_{se}^{(E_c)}]^2}. \tag{6.39} $$

When the H$_2$ beam is present no decrease of Sig_{in} is measurable because of out-scattering indicating that the single collision regime is achieved. The measured signal is defined in dimensions of counts per shot, i.e. counts per measurement cycle. In the left graph of Figure 6.3 the raw scattering signals $Sig_{sc}^{(E_c)}$ are plotted against $\underline{v}_{OH}$ for OH colliding with pc-H$_2$, the upper and the lower graph depict the low and the high collision energy intervals. The raw signals are analysed together with the kinematic properties of the two beams to determine two essential quantities: (1) the collision energy is calibrated out of the velocities $\underline{v}_{OH}$ and $\underline{v}_{H_2}$, and (2) cross sections are deduced from the measured signals.

The incoming beam intensity ($Sig_{in}^{(E_c)} = {}^{(on)}\overline{\mathcal{N}}^{(E_c)} - {}^{(off)}\overline{\mathcal{N}}^{(E_c)}$) of the F1(3/2,f) is measured several times during the day to calibrate the system.

The mean scattering signal is normalized by the incoming beam intensity of the F1(3/2,f) to determine the ratio of an individual induced transition: $Sig_{ratio}^{(E_c)} = Sig_{sc}^{(E_c)}/Sig_{in}^{(E_c)}$. Both quantities, $Sig_{ratio}^{(E_c)}$ and $Sig_{sc}^{(E_c)}$ can be used to determine relative cross sections (see section 7.4.1) or to perform signal comparisons (see section 7.4.3), since the signals of final states are compared relative to each other at each individual E_c. For the evaluation of excitation functions, $Sig_{ratio}^{(E_c)}$ is indispensable, because the rate of excitation at each individual E_c is compared. However, to achieve a better day-to-day comparison, the mean scattering signal $Sig_{sc}^{(E_c)}$ of each day is normalized by $Sig_{in}^{(E_c)}$ of the F1(3/2,f) at each day.

6.3.3 Calibration of the collision energy

Usually equation (6.14) is used to calculate the collision energy. Within the experiments conducted here, it turned out that the kinematics during the collision process have to be considered in greater detail. Equation (6.31) and (6.34) express the collision energy and the collision energy distribution, respectively. These equations follow from a model, where two continuous 6D probability number-density distribution define the molecular packets. Here, Monte-Carlo simulations are performed, where the probability number-density distribution of both molecular packets is described by a discrete distribution of points in 6D phase-space. The Monte-Carlo approach has several advantages compared to the continuous one, because many properties of the experimental setup can directly be incorporated in the simulations. This will be discussed alongside with the calibration of the collision energy and its distribution.

Since no external forces are present in the collision zone, the particles propagate and overlap in free flight. To model the kinematic effects in detail, the generation of the 6D PSD in the beginning determines the resulting dynamics. On the OH-side the PSD can differ a lot depending on the HV-switching scheme that has been used, which numerical trajectory simulations produce accurately. The PSD of the OH packets, which are used as the starting point for free-flight, are completely defined after the last HV-switching off. These partially non-standard distributions have

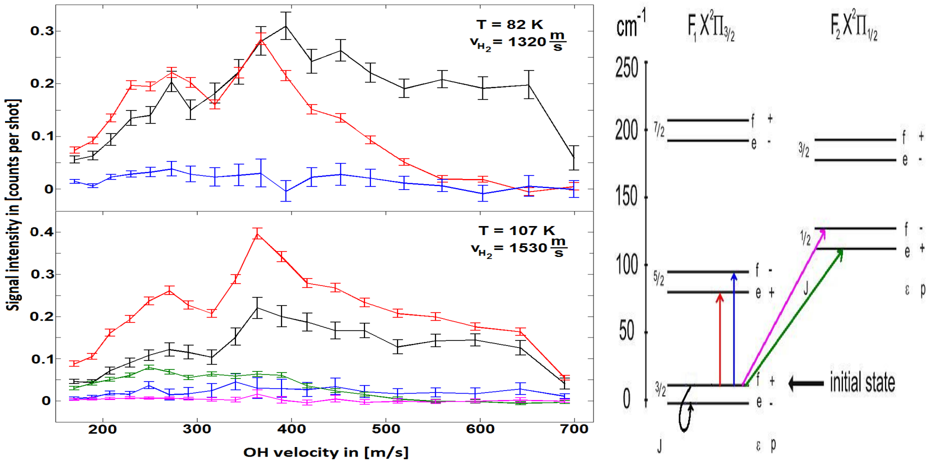

Figure 6.3: The raw scattering signals for collisions of pcH_2 with OH radicals are plotted in the left graph as an example. In the right graph the energy level scheme indicates the inelastic transitions out of the initial F1(3/2,f) state, together with the changes of the Λ-doublet, the rotational quantum state J, or the spin-orbit manifold. The parity of the states is given either by the spectroscopic nomenclature (e and f) or the parity (+ and -). The scale on the left shows the energy differences, while the Λ-doublet splittings are exaggerated for reasons of clarity. In both graphs the transitions are labeled by the same colour code: F1(3/2,e) is black, F1(5/2,e) is red, F1(5/2,f) is blue, F2(1/2,e) is green and the F2(1/2,f) is pink.

been discussed in detail in chapter 3 . Without any approximations they can be included in the overlap simulations.

A second advantage is the modeling of the free-flight dynamics. Increasing time creates a stronger correlation between the position of a particle in the packet and its velocity: with longer drift times the faster molecules become more likely to be present in the front part of the packet, while the slower ones lag behind. Especially on the H_2-side, where the distance from the skimmer to the interaction zone is very long, these dynamics in phase-space are naturally implemented in the simulations. At the skimmer, the supersonic expansion process is supposed to be completed. Therefore, the skimmer-orifice defines the transverse area in position space, where discrete points are generated. A Gaussian-random number generator models the discrete 6D PSDs, where equation (3.7) and equation (3.6) define the standard deviations in the longitudinal direction for the position space and the velocity space, respectively. Table 3.1 shows the experimentally determined parameters for each relevant temperature. The skimmer and the slit close to the interaction zone confine the 6D phase-space volume in the transverse direction of the scattering plane (the plane defined by the two molecular beams). A reasonable value for the transverse velocity distributions is chosen in the simulations, such that the slit acts like a filter, cutting off the wings of the distribution.

Time t is the only running parameter in the simulations, which is performed in finite time steps Δt. The moment of detection in the experiment defines $t = \tau = 0$ in the simulations. Approaching of both molecular packets happens thus at negative times. As starting point of the simulations, a timing t_{start} is chosen, when no spatial coordinates of both distributions overlap. At each time-step $t_j = t_{start} + j \cdot \Delta t$, with $j = 1, 2, ...$ the relevant parts of each 6D PSD must be identified that could possibly scatter. For both molecular beams, the maximum transverse velocity components specify two cones, as it is indicated in Figure 6.2, which define the intersection volume of the two pulses. At the H_2 side, skimmer and slit are the restricting mechanical constraints for the maximum transverse velocity. On the OH side, both maximum transverse velocity components of the OH packet constitute the largest spatial extent of the OH packet in the overlap region.

At each t_j those molecules of the OH distribution (OH^{t_j} consisting of m^{t_j} elements) and the H_2 distribution (HH^{t_j} containing n^{t_j} elements) are identified which are present in the intersection volume. The collision energy follows from equation (6.14). However, at this point a model of the interaction or the collision process must be defined to relate the elements of the two samples in a physical meaningful way:

1. Straight forward is to state that in the intersection volume every element of OH^{t_j} collides with every element of HH^{t_j}. The gener-

ated sample of collision energies $[E^{t_j}] = [e_1^{t_j}, e_2^{t_j}, ..., e_i^{t_j}, ..., e_{m_{t_j} \times n_{t_j}}^{t_j}]$ contains $\mathcal{N}^{t_j} = m^{t_j} \times n^{t_j}$ elements at every t_j. This strategy is numerically easy, since the elements of both samples are directly used to calculate collision energies. From a statistical point of view a large ensemble is created, which effectively enables meaningful interpretations. However, from a physics point of view, information is lost on the spatial number-density distributions within the intersection volume. An average collision energy of both complete distributions is simulated only.

2. The next obvious step to overcome this loss of information on the number-density distributions, is to sub-divide the intersection volume into smaller volume-units. The smaller the size of these volume-units, the better is the resemblance of the number-density distributions. Quantities like the collision energy could be defined for each volume-unit, in the same way this is done for the complete intersection volume. To determine the collision energy of the whole intersection volume, a weighting on the number of events per volume-unit needed to be done. This procedure can be implemented without any further approximations. However, it becomes numerically demanding, because the number of particles per volume-unit of the whole OH^{t_j} and HH^{t_j} samples decreases linearly with an increasing number of volume-units, if a constant number-density distribution is assumed. Therefore, to achieve a similar statistical significance compared to case 1., the number of events that needed to be simulated increases stronger than linear.

3. A different approach would be to specify an effective interaction distance based on the different long- and short-range interactions which are relevant for the process under investigation. An effective interaction sphere can be used in the simulations, beyond which interactions are too weak or become improbable. Only if particles are within the interaction sphere, a collision is approved and the collision energy taken into account. This approach incorporates the influence on number-density distribution inherently, because collisions are more

> likely to happen in regions of higher density. However, numerically this approach is very demanding, if the densities are low. Also the implementation is cumbersome, if every distance between molecules needs to be checked in three dimensions.

Case 1. is implemented because it is numerically the least time-consuming to produce results, and because it offers the possibility to advance the model with the ideas described in case 2. In the following details and results are given of the implementation of case 1. In the following a numerically interesting alternative is developed to determine the $\langle\overline{E}\rangle_\mathcal{T}$ and $\langle\varDelta_{var}E\rangle_\mathcal{T}$, which constitutes an analogy to the theoretical model presented in sections 6.2.3. As described in case 1., the generated sample of collision energies $[E^{t_j}] = [e_1^{t_j}, e_2^{t_j}, ..., e_i^{t_j}, ..., e_{m_{t_j}\times n_{t_j}}^{t_j}]$ contains $\mathcal{N}^{t_j} = m^{t_j} \times n^{t_j}$ elements at every t_j. In analogy to equation (6.29) the instantaneous collision energy $\overline{E}^{t_j}$ at each t_j follows from the calculation of the sample mean

$$\overline{E}^{t_j} = \frac{1}{\mathcal{N}^{t_j}} \sum_{i=1}^{\mathcal{N}^{t_j}} e_i^{t_j}. \tag{6.40}$$

This result is directly used to calculate the instantaneous collision energy distribution. The standard deviation or the variance follow in analogy to equation (6.32) from

$$\left[\varDelta_{std}E^{t_j}\right]^2 = \varDelta_{var}E^{t_j} = \frac{1}{\mathcal{N}^{t_j}} \sum_{i=1}^{\mathcal{N}^{t_j}} \left[e_i^{t_j} - \overline{E}^{t_j}\right]^2. \tag{6.41}$$

It is assumed that all collision products accumulate within the detection volume of the laser (flux-mode conditions) during the overlapping time, starting from the earliest time ($t = t_{start}$) up to the moment of detection ($t = \tau$). In accordance with the theoretical description, the expectation value of the collision energy is determined in analogy to equation (6.31) as a weighted average of the mean collision energies $\overline{E}^{t_j}$ at each timing t_j.

$$\langle\overline{E}\rangle_\mathcal{T} = \frac{\sum_{t_j=t_{start}}^{\tau} \mathcal{N}^{t_j}\overline{E}^{t_j}}{\sum_{t_j=t_{start}}^{\tau} \mathcal{N}^{t_j}}. \tag{6.42}$$

However the implementation is done differently. Instead of performing a weighted averaging, all elements of each $[E^{t_j}]$-sample are summarized to the sample $[E]^{tot}$, which contains all individual collisions $[E]^{tot} = \left[[E^{t_{start}}], ..., [E^{t_j}], ..., [E^{\tau}]\right] = \left[e_1^{t_j}, ..., e_i^{t_j}, ..., e_{\mathcal{N}^{tot}}^{t_j}\right]$ of each t_j. The total number of elements is $\mathcal{N}^{tot} = \sum_j \mathcal{N}^{t_j}$. The expected collision energy at $t = \tau$ follows directly from:

$$\langle\overline{E}\rangle_{\tau} = \frac{\sum_{t_j=t_{start}}^{\tau} \mathcal{N}^{t_j} \overline{E}^{t_j}}{\sum_{t_j=t_{start}}^{\tau} \mathcal{N}^{t_j}} = \frac{\sum_{t_j=t_{start}}^{\tau} \mathcal{N}^{t_j} \frac{1}{\mathcal{N}^{t_j}} \sum_{i=1}^{\mathcal{N}^{t_j}} e_i^{t_j}}{\sum_{t_j=t_{start}}^{\tau} \mathcal{N}^{t_j}} = \frac{1}{\mathcal{N}_{tot}} \sum_{i=1}^{\mathcal{N}_{tot}} e_i^{t_j}. \tag{6.43}$$

In the same way, the collision energy distribution in terms of the standard deviation $\langle\Delta_{std}E\rangle_{\tau}$ or the variance $\langle\Delta_{var}E\rangle_{\tau}$ is determined as

$$(\langle\Delta_{std}E\rangle_{\tau})^2 = \langle\Delta_{var}E\rangle_{\tau} = \frac{1}{\mathcal{N}_{tot}} \sum_{i=1}^{\mathcal{N}_{tot}} \left[e_i^t - \langle\overline{E}\rangle_{\tau}\right]^2 = \frac{1}{\mathcal{N}_{tot}} \sum_{i=1}^{\mathcal{N}_{tot}} (e_i^t)^2 - (\langle\overline{E}\rangle_{\tau})^2. \tag{6.44}$$

The calculations demand less computing time and they need less intermediate steps by using the sample $[E]^{tot}$. This also decreases the numerical error. However, these calculations require a larger store capacity.

In the following several distinct cases are discussed in depth to show the influence of the detailed analysis of the evolution of the collision energy and its distribution. Figure 6.4 contains nine graphs. Each row shows the analysis of a different setting of experimental conditions of OH and H_2 packets overlapping. The first graph in each row [(1a), (2a), (3a)] shows the TOF profiles of the corresponding molecular packets. The OH-TOF is drawn in black and centres at $t = 0$ indicating the actual moment of detection in the experiment. Different H_2-TOFs are plotted in various colours, to illustrate a delay in time relative to the centre of the OH-TOF. The shaded grey areas indicate the longitudinal regions of each packet that have been overlapping before. The second graph in each row [(1b), (2b), (3b)] shows the evolution of the collision energy. At each time-step Δt in the simulation the mean collision energy $E^t = \overline{E}^{t_j}$ from equation (6.40) is plotted as a bullet. Following equation (6.42) the expected collision energy $\langle E\rangle_{\tau=t}$ is plotted as a function of the detection time t as a solid line. The third graph [(1c), (2c), (3c)] of each row illustrates the standard deviation of the collision energy: $\Delta_{std}E^t = \Delta_{std}E^{t_j}$ (bullets) and $\langle \Delta_{std}E \rangle_{\tau=t}$ (solid line) are plotted versus the detection time t following the equations (6.41) and equation (6.44), respectively. If not explicitly mentioned otherwise, the simulations have been performed until a convergence of $< \pm\ 0.2\ \mathrm{cm}^{-1}$ is achieved.

The first row of Figure 6.4 illustrates one particular experimental setting of a series of measurements, which is depicted in the left graph of Figure 6.3. The scattering properties of the OH-H_2 system in the present setup investigated at this datapoint in greater detail: (1) the experimental conditions are calibrated to ensure conditions of flux-mode (section: 6.3.4), and also relative cross sections are determined here (section 7.4.1). The setting of the beam velocities are $v_{OH} = 271$ m/s and $v_{H_2} = 1320$ m/s, the slit on the H_2 side is 4 mm. The second row shows the analysis of the similar settings of the high collision energy interval. The parameters are $\mathrm{v}_{OH} = 271$ m/s, $\mathrm{v}_{H_2} = 1530$ m/s and the H_2 collimation slit is 4 mm. In the third row simulations for a different series of measurements are depicted, where a different geometry of the *Newton-diagram* is investigated. That experiment aims to explore the OH-H_2 system by increasing the collision energy resolution, which is discussed in greater detail in chapter 8. Settings are chosen, where the longitudinal velocity of $\mathrm{v}_{OH} = 1643$ m/s is faster than $\mathrm{v}_{H_2} = 1151$ m/s. This leads to a shorter OH-TOF. The collimation slit is either 3 mm or 2 mm, because the collision energy resolution is crucially dependent on the transverse velocity distribution on the H_2 side in this different setting.

In graph (1a) of Figure 6.4 the OH-TOF is plotted as black solid line. Three H_2 TOFs are depicted as well, which have relative delays of $+10\mu s$ (blue solid line), $0\mu s$ (green solid line) and $-10\mu s$ (red solid line). Graph (1b) illustrates the evolution of the collision energy as a function of the overlap in time of both E^t and $\langle E \rangle_{\tau=t}$. The simulations of all three delays show a similar behaviour as a function of time, where two general features in the numerical results of the collision energy can be observed:

1. By looking at the evolution of the collision energy at each delay

only, both, E^t and $\langle E\rangle_{\tau=t}$ decrease as a function of time. E^t decreases linearly and faster than $\langle E\rangle_{\tau=t}$. This decrease demonstrates the capability of the model to reproduce the correlation of position and velocity within the molecular packet. The fastest particles in front of the packet scatter first and create higher collision energies as slower ones, which scatter later. E^t decreases on average linearly, which indicates that velocity over the extension of the H_2 packet decreases on average linearly as well. Only at the tails E^t shows a non-linear behaviour, because there only few particles scatter and numerical convergence would have needed more extensive averaging. The decrease of $\langle E\rangle_\tau$ is less linear as a function of time, because earlier scattering products contribute to $\langle E\rangle_\tau$ depending on the number of collisions at each time-step.

2. An offset of about 2 cm^{-1} is significant in the comparison of the simulations of different delays. In the $+10\mu s$-delay (blue) the OH-packet overlaps with the rear part of the H_2-packet, while the OH-packet probes the centre part and the front part in the $0\mu s$-delay (green) and the $-10\mu s$-delay (red), respectively. The horizontal black double arrow in the middle of graph (1b) indicates the $\pm 10\mu s$ delay in time between of the packets in the three series of simulations. Again the correlation of position and velocity in the packets explains this effect, because it shows the faster or slower probed parts of phase-space.

The calibration of the collision energy in the experiment follows from graph (1b), (2b) and (3b). At $t = 0$ the simulated $\langle E\rangle_{\tau=0\mu s}$ corresponds to the collision energy measured in the experiment. For an ideal overlap with no delay (green line) $\langle E\rangle_{\tau=0\mu s} = 100\ \text{cm}^{-1}$ is exemplary indicated by arrow (1) in graph (1b). Arrow (2) points to $\langle E\rangle_{\tau=23\mu s}$. At this time the two packets have overlapped completely. The simulated expected collision energy is 98.7 cm^{-1}. A very similar value is found when equation (6.14) $E_c = 98.45\ \text{cm}^{-1}$ is used. This should be the case, because the complete PSDs have overlapped at that time. The expected values of all the velocities that have scattered at that time, correspond to the mean velocities, which are used in the calculations of equation (6.14). Since the detection happened at $\tau = 0\mu s$, the two models predict a considerable shift in the measured collision energy of 1.5 cm^{-1}. Additionally, a mistake in the triggering caused the valve to open $10\mu s$ later, which delayed the arrival of the H_2 packet. The actual experimental conditions of the measurements are simulated in the case of the $-10\mu s$ delay, which is illustrated by the red solid line. Arrow number (3) indicates $\langle E\rangle_{\tau=0\mu s} = 101.9$ cm^{-1}. This leads to an overall energy shift of 3.55 cm^{-1}!

Similar simulations are done for each datapoint of the series of measurements. The results are shown in Table 6.1, where $\overline{v}_{OH}$ is listed in the first column. The results of $\langle E\rangle_\tau$ and E_c can be compared in the second and third column respectively. At the setting of $v_{OH} = 170$ m/s the energy difference is 4.4 cm^{-1}, while the difference at $v_{OH} = 690$ m/s amounts to 2.5 cm^{-1}. A general trend shows that the values of $\langle E\rangle_\tau$ and E_c deviate more for settings where the v_{OH} is slower in the lab frame compared to v_{H_2}. Due to the slower v_{OH}, the overlapping time with the H_2 packet is longer: $26.5\mu s$ (35 mm in the translational direction) for $v_{OH} = 170$ m/s instead of $6.5\mu s$ (7 mm) for $v_{OH} = 690$ m/s. Thereby a larger spatial part and a larger amount of phase-space is probed. This leads in the case of slower OH velocities to more collisions with faster particles, which increases $\langle E\rangle_\tau$ on average.

In the graph (2b) the settings at the higher collision energy of $\mathrm{v}_{OH} = 271$ m/s, $\mathrm{v}_{H_2} = 1530$ m/s are presented. The results show qualitatively the same behaviour in comparison with the case in graph (1b). Again the simulations of two delays of $0\mu s$ (green data) and $-10\mu s$ (red data) have an offset and show a decrease of E^t and $\langle E\rangle_{\tau=0\mu s}$ as a function of time. However, if the results of the two delays are compared, $\langle E\rangle_{\tau=0\mu s}$ is ≈ 1 cm^{-1}, which is a factor two smaller than in the previous case. Also $\langle E\rangle_{\tau=24\mu s} = 136.4$ cm^{-1}, which deviates from the analytic value of $E_c = 137.3$ cm^{-1}. The simulated value of $\langle E\rangle_{\tau=0\mu s} = 138.3$ cm^{-1}, representing the experimental conditions, is again larger due to the TOF delay. Since the properties of the OH-packet did not change, the difference must result either from the change in the H_2 packet or the different kinematics of the overlap in time. The shorter drift time to the collision zone leads to a less

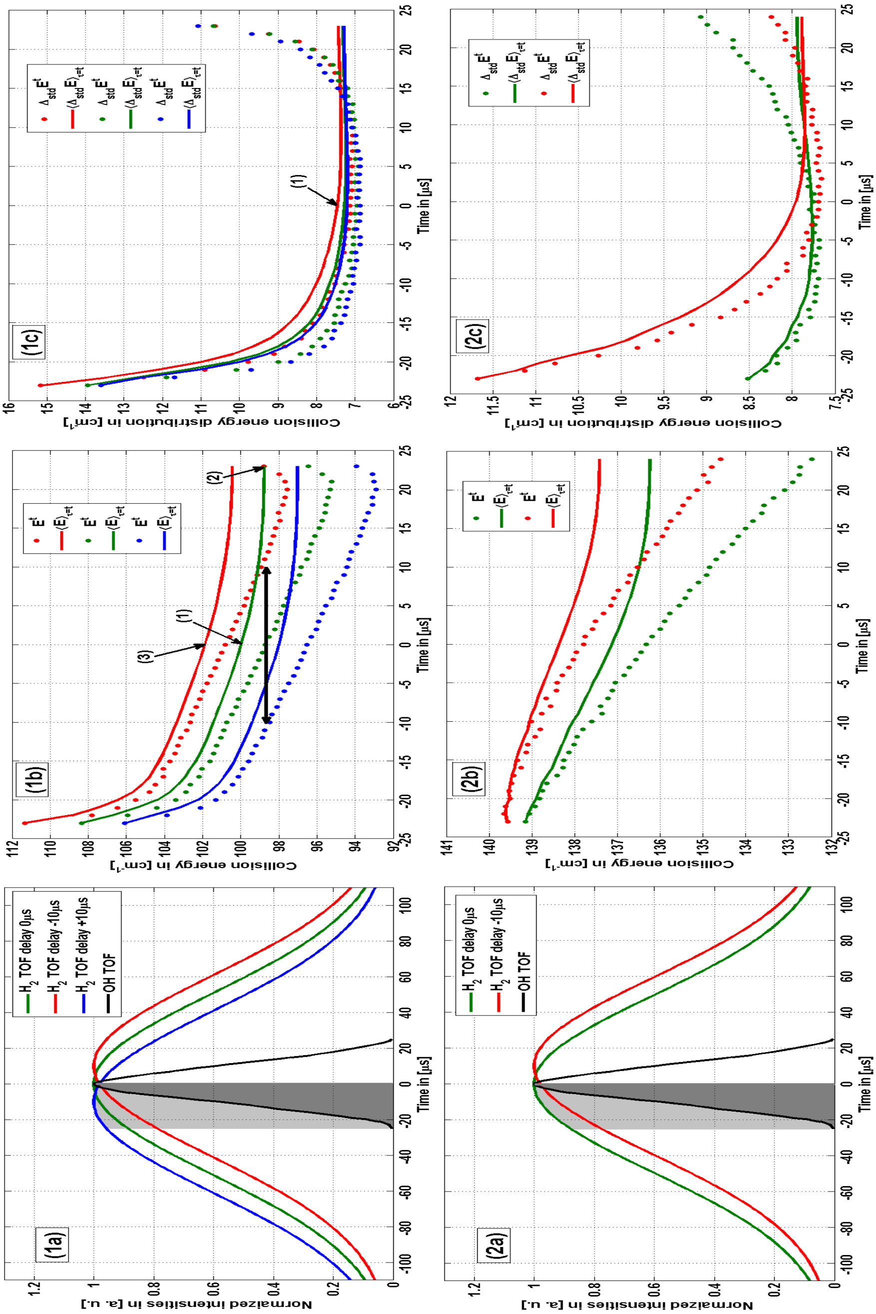
(1a)
H$_2$ TOF delay 0µs
H$_2$ TOF delay -10µs
H$_2$ TOF delay +10µs
OH TOF
Normaized intensities in [a. u.]
Time in [µs]
(1b)
E^t
$\langle E\rangle_{\tau=t}$
(1)
(2)
(3)
Collision energy in [cm^{-1}]
Time in [µs]
(1c)
$\Delta_{std}E^t$
$\langle\Delta_{std}E\rangle_{\tau=t}$
(1)
Collision energy distribution in [cm^{-1}]
Time in [µs]
(2a)
H$_2$ TOF delay 0µs
H$_2$ TOF delay -10µs
OH TOF
Normaized intensities in [a. u.]
Time in [µs]
(2b)
E^t
$\langle E\rangle_{\tau=t}$
Collision energy in [cm^{-1}]
Time in [µs]
(2c)
$\Delta_{std}E^t$
$\langle\Delta_{std}E\rangle_{\tau=t}$
Collision energy distribution in [cm^{-1}]
Time in [µs]

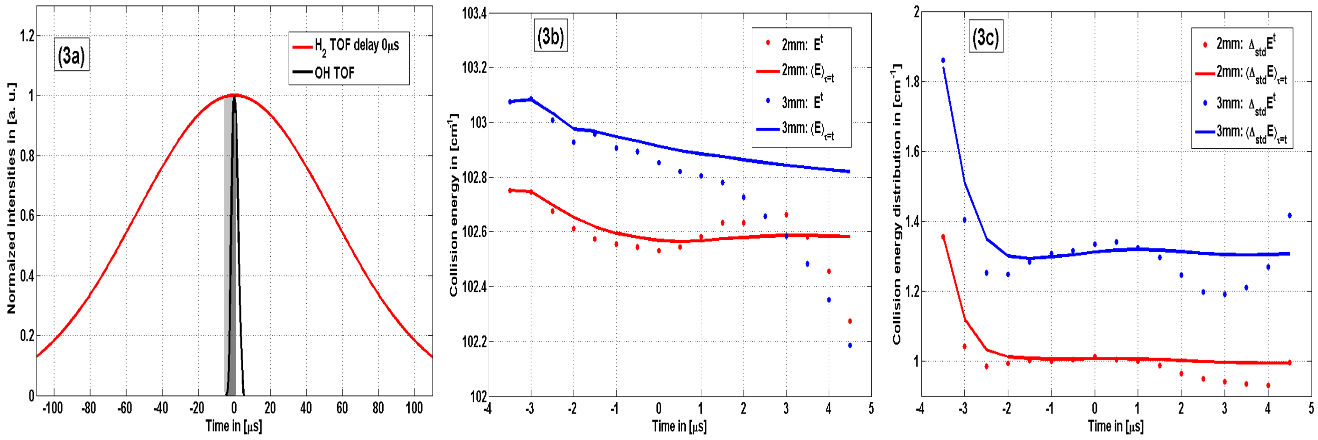

Figure 6.4: Graphs (1a), (2a) and (3a) shows the TOFs of the molecular packets of OH and H_2 for certain relative delays as a function of the detection time t. The TOFs are sometimes delayed in time such that centres of the packets do not overlap. The second column of graphs (1b), (2b) and (3b) shows the mean collision energy $\overline{E}^{t_j}$ (bullets) from equation (6.40) and the expected collision energy $\langle E\rangle_\tau$ (solid lines) from equation (6.42) as a function of the detection time t. The third column of graphs (1c), (2c) and (3c) shows the standard deviation of the collision energy ΔE^t_{std} (bullets) at each time-step and the expected standard deviation of the collision energy $\langle \Delta_{std} E\rangle_\tau$ (solid lines) as a function of detection time t.

distinctive correlation in phase-space. Additionally, the speed ratio (SR) is higher for the $v_{H_2} = 1530$ m/s case (SR$^{1530} = 68.3$ instead of SR$^{1320} = 64.7$), although the velocity distribution is slightly larger ($\sigma_v^{1530} = 22.4$ m/s instead of $\sigma_v^{1320} = 20.6$ m/s). The similar velocity distributions explain, why the linear decrease of E^t as a function of time is about 6.5 cm^{-1} over the OH pulse duration between t = -20 μs and $t = +20 \mu s$ in both cases. The less stringent correlation explains the smaller offset. If there was no correlation at all, the collision energy would not shift as a function of overlap in time. However, the deviation of $\langle E \rangle_{\tau=24\mu s}$ and E_c cannot be explained conclusively.

In columns six and seven of Table 6.1 the results of the simulations are shown for all the experimental settings. The general trend of an increasing deviation between $\langle E \rangle_\tau$ and E_c as a function of decreasing OH velocities cannot be reproduced. In fact a non-uniform shift between 1 cm^{-1} and 3.5 cm^{-1} is observed. Due to the faster v_{H_2}, the overlap is larger and a larger amount of phase-space is probed in general compared to the previous case in graph (1b). Also the transverse velocity distribution that can pass through the skimmer and slit, increases slightly by 15% (from 15.4 m/s of case 1 to 17.85 m/s here). But both of these effects would be in favour to increase the E^t and $\langle E \rangle_{\tau=t}$. Numerically the simulations of the faster v_{H_2} are more demanding, however, they converge within the given limits. As a test of significance the parameters for the velocity distribution σ_v and the trigger pulse duration d_{tpd} are varied by ±10% and ±20%, which led to shifts in the most extreme cases of ±0.2 cm^{-1} and ±0.4 cm^{-1} mainly caused by changes in σ_v. Without more detailed investigations, these small discrepancies remain unexplained.

In the third row simulations of E^t and $\langle E \rangle_{\tau=t}$ are plotted for the experiment to achieve a higher resolution. The beam parameters are set differently such that v_{OH} is larger than v_{H_2}. The temporal overlap of both packets is quite short, which is illustrated in graph (3a). In this series of measurements the overlap was ideal without any delays between the centres of the packets. In graph (3b) the evolution of E^t and $\langle E \rangle_{\tau=t}$ are plotted as a function of the overlap in time. For the simulations of both slit widths E^t and $\langle E \rangle_{\tau=t}$ as a function of time stay constant within

Table 6.1: The different methods to determine the collision energy are compared. The packet properties define the mean velocities of $\overline{v}_{H_2}$ and $\overline{v}_{OH}$. The two H_2 velocities correspond to two broad intervals of collision energies, while the variation of $\overline{v}_{OH}$ allows a more detailed scanning. For each collision energy range, $\langle E\rangle_\tau$ and $\langle \Delta_{std}E\rangle_\tau$, which are determined from the overlap simulations, can be compared to the values of E_c and $\Delta_{std}E$, which are calculated from equations (6.14) and (6.16), respectively.

$\overline{v}_{OH}$	$\overline{v}_{H_2} = 1320$				$\overline{v}_{H_2} = 1530$				$[m/s]$
	$\langle E\rangle_\tau$	E_c	$\langle \Delta_{std}E\rangle_\tau$	$\Delta_{std}E$	$\langle E\rangle_\tau$	E_c	$\langle \Delta_{std}E\rangle_\tau$	$\Delta_{std}E$	$[\text{cm}^{-1}]$
170	113.51	109.11	8.27	10.62	151.44	150.19	8.46	14.46	
189	111.23	106.99	7.98	10.51	148.64	147.65	8.04	14.32	
208	108.98	104.92	7.92	10.39	146.90	145.16	7.84	14.20	
229	106.34	102.69	7.71	10.27	143.85	142.47	7.75	14.05	
249	104.09	100.64	7.53	10.15	141.71	139.98	7.93	13.91	
271	101.90	98.45	7.50	10.02	138.37	137.29	7.96	13.76	
291	99.73	96.52	7.39	9.91	136.81	134.93	8.36	13.62	
316	97.39	94.19	7.25	9.76	134.65	132.05	8.65	13.46	
341	95.14	91.95	7.13	9.61	132.33	129.26	8.89	13.28	
364	92.96	89.98	7.11	9.48	130.01	126.78	9.01	13.13	
390	90.91	87.84	6.99	9.33	127.39	124.07	9.06	12.95	
417	88.66	85.73	6.93	9.18	124.76	121.37	9.06	12.77	
447	86.25	83.52	6.79	9.01	121.77	118.49	8.99	12.57	
478	83.99	81.37	6.65	8.84	118.79	115.66	8.74	12.37	
513	81.65	79.12	6.58	8.65	115.64	112.63	8.66	12.14	
553	79.36	76.77	6.54	8.43	112.41	109.40	8.36	11.88	
595	76.87	74.56	6.36	8.21	109.07	106.27	8.16	11.62	
643	74.72	72.36	6.17	7.96	105.89	103.00	7.79	11.31	
690	73.01	70.53	6.78	7.72	102.88	100.15	7.51	11.03	

the numerical error uncertainty. The OH packet is probing only a very small part of the PSD compared to the cases discussed in graph (1b) and (2b). Nevertheless, an energy shift was also found for the high resolution measurements, which cannot be explained by a delay of the pulses. However, the scattering geometry is extremely sensitive to the scattering angle. A misalignment of the scattering angle of 0.5° already causes a shift in collision energy of ≈ 2 cm^{-1}. The spherical vacuum chamber, where the scattering experiment is taking place (Figure7.1) has been built by the company PINK. The test certificate confirms that a misalignment of up to 2° for the CF100 flanges is possible. Although both molecular beam lines have been aligned optically with a theodolite, displacements of the skimmer, slits, or unequal tightened flanges combine to further inaccuracies in the alignment of both sources. Therefore, the energy shift can only be attributed to a misalignment of 0.5°. If a mean scattering angle of 45.5° is used in the simulations, the results of all experimental settings show that the same values are found for $\langle E\rangle_{\tau=0}$ and E_c.

6.3.4 Calibration of flux-mode conditions

The calibration of the flux-mode is a standard procedure in scattering experiments [107] [47]. It is shown here in detail, because it is a central argument in the discussions of the scattering results in sections 7.4.1 and 8.3.2. To extract a cross section from the experimental data, the measured scattering signal, which is defined in equation (6.38), must be related to the number of created scattering products, given by equation (6.24). The evolution of scattering products as a function of the overlap in time has already been discussed in section 6.2.2. Since the detection method is Laser Induced Fluorescence in this experimental setup, the measured scattering signal at a time t, is directly proportional to those products, which are present in the detection volume of the laser. Depending on the differential cross section of the probed transition or experimental constraints in the detection method, conditions can arise, where some products are not detected. A detailed analysis has to be performed, which is known as number-density to flux transformation [110] [111]. There, a detection probability ($DP(t)$) is simulated, including all experimental properties starting from the product creation as a function of the overlap in time,

Table 6.2

$\overline{v}_{OH}$	$\overline{v}_{H_2} = 1151$							$[m/s]$
	$\langle E\rangle_\tau^{2mm}$	$\langle E\rangle_\tau^{3mm}$	E_c	$\langle \Delta_{std}^{2mm}E\rangle_\tau$	$\langle \Delta_{std}^{3mm}E\rangle_\tau$	$\Delta_{std}^{2mm}E$	$\Delta_{std}^{3mm}E$	[cm^{-1}]
1410	77.92	77.90	77.92	1.29	1.45	1.69	1.88	
1420	78.95	78.79	78.95	1.27	1.45	1.69	1.88	
1430	79.67	79.67	79.80	1.28	1.42	1.70	1.89	
1441	80.96	80.72	80.96	1.25	1.38	1.71	1.90	
1453	81.86	81.86	81.99	1.26	1.39	1.71	1.91	
1467	83.18	83.18	83.18	1.18	1.35	1.72	1.92	
1478	84.63	84.35	84.63	1.19	1.37	1.73	1.93	
1487	85.37	85.33	85.36	1.14	1.34	1.74	1.94	
1497	86.41	86.29	86.42	1.17	1.33	1.74	1.95	
1507	87.47	87.33	87.47	1.15	1.32	1.75	1.96	
1516	88.61	88.32	88.62	1.11	1.35	1.76	1.97	
1525	89.50	89.51	89.61	1.11	1.33	1.77	1.97	
1536	90.29	90.29	91.01	1.06	1.40	1.78	1.99	
1545	91.71	91.43	91.70	1.03	1.32	1.79	2.00	
1553	92.29	92.23	92.30	1.02	1.35	1.79	2.01	
1561	92.78	92.76	93.20	0.94	1.31	1.80	2.01	
1571	94.39	94.31	94.38	0.99	1.33	1.81	2.03	
1580	95.34	95.33	95.32	0.94	1.32	1.82	2.04	
1592	96.69	96.67	97.07	0.98	1.30	1.83	2.05	
1603	98.01	97.97	98.00	0.97	1.32	1.84	2.06	
1613	99.13	99.13	99.20	0.99	1.32	1.86	2.08	
1623	100.50	100.41	100.50	0.98	1.31	1.87	2.09	
1633	101.73	101.65	101.72	0.99	1.32	1.88	2.10	
1643	102.86	102.57	102.86	1.00	1.32	1.89	2.12	

the details of the detection system, and the product distribution depending on the DCS such that the relation holds

$$Sig_{sc}^{E_c}(t) = DP(t) \cdot \langle \bar{N}^f \rangle_{\tau=t}. \tag{6.45}$$

These simulations can be very extensive and time-consuming. Therefore, it is beneficial to ensure conditions of the so-called flux-mode, where DP is unity. To determine the flux-mode conditions for this experiment, a number of things have to be regarded. The intersection volume of the two molecular pulses, where scattering can happen only, is basically defined by the extensions of the small OH packet. A very large laser-spot is used with a diameter of 9 mm to illuminate all products independent of their direction of propagation after the collision. From a kinematic point of view, the OH-H_2 system has big advantage because of the large mass difference between OH and H_2. The direction of propagation of OH radicals is hardly affected in a collision. Also changes in the differential cross section from forward to backward scattering and the resulting Doppler-shifts or Doppler-broadenings due to the various recoil velocities are well covered by the laser bandwidth of 2 GHz. Nevertheless, if the detection with the pulsed laser is performed too late, some products will have escaped from the detection volume. To find the correct timing for the moment of detection, the production of the scattering products was scanned as a function of the overlap in time.

Both graphs in Figure 6.5 show datapoints of increasing scattering signals of different rotational excitations as a function of the detection time. In the left graph, the experimental settings are $v_{OH} = 271$ m/s, $v_{H_2} = 1530$ m/s and the H_2 collimation slit is 4 mm. Three rotational excitations have been recorded, the Λ-doublet changing transition F1(3/2,e) is plotted in black, while the rotational excitation to the F1(5/2,e) and F1(5/2,f) is depicted in red and blue, respectively. The experimental settings shown in the right graph are $v_{OH} = 1643$ m/s, $v_{H_2} = 1151$ m/s and the H_2 collimation slit is 3 mm. Here, only the rotational excitation to the F1(5/2,e) was measured. In all measurements averaging was done until the error bar was $\pm\Delta_{ci}^{(E_c)} \approx 10\%$ of the maximum value.

To ensure that flux-mode conditions are fulfilled, the product creation as a function of time is calculated as well. Instead of using equation (6.28) di-

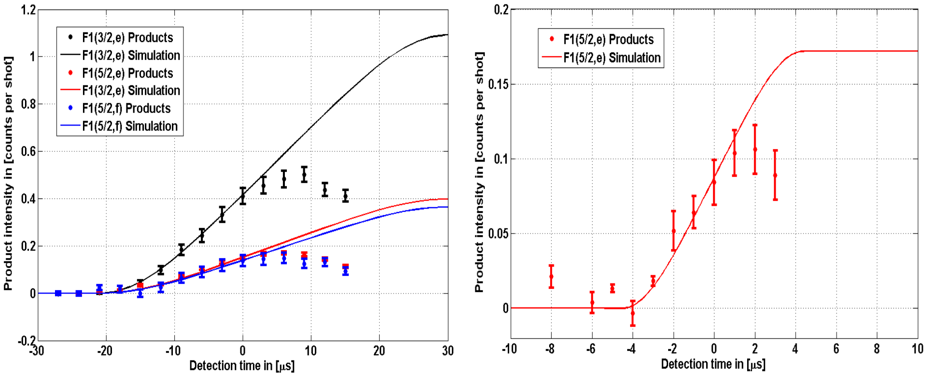

Figure 6.5: The left graph shows the results of the experimental settings of v_{OH} = 271 m/s, v_{H_2} = 1530 m/s and collimation slit-width 4 mm, while in the right graph the results are plotted for the settings of v_{OH} = 1643 m/s, v_{H_2} = 1151 m/s and the H_2 collimation slit is 3 mm. The simulated product creation as a function of the overlap in time is plotted together with the three series of measurements.

rectly, some approximations are made. By looking at graph (1b) of Figure 6.4 the expected collision energy $\langle E\rangle_{\tau=t}$ decreases during the overlapping in time from $\langle E\rangle_{\tau=-20\mu s} \approx 106$ cm^{-1} to $\langle E\rangle_{\tau=15\mu s} \approx 101$ cm^{-1}. In the right graph of Figure 7.2, the theoretical relative cross sections for OH - n-H_2 are plotted as solid lines. They are convoluted to account for the experimental collision energy resolution, which evolves from $\langle \Delta_{std}E\rangle_{\tau=-20\mu s} \approx$ 10 cm^{-1} to $\langle \Delta_{std}E\rangle_{\tau=15\mu s} \approx 7$ cm^{-1}. The convoluted theoretical cross sections show a deviation with $< 10\%$ within the collision energy range probed during the scan of the overlap in time. Also the relative velocity is deviating in this energy range with $< 3\%$. Therefore, the cross section $(\sigma_f(\overline{v_{rel}}))$ and the relative velocity $(\overline{v_{rel}})$ are assumed to be constant in these simulations. To evaluate $\langle N^f\rangle_{\tau=t}$ of equation (6.28) instead, the spatial number-density distribution $n^r_{OH/H_2}(\underline{\mathrm{r}}_{OH/H_2}, t)$ of both molecular packets are approximated by Gaussian functions in the longitudinal and transverse directions. The H_2 beam is described in the longitudinal direction by equation (3.5) with the fitted parameters from Table 3.1. In the transverse direction the slit width determines the spatial extension of the

H_2 packet. The OH packet is approximated by fitting the numerical trajectory simulations of the Stark-decelerator of all three dimensions. Since the absolute number-densities are not determined, the relation (6.46) at a certain time of detection τ can only be given as a proportionality of

$$Sig_f^{(E_c)}(\tau) \propto DP_f^{(E_c)}(\tau) \cdot \langle N_f^{(E_c)} \rangle_\tau = DP^{(E_c)}(\tau) \cdot \mathit{\Gamma}_f \cdot \overline{v_{rel}} \cdot \sigma_f(\overline{v_{rel}}) \times$$

$$\int_{-\infty}^{t=\tau} \int_{3D} \int_{3D} \delta_{\underline{\mathrm{r}}_{OH}\underline{\mathrm{r}}_{H_2}} n_{OH}^{r}(\underline{\mathrm{r}}_{OH}, t) \cdot n_{H_2}^{r}(\underline{\mathrm{r}}_{H_2}, t) d^3\underline{\mathrm{r}}_{OH} d^3\underline{\mathrm{r}}_{H_2} dt. \tag{6.46}$$

In both graphs of Figure 6.5, the results of $\langle N_f^{(E_c)} \rangle_{\tau=t}$ are plotted as a function of time. The intensity is scaled with a constant factor to fit the experimental data of the different final states. The experimental data follow the simulation of $\langle N_f^{(E_c)} \rangle_{\tau=t}$ very well, starting from $t = -20\mu s$ up to $t = 0\mu s$ in the left graph and from $t = -4\mu s$ up to $t = 0\mu s$ in the right graph. Up to $t = 0\mu s$ this agreement demonstrates the conditions of flux-mode, with $DP_f^{(E_c)} = 1$. After $t = 0\mu s$ the experimental signals deviate from the simulations indicating that some products have left the detection volume already. The timing at $t = 0\mu s$ is chosen as the moment of detection in the experiment and coincides with the centre of the OH TOFs as shown in graphs (1a), (2a) and (3a) of Figure 6.4. The two extreme cases within the experimental settings are investigated here, to ensure the flux-mode conditions are achieved. In the case of the left graph, the molecules scattered into the F1(3/2,e) channel have the largest recoil velocities $\underline{\mathrm{v}}'_{rel}$ compared to other inelastic channels and the spatial dimensions of the OH packet packet are the largest. In the right graph the F1(5/2,e) channel with largest collision energy is investigated, where the OH radicals have the largest recoil velocities $\underline{\mathrm{v}}'_{rel}$. In both cases the simulations reproduce the measurements rather well. The LIF detection throughout the experiments presented here, are performed under flux-mode conditions. Therefore, no number-density to flux transformation is required.

		e				*f*			
F	J	**LT**	Γ_f	E_{rot}	P	**LT**	Γ_f	E_{rot}	P
F1	$\frac{3}{2}$	P_1	$\frac{1}{3}$	-0.055	$-$	$Q_1 + Q_{21}$	$\frac{3}{5}$	0.000	$+$
	$\frac{5}{2}$	P_1	$\frac{2}{5}$	83.668	$+$	Q_1	$\frac{1}{2}$	83.869	$-$
F2	$\frac{1}{2}$	$Q_1 + Q_{21}$	$\frac{3}{4}$	126.241	$+$	P_{12}	$\frac{1}{2}$	126.398	$-$

Table 6.3: Parameters and properties of the OH radical are summarized, which are relevant for the experiment. The spin-orbit manifold and the rotational state are indicated in the first and second column, respectively. In columns 3-5 and 6-8, the laser transition (**LT**) within the (A $^2\Sigma^+$, v' $= 1 \leftarrow$ X $^2\Pi_{3/2}$, v $= 0$) band, the excitation rates and excitation energy of the rotational threshold E_{rot} for each Λ doublet substate is listed.

6.4 Conclusion

The improvement of experimental techniques has pushed the accuracy and the control of measurable parameters to a point, where underlying properties of the PSDs show a profound influence on the signals. Consequently, a more detailed description of the phase-space dynamics is indispensable to accurately identify the actual contributions to the measured quantities. Firstly, a general model is presented to determine the evolution of experimental parameters as a function of the overlap in time of two 6D PSDs modeling the molecular beams. Secondly, the numerical implementation, which accounts for the constraints of the experimental setup, precisely describes the evolution of the scattering signals. The numerical results are essential for the calibration of the collision energy and the collision energy distribution. These investigations show the sensitivity available in modern cross beam scattering experiments and the need for a qualitative and quantitative description.

Chapter 7

State-to-state inelastic scattering of OH and hydrogen

7.1 Introduction

A detailed understanding of the dynamics of particles in the gas phase is of fundamental importance to many areas of physics and chemistry [10]. Inelastic collisions are mainly responsible for the energy transfer in gases to establish a thermodynamic equilibrium. Thermalisation phenomena such as heat transfer in the atmosphere or the re-distribution of energy after a chemical reaction are due to inelastic collisions. On the other hand, inelastic collisions are also responsible for non-equilibrium phenomena. The cooling of individual degrees of freedom during a adiabatic expansion is one example. In interstellar space, inelastic collisions are made responsible for non-thermal population distributions that lead to maser activity. Especially, OH - H_2 collisions are supposed to be the precursor for the OH maser activity [115].

Reactive collisions are the heart of chemical reactions. The reaction of $\cdot OH + H_2 \rightleftharpoons H_2O + \cdot H$ is of main interest, because it is a crucial step within the benchmark chain reaction of oxygen and hydrogen forming water. Many distinct properties can be studied in this part of the chain reaction: the reaction has a barrier of 26.05 kJ/mol (2178 cm^{-1} or 0.27 eV), which is needed to activate the reaction, although OH is a radical. Here the entrance channel is important to investigate how the activation of the reaction works [116]. The process of oxidation is not only one of the most fundamental chemical processes, oxidation of particles in the atmosphere by OH radicals is ubiquitous [117]. For the study and the modeling of the dynamics in combustion or oxidation processes in bulk systems, both reactive and inelastic collisions are of utmost significance.

To study collisions between individual particles, such as atoms and molecules, the crossed molecular beam technique is one of the most commonly used experimental methods. In the 1950's this technique has been introduced for the first time and it has been advanced and refined ever since. The quest of gaining more control over internal and external degrees of freedom of the particles before and during the collision process, as well as the observation of the dynamics at any time, has been a driving force to develop further experimental and theoretical methods. The collision energy is one of the most crucial parameters in a collision experiment, therefore, it has always been of great interest to be able to control, to vary and to define the collision energy better. With the advent of laser-based radiation sources more powerful detection and manipulation techniques have been invented to determine the products' state-, angular- and energy-distributions.

Nowadays a large variety of sophisticated techniques have been refined to tune the mean velocities of the particles prior to collision, to produce narrower velocity spreads [20] and to select internal quantum states [3]. These advances made it possible, for instance, to resolve the threshold behaviour of rotational energy transfer [118][66], or to increase the collision energy to overcome the reaction barrier for reactive scattering [119][120]. Narrower velocity distributions lead to smaller collision energy distributions, which made it possible to observe quantum mechanical phenomena such as resonances [121] [122] [16] [15] in the integral cross sections or diffraction oscillations in the differential cross section [23].

Hand in hand with the experimental progress also the theoretical modeling proceeded to accurately describe the processes governing scattering dynamics. Nowadays scattering cross sections of molecules with structureless particles like rare-gas atoms can be calculated in extremely good agreement with the available experimental data. This represents the current state-of-the-art understanding of molecular dynamics at the quantum mechanical level. However, to model molecule-molecule interactions the complexity increases a lot due to the fact that additional internal and external degrees of freedom come into play. Including higher order multipole-interactions and the different couplings bring out the challenge for *ab initio* quantum scattering calculations. Additionally to this general complexity the OH-H_2 system adds an extra level of complexity, because OH is an open-shell molecule.

Since the observation of maser activity, especially the OH-maser and the pumping mechanism have been of special interest for the astrophysics community. The first experimental investigations on OH - H_2 collisions were performed by Andresen and coworkers [123], who determined collision cross sections for inelastic excitations out of the rotational ground state ($X^2\Pi_{3/2}$, J=3/2) with equally populated Λ-doublet substates e and f. They discovered a clear preference to populate the lower Λ-doublet state within the $^2\Pi_{3/2}$ manifold, while it is more likely to populate the upper Λ-doublet states in spin-orbit changing excitations to the $^2\Pi_{1/2}$ manifold. This encouraged many theoreticians to calculate cross sections for inelastic processes between rotational, Λ-doublet, and fine structure states [124] [125] [126].

Schreel and ter Meulen conducted a more detailed experiment by investigating the inelastic scattering processes with the crossed molecular beam method [118]. Measurements were carried out between OH radicals colliding with normal-H_2 or para-H_2 at a collision energy of 600 cm^{-1}. All energetically available rotational and Λ-doublet states of both spin-orbit manifolds could be resolved. Careful quantum-state selection of the OH radicals using a hexapole state-selector and spectroscopic analysis of the population distributions of the H_2 beam turned out to be essential for a quantitative comparison with theoretical cross sections. Schreel and ter Meulen compared their measured cross sections to theoretical ones [118] and found the best agreement with the cross sections determined from the potential of Offer and van Hemert [127] [128]. Compared to previous potentials [129] [130], these were the first theoretical investigations that took rotational states higher than J=0 and J=1 of the H_2 molecule into account and that considered out-of-plane configurations. This analysis showed the large influence of higher rotational states of both OH and H_2 on the collision cross sections. The overall agreement of the calculated cross sections of the various *ab initio* potentials showed similar trends. Compared to the experiment, excitations within the same spin-orbit manifold ($^2\Pi_{3/2} \rightarrow ^2\Pi_{3/2}$) agreed better than spin-orbit changing transitions ($^2\Pi_{3/2} \rightarrow ^2\Pi_{1/2}$). If the Λ-doublet cross sections of Schreel and ter Meulen were averaged [118], they showed similar behaviour to the findings of Andresen and coworkers [123]. However, the cross sections between OH and H_2 showed in general a preferential population of the lower Λ-doublet states for excitations in both spin-orbit manifolds, which did not favour a population inversion that could lead to OH maser activity. Further differences remained between theory and experiment, which were asserted to parts of the *ab initio* potential, the procedure to determine the inelastic scattering cross sections, and/or experimental uncertainties (see [118] and [130]).

Within the scope of this thesis, further investigations are undertaken to unravel the still open questions of the OH-H_2 system. Two different experimental approaches are used and compared in a combined experimental and theoretical effort. This chapter contains a set of experiments, where quantum state-to-state resolved inelastic cross sections for Λ-doublet, rotational and spin-orbit changing transitions are determined as a function of the collision energy for the first time. In a second experimental investigation, which is described in the following chapter, the collision energy distribution was decreased such that structures in the integral cross section are resolved, which lie around the threshold of a distinct rotational inelastic transition. Absolute integral cross sections are calculated from a new *ab initio* PES. Comparison between theory and experiment is shown in terms of excitation functions, relative cross sections and ratios of signal-intensities, which identify and characterize the ongoing dynamics in unprecedented detail. Throughout the experimental studies, the influence of kinematic effects on cross beam scattering is described, which have their origin in the beam dynamics of the interacting molecular packets.

7.2 Experimental setup and method

In order to perform a crossed beam scattering experiment, the experimental setup that has been used in previous experiments [107] is modified. Additionally to the already existing Stark-decelerator a second beam source is installed, where an Even-Lavie valve is mounted on top of a helium cryostat. A schematic overview of the experimental setup is shown in Figure 7.1. Details of the production method, the Stark-manipulation and the detection of OH radicals have already been explained in great detail in [57]. In this section only those parts are recapitulated that are relevant for the scattering experiments.

After leaving the Stark-decelerator, OH molecules in the low-field seeking quantum state (X $^2\Pi_{3/2}$, v = 0, J = 3/2, f) enter the detection chamber by flying through an aperture, which shields not only the detection zone from any kind of residual electric field of the Stark-decelerator but also serves as a differential pumping stage. The OH packet overlaps with the target beam of H_2 molecules at a distance of 61 mm behind the last stage of the decelerator. The crossing angle of the two beams is 45°. The target beam packets are produced with a commercial Even-Lavie valve, which is mounted on top of a helium-cryostat. The temperature of the valve can be stabilized in principle at any value between 10 K and 300 K. Since the boiling point of H_2 is around 20 K the valve has never been cooled down further than 40 K, in order to avoid clustering in the beam or any kind of mechanical clogging of the nozzle. Within this temperature range velocities between 950 m/s and 2500 m/s are accessible. Tests have shown that the supersonic expansion of H_2 molecules is completed 150 mm downstream, where a 50 mm long conical skimmer of 3 mm diameter is mounted as a differential pumping stage. The intersection volume of the two beams is 300 mm further downstream of the skimmer. In order to collimate the target beam in the transverse direction a slit of adjustable width (slitwidths: 5, 4, 3, 2, 1, and 0.5 mm) is installed 60 mm in front of the interaction volume. A Fast Ion Gage (FIG, B-451 Fast Ion Gage Tube from Jordan TOF Products, Inc.) is used to characterize target beam properties such as arrival time and pulse duration from time of flight measurements. It is mounted on a translation-stage feed-trough, which enables measurements

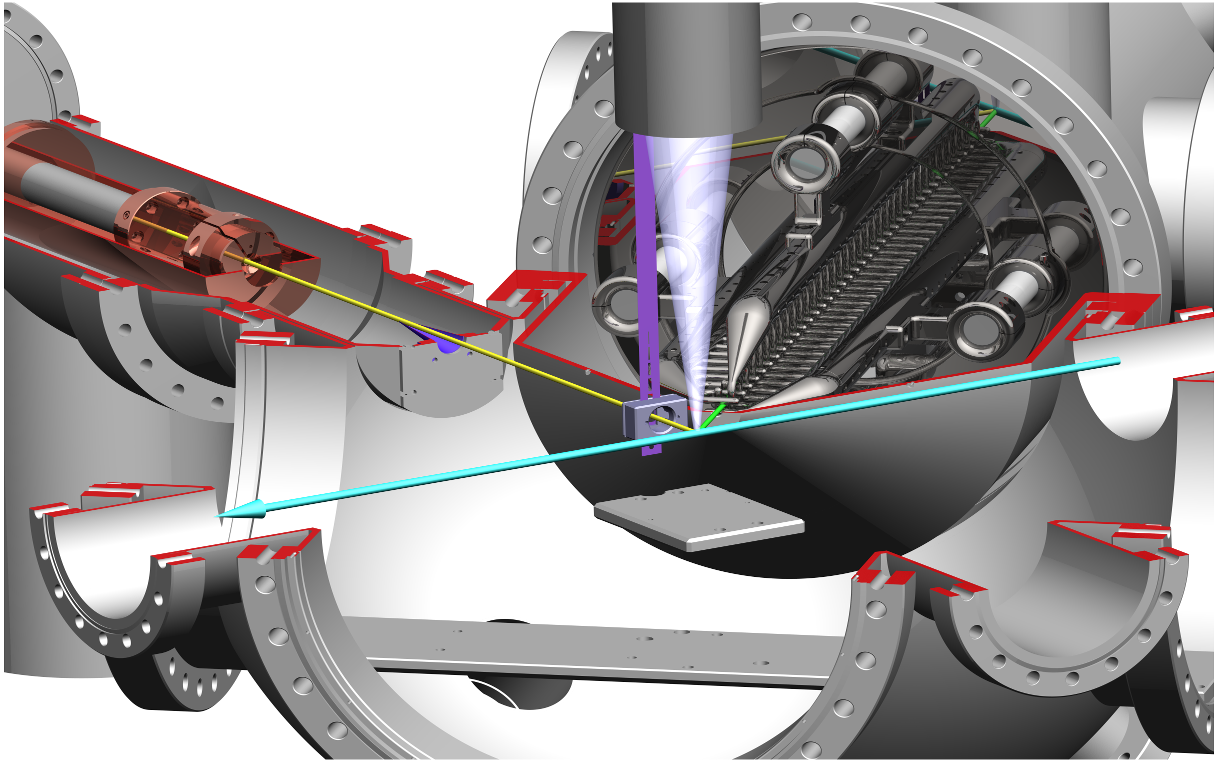

Figure 7.1: The 3D drawing shows the experimental setup with the collision zone in the centre, where the OH packet out of the Stark-decelerator(green arrow) crosses the H_2 packet from the Even-Lavie valve, which is mounted on top of the helium cryostat (yellow arrow). Scattering products are probed with the laser beam intersecting in the collision zone (blue arrow).

with the same detector at various positions downstream of the collimation slit. A caliper ruler on the feedthrough enables the exact re-positioning within ± 10 μm. Throughout the experiment always two positions are used to perform TOF measurements: one at the intersection point and one 900 mm further downstream. A more detailed characterization and description of the target beam is given in section 3.1.2.

The OH radicals are finally detected via laser induced fluorescence (LIF). The laser beam intersects horizontally under a 45° angle with the OH beam and 90° to the H_2 beam. Transitions are induced on the A $^2\Sigma^+$, v' = 1 ← X $^2\Pi_{3/2}$, v = 0 band around 282 nm band. Fluorescence photons on the A $^2\Sigma^+$, v' = 1 → X $^2\Pi_{3/2}$, v = 1 band around 314 nm are collected vertically at 90° (from the top) by a lens and collimated on a photomultiplier tube (PMT). The diameter of the laser is approximately 9 mm. Special care is taken to ensure that the whole OH packet is illuminated. The laser power is sufficiently high to measure under saturation conditions. Stray light - mainly resulting from the laser radiation - is effectively reduced by light baffles and by optical filtering in front of the PMT.

7.3 Theory

Parallel to the experimental investigations of the OH-H_2 system a collaboration with two theoretical research groups has been initiated. One group is located at the University of Maryland in the United States of America [131]. A second group is located at Radboud Universiteit Nijmegen, the Netherlands [132]. A new state-of-the-art PES for the OH-H_2 system has been developed [133]. Scattering calculations are performed independently in both research groups with mutually different scattering codes. Practically the same absolute integral cross sections have been computed based on the new PES. In the following a short summary is given of the theoretical investigations, based on the correspondence within this collaboration:

PES: Two new *ab initio* PESs have been created using two different methods. First, the correlated coupled cluster method [RCCSD(T)-F12a] is used. However, the RCCSD(T) calculations face the challenge that only

OH-H_2 orientations of plane symmetry can be sampled. To estimate possible deficiencies, which are caused by sampling only the high-symmetry points, a PES with the interaction energies of high-symmetry orientations is calculated with the multi-reference configuration interaction method [MRCISD+Q(Davidson)]. The RCCSD(T) method is used in the first place, because it is expected to be more accurate than MRCI calculations. Both PESs are fit to an analytical form such that scattering and bound state calculations can be performed. The dissociation energy of the OH-oH_2(J=1) van der Waal's complexes is calculated to be D_0 = 53.7 cm^{-1}, which is in excellent agreement with the experimental value of 54 cm^{-1}. The value D_0 = 36.1 cm^{-1} is found for the OH-pH_2(J=0) complex.

Scattering calculations: Two mutually different scattering codes are used to calculate absolute integral cross sections. The US group uses the well established HIBRIDON [134] code, while the Nijmegen group uses a differently implemented code. The results from both codes are practically the same. Comparison of the absolute integral cross sections resulting from the differently modeled PESs are found to be almost identical. Additionally, the RCCSD(T) PES is computed once with the equilibrium and once with the vibrationally averaged bond length of H_2. The resulting cross sections are almost identical too. Based on previous experiences on collisions of OH with rare-gas atoms, the stretching of OH is not expected to have a significant influence on the cross sections. These self-consistent results strongly suggest the PES from the rigid rotor RCCSD(T) calculations to be the most accurate one. Absolute integral cross sections for the inelastic transitions out of the initial state F1(J=3/2,f) into all energetically available final states have been calculated for the collision energy range between 60 and 150 cm^{-1}.

7.4 Results and discussion

In the following the theoretical absolute integral cross sections are compared with experimental data. Three different comparisons are presented to deduce various different properties of OH radicals colliding with nH_2 or pcH_2. Very distinct behaviour is observed, firstly when relative cross sections are evaluated and compared. Differences in the inelastic excitation to final states is discussed. Secondly, the signal intensities of the experiment are compared to the intensities of the absolute integral cross sections, which allows quantitative insights into the strength of different multipole-interactions. At last, comparisons are made to related scattering systems.

7.4.1 State-to-state relative inelastic cross sections of OH scattering with nH_2 or pcH_2

Equation (6.46) is used to compare the theoretical absolute integral cross sections with experimental data. Since the number-densities of the molecular beams are not determined, the theoretical and experimental data are evaluated such that the knowledge on the number-densities is dispensable. Relative cross sections are determined, where the raw signals of different final rotational states (see Figure 6.3) are divided by the excitation rates ($\mathit{\Gamma}_f$) to account for the different spectroscopic transitions used, which are listed in Table 6.3. At each particular collision energy $\langle E\rangle_\tau$, all quantities in equation (6.46) stay the same apart from the cross section $\sigma_f^{(\langle E\rangle_\tau)}$ and the measured signal $SIG_f^{(\langle E\rangle_\tau)}/\mathit{\Gamma}_f$. Therefore, the fraction of an individual final state is compared to the sum over all final states:

$$\frac{SIG_f^{(\langle E\rangle_\tau)}/\mathit{\Gamma}_f}{\sum_f SIG_f^{(\langle E\rangle_\tau)}/\mathit{\Gamma}_f} \quad = \quad \frac{\sigma_f^{(\langle E\rangle_\tau)}}{\sum_f \sigma_f^{(\langle E\rangle_\tau)}}. \tag{7.1}$$

Relative cross sections are determined within two energy ranges, where the valve is stabilized at T = 82 K and T = 107 K. The two collision energy intervals overlap between 100 cm^{-1} and 110 cm^{-1}, where data points of both intervals fit very well within the error-bars. Plotted as a function of the collision energy, the trends of the individual excited states of the relative cross sections continue. In section 3.1.2, the spectroscopic investigations revealed the rotational population distribution after the supersonic expansion of pcH_2 and nH_2, where the first excited rotational J=2 level is populated a little in the pcH_2 beam. Theoretically calculated absolute integral cross sections of OH-H_2(J=2) show similar absolute values compared to OH-H_2(J=1), which are on average three times larger than the cross sections of OH-H_2(J=0). If the amount of H_2(J=2) was non-negligible, it would have led to a different behaviour in the relative cross sections. Based on this and the calculations of the Boltzmann distributions, it can be concluded that the contributions of scattering of OH-H_2(J=2) to the signals can be neglected in these scattering experiments. In Figure 7.2 the results of OH radicals colliding with nH_2 and pcH_2 are plotted against the calibrated collision energy $\langle E \rangle_T$ in the left and right graphs, respectively. The experimental datapoints are plotted with an error bar, which is determined by the standard error of the mean $\pm\Delta_{ci}^{(\langle E \rangle_T)}$ defined in equation (6.39).

A weighted mean is calculated using the theoretical cross section of OH-H_2(J=0) (hereafter referred to as $\sigma_{(J=0)}$) or OH-H_2(J=1) ($\sigma_{(J=1)}$) to represent the experimental conditions of nH_2 ($0.25\ \sigma_{(J=0)}+0.75\ \sigma_{(J=1)}$) and pc$H_2$ ($0.99\ \sigma_{(J=0)}+0.01\ \sigma_{(J=1)}$). In Table 6.1 the values of the collision energy distribution $\langle \Delta_{std} E \rangle_T$ increase with increasing collision energy. The theoretical relative cross sections are convoluted with a Gaussian-distributed energy resolution of $\langle \Delta_{FWHM} E \rangle_T = 2.35 \cdot \langle \Delta_{std} E \rangle_T$, which is plotted by solid curves in the colours corresponding to its final rotational state. $\langle \Delta_{FWHM} E \rangle_T$ increases from 14.5 cm^{-1} to 19.4 cm^{-1} in the first interval of measurements between 73 cm^{-1} and 113 cm^{-1}. An average resolution of 17 cm^{-1} is used in the convolution. Similarly $\langle \Delta_{FWHM} E \rangle_T$ varies from 17.6 cm^{-1} to 21.2 cm^{-1} in the second interval, where an average resolution of 19.4 cm^{-1} is used in the convolution. The colour code indicates the different inelastic transitions, which are schematically illustrated in the right graph of Figure 6.3: F1(3/2,e) is black, F1(5/2,e) is red, F1(5/2,f) is blue, F2(1/2,e) is green and the F2(1/2,f) is pink.

Figure 7.2 illustrates the results of OH colliding with nH_2 and pcH_2. The upper two graphs illustrate the results of OH radicals colliding with nH_2, while the lower two graphs illustrate the results of OH radicals colliding with pcH_2. The two left graphs show all rotationally inelastic channels, while the right graphs show the weaker channels on an expanded vertical scale. Qualitatively, two main conclusions can directly be made:

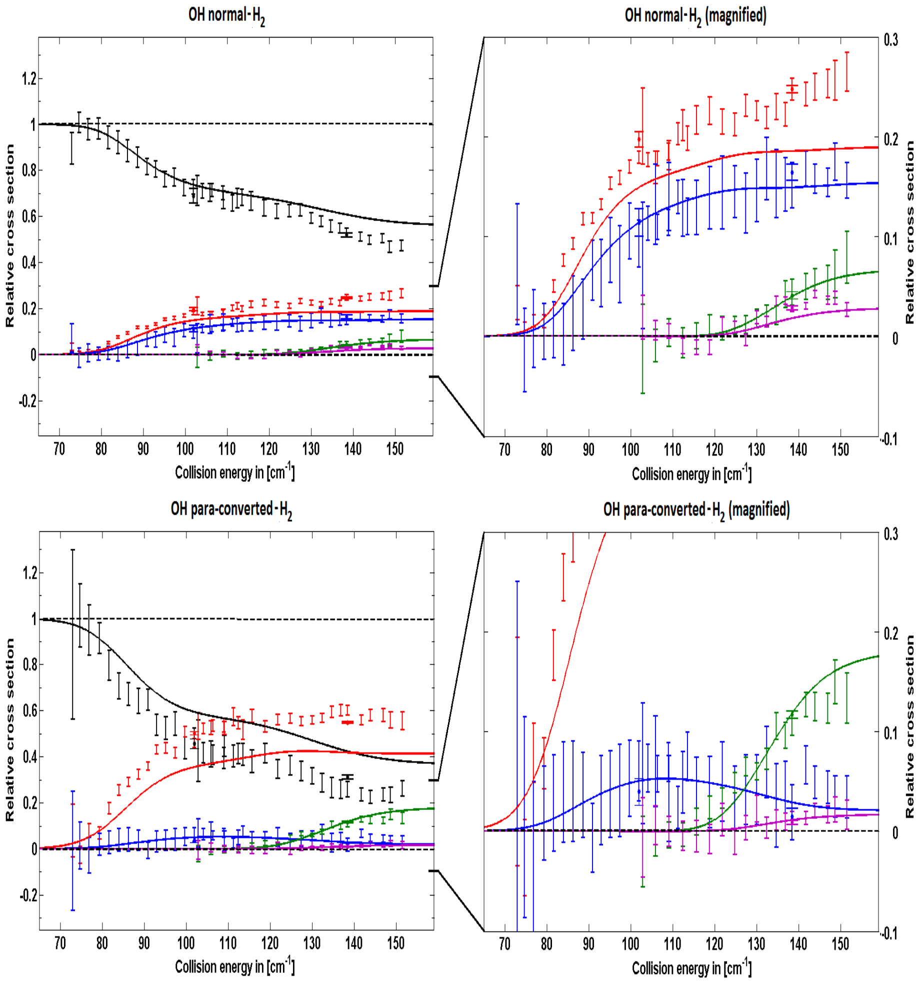

Figure 7.2: The results of theoretical and experimental relative cross sections are compared. The upper and lower two graphs illustrate the results of OH radicals colliding with nH_2 and pcH_2, respectively. The two left graphs show all rotationally inelastic channels, while the right graphs show the weaker channels on an expanded vertical scale. The colour code is identical to the schematic drawing in the right graph of Figure 6.3, which illustrates the different inelastic transitions: F1(3/2,e) is black, F1(5/2,e) is red, F1(5/2,f) is blue, F2(1/2,e) is green, and F2(1/2,f) is pink.

1. The relative cross sections behave totally different, if the H_2 target is exchanged. This demonstrates that the underlying scattering dynamics change significantly.

2. The theoretically calculated relative cross sections agree very well with the experimental ones in both, the normal and the para-converted cases. The rotational thresholds are clearly resolved in the experiment. The qualitative behaviour of the relative cross sections as a function of $\langle E \rangle_T$ are reproduced correctly in theory and experiment within the investigated collision energy range: especially the F1(3/2,e) channels for both H_2 beams show a step-like decrease in the relative cross sections towards higher collision energies. In the OH-pcH_2 case, the relative cross sections of F1(5/2,f) show an increase between the threshold and $\langle E \rangle_T \approx 110$ cm^{-1} followed by a decrease towards higher collision energies.

A more detailed investigation reveals that in the OH-pcH_2 case, shown in the right graph, the excitation to F1(5/2,e) is far more probable than the excitation to F1(5/2,f). The F1(5/2,e) even becomes the dominating channel at higher collision energies. A similar trend is observed for the spin-orbit changing transitions, where F2(1/2,e) shows a larger probability to be excited than F2(1/2,f). These clear propensities to populate certain final states are also observed in the collision of OH with rare gas targets [135]. This behaviour is explained by looking at the properties of the pcH_2 target. From the spectroscopic investigations in section 3.1.2 it is known that 99 % of the colliding H_2 molecules populate the lowest rotational J=0 level after the supersonic expansion. There, electric multipole moments average to zero and H_2(J=0) behaves like a spherical, structureless particle. The interaction between the collision partners OH and H_2(J=0) is of dipole-(induced)dipole character. This interaction induces preferentially parity-conserving transitions like the [F1(3/2,f,+) → F1(5/2,e,+)] or [F1(3/2,f,+) → F2(1/2,e,+)] rather than partity-changing ones like [(F1(3/2,f,+) → F1(5/2,f,-)] or [F1(3/2,f,+) → F2(1/2,f,-)]. Further similarities to other systems, where OH scatters with different targets, are discussed in section 7.4.4.

If nH_2 is the target beam, the Λ-doublet changing transition to F1(3/2,e) is the most probable one at all collision energies studied in this experiment. It is three times more probable than the first rotational excitations to F1(5/2,e) and F1(5/2,f) and roughly seven times more probable than the spin-orbit changing transitions to F2(1/2,e) and F2(1/2,f). Compared to the OH-pcH_2 scattering no large propensities are observed. The excitation to the final states F1(5/2,e) and F2(1/2,e), is in both cases slightly more probable than the excitation to F1(5/2,f) and F2(1/2,f), respectively. This is attributed to the contribution of the 25% of para-H_2(J=0), where the large propensity for parity-conserving transitions rules the OH-H_2(J=0) interactions. The rotational state distribution of H_2 is known in the collision zone. After the supersonic expansion 75% of molecules in the ortho-configuration end up in the J=1, while the 25% of para-H_2 end up in the J=0. In H_2 rotational states greater than zero have higher order multipole moments like quadrupole or hexadecapole moments. This leads to additional interactions in the scattering process. In OH-H_2(J=1) collisions, the OH-dipole - H_2-quadrupole and the OH-quadrupole - H_2-quadrupole interactions cause inelastic transitions, where especially the dipole-quadrupole interaction induces a parity change [136].

7.4.2 Relative cross sections for OH with para-H_2(J=0) or ortho-H_2(J=1)

If one compares theory and experiment in greater detail in both graphs of Figure 7.2, the relative cross sections are seen to deviate the most for the F1(5/2,e) channel. For both H_2 target beams, theory predicts systematically ≈20% smaller values for the excitation to the F1(5/2,e) level than those found in the experiment. Due to the complexity and the variety of interactions, it seems impossible to isolate the origin of this discrepancy. However, the influence of different interactions can be investigated further by using the knowledge of the different signal intensities due to the difference mixtures of oH_2 and pH_2 in the target beams. When OH is scattered with nH_2 the signal intensity (SIG_{nH_2} is larger than the scattering with pcH_2 (SIG_{pcH_2}). To disentangle the contributions in the signal of OH-H_2(J=0) (hereafter referred to by $SIG_{H_2(J=0)}$) from OH-H_2(J=1)

($SIG_{H_2(J=1)}$), the measured signals are related to the ortho-to-para ratios in the two corresponding H_2 mixtures.

$$SIG_{nH_2}^{(\langle E\rangle_\tau)} = 0.25 \cdot SIG_{H_2(J=0)}^{(\langle E\rangle_\tau)} + 0.75 \cdot SIG_{H_2(J=1)}^{(\langle E\rangle_\tau)} \tag{7.2}$$

$$SIG_{pcH_2}^{(\langle E\rangle_\tau)} = 0.99 \cdot SIG_{H_2(J=0)}^{(\langle E\rangle_\tau)} + 0.01 \cdot SIG_{H_2(J=1)}^{(\langle E\rangle_\tau)} \tag{7.3}$$

This approach depends on the assumption that all parameters in equation (6.46) stay the same at each $\langle E\rangle_\tau$ for each final state apart from the cross section $\sigma_f(\overline{v_{\langle E\rangle_\tau}})$. If the H_2 mixture is exchanged from nH_2 to pcH_2 the number-density of the H_2 packet $n^r_{H_2}(\underline{\mathrm{r}}_{H_2}, t')$ could change. It was impossible to measure the absolute number-density of the H_2 beam in this setup. However, there are strong indications to assume that the number-density is the same for both H_2 mixtures. The experimental parameters of the H_2 valve (the temperature, the trigger pulse duration and the stagnation pressure) are kept the same, when exchanging the H_2 mixtures. According to the ideal gas equation the number-density in the valve should stay the same. The background pressure of the source chamber is constant within the usual fluctuations during the measurements. The strongest argument, nevertheless, is illustrated in the left and the central graph of Figure 3.3, where the TOFs of the expanded nH_2 and pcH_2 packets are compared. The intensities are the same within the noise and there is no indication that H_2(J=0) should be differently ionized by the FIG than H_2(J=1). Equally important is the same temporal pulse shape of both samples for the overlap in time.

Relative cross sections are calculated from the disentangled signals of $SIG_{H_2(J=0)}$ and $SIG_{H_2(J=1)}$ using the relation (7.1). In Figure 7.3, the relative cross sections of OH-H_2(J=1) and OH-H_2(J=0) are plotted together with the convoluted theoretical ones in the left and right graphs, respectively. In the case of OH-H_2(J=1) scattering the agreement between theory and experiment is excellent. The datapoints reproduce the theoretical relative cross sections within the experimental error bar for all final rotational inelastic transitions. Only towards higher collision energies small deviations are observed.

In the lower graphs the results of OH-H_2(J=0) are compared. The agreement between theory and experiment is good, although not as excellent as

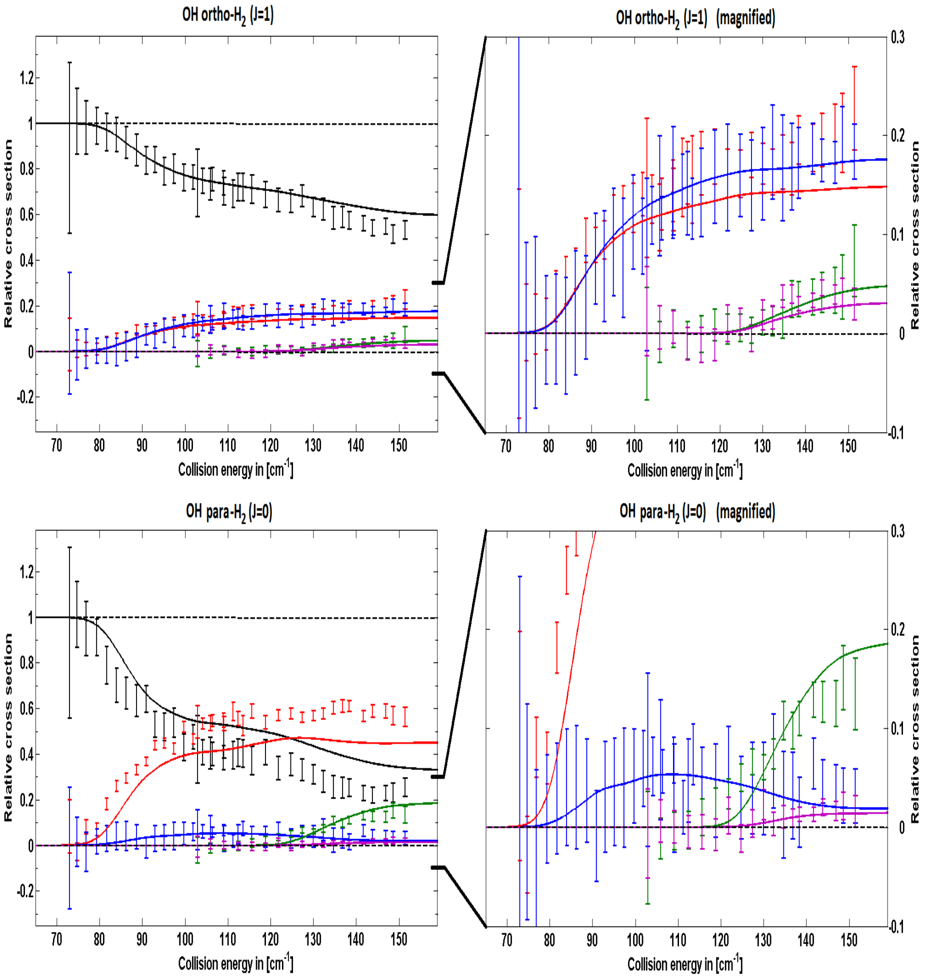

Figure 7.3: Experimental and theoretical relative cross sections of collisions between OH-H$_2$(J=1) are shown in the upper two graphs, while the ones for collisions between OH-H$_2$(J=0) are plotted in the lower two graphs. The two left graphs show all rotationally inelastic channels, while the right graphs show the weaker channels magnified. The previous colour code is used: F1(3/2,e) is black, F1(5/2,e) is red, F1(5/2,f) is blue, F2(1/2,e) is green, and F2(1/2,f) is pink.

in the OH-H_2(J=1) case. The propensities for the parity-conserving transitions of the [F1(3/2,f,+) → F1(5/2,e,+)] and [F1(3/2,f,+)→ F2(1/2,e,+)] excitation are reproduced exactly as well as the parity-changing ones like of [F1(3/2,f,+) → F1(5/2,f,-)] and [F1(3/2,f,+) → F2(1/2,f,-)]. The qualitative behaviour of the relative cross sections as a function of the collision energy are reproduced with a very good agreement: the excitation to F1(3/2,e) shows again a step-like decrease in the relative cross sections towards higher collision energies. The relative cross section of F1(5/2,f) in the OH-H_2(J=0) shows again an intensity increase up to $\langle E \rangle_T \approx 110$ cm^{-1} followed by a decrease towards higher collision energies. Compared to the experimental data, the relative cross sections of F1(3/2,e) and F2(1/2,e) are overestimated, while the one of F1(5/2,e) is underestimated by theory with about 20 %. Scaling of certain terms in the PES increased the inelastic cross section of the F1(5/2,e) only, while all other cross section are left unaffected. Also the resonance structure of the cross section close to threshold is not changed. An even better agreement between theory and experiment is achieved by this scaling in the relative cross sections. However, there are concerns, whether a selective scaling of the expansion coefficients can be justified within the boundaries, which is given by the fit to the available *ab initio* data points [131] [132].

If one wants to study population inversion of the Λ-doublet states that could lead to OH maser activity, one must investigate the averaged cross sections out of the OH($^2\Pi_{3/2} J = 3/2$) states of both parities e and f for both OH-pH_2($J = 0$) and OH-oH_2($J = 1$) collisions. In the OH-pH_2 case, a large propensity for parity-conserving transitions in both spin-orbit manifolds has been observed in this experiment. The inelastic cross sections out of the initial $F_1, J = 3/2, e$ level could not be measured in this experiment. However, they were calculated [132]. If one compares the results for OH-pH_2 and OH-oH_2 cross sections out of the $J = 3/2, e$ level in comparison with the inelastic cross sections out of the $J = 3/2, f$ level, one observes that for OH-H_2 collisions out of the e level the trends are similar to those found for the initial level of parity f: a strong propensity for parity-conserving transitions over parity changing transitions is found for OH-pH_2($J = 0$) collisions, and almost no preference are found for OH-oH_2($J = 1$) collisions. However, when the transitions out of the e

and f levels in OH-pH$_2$ are mutually compared, the $f \rightarrow e$ transitions have larger cross sections than the $e \rightarrow f$ transitions. The difference is substantial especially for the $J = 3/2 \rightarrow J = 5/2$ transition in the spin-orbit conserving manifold. When starting from equally populated Λ-doublet levels, this will lead to a larger population of the lower Λ-doublet levels of spectroscopic parity e. Although only a limited range of collision energies have been investigated from a single initial $J = 3/2$ state of OH and the other cross sections are just calculated, not rate constants, it is concluded that this probably excludes inelastic collisions of OH with H$_2$ to be the pumping mechanism for the OH maser. This conclusion agrees with that of earlier work by Schreel and ter Meulen [118], who concluded from their experimental data with and without hexapole selection of the initial OH state, that the transition to the lower Λ-doublet component is more probable in both spin-orbit manifolds. Also Andresen and coworkers [115, 123] concluded that collisions between OH and H$_2$ do not produce population inversion that could lead to maser activity, for slightly different reasons. They measured cross sections for transitions out of the OH($^2\Pi_{3/2}$) ground state with equally populated e and f Λ-doublet components. They determined preferential excitation of the lower Λ-doublet components in the spin-orbit conserving manifold and of the upper Λ-doublet components in the spin-orbit changing manifold. This ruled out a particular pumping mechanism proposed by Andresen [137].

7.4.3 Comparison of signal intensity ratios

The results of the previous sections show that the different relative cross sections originate from two mutually different scattering processes, the different multipole-interactions present in collisions between OH radicals with either pH$_2$(J=0) or oH$_2$(J=1). Equations (7.3) and (7.2) are used together with equation (6.46) such that the ratio of measured signals is compared to the ratio of absolute cross sections at each collision energy. Again, the assumption is made that the number-density of the H$_2$ packet is the same under exchange of the gas mixtures of nH$_2$ and pcH$_2$.

$$\frac{SIG_{pcH_2}^{(\langle E\rangle_T)}}{SIG_{nH_2}^{(\langle E\rangle_T)}} = \frac{[0.99 \cdot \sigma_{H_2(J=0)}^{(\langle E\rangle_T)} + 0.01 \cdot \sigma_{H_2(J=1)}^{(\langle E\rangle_T)}]}{[0.25 \cdot \sigma_{H_2(J=0)}^{(\langle E\rangle_T)} + 0.75 \cdot \sigma_{H_2(J=1)}^{(\langle E\rangle_T)}]} \tag{7.4}$$

To compare the experimental data with the smallest error bar possible, the ratios are calculated for each individual inelastic excitation, which makes the comparison independent of the laser excitation scheme. The ratios are determined directly from the measured $SIG_{pcH_2}^{(E_c)}$ and $SIG_{nH_2}^{(E_c)}$. The experimental data could have been evaluated to compare the ratio of $SIG_{H_2(J=0)}^{(E_c)}$ and $SIG_{H_2(J=1)}^{(E_c)}$, but the error propagation would have led to larger error bars. If the number-densities of the packets were determined experimentally, even the absolute values of the cross sections could be compared. Figure 7.4 shows the ratios of all five inelastic excitations. The ratios of the first rotational excitation to F1(5/2,e) and F1(5/2,f) and the spin-orbit changing transitions to F2(1/2,e) and F2(1/2,f) show close to threshold very large error bars, because the signals are very small. They cannot be disentangled easily from the background. For reasons of a more detailed view the error bars have been cut. The ratio of the signal strengths correspond very well to the ratio of the theoretically calculated absolute integral cross sections for all five measured final states. This demonstrates that on a relative scale the interaction strengths of the complex multipole interactions are quantitatively described correctly by theory. The absolute cross sections for OH-H_2(J=1) are on average 2.5 to 3 times larger than the ones for OH-H_2(J=0). The absolute cross sections for collisions between OH and H_2 of higher rotational states, OH-H_2(J>1), should show a similar behaviour like the ones for OH-H_2(J=1). No more multipole-interactions should appear with higher J-states than J>1.

7.4.4 Comparison of OH colliding with H_2 and other targets

The OH-H_2 system is of fundamental interest to study molecular collision properties in general. In the last three sections theoretical calculations are verified on a quantitative base. The scattering behaviour due to the different multipole-interactions of OH with different rotational states of H_2 is well understood. The relative cross sections for OH-H_2(J=0) in section 7.4.1 are explained due to the H_2 properties in the lowest rotational J=0 state. There, the electric multipole moments average to zero and H_2(J=0) behaves like a spherical, structureless particle during the collision. This is long predicted [136] and has been investigated [118]. In this section similarities of the scattering properties are investigated between

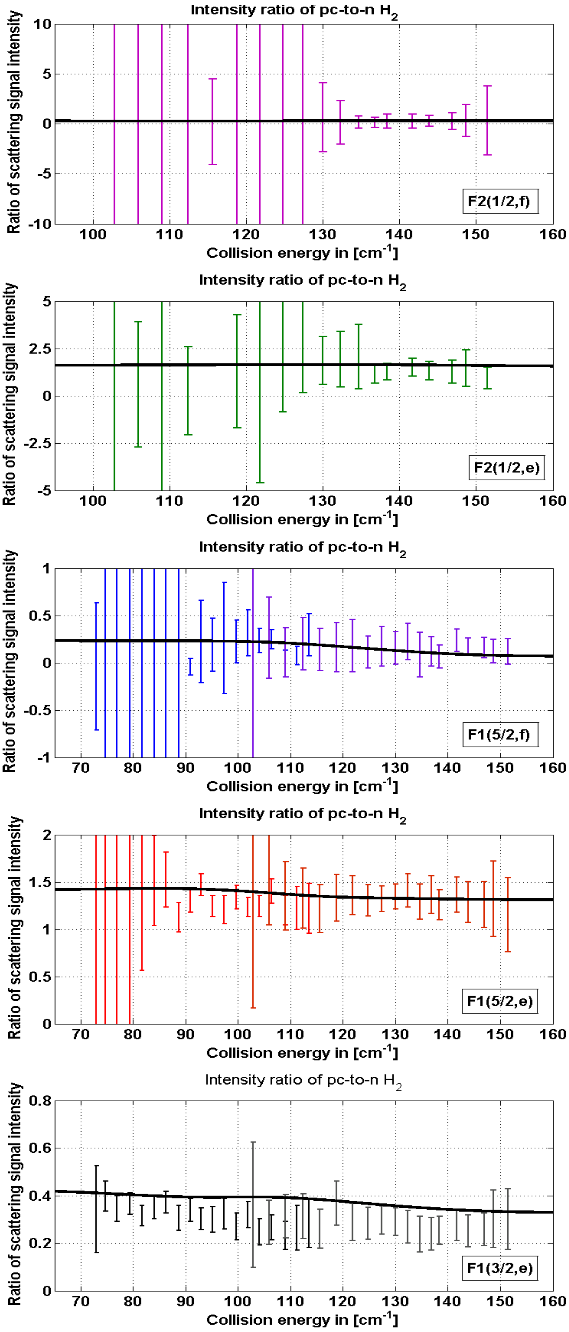

Figure 7.4: The five graphs show the ratio of the scattering signal intensity as a function fof the collision energy for the corresponding inelastically excited channels. The theoretical ratio, determined from the ratio of the absolute cross sections and plotted as black solid line, reproduces the experimentallly determined ratios rather well.

the OH-H_2(J=0) and other systems, where OH is colliding with structureless, spherical particles. The left graph of Figure 7.5 illustrates the experimentally determined relative cross sections of OH-pcH_2, which are plotted together with the theoretical cross sections of OH-helium [138] as solid lines. The theoretical cross sections of OH-pcH_2 are plotted as dashed lines as well. The theoretical data are convoluted in the same way as before.

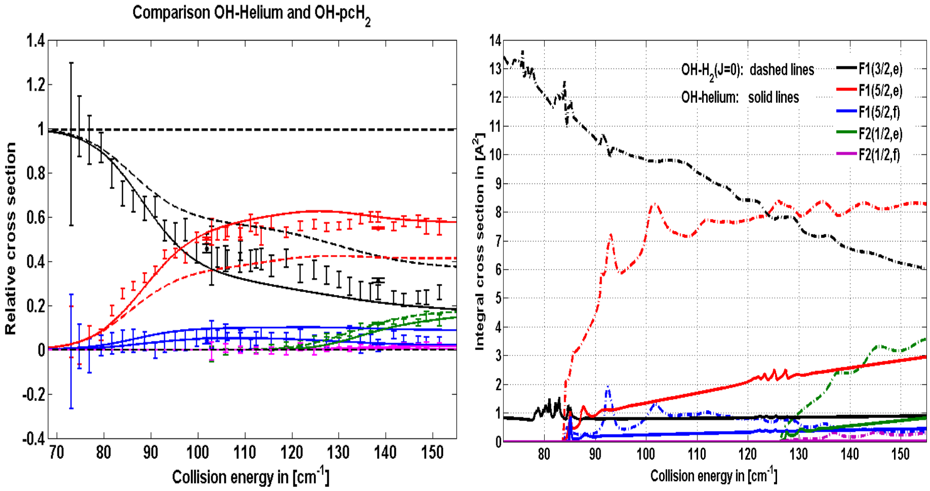

Figure 7.5: In the left graph relative cross sections of OH-pcH_2 are compared with theoretical cross sections of OH-H_2(J=0) (dashed lines) and theoretical cross section for the OH-helium system (solid lines) [138]. In the right graph the theoretical absolute integral cross sections are plotted in the relevant energy range for a comparison.

The astonishing result is that the theoretical OH-helium relative cross sections show an even better agreement with the experimental data than with the theoretical OH-H_2(J=0) ones. This holds for the relative strengths of both the [F1(3/2,f,+) → F1(5/2,e,+)] parity-conserving transition and the or [F1(3/2,f,+) → F1(3/2,e,-)] parity-changing transition. Also the experimental collision energy of 100 cm^{-1} where F1(5/2,e,+) becomes the dominant channel is reproduced better by the calculated OH-He relative cross sections than by the corresponding OH-pH_2 results. The influence of 1% ortho-H_2 in the para-converted target beam cannot account for this discrepancy.

However, if the intensities of the absolute integral cross sections are compared in the right graph of Figure 7.5, the OH-H_2(J=0) system has in general larger cross sections, if the same inelastic final channels are compared. The cross section of the F1(3/2,e) below collision energies of 100 cm^{-1} is more than an order of magnitude larger, while the excitation to all final rotational states is on average 3 - 6 times larger.

OH radicals colliding with structureless, spherical particles like rare gas atoms has been investigated in detail, recently: Scharfenberg and coworkers measured state-to-state inelastic relative cross sections as a function of the collision energy [107, 135], and Sarma and coworkers measured the state-to-state inelastic differential cross sections at particular collision energies [139, 140]. In the OH-helium system very strong propensities for parity-conserving transitions are observed. Especially the excitations into the [F1(3/2,f,+) → F1(5/2,e,+)] and [F1(3/2,f,+) → F2(1/2,e,+)] become the dominating ones, while the Λ-doublet changing transition [F1(3/2,f,+) → F1(3/2,e,-)] becomes less probable with increasing collision energy. General trends in the behaviour of the relative cross sections have been observed, if the scattering system is compared by replacing helium with neon, argon, krypton and xenon as collision target. Two effects influence the distribution of the relative cross sections: the nature of the PES and collision dynamics on the PES. The anisotropy of the PES and the polarizability α_0 of the target particle are two main properties to characterize the nature of the interaction potential, while dynamic effects are proportional to the reduced mass μ. The anisotropy of the PES and α increase, when going from helium to xenon as collision partner. The long range interactions, especially the dispersion and induction terms become of increasing influence, which leads to the trend that the Λ-doublet changing transition [F1(3/2,f,+) → F1(3/2,e,-)] becomes the dominating channel, while the propensities for parity-conserving transitions become less dominant. This behaviour is theoretically understood [141] [142] and quantitatively reproduced by theoretically calculated relative cross sections from *ab initio*

PESs [135]. Theoretical investigations showed for dynamical effects the trend that parity-conserving transitions become more probable and the Λ-doublet changing transition become less pronounced with decreasing reduced mass.

The similar behaviour of the relative cross sections of the OH-H_2(J=0) and the OH-helium system can qualitatively be explained within these trends. The PES of OH-H_2(J=0) shows large similarities to the one of the OH-neon system [133]. The value of $\alpha = 0.80\ 10^{-24}$ cm^3 of H_2(J=0) lies in between the values for neon and argon, which are listed in Table 7.1. Taking only the anisotropy of the PES and the polarizability of H_2(J=0) into account, one would expect the relative cross sections of OH-H_2(J=0) to behave like the ones for OH-neon or OH-argon. However, the dynamical effects of the very small value of the reduced mass in the OH-H_2 system seem to support the trend that parity-conserving transitions become more probable and the Λ-doublet changing transition become less pronounced with decreasing reduced mass. The data for H_2 are taken from [143] [144].

	H_2	helium	neon	argon
μ [amu]	1.79	3.24	9.22	11.93
α [10^{-24} cm^3]	0.80	0.21	0.40	1.64

Table 7.1: The values of μ and α for H_2 are taken from [143] [144], while values for helium, neon and argon are listed in [145].

The OH-helium system was also investigated in comparison with the OH-D_2 system [108]. Although the reduced mass is the same for OH colliding with helium and D_2, totally different relative cross sections were determined. The rotational state distribution of the normal-D_2 target beam was not analyzed experimentally. However, it was assumed that 67 % of D_2 end up in the rotational J=0 state after the supersonic expansion, while 33 % end up in the J=1 state. Compared to the OH-helium system a large cross section was measured for the Λ-doublet changing transition [F1(3/2,f) → F1(3/2,e)] in OH-D_2 collisions. The differences in the relative cross sections compared to OH-helium were attributed to the presence of stronger multipole-interactions and larger induction forces. The influences of isotope effects in general on the scattering behaviour promise to be very interesting, if the target beam of H_2 is replaced by D_2 or HD, which is currently under theoretical investigations [131].

In the experiment performed by Schreel and ter Meulen [118], state-selection of the F1(3/2,f) state of OH was done with a hexapole. The inelastic scattering cross sections of OH colliding with normal-H_2 and para-converted-H_2 showed very similar behaviour for all final inelastic channels. To their own surprise they observed a large cross section for the Λ-doublet changing transition [F1(3/2,f) → F1(3/2,e)]. The similarly observed cross sections for collisions with their normal-H_2 and para-converted-H_2 were explained by the large contribution of OH colliding with para-H_2(J=2). They changed the rotational population distribution in their para-converted-H_2 beam by stabilizing the valve at a lower temperature. There, the population ratio of para-H_2(J=0)/para-H_2(J=2) is larger, which lead to a decrease in the Λ-doublet changing cross section. They concluded that the cross sections of OH colliding with the para-H_2(J=0) must have a small cross section for the Λ-doublet transition in OH, and therefore, must behave like the OH-helium system. The results of this experiment confirm this unambiguously in a direct, state-to-state resolved measurement.

7.5 Conclusion

In this chapter state-to-state rotationally inelastic scattering of quantum-state selected OH radicals ($X^2\Pi_{3/2}$, J=3/2, f) with hydrogen molecules in two distinct rotational quantum states - pH_2(J=0) and oH_2(J=1) is presented. Relative cross sections are determined for a collision energy range between 70 cm^{-1} and 150 cm^{-1}. The threshold behaviour for rotational and spin-orbit changing inelastic excitations is clearly resolved. Two different H_2 mixtures (nH_2 and pcH_2) are used as target beams of OH in the experiment, which consist of different ratios of pH_2(J=0) and oH_2(J=1). Large differences are observed in the strength of relative cross sections. The contributions of different quantum states to the cross sections is disentangled, which reflects the mutually different influence of multipole-interactions in the scattering process. Theoretical absolute integral cross sections are derived from quantum close-coupling scattering calculations performed on a newly state-of-the-art compiled *ab initio* OH-H_2 PES.

Qualitatively and quantitatively the results show overall a very good agreement between theory and experiment. The comparison of relative cross sections showed that scattering of OH with pH_2(J=0) behaves similar to the OH-helium system. The quadrupole moment and even higher multipole-moments in pH_2(J=0) average to zero. This explains that the interactions in OH-pH_2(J=0) collisions behave very similar to the one with structureless particles like rare-gas atoms. Strong propensities for parity conserving transitions are found in accordance with theory. Also broader features in the theoretical cross sections are reproduced correctly by the experiment. The experimental data show a good agreement in comparison with theory, while the cross sections of the two strongest inelastic transitions to F1(3/2,e) and F1(5/2,e) deviate maximal by 20 %. In contrast, the relative cross sections of OH colliding with oH_2(J=1) shows no propensities at all. This behaviour of the cross sections originate from different multipole-interactions, which are present in the oH_2(J=1) collisions. Especially the OH-dipole - H_2-quadrupole and the OH-quadrupole - H_2-quadrupole interactions dominate. The theoretical relative cross sections, which includes these multipole-interactions, show an excellent agreement with the experimental data even within the error bars.

A second comparison between theory and experiment is made, when the ratio of signal intensities is compared to the ratio of the absolute integral cross sections. The experimentally determined ratios agree with the theoretical ones within the experimental error bars. In general, the intensity of the interactions is observed to be on average 2.5 to 3 times stronger for collisions between OH-oH_2(J=1) compared to OH-pH_2(J=0).

Chapter 8

Crossed beam scattering with high collision energy resolution

8.1 Introduction

The dynamics governing interactions in the cold regime are already dominated by quantum mechanical effects, as it is pointed out in the general introduction. There, classical mechanics cannot described the scattering process sufficiently well, because the de Broglie wavelengths of the colliding particles are of comparable size or even larger than the effective molecular interaction ranges [1]. The collision energies in the cold regime range from milli-wavenumbers up to a wavenumber. Collisions in the cold regime are sensitive to the long-range interactions, which are described theoretically by the attractive part within the PES. Different types of scattering resonances occur under distinct conditions [146]. Depending on the height of the centrifugal barrier several quasi-bound states can be present between the centrifugal barrier and the hard core repulsive part of the interaction potential. If the collision energy matches the energy of such a quasi-bound state, so-called orbiting or shape resonances appear. The colliding particles tunnel through and become trapped as a complex behind the centrifugal barrier or the reaction barrier [147] [148]. To each of those quasi bound states corresponds a quantum-scattering state, or a partial wave. It is identified by a value of the total angular momentum J_{tot} that is conserved throughout the collision. Bound states can also be present in the potential well at energies just below a rotational threshold. If the collision energy matches the energy gap to one of these bound states in the potential well of excited states from a energetically lower initial state in one of the reagents, so-called Feshbach resonances can appear. In both types of resonances, the wavefunction shows a high probability to be localized within this metastable state, where the particles are very close, compared to the continuum wavefunctions. The interaction time depends on the lifetime τ_{res} of the metastable state; it is related to the width of the resonance Γ_{res} by the relation $\Gamma_{res} = \hbar\tau_{res}^{-1}$. τ_{res} is usually much longer than the normal interaction time of a scattering event. These properties of resonances are in general responsible for large increases in the integral cross sections (ICS) or drastic changes in the angular distributions of differential cross section (DCS) as a function of the collision energy, which enables the observation experimentally. Knowledge on the strength and the location of resonances provides very detailed information for the modeling of the PES [149] and the ongoing dynamics.

Theory is able to predict the position of resonances very accurately, also the characterization of their nature can be done routinely [138] [150]. Scattering resonances show typically an energetic broadening of one wavenumber or less. Experimentalists face two challenges: (1) the bottleneck in most experiments to resolve resonances is the reduction of the collision energy distribution, which is inherent due to the longitudinal and transverse velocity spreads of each molecular packet (2) instabilities of the setup like drifts, shot-to-shot fluctuations of molecular beams, or the detection laser system define limitations to reproduce the signals around a particular collision energy. The width of the velocity distribution and the angular divergence of each molecular packet determine the collision energy resolution, which is the limiting factor in the experiment to clearly resolve features of the cross sections like thresholds or resonances. The velocity distribution within a molecular beam is usually quantified by the speed ratio S. It is defined by $S = v/\Delta v$ [9], where v is the mean translational velocity and Δv is the width of the velocity distribution. For many different valves S stays constant independent of the valve's temperature. Hence, the decrease of v and Δv at the same rate puts a technological limit onto the achievable collision energy resolution. Shape resonances have been observed in elastic collision experiments already in the 1970s [151] [152] [121] [153] [122]. Enormous experimental efforts using continuous molecular beam sources, which usually show a much higher S compared to pulsed valves and the choice of kinematically favourable systems, where one collision partner has a very low mass, made the observation possible. In the year 2000, an enhancement of the ICS and changes in the DCS due to resonances have been observed in reactive collisions at collision energies between 70 - 1500 cm^{-1} [154] [155].

However, the quest to explore the cold regime and to make use of the long-range interactions experimentally has become a boost recently. The advancements in the technology of pulsed valves [12], which produce internally colder beams, and specially designed cross beam machines offer new possibilities, when small but tunable crossing angles are used. Thereby, a decrease of the collision energy resolution becomes possible, which allows to resolve the contribution of individual partial waves to the scattering cross section [156] [157]. These techniques also enabled the first identification of shape resonances in inelastic collisions [158] [15]. In a merged beam setup, the Penning ionization reaction rate between metastable helium colliding with argon or hydrogen was enhanced due to resonance effects [16].

With the advent of experimental techniques to quantum-state select and to velocity control molecular beams, such as Stark- and Zeeman-decelerators, it became possible to produce molecular packets with very narrow velocity distributions, between 1 and 20 m/s [55]. In a series of experiments, collision energy resolutions have been achieved that are sufficient to accurately measure the threshold behaviour and broader structures in rotationally inelastic relative cross sections as a function of the collision energy [66] [107]. In these experiments a collision energy resolution of up to 15 cm^{-1} was achieved. To resolve scattering resonances with an energetic width of one wavenumber, different experimental schemes must be explored to narrow down the velocity distributions: velocity selectors can be used to minimize the velocity spread mechanically after the supersonic expansion. A different method would be to use a second Stark- or Zeeman-decelerated packet to control the velocity distribution as well as the quantum state prior to the collision. However, both methods would select only a certain part of the phase-space of a molecular packet. A different approach to achieve a high energy resolution is presented by Scharfenberg and coworkers. They discuss in [109] different geometries of the *Newton-diagram* to optimize the collision energy resolution only in the collision energy range, where resonances are predicted or expected, thereby taking advantage of the extremely narrow velocity distributions of the Stark- or Zeeman-decelerated packets.

This enables to investigate inelastic or reactive processes also at higher collision energies with high energy resolution. The collision regime can still be considered as cold, because the motion of the particles relative to each other after the collision can be very slow, after the excitation of an internal degree of freedom or the activation over the reaction barrier. Although the number of partial waves increases with increasing collision energy, quantum mechanical effects like resonances are also predicted at energies up to a few hundred wavenumbers, which corresponds to a temperature regime of a few hundred Kelvin [138] [150].

The experimental investigation undertaken here aim to increase the collision energy resolution at higher collision energies by exploring the properties of a Stark decelerator. Structures in the cross section, originating from quantum effects in a regime, where a lot more partial waves are contributing to the cross section than in the cold regime should be resolved with the achieved resolution. The first part of the chapter contains the theoretical and experimental strategies of the optimization of the collision energy resolution, as well as its implementation in this experimental setup. A comparison of the experimental results with convoluted theoretical cross sections enables a quantitative analysis of the increase in the energy resolution. Secondly, with an increasing collision energy resolution narrow structures in the measured excitation functions are observed. Investigations on their physical origin are discussed in detail in a second part.

8.2 Scattering experiments and optimization of the collision energy resolution

The resolution or the distribution of the collision energy is quantified by the variance $\Delta_{var}E_c$ or the standard deviation $\Delta_{std}E_c$, which is presented in section 6.2. A specific energy resolution is inherent in the experiment due to the finite deficiencies of the experimental parameters. Each beam has a velocity spread around its mean velocity $\bar{v}_1$ and $\bar{v}_2$ in the longitudinal (*long*) and the transverse (*trans*) directions. In particular the parameter-uncertainties are given by the widths of the velocity distributions $\Delta^{long}v_1$, $\Delta^{long}v_2$ and by the widths of the transverse velocity distributions $\Delta^{trans}v_1$, $\Delta^{trans}v_2$, which can also be identified as the angular divergence of the beams. The angular uncertainty $\Delta\alpha$ expresses a combined measure for both transverse velocity distributions, which should not be confused with a constant angular offset of the crossing angle α due to mechanical imperfections.

Analytical evaluation of the collision energy distribution

The distribution of the collision energy is found by calculating the absolute error of the collision energy. From equation (6.14) follows

$$\begin{aligned}\big[\Delta_{std}E_c\big]^2 &= \mu^2\big[[\underline{v}_{rel}]^2(\Delta_{std}v_{rel})^2\big] = \\ &= \mu^2\big[[\underline{v}_1 - \underline{v}_2\cos\alpha]^2(\Delta_{std}^{long}v_1)^2 + [\underline{v}_2 - \underline{v}_1\cos\alpha]^2(\Delta_{std}^{long}v_2)^2 \\ &\qquad + [\underline{v}_1\underline{v}_2\sin\alpha]^2(\Delta_{std}\alpha)^2\big]. \end{aligned} \tag{8.1}$$

The optimization of the collision energy distribution can be identified as a geometrical problem of finding the geometry of the *Newton-diagram*, where all six experimental velocity-parameters are combined such that the relative velocity distribution $\Delta_{std}v_{rel}$ is minimal. A suitable parameter range has to be defined to reduce the collision energy distribution within the collision energy interval of interest. Scharfenberg and coworkers present strategies to optimize the geometries of the *Newton-diagram* on the basis of the experimental circumstances in general [109].

In the experiment discussed here, the setup constrains certain parameters: firstly, the crossing angle is not a tunable parameter, because the valve can only be mounted in 90° or 45° with respect to the Stark-decelerator's beam axis. Secondly, the cryogenic cooled valve needs hours to stabilise at a temperature T_{valve}. Therefore, tuning the velocity of

$\underline{v}_1 = \underline{v}_{H_2}(T_{valve})$ by changing T_{valve} is disadvantageous to perform a scan of the collision energy. Tuning $\underline{v}_2 = \underline{v}_{OH}$ allows to scan a certain collision energy range, while the intersection angle and the target beam velocity are fixed.

The challenge to minimize $\Delta_{std}v_{rel}$ to the lowest possible value has to be investigated quantitatively by taking achievable values from the experimental setup to calculate the expected energy resolution. Properties of the OH packets are well known from the trajectory simulations, while the H_2 beam properties are modeled from the TOF measurements presented in section 3.1.2. A favourable geometry of the *Newton-diagram* is proposed in [109], where the mean velocities of $\underline{v}_{OH}$ and $\underline{v}_{H_2}$ are chosen such that $\underline{v}_{H_2}$ is perpendicular to $\underline{v}_{rel}$. In this configuration $\Delta^{long}_{std}v_{H_2}$ contributes the least to $\Delta_{std}v_{rel}$. Consequently, in this geometry changes in $\Delta^{trans}v_{H_2}$, which is parallel to $\underline{\mathrm{v}}_{rel}$, have a very large influence on Δv_{rel}. The left graph of Figure 8.1 illustrates different geometries of the *Newton-diagram*, where the same mean collision energy is realized. The widths of each velocity distribution around each mean velocity of the colliding packets are schematically depicted by the grey shaded areas. In each geometry those result in different relative velocity distributions. The proposed high resolution (HR) geometry is drawn in red. The geometry, which is implemented for the measurements of the previous chapter 7, should result in a broader collision energy distribution, which is denoted by LR.

In the beginning, a comparable energy range and set of experimental parameters is chosen to compare the experimental conditions and data that have already been simulated in section 6.3.3 and presented in section 7.4.1 respectively, to the proposed HR geometry. The parameters are chosen such that $\underline{v}_{OH}$ is tuned between 1410 m/s and 1643 m/s with a constant $\underline{v}_{H_2} = 1153$ m/s which realizes the condition $\underline{v}_{H_2} \perp \underline{v}_{rel}$ in the *Newton-diagram*. This setting allows to scan the collision energy between 78 and 103 cm^{-1}. By using a phase angle of 30° to create the OH packets, the longitudinal and the transverse distributions correspond to $\Delta^{long}_{std}v_{OH} \approx 7.6$ m/s and $\Delta^{trans}_{std}v_{OH} \approx 3.2$ m/s according to the trajectory simulations. The values on the H_2 side result from the TOF measurements $\Delta^{long}_{std}v_{H_2} \approx 20$ m/s. The transverse velocity distribution $\Delta^{trans}_{std}v_{H_2}$ is calculated as the angular divergence of $\Delta_{std}\alpha_{H_2}$ which is determined by the skimmer and the collimation slit. A collimation-slit width of 3 mm is used to calculate $\Delta_{std}^{3mm}E_c(E_c)$ as a function of the collision energy. It ranges from $\Delta_{std}^{3mm}E_c(78\ \mathrm{cm}^{-1}) \approx 1.9\ \mathrm{cm}^{-1}$ to $\Delta_{std}^{3mm}E_c(103\ \mathrm{cm}^{-1}) \approx 2.1\ \mathrm{cm}^{-1}$. Table 6.2 presents each E_c and $\Delta_{std}^{3mm}E_c(E_c)$ in the columns four and eight, respectively. The results of the LR geometry are presented in Table 6.1, where $\Delta_{std}E_c$ and E_c are listed in columns five and three, respectively. A comparison of the analytically calculated results of the HR and LR geometries shows a decrease of the collision energy distribution by a factor of 4.5, which strongly suggests to exploit the proposed HR geometry of the *Newton-diagram* in the experiment.

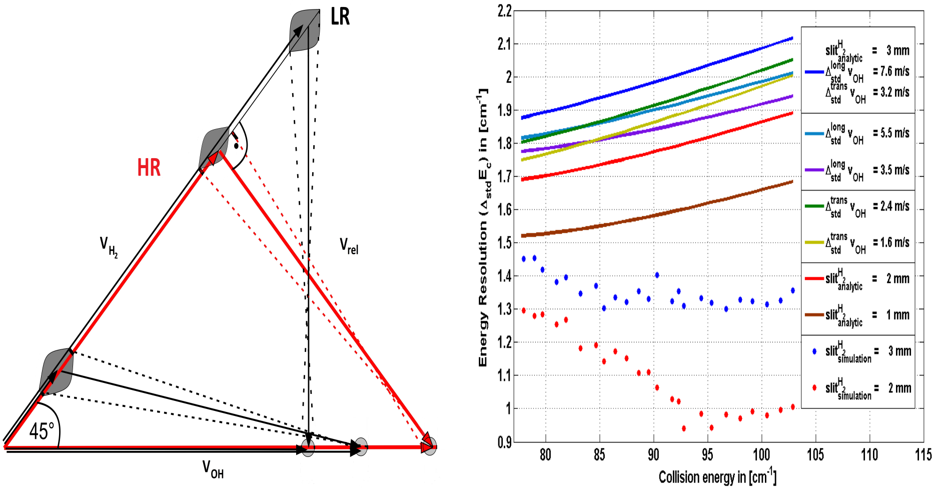

Figure 8.1: The left drawing illustrates how different translational velocities of $\underline{v}_{OH}$ and $\underline{v}_{H_2}$ in the lab frame realize the same relative velocity vector $\underline{v}_{rel}$ in the CM frame. The HR geometry ($\underline{v}_{H_2} \perp \underline{v}_{rel}$) is illustrated in red. The right graph shows the results of the collision energy distribution as a function of the collision energy. Experimentally achievable parameters of the setup are used to compare the results of the analytical calculations with the simulations from the packets' overlap in time, which are depicted by solid lines and by bullets, respectively.

Additional information can be gained from this analytical model. Not only the value of $\mathit{\Delta}_{std}E_c(E_c)$ itself, but also the influence of each velocity distribution can be investigated by using quantitatively different values for the distributions. The right graph of Figure 8.1 shows the results of calculations as solid lines, in which experimentally achievable parameters of the setup are used in equation (8.1) to investigate the improvement of the collision energy resolution $\mathit{\Delta}_{std}E_c$. The setting of the parameters which are used for the comparison with the LR geometry, is illustrated by the uppermost dark-blue solid line. In the following investigations, this set of parametres (i.e. this dark-blue line) serves as a fix-point to relate all quantitative changes in $\mathit{\Delta}_{std}E_c$ by narrowing down individual components of velocity distributions.

- **Improvements in $\mathit{\Delta}_{std}^{long}v_{OH}$** are achieved by using higher phase-angles or by applying longitudinal bunching schemes as presented in section 4.3. By using phase-angles of 45° and 60° $\mathit{\Delta}_{std}^{long}v_{OH}$ is lowered to 5.5 m/s and 3.5 m/s, respectively. In the right graph of Figure 8.1 the results of the calculation are plotted in blue and violet solid lines, which show on average a decrease of the $\mathit{\Delta}_{std}E_c$ by 0.08 cm^{-1} and 0.14 cm^{-1} relative to the uppermost dark-blue solid line. Narrowing of $\mathit{\Delta}_{std}^{long}v_{OH}$ by more than 50% leads to an improvement of 7% in $\mathit{\Delta}_{std}E_c$.

- **Improvements in $\mathit{\Delta}_{std}^{trans}v_{OH}$:** are accomplished most efficiently by applying a transverse bunching scheme, which is demonstrated in section 4.3. In these calculations a narrowing of $\mathit{\Delta}_{std}^{trans}v_{OH}$ of -25% and -50 % is assumed, which corresponds to values for the transverse widths of 2.4 m/s and 1.6 m/s, respectively. This leads to an improvement of $\mathit{\Delta}_{std}E_c$ by 4% to 7%, respectively.

- **Improvements in $\mathit{\Delta}_{std}^{trans}v_{H_2}$:** are reached by reducing the collimation-slit width with the H_2 collimator. The skimmer orifice and the (smaller) slit confine the transverse velocity distribution such that $\mathit{\Delta}_{std}E_c$ is reduced by 0.2 cm^{-1} and 0.4 cm^{-1}, if the slit size is reduced to 2 mm and 1 mm, respectively. Reducing the slit size by 50 % would result in an improvement of $\mathit{\Delta}_{std}E_c$ by 15 %.

Comparing the dependence of $\Delta_{std}E_c$ on the different distributions shows that changes in $\Delta_{std}^{trans}v_{H_2}$ cause by far the largest improvement. This defines the most influential and the limiting parameter in this geometry of the *Newton-diagram*, while $\Delta_{std}^{long}v_{OH}$ and $\Delta_{std}^{trans}v_{OH}$ show similar and less influence. Although these dependencies are very important to investigate, the narrowing of each velocity distribution goes along with a reduction of the signal intensity. Every time the collision energy resolution is increased the signal-to-noise ratio (SNR) drops. Although the SNR can be increased by taking more averages, this defines a limit to the achievable collision energy resolution in the experiment.

Overlap simulations and the energy resolution

A different approach to model the collision energy distribution represent the investigations on the molecular packets' overlap in time, where the colliding packets are described by 6D phase-space number-density distributions. As a function of the overlap in time the experimental parameters of the creation of collision products, the collision energy and the collision energy distribution are simulated. In section 6.2.1, theory is presented, where the PSDs are described as continuous number-density distributions. In section 6.3.3 numerical Monte-Carlo simulations are performed including the actual experimental parameters to determine the collision energy $\langle E\rangle_\tau$ and the collision energy distribution $\langle\Delta_{std}E\rangle_\tau$ at the moment of detection τ.

The third column of graphs (1c), (2c) and (3c) in Figure 6.4 shows the standard deviation of the collision energy $\Delta_{std}E^t$ (bullets) at each (instantaneous) time-step of the numerical simulations and the expected standard deviation of the collision energy distribution $\langle\Delta_{std}E\rangle_\tau$ (solid lines) as a function of the overlap in time t. Graph (1c) illustrates the results of the LR geometry, where the OH packet ($v_{OH} = 271$ m/s) collides with H_2-target beams at $v_{H_2} = 1320$ m/s. The evolution of the instantaneous collision energy distribution ($\Delta_{std}E^t$) shows roughly a constant behaviour as a function of the overlap in time for the different packet-delays. Therefore, the expected collision energy distribution ($\langle\Delta_{std}E\rangle_\tau$) decreases due to the weighted averaging over time. In Table 6.1 all $\langle \Delta_{std}E \rangle_T$ are listed in column four. The values of $\langle \Delta_{std}E \rangle_T$ increase with increasing $\langle E \rangle_T$ and decreasing v_{OH}, because larger parts of the PSD are probed during the overlap in time up to the moment of detection. Graph (2c) shows the results of the setting within the higher collision energy range, where the OH packet (v_{OH} = 271 m/s) collides with a faster H_2-target beam of v_{H_2} = 1530 m/s. The evolution of $\Delta_{std}E^t$ and $\langle \Delta_{std}E \rangle_T$ in this particular case show similar tendencies compared to the simulations of the analogous case depicted in graph (1c), although the influence of the packets' delay is more pronounced. Also no general trend is observed, when $\langle \Delta_{std}E \rangle_T$ of different collision energies are compared, which are listed in column eight of Table 6.1.

Graph (3c) illustrates the results, where settings of the HR geometry are simulated, which have been discussed in the previous section. The overlap simulations are performed for the parameters v_{OH} = 1643 m/s and v_{H_2} = 1151 m/s and two different slit widths of 3 mm and 2 mm, which are depicted in blue and red, respectively. Compared to the LR settings, no clear dependence can be observed of neither $\Delta_{std}E^t$ nor $\langle \Delta_{std}E \rangle_T$ as a function of the overlap in time. The smaller slit size leads to a significantly better resolution $\langle \Delta_{std}E \rangle_T$ in the simulations. The numerical results are listed in the fifth and sixth column of Table 6.2. On average $\langle \Delta_{std}E \rangle_T$ decreases from 1.35 cm^{-1} to 1.1 cm^{-1} if the slit is narrowed from 3 mm to 2 mm.

The results of $\langle \Delta_{std}E \rangle_T$ are plotted in the right graph of Figure 8.1 to be compared to the analytical calculations of $\Delta_{std}E$ from the previous section. The blue and red bullets correspond to the simulations of the slit sizes of 3 mm and 2mm, respectively. The analytical calculations show in general higher values for the width of the collision energy distribution, independent of the geometry of the *Newton-diagram*. This is attributed to an overestimation of the contributions of each velocity component in the analytical case. The numerical simulations account in more detail for three effects: (1) only those parts of the PSDs contribute to the collision energy distribution that have overlapped before the moment of detection, (2) correlations in the PSDs between velocity and position in the packets is accounted for, and (3) actual number-density PSDs model the packets in more detail. All these properties lead to the result that effectively only a part of each velocity distribution contributed to the collision energy distribution in the numerical simulation, while the analytic calculations took the complete PSDs into account.

The analytic calculations show a tendency that $\Delta_{std}E$ increases with increasing E_c as shown by the results plotted as solid lines in the right graph of Figure 8.1. Equation (8.1) supports this observation, because $\Delta_{std}E$ is a function of v_{rel}, which increases with increasing E_c. The changes in Δv_{rel}^2 are negligible, because the properties of the H_2 target beam stay constant. The OH packets are manipulated with the Stark-decelerator and their velocity distributions are constant around the different mean velocities, since the same absolute phase angle ($|\phi|$) is used. The final velocity is tuned by applying differently long durations of acceleration ($-\phi$) and deceleration (ϕ).

The numerical simulations of $\langle \Delta_{std}E \rangle_{\tau}$, however, do not show a dependence on $\langle E \rangle_{\tau}$ conclusively. In the HR simulations a slight decrease of $\langle \Delta_{std}E \rangle_{\tau}$ is observed with increasing $\langle E \rangle_{\tau}$ for both slit widths, which is depicted as bullets in the right graph of Figure 8.1 (and listed in the fifth and sixth column of Table 6.2). This slight decrease rather than an increase of $\langle \Delta_{std}E \rangle_{\tau}$ is attributed to the decreasing amount of spatial overlap in time with increasing $\langle E \rangle_{\tau}$, because v_{OH} becomes faster. In the LR and low collision energy interval (listed in column four of Table 6.1), $\langle \Delta_{std}E \rangle_{\tau}$ shows an increase with increasing $\langle E \rangle_{\tau}$. This increase is again attributed to the larger spatial overlap in time, since v_{OH} is decreasing with increasing v_{rel}. In the LR and high collision energy case, no clear dependence is observed (listed in column eight of Table 6.1).

The general result of these simulations shows that $\langle \Delta_{std}E \rangle_{\tau}$ is determined by the PSDs that have been overlapping in time. If $\langle \Delta_{std}E \rangle_{\tau}$ should be reduced to a minimum, a setting needs to be chosen where the smallest amount of each PSD overlaps. Consequently, only very small parts of each PSD contribute to $\langle \Delta_{std}E \rangle_{\tau}$. Since the velocity distributions on the OH side ($\Delta_{std}^{long} v_{OH}$ and $\Delta_{std}^{trans} v_{OH}$) can be tuned to be very small, it is advisable to have a very fast OH beam, which probes only a very small part of the H_2 packet and its PSD. Therefore, those geometries are best, where the Stark-decelerated packet is fast compared to the target beam. If the proposed HR geometry is implemented in this experimental setup, where $\underline{v}_{H_2} \perp \underline{v}_{rel}$ has to be realized, $\underline{v}_{OH}$ will be roughly 1.4 times larger than $\underline{v}_{H_2}$. This is also favourable from the numerical simulation's point of view to minimize the overlap. Schematically, this is obvious when graphs (1a) and (2a) are compared with graph (3a) in Figure 6.4. Even smaller parts of each PSD would be probed, if $\underline{v}_{OH}$ was even faster. However, the HR geometry offers an additional advantage to the experiment and its numerical modeling: the whole task to minimize the influence of the different velocity distributions is minimized and decoupled from the only velocity distribution, that is not controllable as a parameter: $\Delta_{std}^{long} v_{H_2}$. In contrast, the influence of the slit and hence $\Delta_{std}^{trans} v_{H_2}$ is maximal in the HR geometry; it is experimentally tunable by the collimation-slit width.

It is concluded that these calculations strongly suggest to implement the proposed HR geometry, although the two models find different positive, but not contradicting arguments for it.

8.2.1 Experimental procedures

To analyse improvements in the collision energy resolution qualitatively and quantitatively, the threshold behaviour of a rotationally inelastic transition is investigated. The onset of the signal is measured as a function of the collision energy. Higher energy resolutions result in a steeper slope around threshold, while the onset of the signal is found closer to the real threshold. Possible underlying structures of the cross section should emerge with an increase of the resolution. At the time when the experiment was planned and conducted, no theoretically calculated cross sections were available. A purely experimental approach is presented in this section. Theoretical cross sections which are convoluted with an experimental collision energy resolution, are extremely helpful for a quantitative analysis, which is shown in the next section.

The OH-pcH_2 is chosen as system to investigate the collision energy resolution. The threshold of the rotationally inelastic transition [F1(3/2,f,+)

→ F1(5/2,e,+)] has the advantage that the final state is high-field seeking. The detection happens basically under background-free conditions, because the Stark-decelerator deflects all molecules that populate this quantum-state after the supersonic expansion, compared to low-field seeking quantum states (like F1(5/2,f,-)), where a small amount of molecules is decelerated. The residual background is identified as stray light photons and photons resulting Rayleigh scattering with the background gas. The possible existence of shape resonances at collision energies just above threshold does not seem unlikely, also if the comparison with the OH-helium system [138] in section 7.4.4 is considered.

To implement the HR geometry of the *Newton-diagram* in the setup, the Even-Lavie valve is stabilised at $T_{valve} = 65$ K, which results in $\underline{v}_{H_2} = 1151$ m/s. On the OH side, the nitric-acid is expanded within a helium-neon mixture, which produces an initial mean velocity of 1525 m/s. Different amounts of acceleration and deceleration with a phase angle of $\phi = \mp 30°$ are programmed to vary $\underline{v}_{OH}$ between 1410 m/s and 1643 m/s. The scanned collision energy interval ranges from 78 cm^{-1} to 103 cm^{-1} with a sampling rate of 1 cm^{-1}. The detailed settings are listed in Table 6.2. The signals have been evaluated in the same manner as it is presented in section 6.3.2. The intensities of the incoming OH packets are measured every three hours to guarantee not only a day-to-day stability, but also a better intra-day comparison. This accounts even better for long term drifts of the valve settings and the excimer laser powers, which cannot be compensated completely by the toggling of the various OH velocities. Due to the small overlap of the colliding packets and the smaller collimation-slit widths on the H_2 side, the signal intensities are smaller than in the LR geometry. The left graph of Figure 8.2 shows the normalized signals of the measurements with the collimation-slit widths of 3 mm (black) and 2 mm (blue). The normalized signal is defined as the scattering signal divided by the incoming beam intensity of the F1(3/2,f,+). The error bar is defined as the standard error of the mean $\pm\mathit{\Delta}_{ci}^{(E_c)}$, which is derived in equation (6.39). The normalized signals decrease by a factor of 2, when the collimation-slit width is reduced. The SNR determines to what extent the rotational threshold can be resolved. Below threshold the normalized signals goes to zero. The threshold of 83.9 cm^{-1} is resolved clearly within the SNR.

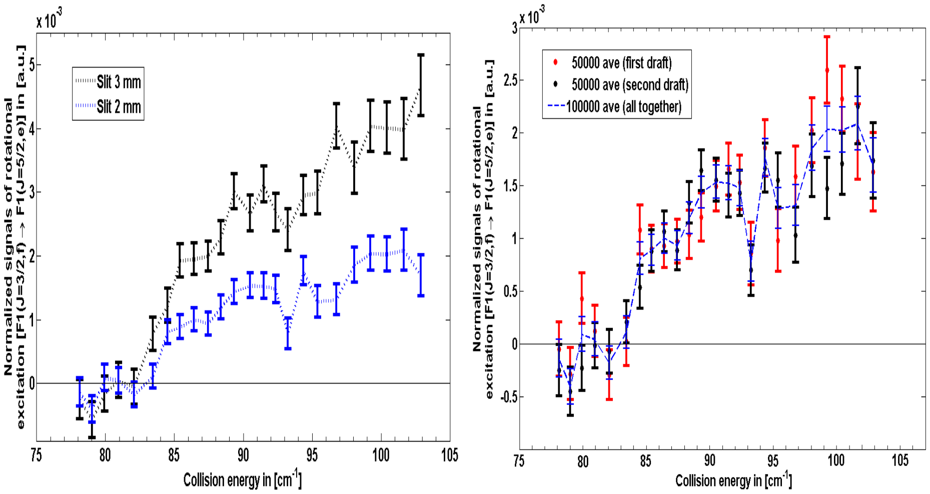

Figure 8.2: The left graph shows the normalized signal for the measurements with the 3 mm (black) and 2 mm (blue) slit widths. The signal decreases by a factor of 2 when the H_2 beam is more collimated. In the right graph two datasets from the series of measurements are plotted to illustrate on the one hand the fluctuations, while on the other hand the reproducibility within the error-bar is evident.

Since the SNR is quite small and large number of averages needs to be taken, the question arises to what extent is the experiment reproducible and to what extent can one rely on an individual datapoint. The right graph of Figure 8.2 shows the results of three datasets with the collimation-slit width of 2 mm. All together 100000 averages (ave) are taken for each collision energy within two campaigns of 50000 ave. The red and black datapoints illustrate the results of the first and the second campaign, respectively. The blue datapoints depict the combined results of the 100000 ave. The error bars are again derived as standard error of the mean $\pm\mathit{\Delta}_{ci}^{(E_c)}$. In between the two campaigns the measurements with the collimation-slit width of 3 mm are taken. The values of the normalized signals are reproduced within the error bar of $\pm 2\mathit{\Delta}_{ci}^{(E_c)}$, and, apart from three datapoints, the values are reproduced even within the error bar of $\pm\mathit{\Delta}_{ci}^{(E_c)}$. The data have been split in different ways, for example only the data, which are taken in the morning are compared to data, which are taken in the afternoon and evening; day-to-day comparisons are made and so on. The conclusions are that the normalized signals at each collision energy are reproducible within the confidence interval, while the fluctuations of the signals are fully explained by statistics.

The normalized signals $Sig_{rate}^{(E_c)}$ are evaluated as excitation functions. In this way the properties of this individual state-to-state transition are investigated best once the cross section σ[F1(3/2,f,+) → F1(5/2,e,+)] is evaluated as a function of the collision energy. The evaluation follows equation (6.46). The conditions of flux-mode are fulfilled as discussed in section 6.3.4. Since the same laser transition is used for all sampled datapoints, $\mathit{\Gamma}_f$ is a constant factor and is neglected. The overlap integrals are calculated from the well known spatial extensions of the packets. Since the absolute value of the number-density is not determined, the cross section is linearly proportional to these properties:

$$\sigma_f(\overline{v_{rel}}) \propto$$

$$\propto \frac{Sig_{rate}^{(E_c)}(\tau)}{\overline{v_{rel}} \cdot \left[\int_{-\infty}^{\tau} \int_{-\infty}^{\infty} \int_{-\infty}^{\infty} \delta_{\underline{\mathrm{r}}_{OH}\underline{\mathrm{r}}_{H_2}} n_{OH}^{r}(\underline{\mathrm{r}}_{OH}, t') \cdot n_{H_2}^{r}(\underline{\mathrm{r}}_{H_2}, t') d^3\underline{\mathrm{r}}_{OH} d^3\underline{\mathrm{r}}_{H_2} dt \right]}. \tag{8.2}$$

The evaluated cross sections as a function of the collision energy define the excitation functions, which are evaluated for three series of measurements of different geometries of the *Newton-diagram*: the HR geometry with the collimation-slit widths of 3 mm and 2 mm and the LR geometry, where the slit width was 4 mm.

8.3 Results and Discussion

In the following two main aspects are discussed, when the experimentally determined excitation functions are compared to theoretical absolute integral cross sections: (1) the improvement of the collision energy resolution is investigated on a quantitative base by comparing the experimentally determined excitation functions with theoretical cross sections, which are convoluted with a given energy resolution. (2) The increase of the collision energy resolution reveals sharp structures in the excitation function. Their physical origin is investigated in further detail.

8.3.1 Improving the resolution of the collision energy

The quantitative analysis of the collision energy resolution is performed by looking the steepness of the slope around the threshold of the excitation function: σ[F1(3/2,f,+) → F1(5/2,e,+)]. Excitation functions are determined for three different experimental settings, where different geometries of the *Newton-diagram* are implemented resulting in different collision energy resolutions. The upper graph of Figure 8.3 shows a series of measurements where the LR geometry is realized and a collimation-slit width of 4 mm is used. The results of the HR geometry with the collimation-slit widths of 3 mm and 2 mm are illustrated in the middle and the lower graphs, respectively. The cross sections are plotted in black with error bars of $\pm\Delta_{ci}^{(E_c)}$ in all three graphs. They are connected with a dotted line as guide to the eye. In all graphs the evaluated values of the cross sections are plotted against $\langle E\rangle_\tau$, which results from the overlap simulations. Their results are listed in detail in Table 6.1 and 6.2.

The rotational threshold of 83.9 cm^{-1} is indicated in all three graphs by a vertical dashed line. Qualitatively, the threshold is resolved in all three geometries. However, rotational excitations below threshold are only possible if the velocity distributions of both beams are wide enough that collision energies greater than the energetic threshold result. In the LR geometry the cross section starts to increase at 75 cm^{-1}. In the HR geometry the threshold is determined between 82 cm^{-1} and 83 cm^{-1}, when the collimation-slit width of 3 mm is used. The threshold is best resolved when the collimation-slit width of 2 mm is used. Here, the increase is steepest and happens between two adjacent datapoints between 83.2 cm^{-1} and 84.6 cm^{-1}. A second feature, which is most pronounced in the measurements with the 2 mm collimation-slit, is the dip of the cross section around 93.2 cm^{-1}, where the signal decreases by 50 % relative to its adjacent data-points at 93.3 cm^{-1} and 94.4 cm^{-1}. The feature at this energy range is illustrated in all three graphs with the text-arrow: ← **1**. The energy range between 90 cm^{-1} and 97 cm^{-1} is investigated in more detail in two more independent and differently performed measurements, which are plotted in both graphs of Figure 8.4. The excitation functions are reproduced within the confidence intervals. The increase of the excitation function at threshold and the decrease around 93.2 cm^{-1} are three or even four times larger than the confidence interval and are not undersampled. To determine a quantitative value of the collision energy resolution, the increase at threshold and the decrease around 93 cm^{-1} show that significant changes of the cross section occur within 1 cm^{-1}, which is the sampling rate. In the right graph of Figure 8.4 the sampling is performed in steps of 0.5 cm^{-1}. This strongly indicates an achieved collision energy resolution of about 1 cm^{-1} to 1.5 cm^{-1} for the measurements with the 2 mm slit width, as otherwise such features in the cross sections would not be resolved.

The excitation function obtained with the collimation-slit width of 3 mm shows the same features compared to the 2 mm one, but less clearly resolved. The threshold increases between 82 cm^{-1} and 96 cm^{-1}, while the decrease of the signal around 93 cm^{-1} is less pronounced and not significant anymore. In the LR measurements no such deviations are observed, because the energy resolution is too low to resolve changes of the cross section within a wavenumber.

A straightforward determination of the collision energy resolution is a direct comparison of how well the theoretical absolute integral cross sections, which are convoluted with any desired experimental collision energy resolution, fit within the experimental confidence intervals. The quantity $\Delta_{FWHM}E = 2.355\Delta_{std}E$ defines the full width at half maximum of a normal distributed function. It is chosen as measure for the collision energy resolution, because the numerically and analytically distributed collision energy distributions show very good agreement with fits to normal distributions. All graphs of Figure 8.4 compare results of the analytic model $\Delta_{FWHM}E_c$, which are plotted as blue solid lines, with the overlap simula-

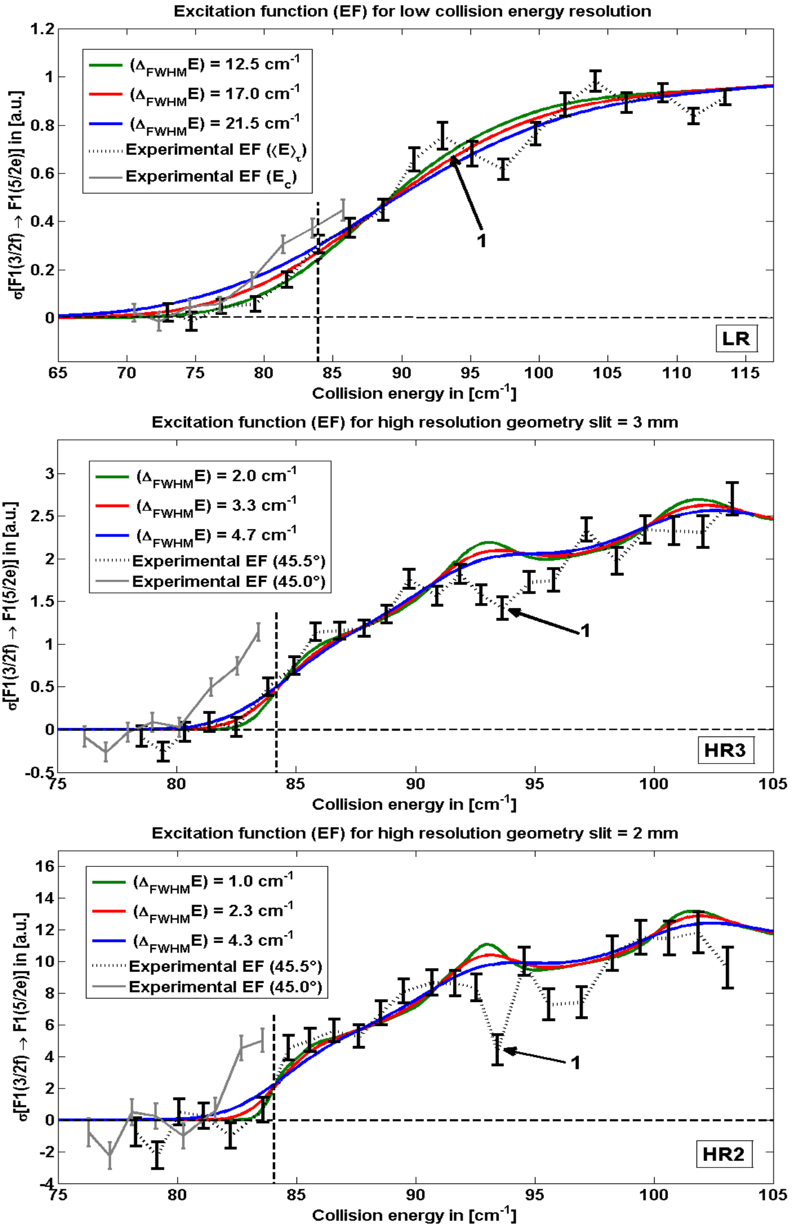

Figure 8.3: The upper, middle and lower graphs show the excitation function measured in the LR geometry, and the HR geometry with the collimation-slit width of 3 mm and 2 mm, respectively.

tions $\langle \Delta_{FWHM} E \rangle_{\mathcal{T}}$, which are plotted as red solid lines. The value based on the experimentally determined cross sections $\Delta^{exp}_{FWHM} E$ and the sampling rate allows a quantitative estimation of the energy resolution, which is plotted as green solid line. In general, the predicted values of the two models $\Delta_{FWHM} E_c$ and $\langle \Delta_{FWHM} E \rangle_{\mathcal{T}}$ coincide well in all three cases. However, the excitation function convoluted with $\Delta^{exp}_{FWHM} E$ fits best within the experimentally determined cross sections and their confidence intervals. It resolves the threshold best in all three series of measurements and the general trends of the excitation functions are reproduced best. $\Delta^{exp}_{FWHM} E$ has the smallest collision energy resolutions compared with the two quantitative models.

If the excitation functions, which are convoluted with $\Delta_{FWHM} E_c$ and $\langle \Delta_{FWHM} E \rangle_{\mathcal{T}}$, are compared to the experimental cross sections, both models seem to overestimate the resolution. The excitation function convoluted with $\langle \Delta_{FWHM} E \rangle_{\mathcal{T}}$ follows the experimental cross sections better than the analytical one, especially around threshold. In the case of the analytical model, the overestimation has been discussed in the last paragraph of [109], when Scharfenberg and coworkers compared their analytical results with direct numerical evaluations of ΔE'. Their packets were modeled with Gaussian-distributed functions, which they did not specify in detail. Their numerical results showed qualitatively the same behaviour as the analytical ones. However, quantitatively the numerical results always showed smaller values of the collision energy resolution. This deviation was attributed to an overestimation of the distribution in the analytical case.

Also the numerical overlap simulations, which determine $\langle \Delta_{FWHM} E \rangle_{\mathcal{T}}$, seem to overestimate the actual collision energy distribution. The overestimation is less than the analytical model, nevertheless a better agreement is possible. In section 6.3.3 three cases are discussed under which conditions a collision can be assumed. The overlap simulations are programmed according to case 1, where all particles of the OH and the HH distribution present in the intersection volume can possibly collide with each other. If case 2 was implemented, which would imply a more detailed sub-division of the intersection volume, $\langle \Delta_{FWHM} E \rangle_{\mathcal{T}}$ might yield a better agreement with $\Delta^{exp}_{FWHM} E$.

If the three convoluted excitation functions are compared, the most striking deviation is observed around 93 cm^{-1}. There, theory predicts an increase of the cross sections, while in the experiment a decrease is observed. Further investigations on this striking feature and the underlying dynamics follow in the next paragraph.

8.3.2 Investigations on the threshold behaviour

The collision energy resolution is increased in this scattering experiment by using two methods which are discussed in the last section 8.3.1. The higher resolution revealed deviations in the experimentally determined cross sections around 93 cm^{-1} that decreases by 50 %. This is in contrary to the theoretically determined excitation function which increases due to a resonance. To verify the decrease of the experimental cross section unambiguously, this collision energy range is investigated in more detail. The same scattering experiment in the HR geometry with the collimation-slit width of 2 mm is performed under two mutually different conditions:

- **First alternative measurement:** OH radicals with a different initial velocity after the supersonic expansion are coupled into the decelerator. The HV-switching of the Stark-decelerator is programmed differently: instead of different amounts of acceleration and deceleration with the same phase-angle a deceleration and acceleration scheme is used to produce the same final velocities at the end of the decelerator. The datapoints between 90.8 cm^{-1} and 98.4 cm^{-1} are measured again. The scattering experiment is still performed under the same conditions in terms of the overlap of the two molecular packets - it is ensured that still the same regions of phase-space are probed. Only the generation of the OH packets is different, which creates a different background and excludes systematic effects.
- **Second alternative measurement:** A different seed gas mixture of helium and neon is used to create an OH-packet with a mean velocity of 1575 m/s after the supersonic expansion. Here, different amounts of deceleration and acceleration with the same phase-angle

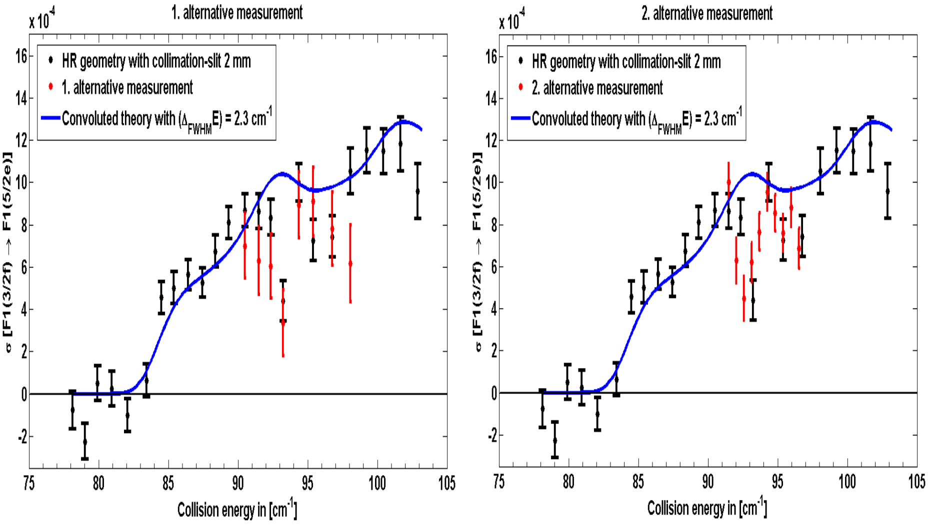

Figure 8.4: The theoretical excitation function is plotted together with the three serieses of measurements.

are used to sample the collision energy range between 91.7 cm^{-1} and 96.7 cm^{-1} with a rate of 0.5 cm^{-1}.

The left and the right graph of Figure 8.4 show the evaluated cross sections of the first and the second alternative measurements in red, respectively. The cross sections of the initial scan of the broader collision energy range are plotted in black as comparison. The cross sections reproduce each other within the error bars. And the decrease of the excitation function is reproduced around 93 cm^{-1}.

A second argument for the reproducibility of the signals is discussed in section 8.2.1. Since the SNR is between 2 and 3, the reproducibility of the normalized signals is taken care of by looking at different datasets. The left graph of Figure 8.2 illustrates how the normalized signals of two measurement campaigns fluctuate. The values of the normalized signals are reproduced within the error bar of $\pm\Delta_{ci}^{(E_c)}$.

The theoretical calculations predict two resonances in the excitation function at collision energies around 93 cm^{-1} and 102 cm^{-1} [131] [132]. The total angular momentum J_{tot} and the overall parity are conserved during the collision and the absolute cross sections are sums of the contributions from different J_{tot} values and different parities obtained from separate calculations. The resonance at 93 cm^{-1} mostly originates from collisions with $J_{\text{tot}} = 6.5$ and 8.5 and odd overall parity, while the largest contributions to the resonance at 102 cm^{-1} correspond to $J_{\text{tot}} = 5.5$ and 6.5 and even overall parity. Furthermore, from plots of the underlying scattering wave functions, the contribution of the partial waves to each resonance is identified, and which states of OH and H_2 are involved. At these collision energies pH_2 remains in its rotational $J = 0$ state. Shape resonances involve a state of OH that is asymptotically open at the given collision energy, but is temporarily trapped by the centrifugal barrier in a partial wave with angular momentum $L > 0$. Feshbach resonances involve states of OH that are closed for large OH-H_2 distances. The collision complex can temporarily access such states at shorter distances, where the potential is sufficiently attractive and more kinetic energy is available, but it must relax back to an open state when the colliding particles fly apart. Both resonances are found to be shape resonances in the F1(5/2,e,+) channel of OH which opens at a collision energy of 83.9 cm^{-1}. The resonance at 93 cm^{-1} corresponds to $L = 7$, while the resonance at 102 cm^{-1} corresponds to $L = 8$. Additionally, the latter resonance has a small Feshbach contribution, mainly for $J_{\text{tot}} = 3.5$ and odd parity, which involves the closed F2(1/2,e,+) state and a partial wave with $L = 3$.

Scaling of certain parts of the potential, which resulted in a profound influence on the intensity of the cross section 7.4.2, turned out to have non-considerable influence on the position of the resonance. The cross sections are determined with two mutually different scattering codes, which excludes any mistakes within the implementation of the scattering codes. On the experimental side, the decrease in the cross section has been reproduced under three different experimental conditions. The experimental data are evaluated separately with two different codes, one written in MATLAB, the second one written in Python. Also here no considerable deviations in the determined cross sections are found. The conclusion up to this moment is that both the theoretical as well as the experimental side have done everything within their capabilities to exclude errors.

In the following various possible mechanisms and unexpected dynamics are discussed that might explain the striking deviation in the excitation function. The main question is: is something going on that has not been included in the theoretical model? Or, has something changed at resonance such that the experimental techniques cannot detect it, which leads to a decrease in the measured signal:

1. **Chemical reaction:** Could the complex undergo a chemical reaction: $\cdot OH + H_2 \rightleftharpoons H_2O + \cdot H$? Can it be induced during the time, when the two particles are orbiting as a complex at resonance? This can be excluded due to the fact that the collision energy of $\approx$ 93 cm^{-1} is much smaller than the energy needed to overcome the reaction barrier of about $\approx$ 2130 cm^{-1} in order to activate the reaction.

2. **Secondary collision:** Could a second collision take place between the OH-H_2 complex with a second H_2 molecule during the lifetime of the complex at resonance. The collision would dissociate the complex, while the final rotational state of the OH radical must not necessarily be the F1(5/2,e) state. To evaluate the probability for such an event, theoreticians estimate the lifetime of the complex at resonance to last about 50 ps, which is approximately ten times longer than the normal collision time. The relative velocity of the complex with a second incoming H_2 molecule is about 1000 m/s. An optimistic value of the H_2 packet density of 10^{14} particles/cm^3 is assumed. To approximate a cross section, first the mean intermolecular distance between the particles at resonance is determined to be between 5 - 7 $\AA$. This leads to a 'hard-core' cross section between 79 - 154 $\AA^2$. Finally, the calculated elastic cross section for OH-H_2 of 200 $\AA^2$ was used, where OH is in the F1(J=3/2,f) state. This leads to a probability of 10^{-5} for a subsequent collision with H_2 during the lifetime of the OH-H_2 complex. Therefore, this scenario is ruled out. Even if a secondary collision takes place, it will not account for the decrease of the cross section by 50%.

3. **Kinematic effects I:** The dynamics at resonance can influence the kinematics of the particles. Here, two different effects can play role. The DCS can undergo big changes under resonance conditions [138]. In this system OH is mainly forward scattered. However, at resonance it can happen that the DCS changes and the particles are preferentially backscattered. In this case, they would fly out of the laser detection volume earlier, which could lead to conditions, where the flux mode would not be fulfilled anymore. Then a lower scattering signal would be measured.

   However, from an experimental point of view, the OH-H_2 system is a kinematic favourable system to ensure conditions of flux-mode because of the large mass difference between OH and H_2. The OH radicals hardly change their direction of flight after a collision. No matter if they are forward, sideward or backward scattered, the remaining recoil velocity is very small compared to $\underline{v}_{CM}$ just above threshold of F1(J=5/2,e) state, which basically defines the direction of propagation in the lab frame. Additionally, the DCS is calculated theoretically for various collision energies below and above the resonance at 93.2 cm^{-1}, which is presented in more detail in Appendix D. Forward scattering is observed in all calculations, which excludes the possibility not to have fulfilled the flux-mode conditions.

4. **Kinematic effects II:** A second, related scenario could be alignment of the scattering products during the collision process at resonance. In this experimental setup, the laser is linearly polarized in the vertical direction. This is perpendicular to the scattering plane, which is defined by the velocity vectors of the two incoming beams. If the OH radicals were aligned preferentially in the vertical direction, the transition dipole moment in OH would be parallel to the laser polarization and the probability of a laser excitation would become very small. Effectively, this would lead to less detected molecules, which results in a decrease of the cross section.

   The alignment after the collision is quantified by calculating the

DCS for each specific OH substate with different $|m_j| = 1/2$, 3/2 and 5/2. In Appendix D the DCS is illustrated at lower or higher collision energies relative to 93.25 cm^{-1}, where theory predicts the shape resonance. Considerable changes are neither observed in the DCS, nor for a specific OH substate as a function of $|m_j|$. It must be concluded that it is not possible from a kinematic point of view to explain the decrease of the cross section due to a loss of scattering products out of the detection volume nor due to alignment effects of the OH radicals.

5. **Para-to-ortho conversion in $\mathbf{H_2}$** The investigations in this paragraph aim around the question, if something happens at resonance during the lifetime of the complex. The interaction of the paramagnetic moment of the OH radical might convert pH$_2$ into oH$_2$ during the complex-lifetime of about 50 ps. The conversion from pH$_2$(J=0) into oH$_2$(J=1) is energetically possible, because additionally to the collision energy of ≈93 cm^{-1} a weakly attractive van-der-Waals potential is present at distances between 2.8 - 5.8 $\mathring{A}$, which is several tens of wavenumbers deep [159]. The binding energy is calculated to be 36.1 cm^{-1} and 53.7 cm^{-1} for complexes of OH(X $^2\Pi$, v=0, J=3/2) with H$_2$(J=0) and H$_2$(J=1), respectively [132]. The OH-oH$_2$(J=1) complex has been measured to be 54 cm^{-1} [159]. The rotational inelastic excitation from pH$_2$(J=0) into oH$_2$(J=1) needs 118 cm^{-1}, while the nuclear spins in H$_2$ must flip simultaneously. The resulting OH-oH$_2$ complex would not have enough energy to dissociate within the lifetime of the resonance, it would be bound for much longer time until a backconversion would happen from oH$_2$(J=1) to pH$_2$(J=0). A loss in the detected OH signal of the F1(5/2,e) state would be measured, because the laser would not be resonant to the transition of the OH-oH$_2$(J=1) complex.

The conversion probability to induce an para-to-ortho conversion in a single collision between H$_2$ and O$_2$ is calculated, based on the publication from Shawn Wagner [48], where the pH$_2$ to oH$_2$ velocity constant is determined near room temperature from different mixtures of H_2 and O_2. Since the magnetic moment of O_2 is comparable to the one in OH, such para-to-ortho conversions are likely to happen in molecular collisions. Some assumptions on the collisional cross sections between H_2 and O_2 are made in favour of the conversion rate. The result shows that roughly a probability of 10^{-6} (1 out of 10^6 collisions) induces a conversion. Although the results of the O_2-H_2 calculations are hardly comparable to OH-H_2 conditions, because the experimental setups and conditions are different, the extremely low conversion probability indicates that this effect is very unlikely to happen in every second collision to cause a decrease of the cross section of 50 %.

The para-to-ortho conversion probability is also theoretically estimated on a qualitative basis in greater detail [132]. The magnitude of the coupling term to induce a para-to-ortho conversion is given by the magnetic dipole-dipole coupling between the OH electronic spin and orbital angular momentum and the nuclear spin angular momentum of each individual H_2 proton. The conversion is exclusively caused by the difference between the two dipole-dipole coupling terms of the two protons in H_2. The magnitude of this coupling is extremely small, because the OH magnetic dipole moment is on the order of a Bohr magneton, while the protons' nuclear angular momenta are only half of a nuclear magneton, which is nearly 2000 times smaller than the Bohr magneton. The estimated magnitude of the coupling term is only on the order of 10^{-4} cm^{-1}. If this is compared to the size of the terms in the anisotropic potential (10 - 100 cm^{-1}) that induce the inelastic processes, one may expect that the cross section for a para-to-ortho conversion is extremely small. Therefore, no further quantitative analysis is undertaken and the para-to-ortho conversion is found to be too improbable to be the effect causing the decrease of the cross section around 93 cm^{-1}.

8.4 Conclusion

The collision energy resolution in this experiment is increased by an order of magnitude using two methods that can be applied in general in crossed beam scattering experiments. The first method is to choose a favourable geometry of the crossed beams, which has been proposed by Scharfenberg and coworkers [109]. The second method is to decrease the influence of the particular velocity distribution, which has the largest influence on the collision energy distribution. The threshold of the same rotational inelastic transition is measured with different collision energy resolutions. Two different theoretical models are used to calculate values for the collision energy distribution. The convolution of theoretical excitation functions with these values allows a quantitative comparison between these models, once they are scaled onto the experimentally determined cross sections. Qualitatively, the excitation function convoluted with the predicted values of the two models coincide well with the experimental cross sections in all three cases. However, the excitation function convoluted with $\Delta^{exp}_{FWHM}E$ fits best within the experimentally determined cross sections and their confidence intervals.

A comparison of both models conjectures an overestimation of parameters in the analytical case, where the mean translational velocities and the whole velocity distributions are used. On a quantitative base the collision energy resolution appears to be better than calculated from the analytic model [109]. Throughout the experiment, careful analysis of the kinematics during the scattering process turned out to be indispensable to calibrate the collision energy and the collision energy distribution. A kinematic model is developed, which describes the creation of scattering products, the collision energy and the collision energy distribution as a function of the colliding packets' overlap in time. The particle packets are modeled by 6D probability number-density distribution in phase-space. The theoretical model is presented for continuous 6D distributions. The simulated values of the expected collision energy and the expected collision energy distribution agree better as the ones from pure analytic calculations. The numerical implementation of the kinematic model is achieved by Monte-Carlo simulations, where discrete 6D PSD are used. This offers several advantages for the quantitative calibration of the collision energy and its distribution: (1) the non-uniform PSDs of Stark-decelerated OH packets, which are well known from trajectory simulations, are included directly; (2) correlations of the PSD in free-flight are accurately implemented; (3) the number-density distributions are included naturally; (4) the collision energy and its distribution is modeled as a function of the overlap in time in analogy to the overlap of the two packets in the experiment. More detailed alterations within the kinematic model might overcome certain numerical limitations and promise even better agreement with the experimental results.

Both models predict an even further increase of the collision energy resolution by reducing the collimation slit-width on the target beam side. In this setting the highest collision energy resolution is observed, which is found to be better than 2 cm^{-1}. Deviations within the excitation function are resolved and are reproduced under different experimental circumstances. The theoretical excitation function, which is convoluted with the experimental collision energy resolution, reproduce the experimentally determined excitation function within the error bars. However, a striking discrepancy is observed around 93 cm^{-1}. Here, theory predicts an increase in the cross section due to a shape resonance. In contrast, the experimentally determined cross sections decrease by a factor of two within the energy range of the resonance. Several possible scenarios of underlying dynamics are investigated in detail. At the moment the conclusion is that within all the capabilities available, the experimental and theoretical excitation functions do not coincide around the resonance. The physical origin for this discrepancy remains unexplained.

Chapter 9

Conclusion

In this thesis a next step has been done to achieve more control over the degrees of freedom of a molecular beam using a Stark-decelerator. This enabled to perform molecular spectroscopy and scattering experiments with a higher resolution.

The general implementation of bunching schemes of a molecular packet in the transverse direction and combinations of both, the longitudinal and the transverse directions inside a Stark-decelerator is demonstrated. By using different $\pm HV$-switching schemes individual dimensions of the phase-space distribution of the molecular packet are manipulated using a common Stark-decelerator setup only. Bunching schemes are implemented to focus the phase-space distributions in their velocity-spaces such that temperatures are generated in these dimensions corresponding to several hundreds of micro-Kelvin. The temperature of the corresponding bunched dimension is decreased by at least an order of magnitude compared to a normally Stark-decelerated packet. In general, this allows to shape the phase-space distribution of the molecular packet to suit best for the subsequent experimental requirements. Depending on the experimental setup and requirements an optimum set for of parameters can be found from simulations. In particular, the transverse bunching became a prerequisite for the high resolution spectroscopy performed in chapter 5. The 2D-bunching can be used to minimize the velocity distributions in the scattering plane of a crossed beam experiment leading to an increase of the collision energy resolution. The optimization of loading a molecular packet into a trap are possible applications of the 3D-bunching.

These transverse cooled OH beams are used to perform high resolution spectroscopy. By applying static electric and magnetic fields in a controlled manner, the amplitude from magnetic and electric dipole transitions are mixed into one signal at a comparable intensity. Three different methods are realized in the experimental setup, which enable measurements to directly compare magnetic and electric transition dipole moments, although they differ by orders of magnitude. Stark-spectroscopy is used to determine the ratio of the electric and the magnetic transition dipole moments along the $A-X$ band by externally applying a static electric field in a controlled manner. By additionally superimposing a static magnetic field a Stark-interference is observed allowing not only to determine the ratio of the electric and the magnetic transition dipole moments but also their relative sign. The resulting comparison is very accurate and excludes many systematic errors present in previous studies [44]. The theoretically calculated ratio of the two transition dipole moments could be reproduced within an error of less than 2% with all three methods presented here.

This general technique requires a single laser power, which does not have to be calibrated. Additionally, a single detection method is used, which does not need to be calibrated either. This allows to measure lines with signals that are two orders of magnitude higher than the intensity of the magnetic dipole one, and nevertheless deduce the magnetic transition dipole moment within a couple of percents, and of course as a signed quantity. The method can easily be applied to many other transitions in OH, and also to many other molecular systems. In general, accurate experimental data are crucial for improving theoretical descriptions. In the OH A-X case, the most recent theoretical calculations of the dipole moments might suffer from systematic errors induced by the Born-Oppenheimer approximation, through the relevant Franck-Condon factors [101] [44]. However, these systematic errors must be less or equal to 2% given the accuracy and reproducability of the three presented results.

In the first scattering experiment state-to-state rotational inelastic scattering of quantum-state selected OH radicals ($X^2\Pi_{3/2}$, J=3/2, f) with hydrogen molecules in two distinct rotational quantum states - $pH_2(J=0)$ and $oH_2(J=1)$ is presented. Relative cross sections are determined within a collision energy range between 70 cm^{-1} and 150 cm^{-1}. The threshold behaviour for rotational and spin-orbit changing inelastic excitations is clearly resolved. Two different H_2 mixtures (nH_2 and pcH_2) are used as target beams of OH in the experiment, which consist of different ratios of $pH_2(J=0)$ and $oH_2(J=1)$. The observed relative cross sections show large differences when the strength of the various final states and their intensity is compared. The contributions of the $pH_2(J=0)$ and $oH_2(J=1)$ to the corresponding cross sections is disentangled, which reflects the mutually different influence of multipole-interactions in the scattering process. Theoretical absolute integral cross sections are derived from quantum close-coupling scattering calculations performed on a newly state-of-the-art compiled *ab initio* OH-H_2 PES.

Qualitatively and quantitatively the results show overall a very good agreement between theory and experiment. The comparison of relative cross sections showed that scattering of OH with $pH_2(J=0)$ behaves similar to the OH-helium system, since the quadrupole moment and even higher multipole-moments in $pH_2(J=0)$ average to zero. Strong propensities for parity conserving transitions are found in accordance with theory. The relative cross sections of OH colliding with $oH_2(J=1)$ shows no propensities at all. This behaviour of the cross sections originate from different multipole-interactions, which are present in the $oH_2(J=1)$ collisions. Especially the OH-dipole - H_2-quadrupole and the OH-quadrupole - H_2-quadrupole interactions dominate. The theoretical relative cross sections, which includes these multipole-interactions, show an excellent agreement with the experimental data even within the error bars. A different comparison between theory and experiment is made, when the ratio of the measured signal intensities is compared to the ratio of the calculated absolute integral cross sections. The experimentally determined ratios agree with the theoretical ones within the experimental error bars. In general, the intensity of the interactions is observed to be on average 2.5 to 3 times stronger for collisions between OH-$oH_2(J=1)$ compared to OH-$pH_2(J=0)$.

A second scattering experiment aims on the increase of the collision energy resolution by an order of magnitude using two methods that can be applied in general in crossed beam scattering experiments. The first method is to choose a favourable geometry of the crossed beams, which has been proposed by Scharfenberg and coworkers [109]. The second strategy is to decrease the influence of the particular velocity distribution, which has the largest influence on the collision energy distribution. In the experiment the threshold of the same rotational inelastic transition is measured using these different approaches, where the collision energy resolution appears to be better than calculated from the analytic model [109]. A kinematic model is developed, which describes the creation of scattering products, the collision energy and the collision energy distribution as a function of the colliding packets' overlap in time. The particle packets are modeled by 6D probability number-density distribution in phase-space. Throughout the experiment, this careful analysis of the kinematics during the scattering process turned out to be indispensable to calibrate the collision energy and the collision energy distribution on a quantitative base correctly. The methods presented here to increase the collision energy resolution are in general applicable to crossed beam setups at any collision energy.

In the setting where the highest collision energy resolution is observed, it is found to be better than 2 cm^{-1}. Sharp structures in the excitation function are resolved and are reproduced under different experimental circumstances. The theoretical excitation function, which is convoluted with the experimental collision energy resolution, reproduce the experimentally determined excitation function within the error bars. However, a striking discrepancy is observed around 93 cm^{-1}. Here, theory predicts an increase in the cross section due to a shape resonance. In contrast, the experimentally determined cross sections decrease by a factor of two within the energy range of the resonance. Several possible scenarios of underlying dynamics are investigated in detail, both experimentally and theoretically. The conclusion for the moment is that the physical origin for this discrepancy remains unexplained, leaving an open question to be investigated further.

Bibliography

[1] Krems, R. V. *Physical Chemistry Chemical Physics* **2008**, *10*, 4079.

[2] Hutzler, N. R.; Lu, H.; Doyle, J. M. *Chemical Reviews* **2012**, *112*, 4803.

[3] van de Meerakker, S. Y. T.; Bethlem, H. L.; Vanhaecke, N.; Meijer, G. *Chemical Reviews* **2012**, *112*, 4828.

[4] Narevicius, E.; Raizen, M. G. *Chemical Reviews* **2012**, *112*, 4879.

[5] Jones, K. M.; Tiesinga, E.; Lett, P. D.; Julienne, P. S. *Reviews of Modern Physics* **2006**, *78*, 483.

[6] Kohler, T.; Goral, K.; Julienne, P. S. *Reviews of Modern Physics* **2006**, *78*, 1311.

[7] Jin, D. S.; Ye, J. *Physics Today* **2011**, *64*, 27.

[8] Jin, D. S.; Ye, J. *Chemical Reviews* **2012**, *112*, 4801.

[9] Scoles, G. *Atomic and molecular beam methods*; Oxford University Press: New York, NY, USA, 1988 & 1992; Vol. 1 & 2.

[10] Levine, R. D.; Bernstein, R. B. *Molecular reaction dynamics and chemical reactivity*; Oxford University Press, 1987.

[11] Pauly, H. *Atom, Molecule, and Cluster Beams*; Springer Series on Atomic, Optical, and Plasma Physics, Vol. 1 & 2; Springer Verlag, 2000.

[12] Hillenkamp, M.; Keinan, S.; Even, U. *The Journal of Chemical Physics* **2003**, *118*, 8699.

[13] Irimia, D.; Dobrikov, D.; Kortekaas, R.; Voet, H.; van den Ende,

D. A.; Groen, W. A.; Janssen, M. H. M. *Review of Scientific Instruments* **2009**, *80*, 113303.

[14] Yan, B.; Claus, P. F. H.; van Oorschot, B. G. M.; Gerritsen, L.; Eppink, A. T. J. B.; van de Meerakker, S. Y. T.; Parker, D. H. *Review of Scientific Instruments* **2013**, *84*, 023102.

[15] Chefdeville, S.; Kalugina, Y.; van de Meerakker, S. Y. T.; Naulin, C.; Lique, F.; Costes, M. *Science* **2013**, *341*, 1094.

[16] Henson, A. B.; Gersten, S.; Shagam, Y.; Narevicius, J.; Narevicius, E. *Science* **2012**, *338*, 234.

[17] Jankunas, J.; Bertsche, B.; Jachymski, K.; Hapka, M.; Osterwalder, A. *The Journal of Chemical Physics* **2014**, *140*, 244302.

[18] Ni, K.-K.; Ospelkaus, S.; Wang, D.; Quemener, G.; Neyenhuis, B.; de Miranda, M. H. G.; Bohn, J. L.; Ye, J.; Jin, D. S. *Nature* **2010**, *464*, 1324.

[19] Ospelkaus, S.; Ni, K.-K.; Wang, D.; de Miranda, M. H. G.; Neyenhuis, B.; Quemener, G.; P. S. Julienne, P. S.; Bohn, J. L.; Jin, D. S.; Ye, J. *Science* **2010**, *327*, 853.

[20] Even, U.; Jortner, J.; Noy, D.; Lavie, N.; Cossart-Magos, N. *The Journal of Chemical Physics* **2000**, *112*, 8068.

[21] Pentlehner, D.; Riechers, R.; Dick, B.; Slenczka, A.; Even, U.; Lavie, N.; Brown, R.; Luria, K. *Review of Scientific Instruments* **2009**, *80*, 043302.

[22] Stolte, S. In *Atomic and molecular beam methods*; Scoles, G., Ed.; Oxford University Press: New York, NY, USA, 1988; Vol. 1, Chapter 25, pp 631–652.

[23] von Zastrow, A.; Onvlee, J.; Vogels, S. N.; Groenenboom, G. C.; van der Avoird, A.; van de Meerakker, S. Y. T. *Nature Chemistry* **2014**, *6*, 216.

[24] Shuman, E. S.; Barry, J. F.; DeMille, D. *Nature* **2010**, *467*, 820.

[25] Stuhl, B. K.; Hummon, M. T.; Yeo, M.; Quemener, G.; Bohn, J. L.; Ye, J. *Nature* **2012**, *492*, 396.

[26] Herzberg, G. *Molecular spectra and molecular structure: Spectra of diatomic molecules*; Krieger Publishing Company: Malabar, Fl, USA, 1989; Vol. 1.

[27] Zare, R. N. *Angular momentum*; John Wiley & Sons: New York, NY, USA, 1988.

[28] Brown, J. M.; Carrington, A. *Rotational spectroscopy of diatomic molecules*; Cambridge University Press, 2003.

[29] Dieke, G. H.; Crosswhite, J. *Journal of Quantitative Spectroscopy and Radiative Transfer* **1962**, *2*, 97.

[30] Hain, T. D.; Weibel, M. A.; Backstrand, K. M.; Curtiss, T. J. *Journal of Physical Chemistry A* **1997**, *101*, 7674.

[31] Freed, K. F. *The Journal of Chemical Physics* **1966**, *45*, 4214.

[32] Dousmanis, G. C.; Sanders, T. M.; Townes, C. H. *Physical Review* **1955**, *100*, 1735.

[33] Meerts, W. *Chemical Physics Letters* **1977**, *46*, 24.

[34] Brown, J.; Hougen, J.; Huber, K.-P.; Johns, J.; Kopp, I.; Lefebvre-Brion, H.; Merer, A.; Ramsay, D.; Rostas, J.; Zare, R. *Journal of Molecular Spectroscopy* **1975**, *55*, 500.

[35] Meerts, W.; Dymanus, A. *Chemical Physics Letters* **1973**, *23*, 45.

[36] ter Meulen, J. J. T.; Majewski, W. A.; Meerts, W. L.; Dymanus, A. *Chemical Physics Letters* **1983**, *94*, 25.

[37] ter Meulen, J. J. T.; Ubachs, W.; Dymanus, A. *Chemical Physics Letters* **1986**, *129*, 533.

[38] Peterson, K. I.; Fraser, G. T.; Klemperer, W. *Canadian Journal of Physics* **1984**, *62*, 1502.

[39] Townes, C. H.; Schawlow, A. L. *Microwave Spectroscopy*; Dover

Publications: New York, 1975.

[40] Ticknor, C.; Bohn, J. L. *Physical Review A* **2005**, *71*, 022709.

[41] Meerts, W. L.; Dymanus, A. *Chemical Physics Letters* **1973**, *23*, 45.

[42] Meerts, W.; Veseth, L. *Journal of Molecular Spectroscopy* **1980**, *82*, 202.

[43] Brown, J.; Kaise, M.; Kerr, C.; Milton, D. *Molecular Physics* **1978**, *36*, 553.

[44] Kirste, M.; Wang, X.; Meijer, G.; Gubbels, K. B.; van der Avoird, A.; Groenenboom, G. C.; van de Meerakker, S. Y. T. *The Journal of Chemical Physics* **2012**, *137*, 101102.

[45] Luque, J.; Crosley, D.; *LIFBASE: Database and Spectral Simulation Program (Version 1.5) î, SRI International Report MP 99-009.*

[46] Corney, A. *Atomic and Laser Spectroscopy (Oxford Classic Texts in the Physical Sciences)*; Oxford University Press: London, 2006.

[47] Kirste, M.; Wang, X.; Schewe, H. C.; Meijer, G.; Liu, K.; van der Avoird, A.; Janssen, L. M. C.; Gubbels, K. B.; Groenenboom, G. C.; van de Meerakker, S. Y. T. *Science* **2012**, *338*, 1060.

[48] Wagner, S. *Magma (New York, N.Y.)* **2014**, *27*, 195.

[49] Silvera, I. F. *Reviews of Modern Physics* **1980**, *52*, 393.

[50] Pratt, S.; Dehmer, P.; Dehmer, J. *Chemical Physics Letters* **1984**, *105*, 28.

[51] van de Meerakker, S. Y. T.; Bethlem, H. L.; Meijer, G. *Nature Physics* **2008**, *4*, 595.

[52] Bethlem, H. L.; Berden, G.; Meijer, G. *Physical Review Letters* **1999**, *83*, 1558.

[53] Scharfenberg, L.; Ph. D. thesis; Technische Universität; Berlin, Deutschland; 2012.

[54] Faircloth, D. C. **2014**, 39 p; Comments: 39 pages, contribution to

the CAS-CERN Accelerator School: Ion Sources, Senec, Slovakia, 29 May - 8 June 2012, edited by R. Bailey, CERN-2013-007.

[55] Bethlem, H. L.; Crompvoets, F. M. H.; Jongma, R. T.; van de Meerakker, S. Y. T.; Meijer, G. *Physical Review A* **2002**, *65*, 053416.

[56] van de Meerakker, S. Y. T.; Vanhaecke, N.; Bethlem, H. L.; Meijer, G. *Physical Review A* **2006**, *73*, 023401.

[57] Scharfenberg, L.; Haak, H.; Meijer, G.; van de Meerakker, S. Y. T. *Physical Review A* **2009**, *79*, 023410.

[58] van de Meerakker, S. Y. T.; Vanhaecke, N.; Bethlem, H. L.; Meijer, G. *Physical Review A* **2005**, *71*, 053409.

[59] Gubbels, K.; Meijer, G.; Friedrich, B. *Physical Review A* **2006**, *73*, 063406.

[60] Putzke, S.; Ph. D. thesis; Freie Universität Berlin; Berlin, Deutschland; 2012.

[61] Carr, L. D.; DeMille, D.; Krems, R. V.; Ye, J. *New Journal of Physics* **2009**, *11*, 055049.

[62] van Veldhoven, J.; Küpper, J.; Bethlem, H. L.; Sartakov, B.; van Roij, A. J. A.; Meijer, G. *The European Physical Journal D* **2004**, *31*, 337.

[63] Hudson, E. R.; Lewandowski, H. J.; Sawyer, B. C.; Ye, J. *Physical Review Letters* **2006**, *96*, 143004.

[64] Hudson, J. J.; Kara, D. M.; Smallman, I. J.; Sauer, B. E.; Tarbutt, M. R.; Hinds, E. A. *Nature* **2011**, *473*, 493.

[65] Truppe, S.; Hendricks, R.; Tokunaga, S.; Lewandowski, H.; Kozlov, M.; Henkel, C.; Hinds, E.; Tarbutt, M. *Nature Communications* **2013**, *4*.

[66] Gilijamse, J. J.; Hoekstra, S.; van de Meerakker, S. Y. T.; Groenenboom, G. C.; Meijer, G. *Science* **2006**, *313*, 1617.

[67] Crompvoets, F. M. H.; Bethlem, H. L.; Jongma, R. T.; Meijer, G.

Nature **2001**, *411*, 174.

[68] Heiner, C. E.; Carty, D.; Meijer, G.; Bethlem, H. L. *Nature Physics* **2007**, *3*, 115.

[69] Zieger, P. C.; van de Meerakker, S. Y. T.; Heiner, C. E.; Bethlem, H. L.; van Roij, A. J. A.; Meijer, G. *Physical Review Letters* **2010**, *105*, 173001.

[70] Bethlem, H. L.; Berden, G.; Crompvoets, F. M. H.; Jongma, R. T.; van Roij, A. J. A.; Meijer, G. *Nature* **2000**, *406*, 491.

[71] van de Meerakker, S. Y. T.; Smeets, P. H. M.; Vanhaecke, N.; Jongma, R. T.; Meijer, G. *Physical Review Letters* **2005**, *94*, 023004.

[72] Sawyer, B. C.; Lev, B. L.; Hudson, E. R.; Stuhl, B. K.; Lara, M.; Bohn, J. L.; Ye, J. *Physical Review Letters* **2007**, *98*, 253002.

[73] van de Meerakker, S. Y. T.; Vanhaecke, N.; van der Loo, M. P. J.; Groenenboom, G. C.; Meijer, G. *Physical Review Letters* **2005**, *95*, 013003.

[74] Hoekstra, S.; Gilijamse, J. J.; Sartakov, B.; Vanhaecke, N.; Ludwig; van de Meerakker, S. Y. T.; Meijer, G. *Physical Review Letters* **2007**, *98*, 133001.

[75] Gilijamse, J. J.; Hoekstra, S.; Meek, S. A.; Metsälä, M.; de Meerakker, S. Y. T. v.; Meijer, G.; Groenenboom, G. C. *The Journal of Chemical Physics* **2007**, *127*, 221102.

[76] Baranov, M.; Dobrek, L.; Góral, K.; Santos, L.; Lewenstein, M. *Physica Scripta* **2002**, *T102*, 74.

[77] Ketterle, W.; Pritchard, D. E. *Physical Review A* **1992**, *46*, 4051.

[78] Wangler, T. P. *RF linear accelerators*; Wiley-VCH: Weinheim, 2008; Vol. 2., compl. rev. and enlarged ed.

[79] Hinterberger, F. *Physik der Teilchenbeschleuniger und Ionenoptik : mit durchgerechneten Beispielen und 105 Uebungsaufgaben mit vollstaendigen Loesungen*; Springer: Berlin [u.a.], 2008; Vol. 2. Aufl.

[80] Lee, S. Y. *Accelerator physics*; Gasdynamics: A Series of Monographs, Vol. Repr.; World Scientific: Singapore, 1999.

[81] Maréchal, E.; Guibal, S.; Bossennec, J.-L.; Barbé, R.; Keller, J.-C.; Gorceix, O. *Physical Review A* **1999**, *59*, 4636.

[82] Myrskog, S. H.; Fox, J. K.; Moon, H. S.; Kim, J. B.; Steinberg, A. M. *Physical Review A* **2000**, *61*, 053412.

[83] Chu, S.; Bjorkholm, J. E.; Ashkin, A.; Gordon, J. P.; Hollberg, L. W. *Optics Letters* **1986**, *11*, 73.

[84] Ammann, H.; Christensen, N. *Physical Review Letters* **1997**, *78*, 2088.

[85] Summhammer, J.; Niel, L.; Rauch, H. *Zeitschrift fur Physik B* **1986**, *62*, 269.

[86] Crompvoets, F. M. H.; Jongma, R. T.; Bethlem, H. L.; van Roij, A. J. A.; Meijer, G. *Physical Review Letters* **2002**, *89*, 093004.

[87] Crompvoets, F. M. H.; Bethlem, H. L.; Küpper, J.; van Roij, A. J. A.; Meijer, G. *Physical Review A* **2004**, *69*, 063406.

[88] Wedler, G. *Lehrbuch der physikalischen Chemie*; Gasdynamics: A Series of Monographs, Vol. 5. Auflage; Wiley-VCH-Verlag: Weinheim, 1999.

[89] van de Meerakker, S. Y. T.; Jongma, R. T.; Bethlem, H. L.; Meijer, G. *Physical Review A* **2001**, *64*, 041401.

[90] Falkenau, M.; Volchkov, V.; Rührig, J.; Griesmaier, A.; Pfau, T. *Physical Review Letters* **2011**, *106*, 163002.

[91] Kirste, M.; Sartakov, B. G.; Schnell, M.; Meijer, G. *Physical Review A* **2009**, *79*, 051401(R).

[92] Meek, S.; Santambrogio, G.; Sartakov, B.; Conrad, H.; Meijer, G. *Phys. Rev. A* **2011**, *83*, 033413.

[93] Vanhaecke, N.; *private communication*; 2014.

[94] DeMille, D. *Physical Review Letters* **1995**, *74*, 4165.

[95] Bowers, C. J.; Budker, D.; Freedman, S. J.; Gwinner, G.; Stalnaker, J. E.; DeMille, D. *Physical Review A* **1999**, *59*, 3513.

[96] Loftus, T. H.; Swallows, M. D.; Griffith, W. C.; Romalis, M. V.; Heckel, B. R.; Fortson, E. N. *Physical Review Letters* **2011**, *106*, 253002.

[97] Bouchiat, M. A.; Bouchiat, C. *Journal de Physique France* **1975**, *36*, 493.

[98] Gilbert, S. L.; Watts, R. N.; Wieman, C. E. *Physical Review A* **1984**, *29*, 137.

[99] Noecker, M. C.; Masterson, B. P.; Wieman, C. E. *Physical Review Letters* **1988**, *61*, 310.

[100] Wood, C. S.; Bennett, S. C.; Cho, D.; Masterson, B. P.; Roberts, J. L.; Tanner, C. E.; Wieman, C. E. *Science* **1997**, *275*, 1759.

[101] van der Loo, M. P. J.; Groenenboom, G. C. *The Journal of Chemical Physics* **2007**, *126*, 114314.

[102] Sartakov, B.; *private communication*; 2014.

[103] Shuman, E. S.; Barry, J. F.; DeMille, D. *Nature* **2010**, *467*, 820.

[104] Hummon, M. T.; Yeo, M.; Stuhl, B. K.; Collopy, A. L.; Xia, Y.; Ye, J. *Physical Review Letters* **2013**, *110*, 143001.

[105] Barry, J. F.; McCarron, D. J.; Norrgard, E. B.; Steinecker, M. H.; DeMille, D. *Nature* **2014**, *512*, 286.

[106] Stuhl, B. K.; Sawyer, B. C.; Wang, D.; Ye, J. *Phys. Rev. Lett.* **2008**, *101*, 243002.

[107] Scharfenberg, L.; Kłos, J.; Dagdigian, P. J.; Alexander, M. H.; Meijer, G.; van de Meerakker, S. Y. T. *Physical Chemistry Chemical Physics* **2010**, *12*, 10660.

[108] Kirste, M.; Scharfenberg, L.; Kłos, J.; Lique, F.; Alexander, M. H.;

Meijer, G.; van de Meerakker, S. Y. T. *Physical Review A* **2010**, *82*, 042717.

[109] Scharfenberg, L.; van de Meerakker, S. Y. T.; Meijer, G. *Physical Chemistry Chemical Physics* **2011**, *13*, 8448.

[110] Naulin, C.; Costes, M.; Benseddik, A.; Dorthe, G. *Laser Chemistry* **1988**, *8*, 283.

[111] Sonnenfroh, D. M.; Liu, K. *Chemical Physics Letters* **176**, *183*, 1991.

[112] Eyles, C. J.; Brouard, M.; Chadwick, H.; Hornung, B.; Nichols, B.; Yang, C.-H.; Klos, J.; Aoiz, F. J.; Gijsbertsen, A.; Wiskerke, A. E.; Stolte, S. *Physical Chemistry Chemical Physics* **2012**, *14*, 5403.

[113] McBane, G. C. *Simulation and Analysis of Image Data from Crossed Beam Experiments*; Chapter 14, p 215.

[114] Shagam, Y.; Narevicius, E. *The Journal of Physical Chemistry C* **2013**, *117*, 22454–22461.

[115] Andresen, P.; H‰usler, D.; L¸lf, H. W. *The Journal of Chemical Physics* **1984**, *81*, 571.

[116] Loomis, R. A.; Schwartz, R. L.; Lester, M. I. *The Journal of Chemical Physics* **1996**, *104*, 6984.

[117] Forster, P.; Ramaswamy, V.; Artaxo, P.; Berntsen, T.; Betts, R.; Fahey, D.; Haywood, J.; Lean, J.; Lowe, D.; Myhre, G.; Nganga, J.; Prinn, R.; Raga, G.; Schulz, M.; Dorland, R. V. *Changes in Atmospheric Constituents and in Radiative Forcing. In: Climate Change 2007: The Physical Science Basis. Contribution of Working Group I to the Fourth Assessment Report of the Intergovernmental Panel on Climate Change [Solomon, S., D. Qin, M. Manning, Z. Chen, M. Marquis, K.B. Averyt, M.Tignor and H.L. Miller (eds.)]*; Cambridge University Press: Cambridge, United Kingdom and New York, NY, USA, 2007.

[118] Schreel, K.; ter Meulen, J. J. T. *The Journal of Chemical Physics* **1996**, *105*, 4552.

[119] Skouteris, D.; Manolopoulos, D. E.; Bian, W.; Werner, H. J.; Lai, L. H.; Liu, K. *Science* **1999**, *286*, 1713.

[120] Skodje, R. T.; Skouteris, D.; Manolopoulos, D. E.; Lee, S. H.; Dong, F.; Liu, K. *Physical Review Letters* **2000**, *85*, 1206.

[121] Toennies, J. P.; Welz, W.; Wolf, G. *The Journal of Chemical Physics* **1976**, *64*, 5305.

[122] Toennies, J. P.; Welz, W.; Wolf, G. *The Journal of Chemical Physics* **1979**, *71*, 614.

[123] Andresen, P.; Aristov, N.; Beushausen, V.; H‰usler, D.; L¸lf, H. W. *The Journal of Chemical Physics* **1991**, *95*, 5763.

[124] Schinke, R.; Andresen, P. *The Journal of Chemical Physics* **1984**, *81*, 5644.

[125] Dewangan, D. P.; Flower, D. R.; G., D. *Journal of Physics B: Atomic, Molecular and Optical Physics* **1986**, *19*, 747.

[126] Corey, G. C.; Alexander, M. H. *The Journal of Chemical Physics* **1988**, *88*, 6931.

[127] Offer, A. R.; van Hemert, M. C. *The Journal of Chemical Physics* **1993**, *99*, 3836.

[128] Offer, A. R.; Hemert, M. C. v.; Dishoeck, E. F. v. *The Journal of Chemical Physics* **1994**, *100.*

[129] Kochanski, E.; Flower, D. *Chemical Phyics* **1981**, *57*, 217.

[130] Miller, S. M.; Clary, D. C.; Kliesch, A.; Werner, H.-J. *Molecular Physics* **1994**, *83*, 405.

[131] Ma, Q.; Kłos, J.; Dagdigian, P. J.; Alexander, M. H.; *private communication*; 2013.

[132] van der Avoird, A.; *private communication*; 2013.

[133] Ma, Q.; Kłos, J.; Alexander, M. H.; van der Avoird, A.; Dagdigian, P. J. *The Journal of Chemical Physics* **2014**, *141*, 174309.

[134] HIBRIDON; *is a package of programs for the time-independent quantum treatment of inelastic collisions and photodissociation written by M. H. Alexander, D. E. Manolopoulos, H.-J. Werner, B. Follmeg, and others. More information and/or a copy of the code can be obtained from the website, http://www2.chem.umd.edu/groups/alexander/hibridon/hib43.*

[135] Scharfenberg, L.; Gubbels, K. B.; Kirste, M.; Groenenboom, G. C.; van der Avoird, A.; Meijer, G.; van de Meerakker, S. Y. T. *The European Physical Journal D* **2011**, *65*, 189.

[136] Oka, T. *Advances in Atomic and Molecular Physics* **1973**, *9*, 127.

[137] Andresen, P. *Astronomy and Astrophysics* **1986**, *154*, 42.

[138] Gubbels, K. B.; Ma, Q.; Alexander, M. H.; Dagdigian, P. J.; Tanis, D.; Groenenboom, G. C.; van der Avoird, A.; van de Meerakker, S. Y. T. *The Journal of Chemical Physics* **2012**, *136*, 144308.

[139] Sarma, G.; Marinakis, S.; ter Meulen, J. J.; Parker, D. H.; McKendrick, K. G. *Nature Chemistry* **2012**, *4*, 985.

[140] Sarma, G.; Saha, A. K.; ter Meulen, J. J.; Parker, D. H.; Marinakis, S. *The Journal of Chemical Physics* **2015**, *142*, 034309.

[141] Dagdigian, P. J.; Alexander, M. H.; Liu, K. *The Journal of Chemical Physics* **1989**, *91*, 839.

[142] Esposti, A. D.; Berning, A.; Werner, H.-J. *The Journal of Chemical Physics* **1995**, *103*, 2067.

[143] Kołos, W.; Wolniewicz, L. *The Journal of Chemical Physics* **1967**, *46*, 1426.

[144] Machado, A. M.; Masili, M. *The Journal of Chemical Physics* **2004**, *120*, 7505.

[145] Lide, D. R. *CRC Handbook of Chemistry and Physics*; CRC Press: Boca Raton, 1990; Vol. 71.

[146] Child, M. S. *Molecular Collision Theory*; Academic: London/New

York, 1974.

[147] Brouard, M.; Vallance, C. *Tutorials in molecular reaction dynamics*; Royal Society of Chemistry, 2010.

[148] Chandler, D. W. *The Journal of Chemical Physics* **2010**, *132*, 110901.

[149] Zare, R. N. *Science* **2006**, *311*, 1383.

[150] Gubbels, K. B.; Meerakker, S. Y. T. v. d.; Groenenboom, G. C.; Meijer, G.; Avoird, A. v. d. *The Journal of Chemical Physics* **2012**, *136*, 074301.

[151] Schutte, A.; Bassi, D.; Tommasini, F.; Scoles, G. *Physical Review Letters* **1972**, *29*, 979.

[152] Schutte, A.; Bassi, D.; Tommasini, F.; Scoles, G. *The Journal of Chemical Physics* **1975**, *62*, 600.

[153] Grover, J.; Toennies, J.; Welz, W.; Wolf, G. *Chemical Physics Letters* **1977**, *48*, 24.

[154] Kendrick, B. K.; Jayasinghe, L.; Moser, S.; Auzinsh, M.; Shafer-Ray, N. *Physical Review Letters* **2000**, *84*, 4325.

[155] Skodje, R. T.; Skouteris, D.; Manolopoulos, D. E.; Lee, S.-H.; Dong, F.; Liu, K. *The Journal of Chemical Physics* **2000**, *112*, 4536.

[156] Dong, W. R.; Xiao, C. L.; Wang, T.; Dai, D. X.; Yang, X. M.; Zhang, D. H. *Science* **2010**, *327*, 1501.

[157] Berteloite, C.; Lara, M.; Bergeat, A.; Le Picard, S. D.; Dayou, F.; Hickson, K. M.; Canosa, A.; Naulin, C.; Launay, J.-M.; Sims, I. R.; Costes, M. *Physical Review Letters* **2010**, *105*, 203201.

[158] Chefdeville, S.; Stoecklin, T.; Bergeat, A.; Hickson, K. M.; Naulin, C.; Costes, M. *Physical Review Letters* **2012**, *109*, 023201.

[159] Loomis, R. A.; Lester, M. I. *Annual Review of Physical Chemistry* **1997**, *48*, 643.

Appendix A: Bunching for smaller line-widths

The phase-space distributions for the OH molecules at the end of the decelerator is simulated for both low-field seeking Stark components MΩ = -3/4 (black dots) and MΩ = -9/4 (blue dots). The left column of Figure 9.1 shows the results of a normal guiding switching sequence, the right column illustrates the bunched sequence which is used throughout the whole E1-M1 interference experiments. The graphs at the bottom show the corresponding Doppler-profiles. Table 9.1 lists the simulated parameters: temperature (Ty) in [mK] of the OH beam in the transverse horizontal direction along the detection laser, the number of particles which are stably transported through the decelerator as a ratio of the two low-field seeking Stark components, the Doppler-shift in [MHz] and the Doppler-broadening, calculated from the standard deviation of the velocity in the y-direction.

Bunched	’MΩ = -3/4’	’MΩ = -9/4’
Ty	4.3204	4.9026
particle ratio	1	3.0
Doppler-shift	1063	1063
Doppler-broardening	5.15	5.49

Guiding	’MΩ = -3/4’	’MΩ = -9/4’
Ty	8.39	24.88
particle ratio	1	4.3
Doppler-shift	1063	1063
Doppler-broardening	7.18	12.36

Table 9.1: Comparison of the simulated parametres of the OH packet.

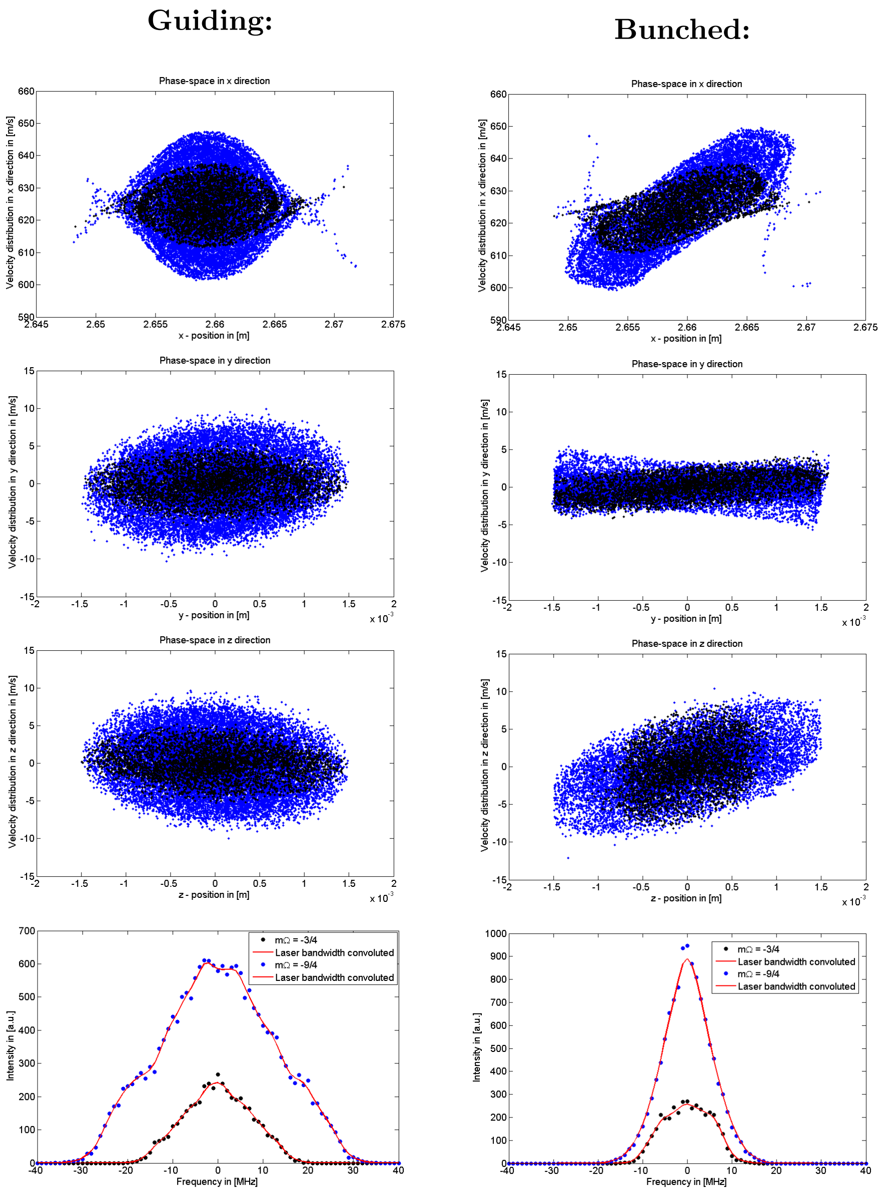

Figure 9.1: The left and the right column shows the comparison of the normally guided and the transverse bunched molecular packets.

The populations and the line profiles of the energy levels in zero field cannot be inferred from the simulated distributions of the 'MΩ = -3/4' and the 'MΩ = -9/4' components, since the <u>*SMF*</u> interferes within rescrambling process. The Doppler profiles of the different energy levels that correspond to F and M_F hyperfine resolved Zeeman sub-states. However, one observes here:

- Although the Doppler-profiles of the 'MΩ = -3/4' has a 'box'-like shape, while the 'MΩ = -9/4' component shows a rather trapeze-like profile, both are symmetric around $v_y = 0$ m/s. The asymmetric line-profiles cannot be explained by the bunching sequence.
- Also shifts in the transition frequencies of individual lines cannot be explained by a Doppler-shift that might have occurred during the optimized switching of the bunching sequence.

Appendix B: Calibration of the static electric and magnetic field

Both graphs of Figure 5.1 show the geometry of the two plates and the two coils which determine the field distributions of $\underline{SEF}$ and $\underline{SMF}$. The combined field configurations are simulated using the commercial software COMSOL. A common ground is used for the current generator which cause $\underline{SMF}$, the positive and negative voltage supplies which create the $\underline{SEF}$, and the whole experimental apparatus.

Calibration of $\underline{SMF}$:

The field strength is measured by using the commercial Tesla metre FM 302 (Projekt Elektronik) and its sensor AS - NTM-2 to calibrate $\underline{SMF}$ in the interaction zone at the centre of the two coils. The coordinate system is defined such that the translational axis of the decelerator is the x-axis, perpendicular to it in the horizontal plane the y-axis (where the cw laser is aligned) and the z-axis the vertically to it as illustrated in Figure 5.1. Table 9.2 shows the measured and the simulated values of $\underline{SMF}$ for the experimental cases of 46 G and -30 G. The measurements demonstrate, that the simulated absolute values for $\underline{SMF}$ are present in the interaction zone. Time dependent measurements showed that the $\underline{SMF}$ is stable with $\leq$1 % within the data-acquisition duration of 25 μs. COMSOL simulations revealed inhomogeneities of the $\underline{SMF}$ to be around 1 %.

Calibration of $\underline{SEF}$:

The positive and negative voltages V are applied to create $\underline{SEF}$ with the dimensions [$\pm V/(25\text{mm})$]. The field strength is determined measuring the applied voltages. The absolute value is $\underline{SEF}$ fluctuates with $\leq$1 %. The

$\underline{SMF}$	$\underline{SMF}_{ex}$ **[G]** (I = 13.4 A)	$\underline{SMF}_{sim}$ **[G]**	$\underline{SMF}_{ex}$ **[G]** (I = 20.0 A)	$\underline{SMF}_{sim}$ **[G]**
$\underline{SMF}_x$	0	0	0	0
$\underline{SMF}_y$	0.1 *pm* 0.6	0	0.0 *pm* 0.7	0
$\underline{SMF}_z$	29.6 *pm* 0.8	30	45.4 *pm* 0.8	46

Table 9.2: The measured values of $\underline{SMF}$ of 46 G and -30 G in columns two and four, respectively. The columns three and five show the simulated values.

inhomogeneities of the $\underline{SEF}$ are radially symmetric to the x-axis due to the holes and the finite size of the capacitor plates. Simulations find the largest deviations along the x-axis to be between 1-1.5 % fo the absolute value.

Appendix C: Formal description of the overlap problem

For reasons of completeness a mathematically formal description is presented in the following to give a different insight to the definition and the formalism, where different values like the collision energy are defined as a function of the overlap of molecular beams in time [93].

Imagine the 6-dimensional (6D) PSDs of two molecular beam are represented by a 6D probability density distribution $P_1(\underline{r}_1, \underline{v}_1, t)$ and $P_2(\underline{r}_1, \underline{v}_2, t)$, respectively. The expected value of any function $\langle f \rangle_t$ of the 12D variables at time t is given by:

$$\langle f \rangle_t = \int_{12D} f(\underline{r}_1, \underline{r}_2, \underline{v}_1, \underline{v}_2, t) \cdot P_1(\underline{r}_1, \underline{v}_1, t) P_2(\underline{r}_2, \underline{v}_2, t) d\underline{r}_1 d\underline{r}_2 d\underline{v}_1 d\underline{v}_2 \tag{9.1}$$

The function f can be defined differently, for example, if one was interested in the expected value of the collision energy, it would follow from: $f = \frac{\mu}{2}\underline{v}_{rel}^2 = \frac{\mu}{2}|\underline{v}_1 - \underline{v}_2|^2$. However, the quantity of interest is not the expected value of f, but the expectation value of f. In example, even if the beams do not meet at all, $\langle f \rangle_t$ is well defined, corresponding to the definition of equation (9.1). From a physics point of view, if one is interested in the mean collision energy, implicitly one is referring to only those pair of particles, which can collide. Therefore the relevant function to use is $f = \frac{\mu}{2}|\underline{v}_1 - \underline{v}_2|^2 \delta_{\underline{r}_1 \underline{r}_2}$, where $\delta_{\underline{r}_1 \underline{r}_2}$ accounts for only those pairs of particles that can collide. At the same time, one needs to count only the pairs of particles which can collide, i.e. normile by the expected value of $\delta_{\underline{r}_1 \underline{r}_2}$ which reflects the 'spatial overlap' of the beams. For example, the (instantaneous) mean collision energy at time t is given by:

$$\langle E\rangle_t^{phys} = \frac{\int_{12D} \frac{\mu}{2}|\underline{v}_1 - \underline{v}_2|^2 \delta_{\underline{r}_1\underline{r}_2} \cdot P_1(\underline{r}_1, \underline{v}_1, t) P_2(\underline{r}_2, \underline{v}_2, t) d\underline{r}_1 d\underline{r}_2 d\underline{v}_1 d\underline{v}_2}{\int_{12D} \delta_{\underline{r}_1\underline{r}_2} \cdot P_1(\underline{r}_1, \underline{v}_1, t) P_2(\underline{r}_2, \underline{v}_2, t) d\underline{r}_1 d\underline{r}_2 d\underline{v}_1 d\underline{v}_2} \tag{9.2}$$

In an experiment, one is not only interested in the instantaneous values of f, but also what has been accumulated up to a certain moment τ. This can be the moment of detection. To sum up the contributions from earlier instantaneous $\langle E\rangle_t^{phys}$ over time a weighted averaging is performed to calculate the expectation value in time up to the moment τ, which is in the following denoted by $\langle\langle E_c\rangle\rangle_\tau^{phys}$. The weighting function is again the spatial overlap, which accounts for the fact that when the overlap is small it should count less, as when the intense parts of the beam collide. This follows from the integration over time starting from the earliest time $(-\infty)$ up to the moment τ:

$$\begin{aligned} \langle\langle E_c\rangle\rangle_\tau^{phys} = & \left[\frac{\int_{-\infty}^{\tau} \langle E\rangle_t^{phys} \cdot \int_{12D} \delta_{\underline{r}_1\underline{r}_2} \cdot P_1(\underline{r}_1, \underline{v}_1, t)}{\int_{-\infty}^{\tau} \int_{12D} \delta_{\underline{r}_1\underline{r}_2} \cdot P_1(\underline{r}_1, \underline{v}_1, t)} \times \right. \\ & \left. \frac{P_2(\underline{r}_2, \underline{v}_2, t) d\underline{r}_1 d\underline{r}_2 d\underline{v}_1 d\underline{v}_2 dt}{P_2(\underline{r}_2, \underline{v}_2, t) d\underline{r}_1 d\underline{r}_2 d\underline{v}_1 d\underline{v}_2 dt}\right] \end{aligned} \tag{9.3}$$

Three physical quantities are discussed throughout the experiment that are defined within this formalism:

- **mean scattering signal:** $f = \mathit{\Gamma}_f \cdot |\underline{v}_1 - \underline{v}_2|^2 \cdot \sigma(|\underline{v}_1 - \underline{v}_2|^2) \cdot \delta_{\underline{r}_1\underline{r}_2}$.
- **mean collision energy:** $f = \frac{\mu}{2}|\underline{v}_1 - \underline{v}_2|^2 \delta_{\underline{r}_1\underline{r}_2}$.
- **variance of the collision energy:** $f = \frac{\mu^2}{4}[\underline{v}_{rel}^2 - \langle\underline{v}_{rel}\rangle^2]^2 \delta_{\underline{r}_1\underline{r}_2} = \frac{\mu^2}{4}(\underline{v}_{rel}^4 - \langle\underline{v}_{rel}^2\rangle^2)\delta_{\underline{r}_1\underline{r}_2}$.

Appendix D: Theoretical differential cross section

Differential cross sections (DCS) are calculated for the rotationally inelastic excitation σ[F1(3/2,f,+) $\rightarrow$ F1(5/2,e,+)] and illustrates the product distribution in the CM frame. The DCS is given in dimensions of $[\AA^2/sr]$. In Figure 9.2 to the right graphs show calculations of the DCS at the collision energies of 89.25 cm^{-1}, 91.25 cm^{-1}, 93.25 cm^{-1}, 95.25 cm^{-1}, and 97.25 cm^{-1} [132]. At all collision energies the DCS shows preferentially a forward scattering. No considerable change in the DCS at 93.25 cm^{-1} is observed compared to the ones at other collision energies. The theoretically predicted shape resonance shows no effect in the DCS.

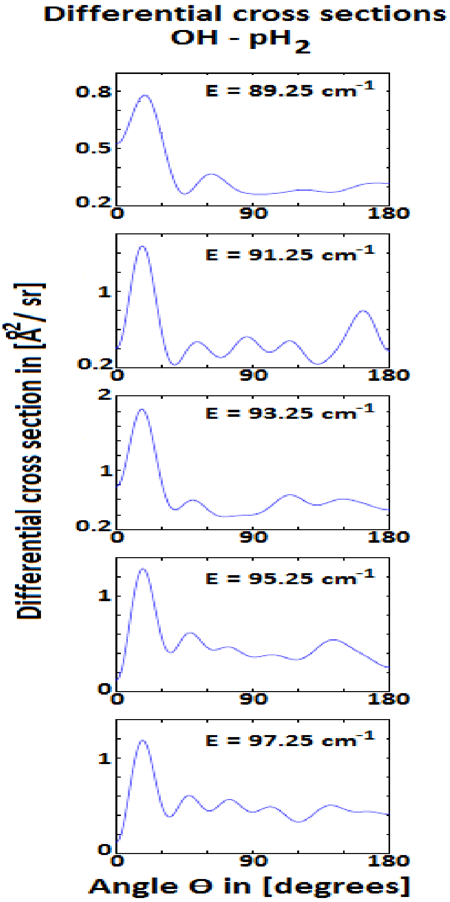

Figure 9.2

The graphs of Figure 9.3 show the comparison of calculated DCSs again at different collision energies of 89.25 cm^{-1}, 91.25 cm^{-1}, 93.25 cm^{-1}, 95.25 cm^{-1}, and

97.25 cm^{-1} around the (calculated) resonance at 93.25 cm^{-1} [132]. However in these graphs the DCS is split into different final substates of OH to be able to quantify an alignment after the collision. The alignment is defined (as usually) with respect to the z-axis in the direction of the incident OH packet. Although the laser is polarized perpendicular to this direction, it will be neverthelss obvious, if something interesting is happening due to alignment effects. The alignment is expressed by distinguishing the final OH substates with different values of $|m_j| = 1/2$, 3/2 and 5/2.

The DCS shows primarily forward scattering for the OH substates $|m_j| = 1/2$ and $|m_j| = 5/2$. The only variation is observed for the $|m_j| = 3/2$ substates of OH, where a mainly forward scattered DCS at 89.25 cm^{-1} changes to a much more backward scattered one at 97.25 cm^{-1}. If the DCS intensities in $[\AA^2/sr]$ of these changes in the DCS of $|m_j| = 3/2$ are compared with the other two substates of OH, the effect is small. Nothing special seems to occur at 93.25 cm^{-1}, neither as a function of the collision energy nor $|m_j|$ dependent.

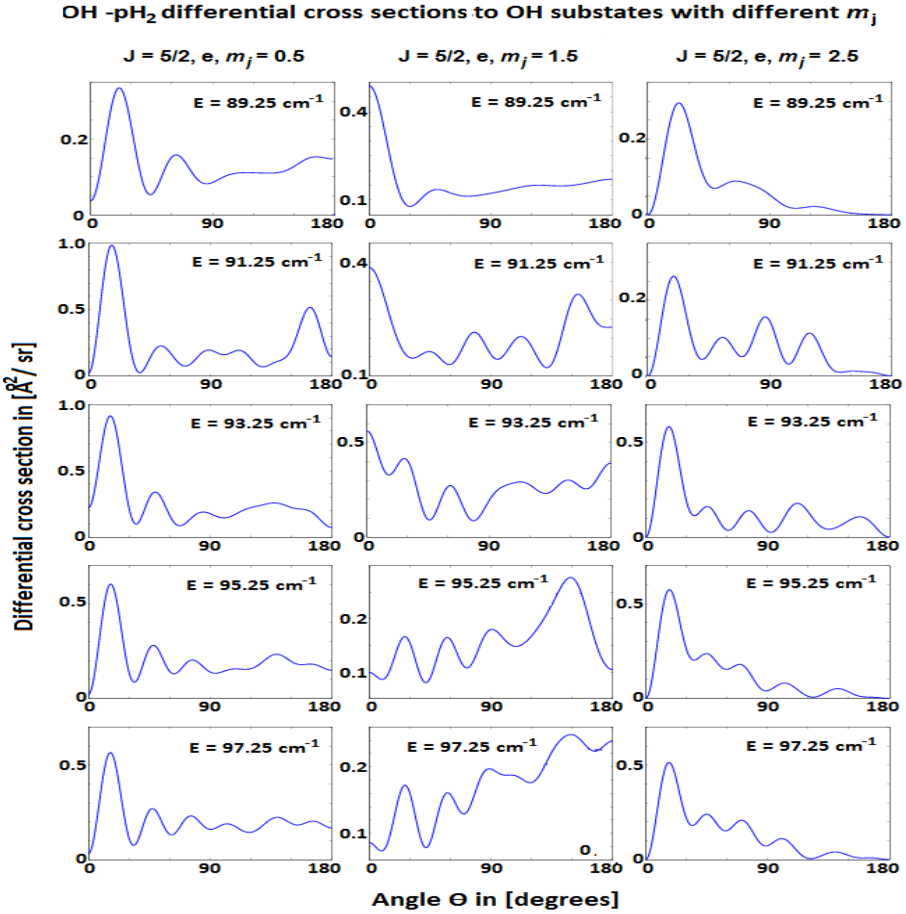

Figure 9.3: The DCS is calculated for each OH substate with different $|m_j| = 1/2, 3/2$ and $5/2$ and illustrated in the left, middle and right column of graphs, respectively. No dramatic changes in the DCS can be observed at lower or higher collision energies compared to the one at 93.25 cm^{-1}, where theory predicts a shape resonance.

Samenvatting

In dit proefschrift zijn verschillende experimenten beschreven die uitgevoerd zijn aan een bundel van hydroxyl (OH) radicalen, zowel hoge resolutie spectroscopische metingen als botsingsstudies. Deze experimenten benutten de extreme controle die een zogenaamde Stark-afremmer mogelijk maakt over de bundel van OH radicalen. In een eerste experiment, is een nieuwe methode gedemonstreerd om met behulp van een Stark-afremmer een nog betere controle te verkrijgen over alle externe vrijheidsgraden van de moleculaire bundel. Zowel de voorwaartse (longitudinale) als de zijwaartse (transversale) fase-ruimte verdelingen van het moleculaire pakket kunnen gemanipuleerd worden met specifiek hiervoor geoptimaliseerde schakel sequenties van de op de afremmer aangelegde hoogspanning. Zogenaamde "bunching"-schema's zijn voor beide richtingen geïmplementeerd, onafhankelijk van elkaar of gezamenlijk. Het gebruik van dergelijke bunching-schema's leidt tot een rotatie van de verdeling van de moleculen in de fase-ruimte, en zo kan een pakket moleculen – bij overigens gelijkblijvende fase-ruimte-dichtheid – opgerekt worden in de ruimte en gecomprimeerd worden in de snelheid. Op deze manier wordt een koeling van het moleculaire ensemble in de corresponderende richting (longitudinaal of transversaal) bewerkstelligd. Temperaturen die op deze manier bereikt kunnen worden zijn een fractie van een milli-Kelvin, minstens een grootte-orde lager dan temperaturen die bij "normaal" gebruik van een Stark-afremmer gehaald kunnen worden. Meer algemeen maken deze bunching-schema's het mogelijk om de vorm van de zes-dimensionale faseruimte-verdeling van een moleculair pakket zó te prepareren dat deze optimaal is voor het beoogde experiment.

In de spectroscopische experimenten is de intensiteit van de (zwakke) magnetische dipool-overgang in de $A{-}X$ band van OH nauwkeurig bepaald ten opzichte van de intensiteit van de elektrische dipool-overgang, ondanks het feit dat deze intensiteiten meer dan drie grootte-ordes van elkaar verschillen. In deze experimenten is een transversaal bunchings-schema gebruikt in de Stark-afremmer om de overblijvende Doppler verbreding in de moleculaire OH bundel verder te reduceren, en om aldus de spectrale resolutie te verhogen. De metingen zijn uitgevoerd in gecontroleerde statische magnetische en elektrische velden. Stark-spectroscopie in een gecontroleerd elektrisch veld is gebruikt om een eerste indicatie te krijgen van de verhouding van de groottes van de magnetische en elektrische overgangs dipool-momenten. Door tevens een gecontroleerd statisch magnetisch veld aan te leggen is er een interferentie tussen de magnetische en elektrische overgangen gecreëerd. De waargenomen interferentie maakt het niet alleen mogelijk om de verhouding van de groottes van de overgangs dipool-momenten extreem nauwkeurig te bepalen, maar het maakt ook het bepalen van de onderlinge richting mogelijk. De gebruikte methode – het meten van de intensiteit van het laser geïnduceerde fluorescentie signaal van OH in afhankelijkheid van de aangelegde externe velden – heeft als voordeel dat noch het laser vermogen, noch de fluorescentie detectie geijkt hoeven te worden. In de juiste combinatie van externe velden hebben de magnetische en elektrische dipool-overgangen een vergelijkbare intensiteit, en kan met de interferentie methode de relatieve intensiteit zeer nauwkeurig bepaald worden. De experimenteel gevonden verhouding voor de $A - X$ band in OH heeft een relatieve fout van slechts 2% en stemt binnen deze foutenmarge overeen met de theoretisch berekende waarde. Deze methode kan niet alleen gebruikt worden voor andere overgangen van het OH radicaal, maar is zeer algemeen toepasbaar.

In de botsingsexperimenten, kruist de bundel met snelheids- en toestands-geselecteerde OH radicalen ($X^2\Pi_{3/2}$, J=3/2, f) een bundel van waterstof (H_2) moleculen en zijn rotationeel-inelastische verstrooïingsprocessen bestudeerd. De waterstof moleculen bevinden zich in de laagste rotationele niveau's van de twee distinct verschillende kernspin configuraties die er zijn, namelijk ortho-H_2 (oH_2(J=1)) en para-H_2 (pH_2(J=0)). Door gebruik te maken van twee gas-mengsels met verschillende maar bekende concentraties van waterstof in elk van deze spin configuraties, is het mogelijk om de individuele bijdragen aan de inelastische botsingen van puur oH_2(J=1) en puur pH_2(J=0) te ontrafelen. Door de snelheid van de OH bundel te variëren, is het mogelijk geweest botsingen te bestuderen bij verschillende botsings-energieën in het gebied tussen 70 cm^{-1} en 150 cm^{-1}, het energie-gebied waarin de eerste rotationeel aangeslagen niveau's van OH zich bevinden. De experimenteel waargenomen relatieve botsingsdoorsnedes zijn sterk verschillend voor botsingen van OH met oH_2(J=1) en pH_2(J=0), wat goed overeenkomt met de uitkomst van geavanceerde quantummechanische berekeningen en wat verklaard kan worden door de verschillende multipool-interacties die in het botsingsproces een rol spelen. Het botsingsproces van OH radicalen met para-H_2(J=0) vertoont sterke overeenkomsten met het botsingsproces van OH met edelgas atomen en dit is kwalitatief verklaard.

Om de resolutie in de botsingsexperimenten te verhogen, is gebruik gemaakt van een meer optimale geometrie van de kruisende bundels dan de "standaard" geometrie van loodrecht kruisende bundels en is er tevens voor gezorgd dat de transversale snelheidsspreiding in de waterstof bundel verkleind is. Een kinematisch model is opgezet om de te verwachten energie resolutie als functie van de experimentele parameters, zoals de hoek waaronder de bundels elkaar kruisen en de longitudinale en transversale snelheidsspreiding in elk van de bundels, te kunnen voorspellen. Gedetailleerde Monte-Carlo simulaties zijn uitgevoerd om de botsingsenergie en de daarbij behorende energie resolutie te ijken. Zowel de Monte-Carlo simulaties als het experiment laten zien dat er een energie resolutie van beter dan 2 cm^{-1} bereikt kan worden. Met deze hoge energie resolutie is het mogelijk gebleken om scherpe, reproduceerbare structuren in de excitatie functie voor OH-pH_2(J=0) zichtbaar te maken. Hoewel de algemene vorm van de experimenteel bepaalde excitatie functie in het gebied tussen 80 cm^{-1} en 115 cm^{-1} goed gereproduceerd wordt door berekeningen, kan de waargenomen scherpe structuur in de excitatie functie vooralsnog niet verklaard worden.

Summary

This thesis describes high resolution spectroscopic measurements and collision studies that are carried out with a beam of hydroxyl (OH) radicals. These experiments exploit the extreme control that a so-called Stark-decelerator allows over the beam of OH radicals. In a first experiment, a new method is demonstrated in which a Stark-decelerator is used to better control all external degrees of freedom of the molecular beam. Both the forward (longitudinal) and the lateral (transverse) phase-space distributions of a packet of molecules can be manipulated with specially optimized timing sequences that control the high voltages applied to the Stark-decelerator. These so-called 'bunching'-schemes can be implemented for all directions, either independent of each other or simultaneously. The use of such bunching-schemes leads to a rotation of the distribution of molecules in phase-space and allows a packet of molecules to be stretched in real space and compressed in velocity-space, while the phase-space density remains constant. In this way, a cooling of the molecular ensemble in the corresponding direction (longitudinal or transverse) is obtained. Temperatures of a fraction of a milli-Kelvin can be reached in this way, which are at least one order of magnitude lower than temperatures obtained using the 'normal' mode of operation of a Stark-decelerator. In general, these bunching-schemes enable the preparation of the six-dimensional phase-space distribution of the molecular packet in a shape that is optimal for the intended subsequent experiment.

In the spectroscopic experiments, the strength of the (weak) magnetic dipole transition in the $A-X$ band of OH is accurately determined relative to the strength of the electric dipole transition, despite the fact that these strengths differ by more than three orders of magnitude. In these experiments, a transverse bunching-scheme is applied to the Stark-decelerator

to further reduce the Doppler broadening of the packet of OH radicals, to thereby increase the spectral resolution. The measurements are performed in well-defined static magnetic and electric fields. Stark-spectroscopy in a controlled static electric field is used to get a first indication of the ratio of the electric to the magnetic transition dipole moments. By additionally applying a static magnetic field, an interference is created between the electric and magnetic dipole transitions. The observed interference not only allows the ratio of the transition dipole moments to be determined extremely accurately, but it also enables the mutual direction of the transition dipole moments to be determined. The method used – the measurement of the intensity of the laser induced fluorescence signal of OH as a function of the strength of the applied external fields – has the advantage that neither the laser power nor the fluorescence detection needs to be calibrated. Using the appropriate strengths of the external fields, the magnetic and electric dipole transitions are of comparable intensity, and the interference method then allows the accurate determination of their relative intensities. The experimentally found ratio in the $A-X$ band of OH has a relative error of only 2%, and the theoretically calculated value agrees within this error margin. This method can be used not only for other transitions of the OH radical, but for other general applications as well.

In the crossed beam scattering experiments, rotationally inelastic collision processes between velocity-controlled and quantum state-selected OH radicals ($X^2\Pi_{3/2}$, J=3/2, f) and hydrogen (H_2) molecules are studied. The hydrogen molecules are in the lowest rotational levels of one of its two distinct nuclear-spin configurations, namely ortho-H_2 (oH_2(J=1)) or para-H_2 (pH_2(J=0)). By using two gas mixtures with different but known concentrations of these nuclear-spin configurations, it is possible to unravel the individual contributions of pure oH_2(J=1) and pure pH_2(J=0) to the inelastic scattering processes. By varying the velocity of the OH beam, it has been possible to study the scattering processes at a range of different collision energies between 70 cm^{-1} and 150 cm^{-1}, where the first rotationally excited levels of OH are located. The experimentally observed relative cross sections are very different for collisions of OH with oH_2(J=1) and pH_2(J=0), which agrees well with the outcome of advanced quantum mechanical calculations. It is the different multipole interactions, which play a role in the scattering process, that explain the observed differences. The scattering process of OH radicals with para-H_2(J=0) shows strong similarities with the scattering process of OH with rare gas atoms, and this is qualitatively explained in this thesis.

To increase the resolution in the scattering experiments, a more optimal geometry of the crossed beam setup is used, that differs from the 'standard' geometry in which the beams cross each other perpendicularly. In addition, the width of the transverse velocity distribution of the hydrogen beam is reduced. A kinematic model is developed to predict the expected energy resolution as a function of the experimental parameters, i.e., the actual angle at which the beams intersect and the widths of the longitudinal and transverse velocity distributions of both beams. Detailed Monte-Carlo simulations are carried out to calibrate the actual collision energy and the corresponding energy resolution. Both the Monte-Carlo simulations and the experimental data show that an energy resolution better than 2 cm^{-1} can be achieved. This high collision energy resolution has enabled the reproducible observation of sharp structures in the excitation function for OH-pH_2(J=0). Although the overall shape of the experimentally determined excitation function is reproduced well by the theoretical calculations in the range between 80 cm^{-1} and 115 cm^{-1}, the observed sharp structure in the excitation function can not be explained yet.